INFLUENCE OF BOUNDARY CONDITIONS ON THE HYDRAULIC-MECHANICAL BEHAVIOUR OF AN UNSATURATED SWELLING SOIL

by

Gregory Allen Siemens

A Thesis
Submitted to the Faculty of Graduate Studies
in Partial Fulfillment of the Requirements
for the Degree of

DOCTOR OF PHILOSOPHY

Department of Civil Engineering
University of Manitoba
Winnipeg, Manitoba

ABSTRACT

The hydraulic-mechanical behaviour of swelling clay is examined in this thesis. The study includes laboratory testing and numerical modeling which considers the influence of boundary conditions on the hydraulic-mechanical behaviour of a compacted unsaturated swelling clay soil.

The laboratory testing component of this research consists of three (3) series of tests using a newly modified triaxial apparatus on which mechanical and hydraulic boundary conditions are altered during liquid infiltration. Mechanical boundary conditions range from constant volume to constant mean stress and also include constant stiffness which is a spring type boundary consisting of both volume expansion and mean stress increase. Hydraulic boundary conditions include drained and undrained flow into triaxial specimens.

The numerical modeling component of this research includes the creation of a new capillary tube model for swelling clay materials and incorporates dynamic changes to the cross-sectional area for flow. Laboratory results are modeled using the capillary tube model, an empirical hydraulic model, D'Arcy's Law, and in an elastic-plastic context for unsaturated soil.

Results of the laboratory and numerical modeling components show that boundary conditions dominate the hydraulic-mechanical behaviour of unsaturated swelling clay soil during liquid infiltration. In particular, a mechanism is shown to explain how hydraulic conductivity of a swelling soil can decrease with increasing water content at constant void ratio. Finally hydraulic and mechanical behaviour cannot be considered separately in swelling materials due to the intimate relationship in their response.

ACKNOWLEDGEMENTS

Sincerest gratitude to my advisor Dr. James Blatz for his unending patience, encouragement, and mentorship during this program. Dr. Blatz made time for all my questions and provided support to me both personally and professionally. I thoroughly enjoyed being his grad student and look forward to working together with him in the future.

Thank you to the geotechnical professors including Dr. Jim Graham, Dr. Marolo Alfaro, and Dr. Jamie VanGulck for their friendship, advice, and encouragement.

Thanks to Kerry Lynch and Narong Piamsalee for fixing everything I broke in the laboratory as well as guidance and support. Thanks to Norma Lindsay, Glenda Phillips, Kathie Anderson, and Donna Parkhurst for their administrative support.

Thanks to the geotechnical graduate and summer students for their friendship, discussions, and assistance during this program. I would like to specifically acknowledge David Anderson, Deni Priyanto, Tim Krahn, Mike Van Helden, Neil Privat, Blake Holowick and Jared Baldwin for their assistance in the laboratory.

Financial support is acknowledged from the National Science and Engineering Research Council of Canada, Petro-Canada Resources of Canada, Department of Civil Engineering, Faculty of Engineering, Faculty of Graduate Studies, friends and colleagues of Neil Burgess, and Atomic Energy of Canada Limited.

A big thanks to my family: Ed and Vi Siemens, Tim and Wanda Kretchmer, Rachel Siemens, and Chad and Jolene Kretschmer for their love and support during my studies. Finally, thanks to my loving and supportive wife Sonya who has been a source of fun, support, and encouragement throughout our married life together. I look forward to the next step in our lives as we move to Kingston.

TABLE OF CONTENTS

LIST OF SYMBOLS AND ABBREVIATIONS

Symbols

δ - diameter of tube

δ_s - diameter of the tube in which the interface is located

Δ - change

ε_i - strain in the i^{th} plane

ε_v - volumetric strain

η - viscosity

μ_a - viscosity of Fluid 'a'

μ_b - viscosity of Fluid 'b'

ν - Poisson's Ratio

Π - osmotic suction

θ - contact angle

ρ - density of fluid (water)

ρ_d - dry density

σ - surface tension

- also standard deviation

σ_i - total stress in the i^{th} direction

σ_r - radial stress

σ^2 - variance of a fitted curve

ω - molecular mass of air

Ψ - total suction

A - area of flow

- also cross-sectional area

B - degree of bentonation

C - air concentration

d1 - initial main tube diameter

d2 - minimum main tube diameter

d3 - peripheral tube diameter

D - diffusion coefficient

e - void ratio $= (\text{volume of voids}) / (\text{volume of solids})$

E - Young's Modulus

f_c - clay fraction

f_m - montmorillonite fraction of clay

G_s - specific gravity

- also specific gravity of non-clay material

G_n - specific gravity of non-swelling clay

h - height of specimen

i - gradient

k - hydraulic conductivity

- also slope of tension line

l_a - distance from upstream end to water-air interface

L - length of tube over which flow is calculated

- also total length of tube

LC - load collapse line

L_s - length of the tube in which the interface is located

LY - load yield line

H - total head

m - mass of air

M - molecular mass of air

- also slope of critical state line

n - number of moles of gas

N_b - total number of serial sections

N_b^- - number of tubes upstream of the interface

N_b^+ - number of tubes downstream of the interface

p - mean stress $= (\sigma_1 + 2\sigma_2)/3$

p' - mean effective stress

P - gas pressure

	- gas pressure at water – air interface
p_a	- upstream pressure
p_b	- downstream pressure
$(p_c)_s$	- capillary pressure in the tube in which the interface is located
P_{cap}	- capillary pressure
P_e	- pressure applied at perimeter of specimen
p_{equil}	- equilibrium mean stress
p_o	- pre-consolidation pressure on constant suction plane
p_o^*	- pre-consolidation pressure at zero suction
p_s	- pressure just upstream of interface
P_{swell}	- 'swell pressure'
P_w	- pressure applied at inside radius of specimen
q	- deviator stress $= (\sigma_1 - \sigma_3)$
	- also flow rate
Q	- bulk flow
	- also equilibrium flow rate,
r	- tube radius
R	- universal gas constant
R^2	- multiple coefficient of determination
r_e	- outside radius of specimen
r_w	- inside radius of specimen
S	- suction
SI	- suction increase line
SY	- suction yield line
t	- time
T	- absolute temperature
T-Line	- tension line
u_a	- pore air pressure
u_w	- pore water pressure
V	- specific volume $= (1 + e)$

- gas volume

x - slope of mean stress/volume strain

Abbreviations

AECL - Atomic Energy of Canada Limited
AEV - air entry value
BBM - Barcelona Basic Model
BExM - Barcelona Expansive Model
BSB - bentonite sand buffer
CMS - constant mean stress infiltration test
CMSD - constant mean stress – drained infiltration test
CSC - critical swelling curve
CSL - Critical State Line
CS25 - constant stiffness (x = -25 kPa/% volume strain) infiltration test
CS75 - constant stiffness (x = -75 kPa/% volume strain) infiltration test
CV - constant volume infiltration test
DDL - diffuse double layer
DPT - differential pressure transducer
ECDD - effective clay dry density
EMDD - effective montmorillonite dry density
HITEP - High Temperature High Pressure
ITT - Isothermal Test
LVDT - Linear Variable Displacement Transducer
MIP - mercury intrusion porosimetry
PLC - programmable logic controller
RH - relative humidity
SEM - scanning election microscopy
SWCC - soil water characteristic curve
Swell rate - number of peripheral tubes/length of main tube
WC - gravimetric water content
WRC - water retention curve

LIST OF TABLES

LIST OF FIGURES

CHAPTER 1: INTRODUCTION

1.1 General Overview

Unsaturated soil mechanics considers soil to be a three component system that includes solid particles, liquid, and gas which are usually situated above the water table. Historically in engineering practice, soils have generally been considered as a two-phase system that is either fully saturated (solid particles and liquid) or fully dry (solid particles and gas). In typical engineering applications located near the ground surface, fully saturated or fully dry soils are the exception rather than the norm. Therefore, unsaturated soil mechanics is of considerable importance to practitioners and researchers around the world. Environmental factors play an important role in this zone since it is subjected to changes in water content due to daily and seasonal fluctuations in temperature, precipitation, relative humidity, and regional groundwater conditions. These environmental factors can change simultaneously and, in turn, alter the

mechanical, hydraulic, and thermal characteristics of an unsaturated soil. Geotechnical engineering applications that involve infrastructure in the near surface environment can be affected significantly by alterations in soil properties due to environmental factors.

A broad knowledge base exists in the literature to demonstrate the intimate linkage between water content and hydraulic-mechanical performance of high plastic clay soils (Fredlund and Rahardjo 1993, Alonso et al. 1990, Toll 1990, Wheeler and Sivakumar 1995, Delage and Graham 1995, Tang and Graham 2000, and others). In cases where high plastic clays are unsaturated, their behaviour is not only related to applied total stresses generated by engineering activities, but also to changes in water content that can occur over the operating lifespan of engineering works. As such, there is a need for replication of these physical conditions in controlled experiments over a wide range of scales so that appropriate constitutive parameters, required in numerical modeling, can be measured.

Traditionally in soil mechanics, bulk soil behaviour is modeled at the specimen scale or higher. One example is water movement through porous media which is interpreted using D'Arcy's Law (D'Arcy 1856). In the case of compacted high plastic unsaturated clays, bulk hydraulic and mechanical behaviour is dominated by swelling mechanisms occurring on the pore scale or at the molecular level (Mitchell 1993). Consideration of behavioural mechanisms occurring on these

smaller scales provides new understanding of the physics of unsaturated swelling soil behaviour. This, in turn, should lead to improvements in development of realistic constitutive models.

An important application utilizing unsaturated high plastic soils is waste containment. Currently much of unsaturated soils research, conducted throughout the world, is focused on this type of application. Swelling clay materials are often chosen as barriers for their self-healing capabilities. Barrier materials are designed to support waste, transfer thermal energy, inhibit groundwater movement, and restrict transport of waste products. Over their lifetime, compacted clay-based barriers could be subjected to changes in water content due to thermal and hydraulic gradients as well as stress changes. Under drying conditions swelling soils shrink due to increasing suction, while during wetting conditions they swell which may reduce permeability (Cui et al. 2001, Garcia-Bengochea 1979, Hoffman et al. 2006). Understanding how unsaturated materials behave when exposed to drying and wetting conditions in these engineering applications as well as the influence of micro scale mechanisms on bulk behaviour is extremely important considering the environmental implications associated with failure of waste containment barriers.

Currently proposed numerical models are continuously incorporating new theoretical relationships for constitutive behaviour (Alonso et al. 1990, Toll 1990, Wheeler and Sivakumar 1995, Alonso et al. 1999, Tang and Graham 2000, Blatz

and Graham 2003, Gallipoli et al. 2003, Datcheva and Schanz 2003, Garitte et al. 2006, Oka et al. 2006, Priyanto et al. 2006). At the same time, improved computing power provides the ability to solve increasingly complex problems more rapidly. There is a continued need for advanced testing methods to provide measured parameters, required in many of the models, which currently have to be assumed. The next logical step is to develop laboratory testing equipment as well as full-scale field tests to measure the physical response of soils. Test conditions should include total stresses and environmental conditions such as changes in water content and/or temperature. Interpretation of laboratory and field tests provide measured parameters to calibrate and validate numerical models which can then be used to predict behaviour in more general cases.

Accurate numerical models using parameters calibrated from physical measurements and developed based on an understanding of the physical behaviour occurring on a wide range of scales allows more accurate prediction of soil response. This could be possible even under widely varying conditions over extended periods of time. With new laboratory tests that provide general control of soil states, more accurate parameters can be generated for model input. Consideration of mechanisms occurring on the pore scale and lower gives new understanding as well as direction on development of future models and laboratory testing programs. Finally hydraulic, mechanical, and thermal behaviour in unsaturated high plastic clay materials cannot be considered in

isolation because of their intimately coupled relationship (Vu and Fredlund 2004). The current research provides a further step in understanding the behaviour of unsaturated compacted clay barrier materials. It is specifically focused on combined hydraulic-mechanical behaviour using laboratory experiments, constitutive modeling, and consideration of micro scale mechanisms which may dominate bulk soil behaviour.

1.2 Background

To properly understand the context of the current research program, a summary of work conducted at the University of Manitoba and Atomic Energy of Canada Limited (AECL) is provided in this section. It is important to note that although this work is focused on a specific material and application related to high level radioactive waste storage, the goal of this research is to better define fundamental behaviour of unsaturated swelling clay materials.

Research directed at defining the behaviour of high-plastic compacted clay materials at the University of Manitoba began in the late 1980's. Initially this work focused on definition of traditional stress-strain behaviour of a saturated clay-sand material and moved on to consider the impact of compaction, high pressure, creep, and temperature as well as the applicability of effective stress theory in this material (Sun 1986, Wan 1987, Saadat 1988, Oswell 1991, Yin 1990, Yarachewski 1993, Lingnau 1993, Tanaka 1995, Crilly 1996). Once saturated behaviour was well-defined, research turned to the unsaturated realm.

Again, initial efforts began by defining the stress-strain behaviour, this time considering the impact of suction, pressure, temperature, as well as development of the thermocouple psychrometer to measure the stress-state variable suction (Wan 1996, Tang 1999, Wiebe 1996, Blatz 2000, Anderson 2003).

Fluid movement in unsaturated and saturated materials has also been studied but largely has been considered separate from the mechanical behaviour. Water flow through saturated clay-sand material was analyzed under low gradients (Dixon 1995). Air pressure driven, two-phase flow through saturated and unsaturated material were also examined (Kirkham 1995, Gelmich Halayko 1998, Hume 1999).

Results of this extensive research program have provided elastic-plastic models for both saturated and unsaturated soil behaviour and new understanding of saturated flow and gas breakthrough behaviour. Simultaneous consideration of mechanical and hydraulic behaviour and their combined impacts is now the focus of the program.

During this same period, full-scale experiments were conducted at Atomic Energy of Canada Limited's (AECL's) underground research laboratory to provide data for calibration and validation of numerical models developed to predict the behaviour of proposed repository systems. One such experiment was the isothermal test (ITT) that monitored behaviour during flow of groundwater into

a borehole filled with a swelling clay-sand mixture (Dixon et al. 2002b). Results show swelling occurring at the rock-soil interface combined with an increase in density at the center of the borehole. Attempts to model transient water uptake and final distribution of phase properties in the ITT (Thomas et al. 2003) have been unsuccessful using traditional hydraulic conductivity variation that assumes an increase in hydraulic conductivity with increasing water content. During this modeling procedure, the influence of the boundary conditions on the hydraulic-mechanical swelling soil behaviour was not considered explicitly. Another aspect which was not considered was the undrained air phase. Experimental results could only be matched in the numerical model through modification of the hydraulic conductivity function as shown in Figure 1.1. The modified curve has hydraulic conductivity increasing with saturation from 0-85% above which hydraulic conductivity decreases several orders of magnitude. Conventional understanding observes increasing hydraulic conductivity with increasing saturation due to higher connectivity of the water phase. Even though the authors admitted that the modified conductivity function was 'unconventional' in nature, the end of test water contents could not be matched to the test measurements in any other way. This was assumed, despite the fact that hydraulic conductivity measurements on samples taken during the decommissioning of the ITT showed no change in their hydraulic behaviour (Dixon et al. 2002b). To better understand mechanisms occurring during these types of large-scale experiments, field simulated conditions should be applied in the laboratory ensuring all soil states are controlled and/or measured.

To apply these field simulated conditions in the laboratory, infiltration boundary conditions must be understood and conceptualized. The example illustrated is specific to high level waste repositories but the boundary conditions encountered are consistent with many typical engineering applications. In a nuclear waste repository the temperature of waste containers immediately following emplacement could be greater than the surrounding engineered barriers and host rock. During thermal energy release, water is expected to move away from the container resulting in drying conditions near the container and water content increase near the soil-rock interface. After an extended period of time, the regional groundwater recovers and water infiltrates into the repository.

Boundary conditions which could occur during water infiltration into an underground waste repository are shown in Figure 1.2. During the water infiltration phase, three (3) mechanical boundary conditions are identified. Near the container, there is room for soil expansion due to previous shrinkage following container emplacement and drying. This is a constant mean stress boundary condition. During infiltration the soil must support the container and gaps for swelling should be available due to the previous shrinkage. At the soil-rock interface, a constant volume boundary condition exists since the soil near the rock has limited room to expand during infiltration. Any volume available for expansion is due to compaction compliance during placement. Between the extreme boundary conditions, expansion occurs against a flexible

spring type boundary. The stiffness of the boundary depends on the proximity relative to the constant mean stress and constant volume conditions. As the soil expands in this area, resistance to expansion increases since the overall volume of the repository is essentially constant.

This research program is aimed at understanding the hydraulic-mechanical behaviour of unsaturated swelling clay during water infiltration under controlled boundary conditions. This program includes both laboratory testing and numerical modeling. A testing apparatus was modified to apply radial flow conditions in the triaxial cell. This apparatus allows for control and/or measurement of unsaturated state parameters including mean stress (p), suction (S), volume (V), and deviator stress (q). Boundary conditions can be applied during infiltration in order to define a volume change – equilibrium mean stress relationship. The numerical modeling aspect of this research includes the development of a capillary tube model that incorporates a swelling mechanism, as well as interpretation of laboratory results. The capillary tube model applies flow through an individual flow path that reduces in area as water flows along its length. Capillary tube results are compared with laboratory data in order to determine if it is capturing observed behaviour. To the author's knowledge both the automated triaxial testing and this type of capillary tube model have never been performed before in the context of swelling soil media.

1.3 Hypotheses and Objectives

The purpose of this research program is to investigate the influence of boundary conditions on the behaviour of unsaturated compacted swelling clay. This program includes two major areas of work: laboratory testing and numerical modeling. As a result, two hypotheses are presented that are intimately related. The first hypothesis provides the basis for the physical experiments while the second hypothesis provides a basis for the numerical models' ability to represent the physical tests. The hypotheses and research objectives are summarized in this section.

Hypothesis #1

Mechanical boundary conditions dominate the behaviour of a compacted unsaturated swelling clay-sand soil that is subjected to liquid infiltration. Boundary condition effects can cause compacted swelling clay to decrease in permeability while at constant volume (void ratio).

Hypothesis #2

Boundary conditions and a swell mechanism control the flow of water through a capillary tube which incorporates transient changes to its diameter.

To examine the two hypotheses, the objectives of this research program are divided in two main areas: laboratory testing and modeling (as summarized below).

Laboratory Testing Objectives:

1. To modify a triaxial testing apparatus to provide new capabilities of imposing liquid infiltration while measuring and/or controlling stress-state parameters including mean stress, suction, volume, and deviator stress. The testing apparatus includes a new suction measurement device, with a wide range of measurement, which is embedded inside triaxial specimens.
2. To perform constant volume, constant stiffness, and constant mean stress infiltration tests on swelling clay using the modified apparatus with new capabilities. These tests are automatically performed by a custom data acquisition/control system developed for the triaxial apparatus.
3. To measure the end of test spatial distribution of gravimetric water content and bulk density to calculate dry density and saturation following constant volume, constant stiffness, and constant mean stress infiltration tests.
4. To compare volume, mean stress, water uptake, and suction response during constant volume, constant stiffness, and constant mean stress infiltration tests, as well as internal spatial distributions of phase relationships in test specimens.

Modeling Objectives:

1. To create a capillary tube model for flow through swelling soil. To represent the soil's swelling nature during water uptake by reducing flow area as water moves along the tube. The model is to allow control of

upstream and downstream boundary conditions, the ability to close the downstream end of the tube structure, as well as incorporate diffusion of air through water.

2. To perform a series of capillary tube models to examine the impact of geometry, swell rate, and boundary conditions on material performance.
3. To model infiltration results from the experimental laboratory testing program using the capillary tube model, an empirical hydraulic model, and D'Arcy's Law.
4. To interpret laboratory tests using constitutive models combined with the capillary tube model.

1.4 Organization of Thesis

The thesis is organized as follows: Chapter 2 provides a literature review required in order to understand the work and concepts presented in this thesis. The materials and preparation procedures are presented in Chapter 3. Chapter 4 summarizes the equipment used in the research program. Development of the modified triaxial apparatus is discussed in Chapter 5 followed by examination of the laboratory results from infiltration tests in Chapter 6. Chapter 7 provides the development of the new capillary tube model followed by presentation of the capillary tube model results in Chapter 8. Numerical modeling using hydraulic and using an elastic-plastic context is summarized in Chapter 9 to bring together the results of the preceding chapters. Finally Chapter 10 summarizes the conclusions and recommendations of this

research program comparing them to the original objectives and hypotheses. Future research direction and work recommended to further this area of study are presented.

1.5 Co-Authorship

This study was initiated by Dr. James A. Blatz. Greg A. Siemens modified the testing apparatus, conducted the laboratory tests, created the capillary tube model, interpreted the results and wrote the manuscripts under the supervision of Dr. James A. Blatz. Parts of Chapter 3, Chapter 4, Chapter 5 and Chapter 6 were published as annual reports to Ontario Power Generation (OPG) co-authored by Blatz and Siemens (2004, 2005, 2006). Descriptions and development of the laboratory testing equipment provided in Chapter 4 also appear in manuscripts prepared for ASCE Geotechnical Journal of Geotechnical and Geoenvironmental Engineering and Canadian Geotechnical Journal co-authored by Greg A. Siemens and James A. Blatz as well as presented at the Fourth International Conference on Unsaturated Soils held in Carefree, Arizona 2-6 April 2006 co-authored by Greg A. Siemens, James A. Blatz and Deni G. Priyanto. Chapter 6 is a modified manuscript of the one prepared for the American Society of Civil Engineer's Journal of Geotechnical and Geoenvironmental Engineering co-authored by Greg A. Siemens and James A. Blatz. Chapter 7 and Chapter 8 is the current manuscript for a paper in preparation to be submitted to the Canadian Geotechnical Journal co-authored

by Greg A. Siemens, James A. Blatz and Doug Ruth. Finally Chapter 9 is a draft manuscript in preparation for submission to a journal.

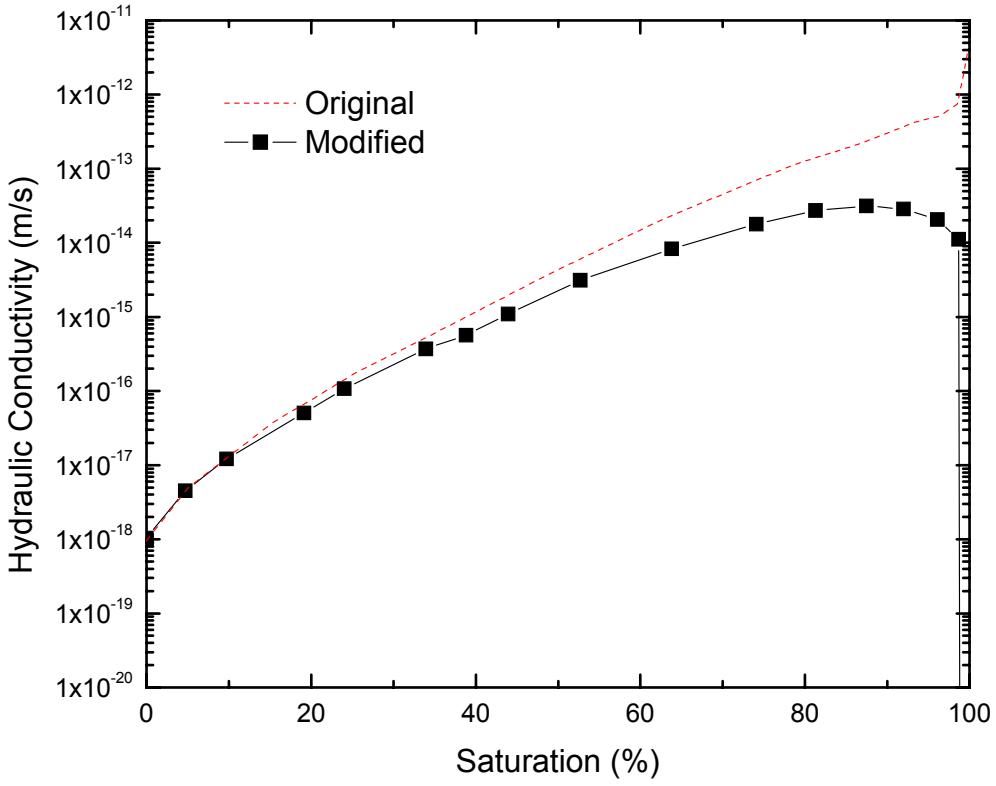

Figure 1.1. Original and modified hydraulic conductivity curve used to model the isothermal test (ITT) (after Thomas et al. 2003).

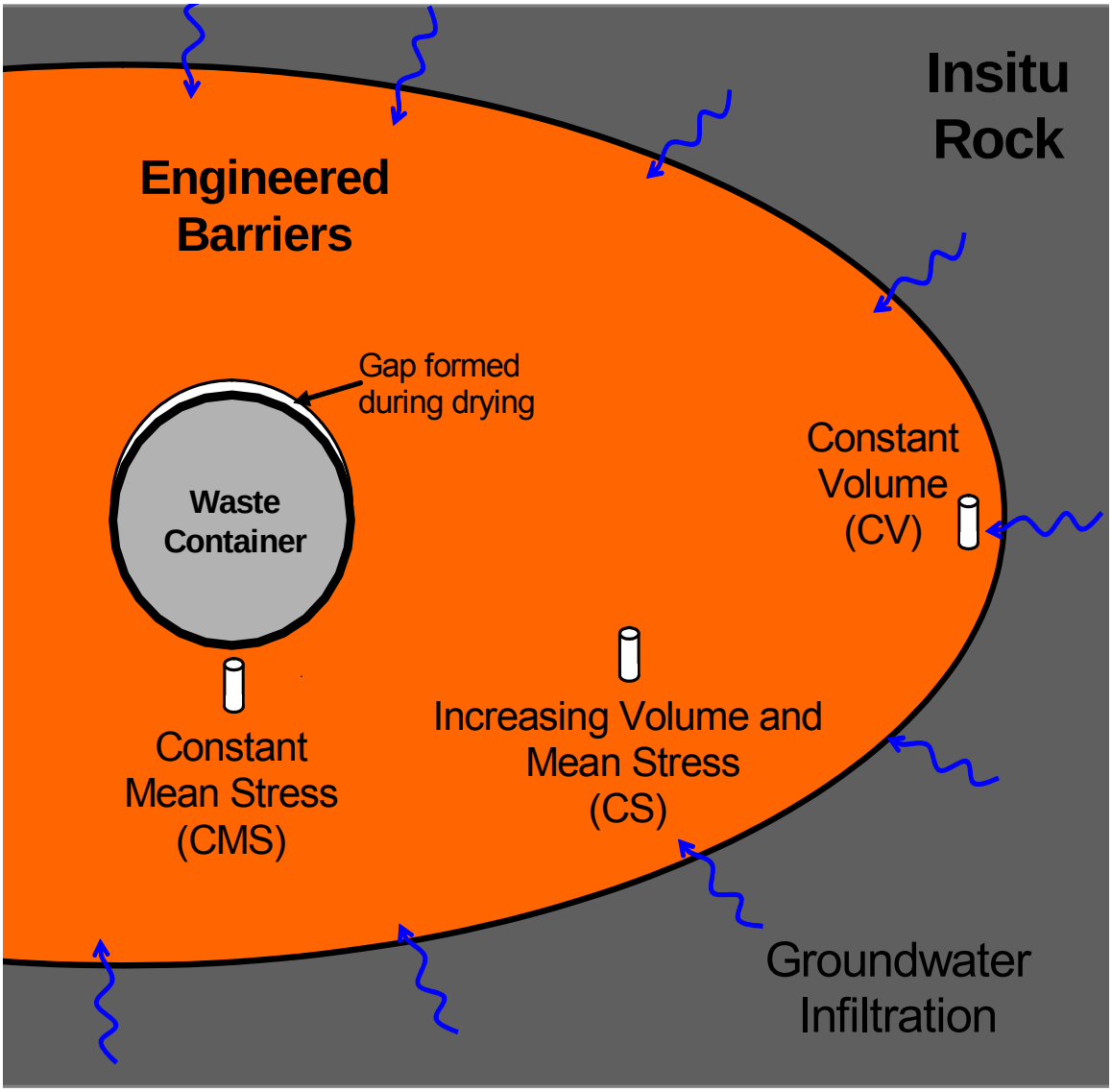

Figure 1.2. Infiltration boundary conditions in a deep underground waste repository.

CHAPTER 2: LITERATURE REVIEW

2.1 Introduction

The focus of this thesis is the examination of the behaviour of unsaturated compacted swelling clay soil during infiltration under controlled boundary conditions. The goal is to provide the necessary experimental measurements and theoretical basis to support development of a fully coupled hydraulic-mechanical framework on which to model unsaturated compacted clay materials. This framework is based on a fundamental understanding of the physical behaviour occurring at scales ranging from the molecular to the pore to laboratory and larger. This chapter summarizes a review of the relevant literature to provide a background on clay mineralogy and soil structure, soil suction, swelling soil behaviour, flow in porous media, and mechanical modeling of unsaturated soil that is pertinent to the understanding and interpretation of the experimental and numerical evidence presented in this thesis. The review

provides a background for the motivation of the research reported in this thesis and is followed by a justification for that research.

2.2 Clay Mineralogy and Soil Structure

Mineralogy and structure form the building blocks from which soils are constructed. In expansive materials these building blocks also change in size as a result of molecular processes. From a bulk soil perspective, volume changes and/or induced stresses occur depending on the boundary conditions imposed, thus affecting its hydraulic and mechanical performance. This section presents the state of our understanding of clay mineralogy and structure which may dominate features of large-scale behaviour.

2.2.1 Clay Mineralogy

Large scale hydraulic-mechanical behaviour of porous media is governed by mechanisms which occur on a microscopic scale (Mitchell 1993). In clay dominated soils (clay fraction approximately greater than 25%), clay mineralogy generally dominates overall behaviour. In swelling clay soils, which is the focus of this research, expansion and contraction occurs on the particle level during conditions of wetting and drying respectively (Mitchell 1993).

Common clay minerals are known to be swelling including montmorillonite, vermiculite, halloysite, and chlorite. The clay used in this research is composed

mainly of montmorillonite, which is one of the main classes of swelling minerals, and therefore its mineralogy is reviewed in detail.

The building blocks of swelling clay particles are relatively large sheets composed mainly of silica, aluminium, oxygen, hydrogen, and magnesium molecules (Mitchell 1993). The two (2) main types are phyllosilicate sheets composed of silica and oxygen, and octahedral sheets composed of oxygen, hydrogen, as well as aluminium and/or magnesium as shown in Figure 2.1. Montmorillonite, also displayed in Figure 2.1, is known as a 2:1 clay mineral with one octahedral sheet of aluminium and magnesium between two (2) phyllosilicate sheets. Combined they form a single montmorillonite particle (Mitchell 1993).

The faces of montmorillonite particles are negatively charged due to their chemistry and formation. The main source of net negative charge is generally isomorphous substitution of magnesium for aluminium in the octahedral sheet. To satisfy the overall negative charge of the particle, interlayer cations are present between the neighbouring clay particle faces. The distribution of cations and anions adjacent to the clay molecular face is known as the diffuse double layer (DDL) (Gouy 1910, Stern 1924). The DDL consists of three (3) parts including the negatively charged surface of the clay particle, the Stern layer which consists of only cations, followed by the Gouy layer which consists of both cations and anions. The net charge of the DDL is zero as the total number of

positively charged particles equals the negatively charged ones. The thickness of the DDL is a function of temperature, concentration of cations, valence of the cations, and charge of the clay particle (Mitchell 1993). Under isothermal conditions, possible changes to the thickness of the DDL are the result of altering the number (or concentration) of cations or altering the valence through replacement of existing cations with ones that have higher or lower charge.

The particular bentonite mineral used in this research is named Wyoming Bentonite although it could have been mined in the states of Wyoming, Montana or, South Dakota. Bentonite was formed from volcanic ash which was deposited into salt water lakes during the Cretaceous Period (67-144 Ma ago) (Slaughter and Earley 1965). The ash came from volcanic activity in the Western Cordillera in North America and was blown east by the prevailing winds. Bentonite deposits have been found as far north as Saskatchewan. They were originally deposited in salt water lakes which covered central North America at the time. The ash deposits were covered and buried, and later altered to form bentonite (Slaughter and Earley 1965).

The swelling exhibited by montmorillonite is caused due to replacement of cations in the DDL with water molecules. Although water molecules have no net charge their dipolar nature gives them the ability to satisfy the clay particle's net negative charge by orientating their axis to allow the hydrogen atoms to interact with the mineral surface. Cations are preferred by the DDL instead of water but

in their absence water is accepted; this leads to expansion. Increasing the water content of a montmorillonite dominated material results in increased availability of water molecules for the DDL and leads to further expansion. Decreasing water content of the same material results in shrinkage. Increasing pore fluid salinity reduces the swell potential of swelling materials (Dixon et al. 2002a) and corresponds to a reduction in the size of the DDL (Gouy 1910, Stern 1924).

The features discussed to this point are related to the specific minerals and their physical properties. The following section focuses on how the particles interact.

2.2.2 Soil Structure

Soil structure at the micro scale drives large scale hydraulic and mechanical behaviour (Barden and Sides 1970). In both swelling and non-swelling compacted clay-sand materials, multi-modal pore size distributions have previously been observed (Garcia-Bengochea et al. 1979, Juang and Holtz 1986). Mercury Intrusion Porosimetry (MIP) results on a bentonite-sand material are shown in Figure 2.2 (Wan 1996) and a schematic of a micro and macro pore model is illustrated in Figure 2.3. The bimodal distribution has peaks at pore sizes of approximately 0.014 μm and 14 μm levels.

The bimodal pore size distribution is due to both hydration of the particles and the energy used during compaction. During initial hydration, highly plastic clays form peds, or groups of clay particles (Figure 2.3). Pores within individual peds form the micro porosity (also known as intra ped pores). Micro porosity

properties, including size and particle distribution, are a function of the water content during preparation (Wan et al. 1990). The size of the micro pores has been reported to be on the same order as that of the clay particles (Young and Warkentin 1975, Mitchell 1993, Hillel 1980). Water content during mixing has also been found to alter the water retention curve or soil water characteristic curve (WRC or SWCC, Blatz et al. 2002), which is likely due to the change in ped properties.

During compaction the macro porosity is formed as a function of the energy used. Macro porosity (also known as inter ped pores) comprises the space between peds (aggregation of clay minerals) and its distribution is a function of the compaction effort (Wan et al. 1990).

2.3 Soil Suction

Traditional soil mechanics considers soil to be a two-phase system which is either fully saturated (soil and water) or fully dry (soil and air). Two-phase systems are the exception rather than the norm in geotechnical engineering applications that occur in the near surface environment above the water table. Under hydro-static conditions and moving up from the water table, negative pore pressure (suction) is observed but the soil remains a two-component system until the air entry value (AEV) is reached (Corey 1977). Above this point, soil is a three-phase system including solids, water, and air. A schematic of an element of unsaturated soil with the three (3) components is shown in Figure 2.4a.

The generic term ‘suction’ has been used up to this point somewhat liberally. In this program the term ‘suction’ refers to total suction, which includes two (2) main components. Total suction is composed of two (2) constituent components: matric suction and osmotic suction. Summed together they are known as total suction as shown in the expression

$$\Psi = (u_a - u_w) + \Pi \qquad [2.1]$$

where

Ψ = total suction,

u_a-u_w = pore air pressure - pore water pressure = matric suction, and

Π = osmotic suction.

It is important to explicitly note what type of suction is being discussed. Matric suction is a function of the tension forces that exist as a result of negative pore pressures in unsaturated soil, while osmotic suction is a function of the pore fluid chemistry. Often the term suction is loosely used in reference to any one (or all) of these components interchangeably. Strictly speaking, one of total, matric, or osmotic suction should be used explicitly to avoid potential confusion.

Total suction results in tension forces between the pore fluid and the surrounding soil. The tension forces also affect the movement of water molecules into the surrounding air space. As such, the relative humidity of air in equilibrium with the

surrounding soil can be related to the total suction. Air in equilibrium with a saturated soil that has no dissolved salts has relative humidity equal to 100% (Ridley and Wray 1996). This is similar to the air space above distilled water in a closed environment. When negative pore pressures are observed, or dissolved salts are present in the pore fluid, water molecules are pulled out of the surrounding air and its relative humidity decreases below 100%. From thermodynamics, the relationship between total suction and relative humidity, known as the Kelvin equation, is

$$\Psi = -\frac{RT}{M}\ln(RH) \qquad [2.2]$$

where

R = universal gas constant,

T = absolute temperature,

M = molecular mass of air, and

RH = relative humidity.

A plot of the relationship is shown in Figure 2.5. Researchers throughout the world have created new methods for suction control and measurement by exploiting this connection. Notable non-linearity in the RH – total suction plot is shown in the inset on Figure 2.5. This shows the need for high accuracy in relative humidity instruments used to infer suction when measuring in this range.

Fredlund and Morgenstern (1977) presented evidence that soil suction is an independent state variable. State variables are defined as a group of non-material variables that are sufficient to describe the behaviour under consideration. Independent state variables are ones that are not related to each other. Null tests were performed by varying pore air pressure and pore water pressure in such a way that no net change in soil strength was anticipated. Results showed that, in fact, this was the case and suction is accepted by many as a fully independent stress state variable. Because of this, suction should be controlled and/or independently measured throughout testing consistent with other stress and volume states. Some disagree that soil suction is incontrovertibly a stress state variable and add material properties such as the chi parameter (Bishop 1959, Wheeler et al. 2003, Murray 2002) to the calculation of strength and deformation. This changes the stress state equation to a constitutive equation due to the addition of a material property. Attempts to measure values for these material properties produce illogical results (Fredlund and Morgenstern 1977).

2.3.1 Matric Suction

Matric suction is a measure of the energy required to move water in unsaturated soil (Ridley and Wray 1996). It is the summation of the tension forces that result from the two-phase interactions with the solid particles or between a single fluid and solid particles if suction is less than the AEV. Matric suction occurs at the interface between the water and air components where a meniscus develops due to surface tension effects. A simplified model for matric suction is shown as a

capillary tube immersed into a flat surface of water in Figure 2.4b. As a result of capillary forces, water rises into the tube and a meniscus develops at the water-air interface. The force required to hold the volume of water above the surface of the body can be calculated to determine the suction level developed. The suction force is a function of the size of the capillary tube, the angle of the meniscus with the capillary tube, and the fluid properties of the water and air. In the soil element shown in Figure 2.4a several menisci are shown. Matric suction is the summation of the water-air capillary forces which act on the soil grains. These additional forces affect the strength, deformation, and flow behaviour compared with saturated soil (Fredlund and Rahardjo 1993).

The simplified capillary tube model has been extended to predict suction in materials based on their pore size distribution. The equation which describes suction formed in a capillary tube is

$$P_{cap} = \frac{4\sigma \cos\theta}{\delta} \qquad [2.3]$$

where

P_{cap} = capillary pressure,

σ = surface tension,

θ = contact angle, and

δ = diameter of tube.

From a measured pore size distribution, the suction at specific saturations can be estimated using numerical approximations such as those proposed by Fredlund and Xing (1994). Although there has been some success using these distributions for inert soils, they have not performed well for shrink/swell soils such as the one used in this study. This is likely due to the high activity of the clay particles.

2.3.2 Osmotic Suction

Osmotic suction is the result of pore fluid chemistry creating tension between the fluid and surrounding soil (Ridley and Wray 1996). Air in equilibrium with a mass of water with dissolved salts has a relative humidity less than 100% (Stokes and Robinson 1948). Pore fluid that has dissolved salts has a similar reaction with surrounding air and results in osmotic suction exerted on surrounding soil. It has been reported that the relative effects of osmotic suction compared with matric suction can be assumed to be equal (Ridley and Wray 1996) although no quantitative evidence has been identified. Although pore fluid chemistry affects the behaviour of unsaturated soil, it is questionable to assume that osmotic suction effects equal matric suction effects without evidence.

2.3.3 Water Retention Curve (Soil Water Characteristic Curve)

The water retention curve, also known as the soil water characteristic curve (WRC or SWCC), is arguably the most important relationship developed in the field of unsaturated soil mechanics. The WRC links soil suction to the quantity of water present in the soil and can be expressed as gravimetric water content,

volumetric water content, or degree of saturation. A typical WRC, including drying and wetting curves, is shown in Figure 2.6 and can be divided into three (3) sections. Beginning with the drying curve at the saturated end, the first section has very little reduction in water content with increasing suction. Assuming air pressure is zero, this represents the area above the water table where soil suction exists but the soil is still a two-component system composed of only solids and water (Fredlund and Rahardjo 1993). The second section begins at the air entry value (AEV) and is characterized by decreasing water content with increasing suction. The third section begins at the reduction in slope at what is termed the residual water content. In this section, little reduction in water content is observed. In the three (3) sections, distinct modes of water and air are found. In the first section, continuous water phase with discontinuous air phase is observed. In the second section both phases are continuous while in the third section the air phase is continuous while the water phase is discontinuous.

The wetting curve begins at the highest suction where water content increases and suction decreases and is the same as the drying curve in the third section. In the second section, the wetting curve plots at lower water contents for the same suction. This phenomenon is known as hysteresis in the WRC and is the result of the drying and wetting processes taking different pore size paths from start to finish. One explanation often stated is the ‘bottle neck’ effect where large pores are surrounded by smaller ones. During increasing suction (drying), the

small surrounding pores are not penetrated and thus keep the larger inner pore filled. During decreasing suction (wetting), the larger pores fill last. This mechanism results in the drying curve being at higher water content than the wetting curve.

2.3.4 Suction Measurement

Measurement of suction is extremely important in the understanding of unsaturated soil behaviour. If we accept that suction is a stress-state variable (Fredlund and Morgenstern 1977), it must be measured and/or controlled during all phases of testing. Many instruments exist to measure suction and they can broadly be divided into direct and indirect methods. Methods to explicitly measure osmotic suction do not exist at this time. Therefore either matric or total suction is measured, and then osmotic suction can be calculated or assumed if present.

Direct methods for measuring suction must include intimate contact with the soil as they measure the energy to move fluid in the soil (Ridley and Wray 1996). As such, direct methods are measuring matric suction. The instrument used most often to measure matric suction is the tensiometer. Many types of tensiometers exist and they consist of three (3) basic parts including a porous media that is placed in direct contact with the soil, a reservoir for fluid, and an instrument for measuring the pull of the fluid out of the reservoir and into the surrounding soil.

The tensiometer is generally limited in suction range to less than about 90 kPa because at this negative water pressure air bubbles appear in the reservoir. The bubbles are likely due to small imperfections in the reservoir walls (Ridley and Wray 1996). These air bubbles must be removed in order for any further measurements to take place. Greater suction levels have been measured by pre-pressuring reservoirs to compress the air bubbles and keep them in the imperfections of the reservoir walls but tensiometer measurements are still limited to a relatively lower suction range.

Indirect methods measure another property associated with the soil which is then used to infer total suction. This may include measurement of relative humidity of air in equilibrium with soil, electric or thermal conductivity, resistivity of the soil, or water content. Instruments are initially calibrated against known values and then installed in the soil.

Psychrometers have been used to measure suction since Spanner (1951) introduced the thermocouple psychrometers while working in the field of plant physiology. Psychrometers are used to measure relative humidity of air assumed to be in equilibrium with surrounding soil. Total suction is then calculated from thermodynamics as shown in [2.2]. Psychrometers have been used in field tests (Dixon et al. 2002b) as well as inside triaxial specimens during experimental testing (Wan 1996, Blatz 2000). The main drawback of the psychrometer is the limited range of measurement from about 1-8 MPa total

suction. Previous studies have been limited by this suction measurement range (Blatz and Graham 2003). Suction measurement in the low suction range (<1 MPa) is also difficult in general using relative humidity sensors. This is due to the significant non-linearity that exists in the relative humidity – total suction relationship in this range, as identified in Figure 2.5. Small errors in relative humidity measurement in this range can result in relatively large suction measurement inaccuracies.

Another group of indirect suction measurement instruments are those that measure properties of a substance placed in contact with soil. These include the filter paper method, where water is allowed to move from the soil to the filter paper. Measuring the change in mass of the filter paper allows for calculation of soil suction. Another example is the thermal conductivity sensor. In these types of instruments, a porous ceramic is placed in contact with the soil and water movement into the ceramic occurs. Thermal conductivity of the ceramic is affected by the water content. Calibrating the thermal conductivity of the ceramic with known values of suction allows for indirect measurement of soil suction. The WRC for the material placed in contact with the soil must be known to use this methodology.

A final method used to determine total suction is to measure water content using Time Domain Reflectometry (TDR) (Topp and Davis 1982) and then calculate total suction using the WRC. In this case, the instrument must be calibrated with

the soil and the soil's WRC must be known. Due to hysteresis, the process occurring (either wetting or drying) must be known and incorporated into the calibration and calculation of suction.

A consideration when choosing an instrument for measuring suction is the size of the sensor. The size of the sensor must be small enough, relative to the surrounding material, that its affect on behaviour is minimized. This is especially important in laboratory testing devices where relative sizes and impacts of specimen and sensor must be considered.

2.4 Swelling Soil

Swelling soils are found throughout the world and have both positive and negative effects associated with their swelling properties. Destructive effects to infrastructure have been reported on the order of billions of dollars per year (Jones and Holtz 1973). On the positive side, the self-healing abilities of swelling soils are exploited in the development and design of waste repositories. Compacted swelling clay materials are often used in these applications. As water attempts to transport waste materials into the biosphere the soil swells in response to increasing water content and reduces its conductivity.

Currently, nuclear waste repository concepts are being developed throughout the world and are using compacted swelling clay-based materials. These materials are compacted in an unsaturated state and subjected to conditions over a

long-range of time, including extremely high heat followed by groundwater infiltration while the repositories cool. Currently, waste storage technology research is driving unsaturated soils research for compacted clays around the world. Countries are exploring the use of specific materials and geological formations found in their area. In Canada, current concepts include a long-term waste repository to be located deep underground in a stable granitic deposit (Russell and Simmons 2003, Maak and Simmons 2005). In this concept, waste containers would be surrounded by compacted clay-based materials which are designed to support the containers, conduct heat to surrounding rock, limit container corrosion, and minimize movement of waste materials into the biosphere. Significant research has been performed at the University of Manitoba on compacted clay materials as described in Chapter 1.

2.4.1 Theoretical Predictions of 'Swelling Pressure'

Predictions of 'swelling pressure' are based on DDL theory because the molecular activity of the clay particles can be directly related to the stresses induced under zero volume change conditions. In these calculations, assumptions must be made as to the orientation of the clay particles.

Tripathy et al. (2004) reported on 'swelling pressures' of compacted bentonites. They summarized previous work which suggested that at low dry densities, theoretical predictions overestimate 'swelling pressures' compared with experimental measurements. At high dry densities the opposite was observed to be the case. Their work consisted of making corrections to the relationship

between a midplane potential function and nondimensional distance function relationship. The corrections involved back calculating the midplane potential function from the experimentally measured values, calculating the error between the original midplane potential function and nondimensional distance function, followed by subtracting the error from the original theoretical prediction to gain new functions. Not surprisingly, the calibration process resulted in good predictions for those materials over various ranges of average valence. For verification, the corrected equations were used to calculate 'swell pressures' for materials using their average valence and found to be good predictors although the range of average valences in the verified soils was only from 1.46 – 1.66 and the three (3) calibration equations were valid on average valence ranges of 1.14 – 1.50, 1.66 – 1.73 and 1.97.

Theoretical predictions of 'swelling pressure' ignore the intimate relationship between volume change and swelling induced pressure and are unable to predict volume changes if constant volume boundary conditions are not imposed. Understanding the theory behind volume change due to altering water content is important, but these predictions must be backed up with experimental evidence. As shown above, even the predictions need to be corrected as the laboratory results do not match the theory. Therefore, applying changes in water content in the laboratory and measuring and/or controlling stress and volume states is the best alternative to be able to predict the behaviour of swelling clays under general loading conditions.

2.4.2 Laboratory Testing of Swelling Soils

Experimental investigations into the behaviour of swelling soils are numerous. Many were motivated by expansion under shallow foundations and used one-dimensional testing apparatuses to predict vertical swell magnitudes as well as 'swelling pressures'.

ASTM D 4546 provides three (3) methods for evaluating the 'swell pressure' using the oedometer apparatus. One procedure includes measuring the increase in height of specimens under either a nominal pressure or insitu stress, followed by compaction down to original height and further. The first phase measures volume increase during wetting while the second phase measures the stress to counteract the swell potential. The stress required to bring the specimen to original height is interpreted as the 'swell pressure'. The second procedure involves first loading specimens to the insitu stress level and then inundating them with water while load is added to keep the specimen at constant volume. The final load applied is interpreted to be the 'swelling pressure'.

Many researchers have used these ASTM procedures to obtain measurements of swelling volume potential as well as 'swelling pressure' (Sridharan and Gurtug 2004, Thakur and Sing 2005). Dixon et al. (1996) combined one-dimensional 'swell pressure' measurements with hydraulic conductivity tests in rigid cells. These are essentially oedometer tests using larger specimens. Komine and Ogata (1994) performed tests using the first procedure described above with a

range of vertical stresses as well as constant volume oedometer tests. They reported that the time-dependent swelling was a function of initial dry density, vertical pressure, and initial water content. Maximum swell volume and 'swelling pressure' were only a function of initial dry density and vertical pressure, and was independent of initial water content. Similar tests were also performed while varying bentonite and sand contents as well as pore fluid chemistry (Komine and Ogata 2004). Katti and Shanmugsundaram (2001) performed one-dimensional swelling tests in the oedometer apparatus and correlated their results to micro structural changes in the clay fabric. Their procedure used, allowed zero stress expansion up to 0, 50%, or 75% of the original height followed by measurement of the remaining vertical 'swell pressure'. In their apparatus the top cap moved upwards to the desired height and remained stationary for the remainder of the test. Scanning electron microscope (SEM) photos taken after testing revealed that during swelling the clay peds break down into smaller particles.

Al-Shamrani and Al-Mhaidib (2000) recognized swelling as a three-dimensional phenomenon and performed both oedometer and triaxial swell tests. The triaxial swell tests consisted of infiltrating triaxial specimens and measuring axial and total volume using a stress path cell (Bishop and Wesley 1975). They compared volume swell changes in the oedometer and triaxial tests and also reported swell ratios of vertical swell to volumetric swell in the triaxial tests. Swell ratio was found to be directly related to confining pressure and also increased with time during tests. Parker et al. (1980) also performed swell saturation tests in the

triaxial cell with axial and radial measurement of volume change but only total volume expansion was reported. Komornik et al. (1980) investigated the influence of suction and confining pressure on the swell behaviour of soils. They used hollow test specimens with osmotic suction applied at the center through a semi-permeable membrane and cell pressure applied from the exterior. Changes in suction were applied under constant cell pressures. Results showed either expansion or compression with application of suction. 'Swell pressures' had to be interpreted and mostly extrapolated outside of their measurements. Their results indicated that over a range of 0-1000 kPa suction there is a linear relationship between 'swell pressure' and suction. 'Swell pressure' was shown to decrease with increasing suction values. Also, higher suctions resulted in lower swell volume changes.

Chen and Ng (2005) reported on wetting behaviour of an expansive clay examined in the triaxial cell. Suction control was maintained using the axis translation method (Hilf 1956). Specimens were subjected to constant mean stress suction decreases. During elastic wetting, changes in volume of specimens equalled increase in water content. During plastic wetting, increases in water content were significantly greater than volume expansion. These phenomena were interpreted as specimen expansion occurring at the same time as water was filling the air voids.

Cui et al. (2002) showed evidence for a critical swelling curve (CSC) to account for the coupling between hydraulic and mechanical behaviour of heavily compacted swelling soil. This model was created for soils which are compacted to a degree that no macro porosity exists for collapse to occur. Their goal was to improve volume change predictions and built on the idea that if mean stress is above the 'swelling pressure', no expansion occurs during wetting. The CSC represents a line in suction – mean stress (S-p) space where no volume change takes place, as shown in Figure 2.7. On Figure 2.8, two (2) stress paths are shown including constant mean stress suction decease (vertical line) and constant suction compression (horizontal line). For suction decrease under constant mean stress, the model predicts expansion until the CSC is reached, after which volume is constant. Under constant suction compression, volume decrease occurs along the reload compression modulus for that particular suction level until the CSC is attained. Further compression occurs along the virgin compression line. Therefore the model predicts that the same void ratio is achieved for all constant suction compression stress paths which pass the CSC and finish at equivalent mean stress.

Swelling soil behaviour has been investigated using suction control through vapour equilibrium techniques (Blatz and Graham 2000, Agus and Schanz 2005, Delage et al. 1998, Likos 2004). Vapour equilibrium applies water vapour at specified relative humidity values to specimens to control suction.

2.5 Flow in Porous Media

Understanding flow of both water and air in unsaturated swelling porous media is extremely difficult. In non-swelling unsaturated soils, flow is a function of the permeability, gradient, suction and void ratio (Huang et al. 1998). As discussed above, the WRC is not a unique function and varies for wetting and drying conditions. As such, flow functions in unsaturated media can also have hysteresis. Adding in the dimension that swelling clay changes volume with changes in water content results in movement of both fluids and solid particles through rearrangement. Not only is water flowing between soil particles but also into the peds causing expansion of the peds and collapse of the macro pores. This section summarizes modeling of flow in porous media, different test apparatuses, as well as network modeling.

2.5.1 Conductivity

Modeling of flow in saturated porous media began with D'Arcy (1856) who created an apparatus designed for applying one-dimensional downward flow. D'Arcy found an empirical linear relationship between gradient and flow. One form of D'Arcy's Law is

$$Q = -kiA \qquad [2.4]$$

where

Q = bulk flow,

k = hydraulic conductivity,

i = gradient, and

A = area of flow.

Conductivity, k, is a function of fluid density, gravity, and viscosity, and is often considered a constant in saturated, laminar flow.

D'Arcy's Law has been generally accepted over the years and has been extended to homogeneous and heterogeneous flow in two- and three-dimensions as well as flow in clay, rock, and other porous media. In non-swelling porous media, saturated conductivity is generally considered a function of void ratio (Lambe and Whitman 1979). D'Arcy's Law has also been extended to unsaturated porous media but now conductivity is a function of pore size distribution and volume of voids, as well as suction, degree of saturation, and fluid characteristics.

2.5.2 Physics and Flow of Gases

Gases, as compared with fluids such as water, have greater compressibility. In civil engineering, except in some extreme applications, water is usually taken as being incompressible to make calculations more convenient. The compressibility of gas components does not allow these assumptions to be made.

The volume – pressure – temperature state of a gas is described by Boyle's law, which states

$$PV = nRT \qquad [2.5]$$

where

P = gas pressure,

V = gas volume,

n = number of moles of gas,

R = universal gas constant, and

T = absolute temperature.

From this relationship, it is apparent that for a constant mass of gas under isothermal conditions, an increase in pressure results in a decrease in volume and vice versa. Also, temperature is directly related to both pressure and volume.

Gases can also be dissolved in fluids. Henry's law (Sisler et al. 1953) states that the amount of gas that can be dissolved in a fluid is directly proportional to the absolute pressure of the gas. Therefore, increasing the pressure of a water and air system will drive more air into solution. This phenomenon is exploited in traditional saturated triaxial testing to achieve saturation by increasing the back pressure.

Since gases can be dissolved in fluids, they can also be transported through them, which is known as diffusion. Diffusion occurs due to air concentration gradients within the fluid. The maximum amount of air present in the fluid is

limited by Henry's law while diffusion of air through fluid follows Fick's law (Fredlund and Rahardjo 1993); that is

$$\frac{m}{t} = D\Delta C \qquad [2.6]$$

where

m – mass of air,

t – time,

D – diffusion coefficient, and

C – air concentration.

Movement of air within porous media can occur through advection and diffusion. Advection involves pressure gradients similar to D'Arcy's Law while diffusion is the movement of air through pore fluid due to concentration gradients.

2.5.3 Conductivity Test Apparatuses

Conductivity test apparatuses range in form as well as applied conditions during testing. During conductivity testing on an unsaturated swelling clay soil, changes in gravimetric water content, density, saturation, and suction are anticipated. This makes the choice of device extremely important as well as hydraulic conditions applied during tests. Types of apparatuses include constant volume devices (Dixon et al. 1999) that allow no change in total volume, as well as oedometric type apparatuses that provide for one-dimensional volume change in the direction of flow. Investigations into the anisotropy of hydraulic conductivity

have also been performed in a rigid cell (Leroueil et al. 1990). In these devices all stress states are not explicitly measured and assumptions must be made.

Devices which allow deformation include flexible membrane apparatuses as well as zero stress devices (Rolland et al. 2005) which apply flow into specimens or monitor drainage out of specimens. The axis translation method has also been used to investigate unsaturated conductivity of deformable soil (Huang et al. 1998).

Hydraulic boundary conditions applied during testing, differ between specific apparatuses. Constant head (gradient) boundary conditions apply constant pressures at the inlet and outlet to flow throughout tests (Dixon et al. 1999, Richie and Schnabel 1992). Others apply constant flow rates or add a specified volume of water while monitoring soil response (Cui et al. 2001). Measurement of water and air permeability has been performed by applying simultaneous flow of both components at similar gradients (Corey 1957). Transient measurements of conductivity have also been performed through the traditional falling head test. Finally flow under hydraulic and thermal gradients has been investigated in constant volume devices (Mohammed et al. 1993).

2.5.4 Network Modeling of Flow

Network modeling of flow in porous media is performed by creating a series of interconnected links and nodes to represent the flow properties of porous media. Fatt (1956) first reported network models which used electrical analog circuits to

represent flow. Later Rose (1957) reported the first network modeling completed using computers. Since then models of one-, two- and three-dimensional networks have been developed. Tube and node sizes can now be chosen based on different criteria including MIP test results or X-Ray photography. The capillary tube model is one type of model which represents flow in porous media using tubes and vugs. Flow is then governed by Hagen-Poiseuille's law which is

$$q = \frac{\pi \Delta H r^4}{8 L \eta} \qquad [2.7]$$

where

q = flow rate,

ΔH = change in total head,

r = tube radius,

L = length over which flow is calculated, and

η = viscosity of the fluid.

A simple one tube network model is shown in Figure 2.10 with fluid 'a' displacing fluid 'b'. Also shown on the figure is the pressure distribution across the tube. At the interface between the two (2) fluids a capillary jump occurs in the pressure distribution due to molecular interactions. If the capillary pressure is zero, a flat interface is observed. As shown in Figure 2.10, however; if the forces are not equal, a curved interface forms and represents the pressure increase which is required to achieve equilibrium (Schwartz 1969). Since the flow rates for both

fluids are equal, and the pressure distribution and geometry are defined for the entire system, Hagen-Poiseuille's law can be applied to calculate total flow. Multi-dimensional capillary tube models are formed by connecting tubes at vugs in series and parallel.

Network models for swelling clay are quite limited. Thus far, network models for flow through swelling soil including Abichou et al. (2004) and Tuller and Or (2003) combine Hagen-Poiseuille's law and D'Arcy's Law at the micro scale to calculate flow. In Abichou et al. (2004), flow is considered through a network of tubes and pores. Discrete degrees of 'bentonation', or filling of pores, are modeled in this work, but transient swell of bentonite as water flows through the pore structure is not considered. Tuller and Or (2003) model flow through tactoidal shaped cells for different bentonite contents. In both cases, hydraulic conductivity calculations are used to determine flow through an individual pore throat. Applying D'Arcy's Law in this way for flow through an individual pore is questionable since it was originally developed for bulk flow modeling.

2.6 Constitutive Models for Unsaturated Soil

Elastic-plastic models for soil behaviour are based on soils having both recoverable strains (elastic) up to a yield criterion followed by unrecoverable strains if the yield criterion is exceeded. These types of models link soil strength to soil deformations. Roscoe and Burland (1968) developed the Modified Cam-Clay approach for modeling saturated soils with stress and volume states

including mean effective stress (p'), deviator stress (q) and specific volume (V). This model has been extended by many researchers into the unsaturated range through addition of another stress state which is usually suction (S) (Alonso et al. 1990, Toll 1990, Wheeler and Sivakumar 1995, Delage and Graham 1995, Cui and Delage 1996). All of these models are based on the idea that volume change behaviour can be divided into elastic, or recoverable, and plastic (inelastic), or unrecoverable, strains.

The motivation for creating unsaturated constitutive models was to predict behaviour typical of unsaturated soils. This includes increased volumetric stiffness with increased suction, expansion or collapse mechanisms upon wetting at different stress and volume states, increase in shear resistance with increasing suction, and plastic volumetric strains from increased suction (Alonso et al. 1990). The model proposed by Alonso et al (1990), known as the Barcelona Basic Model (BBM), was originally developed for slightly or moderately expansive soil and has become the most popular unsaturated constitutive model (Wheeler 2006). A schematic of the yield surfaces in p-q-S space is shown in Figure 2.11. At suction equal to zero, the model collapses into the traditional Cam-Clay (Roscoe and Burland 1968). As suction increases, the yield surface increases in size in p-q space indicating an increase in strength with increasing suction. Inside the yield surface all stress paths are elastic. If the yield surface is reached by increasing mean stress, deviator stress, or increases or decreases in suction, inelastic volumetric changes are predicted.

Full BBM definition requires 10 parameters and the original publication suggests stress paths to be performed so the parameters can be determined independently. The model has been used successfully to capture unsaturated behaviour but some of the limitations of the BBM, as described by Wheeler (2006), include diverging normal compression lines with increasing suction, the shape of the yield curve in S-p space as a straight vertical line at a reference pressure, constant slope M for the critical state line in q-p space independent of suction, and predictive abilities in cyclic wetting-drying paths. All except the final limitation were also mentioned in Wheeler and Sivakumar (1995).

Wheeler and Sivakumar (1995) proposed another constitutive model for unsaturated soil based on triaxial tests using suction control on compacted speswhite kaolin samples. Their model is based on Alonso et al. (1990) with some modifications. They added the variable specific water volume instead of water content. They also changed the model based on some of the limitations described above. Later this framework was extended to account for hydraulic hysteresis and other mechanical behaviour by including degree of saturation and modified suction (suction multiplied by porosity) (Wheeler et al. 2003).

Toll (1996) proposed a conceptual model for drying and wetting of soil. The model, based on drying and wetting tests on a reconstituted soil, predicts that beginning with a saturated soil, removal of water corresponds to a similar

reduction in void ratio. As drying continues past a certain suction value, desaturation occurs. Removal of water continues while volume decrease attenuates and then essentially stops with further water content reduction. Rewetting of the soil induces water content increase but hysteresis in the soil does not allow the original water content to be achieved. Volume increase with wetting is observed if the desaturation suction threshold is passed.

Constitutive models for swelling soil behaviour are quite limited. Models are usually calibrated with a specific soil type and preparation procedure. At this time a general model for all unsaturated soil does not exist. Two (2) constitutive models for unsaturated swelling soils are the Barcelona Expansive Model (BExM, Alonso et al. 1999) and the Blatz and Graham (2003) model. The BExM is extends the original BBM to include micro structural and macro structural strains. The BExM was developed on the basis of cyclic wetting and drying tests in an oedometer apparatus that incorporates suction control. For wetting and drying cycles on a highly overconsolidated soil, the model predicts expansion, while compression is predicted when overconsolidation is low. The BExM separates volumetric macro structural strain from micro structural strain to predict swelling and collapse mechanisms.

Blatz and Graham (2003) developed their model based on triaxial tests with suction control as well as tension tests (Tang and Graham 2002) on a similar sand-bentonite mixture as used in this study. A conceptual elastic-plastic

framework of this model is shown in Figure 2.12. Their test data consisted of drying cycles using vapour equilibrium, isotropic loading, and shearing paths. Test ranges were limited by the suction measurement range (1-8 MPa) of the thermocouple psychrometers (Blatz and Graham 2003). Blatz et al. (2006) reported tests on samples subjected to similar drying, compression, and shearing paths over a considerably wider suction range. They showed little difference in the mechanical behaviour of two (2) bentonite mixtures under higher suctions following compaction, although suction was not measured in their tests.

2.7 Justification for Research

Although many studies on swelling soil behaviour have been completed there is still a lack of understanding as to how the materials are affected at the fundamental level by the change in water content and how these affects are influenced by boundary confinement. Previous laboratory testing has not combined measurement and/or control of all stress and volume states including suction, controlled boundary conditions, and liquid infiltration. Numerical models exist to capture the behaviour of these tests but no laboratory equipment existed in which to measure all the input parameters. Also, further understanding of swell mechanisms can be gained by analyzing flow in a capillary tube which represents two-phase flow. Therefore, the next logical step was to modify the existing apparatus to give it the ability to apply simulated field conditions in the laboratory and then measure responses to liquid infiltration under controlled boundary conditions. Results are interpreted to show new limits in swelling soil

behaviour. A new capillary tube model for transient flow was also created to investigate the swelling mechanism and its relation to boundary confinement. This provides new insight to the behaviour of swelling clay soils through consideration of fluid flow through individual pores. To the author's knowledge neither these laboratory tests nor this capillary tube model have been performed previously.

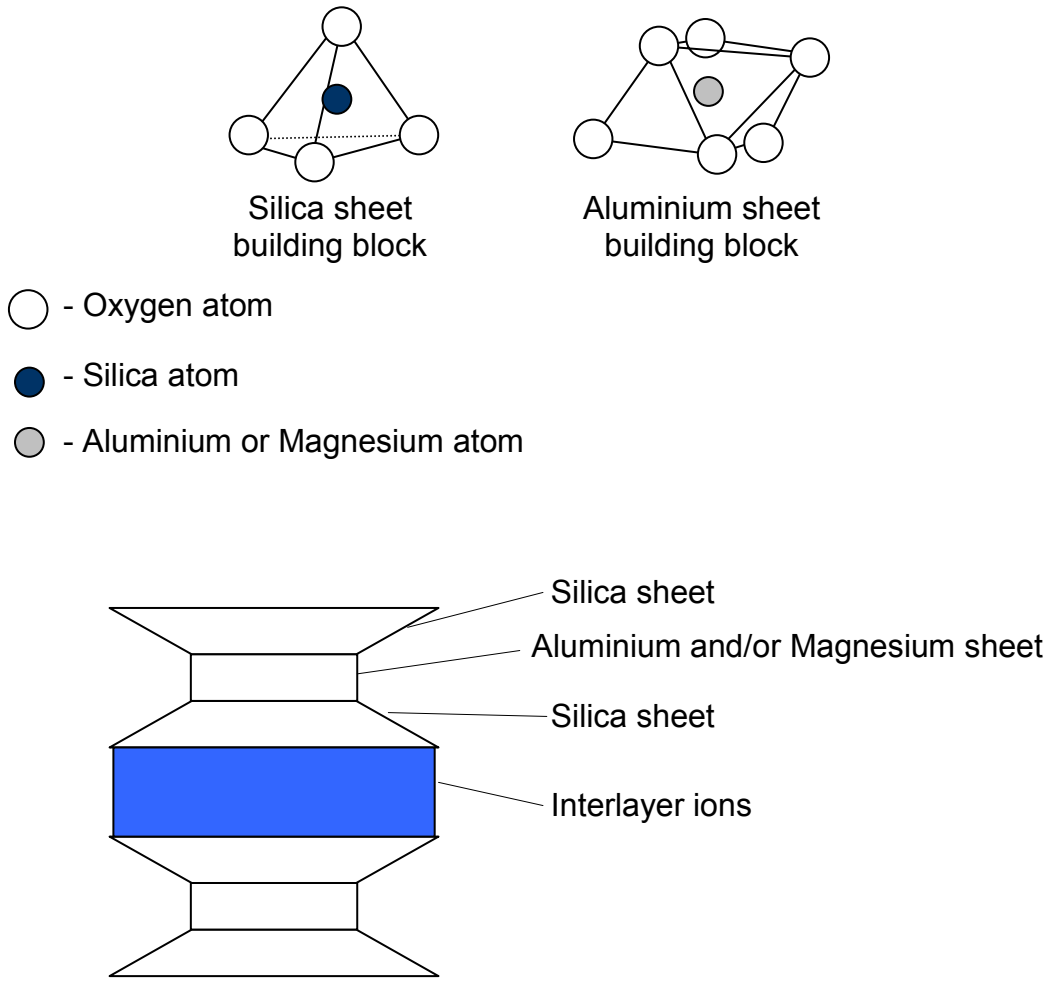

Figure 2.1. Schematic of the molecular structure of montmorillonite (after Budhu 2000).

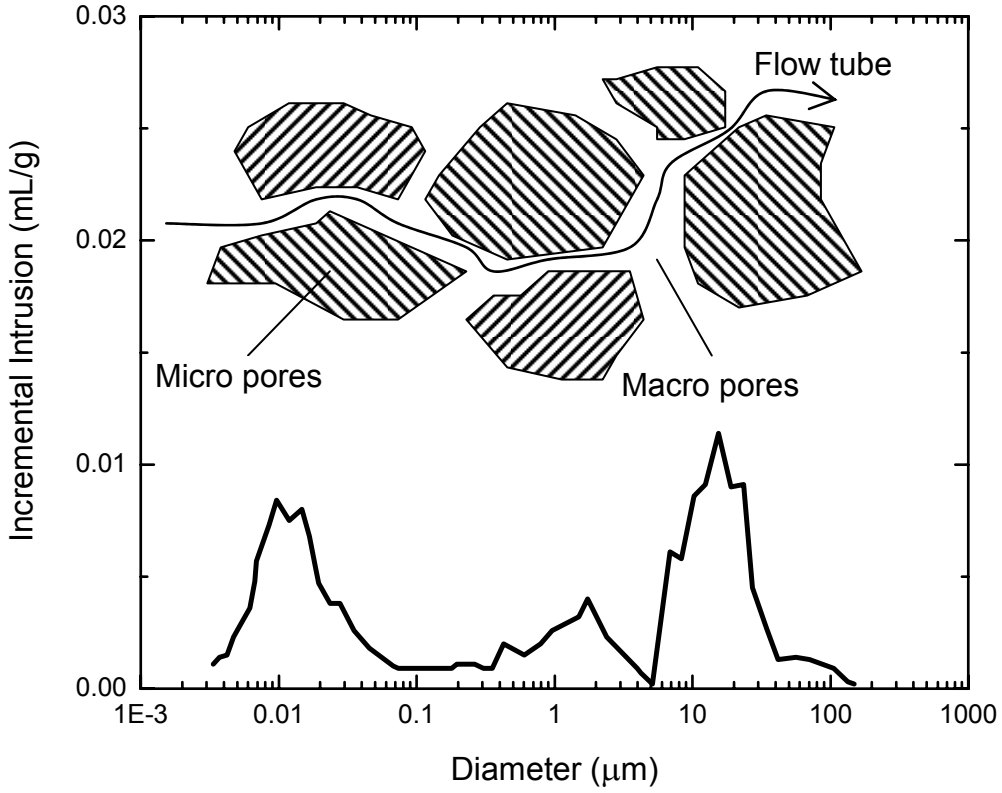

Figure 2.2. Pore size distribution of bentonite sand buffer (BSB) specimens (after Wan 1996).

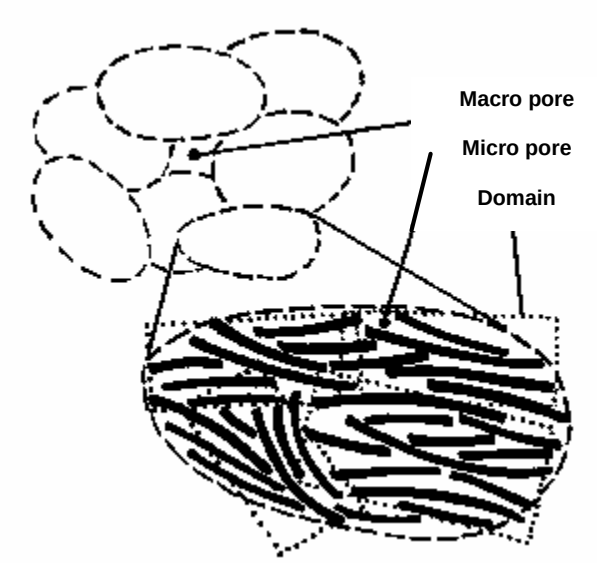

Figure 2.3. Schematic of macro and micro pores (after Dixon et al. 1999).

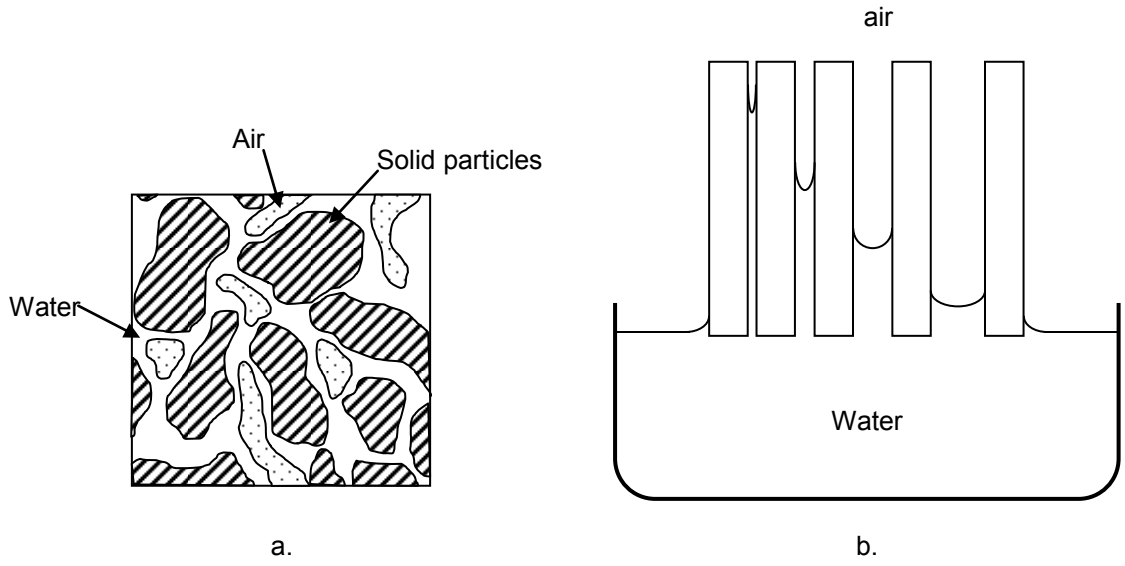

Figure 2.4. Schematic of unsaturated soil element and capillary rise (after Fredlund and Rahardjo 1993).

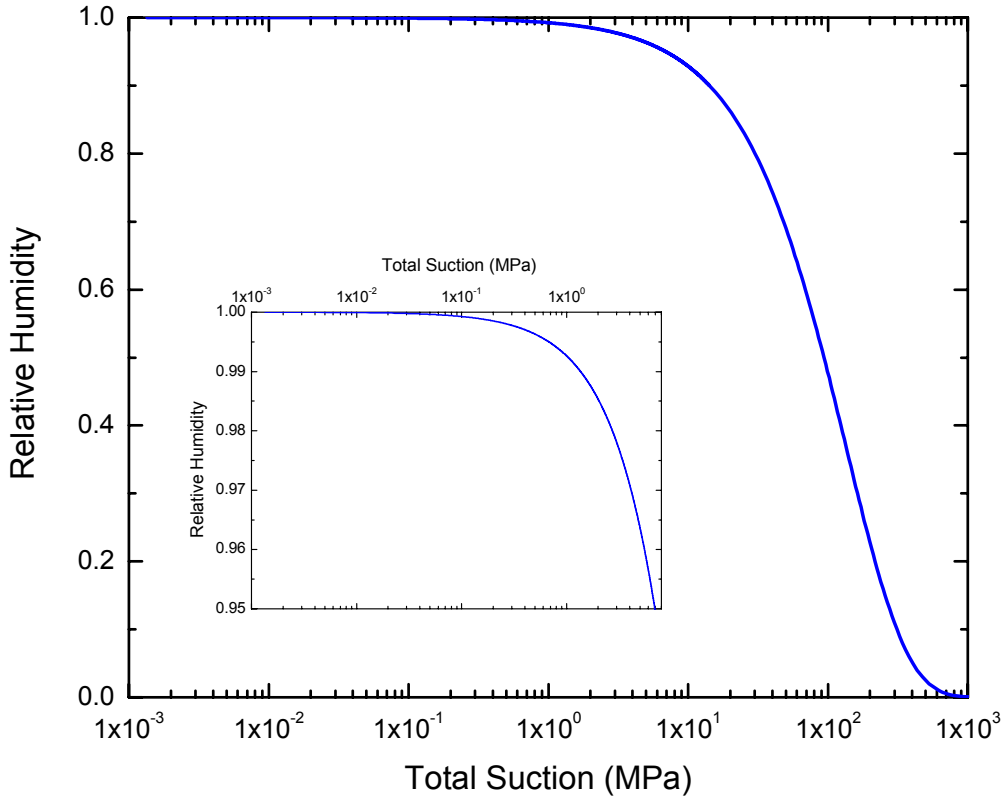

Figure 2.5. Relationship between relative humidity and total suction.

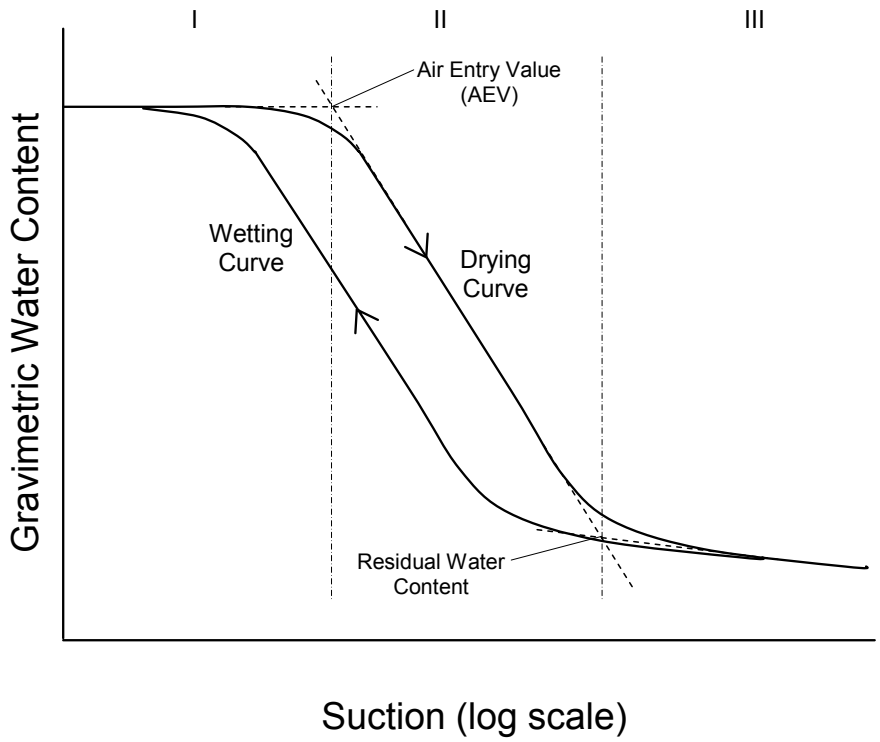

Figure 2.6. Schematic of typical water retention curve (WRC).

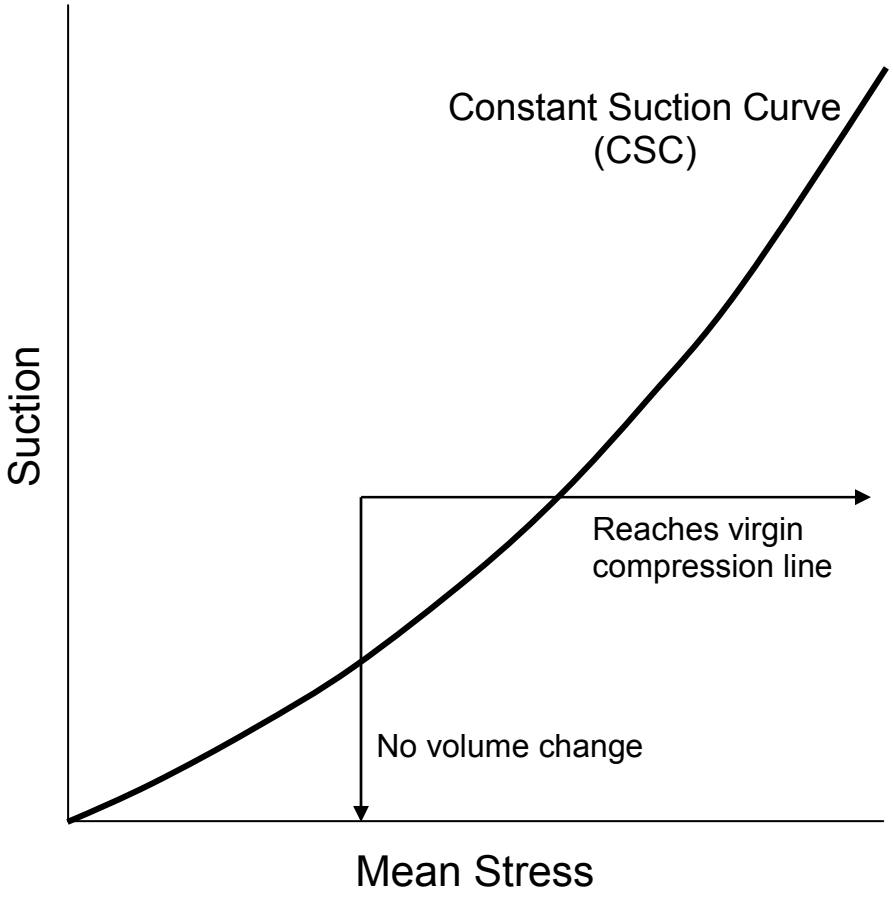

Figure 2.7. Critical swelling curve (CSC) plotted in suction – mean stress (S-p) space (after Cui et al. 2002).

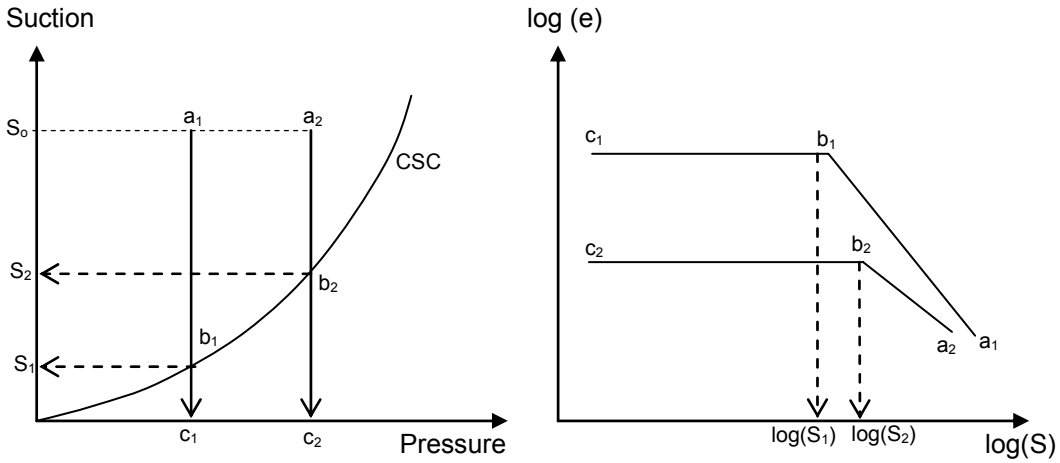

a. Suction decrease under constant pressure

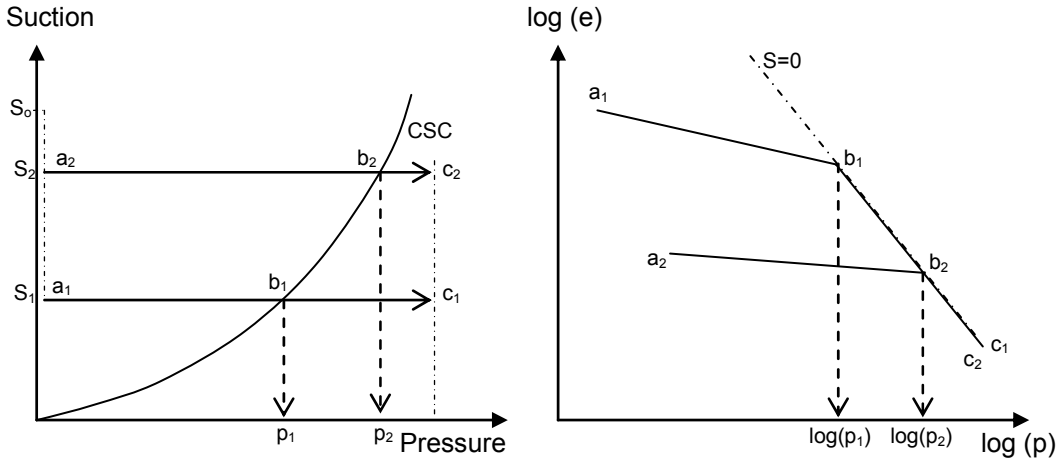

b. Pressure increase under constant suction

Figure 2.8. Example stress paths and volume change predictions using the critical swelling curve (CSC) (after Cui et al. 2002).

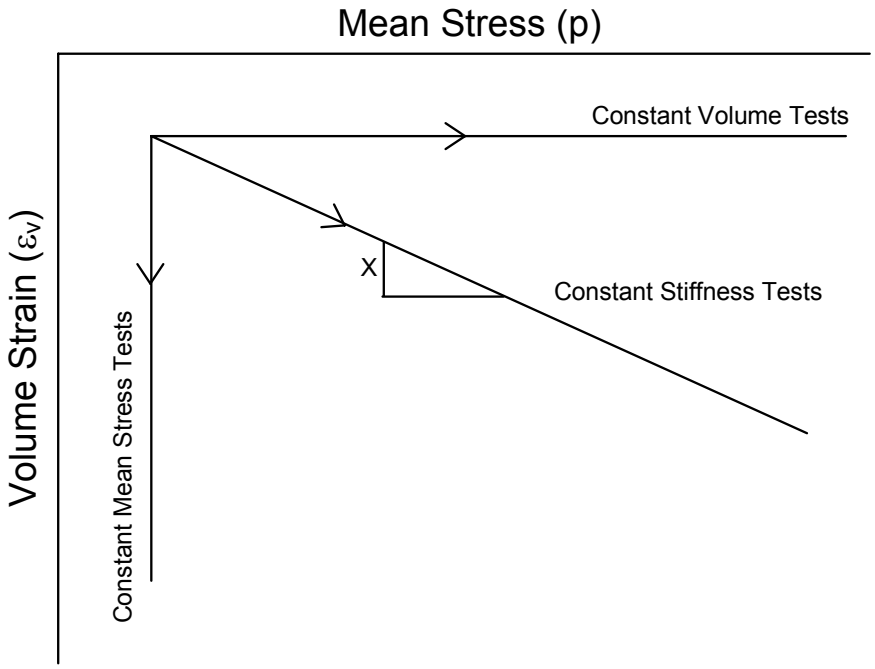

Figure 2.9. Infiltration boundary conditions in mean stress-volume strain space (Siemens and Blatz 2006).

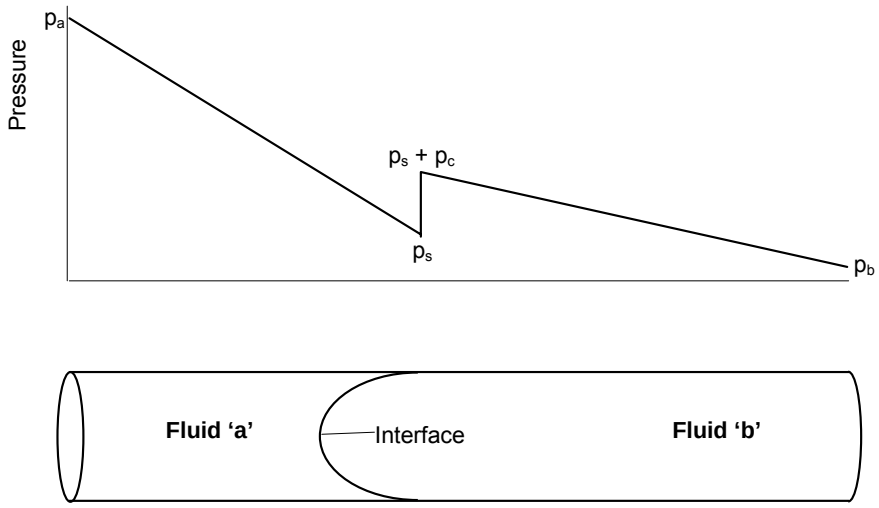

Figure 2.10: Generic capillary tube model.

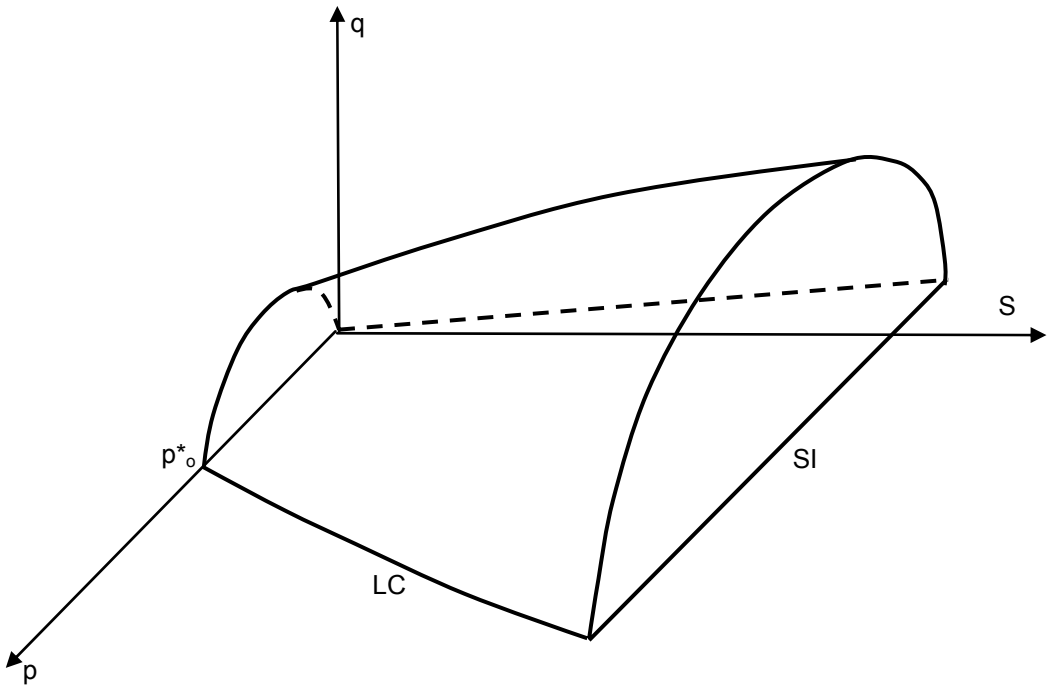

Figure 2.11: Yield surface in deviator, mean, and suction (q-p-S) space (after Alonso et al. 1990).

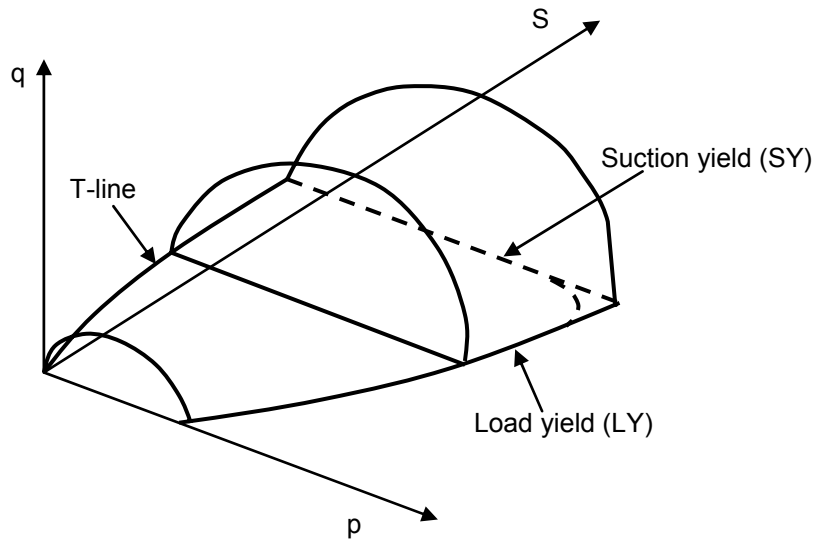

a. Mean stress, deviatoric stress and suction space.

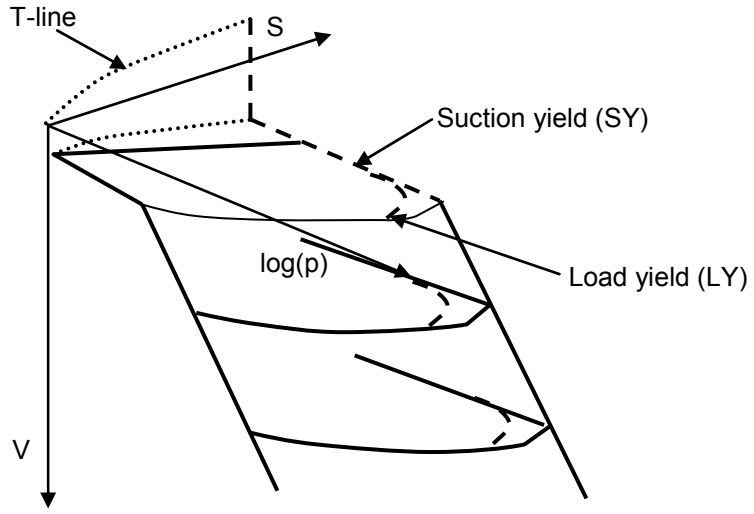

b. Mean stress, specific volume and suction space

Figure 2.12. Conceptual elastic-plastic framework for unsaturated soil. (after Delage and Graham 1995).

CHAPTER 3: MATERIALS AND PREPARATION[1]

3.1 Introduction

The purpose of this study is to examine the behaviour of a clay-sand mixture subjected to wetting conditions under controlled boundary conditions. This chapter provides a summary of the properties of the materials used in this research study and the procedures used to prepare consistent specimens for testing.

3.2 Clay-Sand Material

The material used in this study is a 50:50 mixture (by dry mass) of sodium bentonite and silica sand. In previous publications including numerous theses and journal papers this material was termed 'buffer'. Recently the name was

[1] Sections of this chapter have been published as:
Blatz and Siemens (2004, 2005, 2006) – Ontario Power Generation Reports.

changed to bentonite sand buffer (BSB) to make it consistent with other materials proposed in engineered barriers in the deep geologic repository concept examined by Atomic Energy of Canada (AECL). The bentonite component is a highly plastic bentonite clay and the silica sand is a well-graded sand. The two (2) components are measured dry and then combined with distilled de-aired water to produce consistent specimens used in this study. All specimens are prepared to an initial water content of 19.4% and dry density of 1.67 Mg/m^3 to give a degree of saturation of approximately 85%. Following compaction, specimens are in an unsaturated state and have a continuous air phase. Fredlund and Rahardjo (1993) report that the transition zone between an occluded and a continuous air phase occurs between a degree of saturation of 80-90%. Anderson (2003) confirmed that as-compacted specimens have a continuous air phase while Graham et al. (2002) showed that a continuous air phase can be found in these specimens for degree of saturation up to 93%. This section covers the physical properties of the individual components.

3.2.1 Sodium Bentonite

The sodium bentonite component of BSB is a Wyoming Bentonite. Its original formation was described in section 2.2.1. The Wyoming Bentonite was purchased from Bentonite Corporation of Wyoming under the trade name Standard-Western Bentonite (200 mesh). As received in the laboratory the sodium bentonite is in powder form following processing. It is composed of at least 75% montmorillonite with the remaining being quartz and feldspars.

Liquid and plastic limit testing was completed on the sodium bentonite according to ASTM D 4318. Liquid limit and plastic limit of the sodium bentonite is approximately 555% and 43% respectively resulting in a plasticity index of 511. The CEC for Standard-Western Bentonite (200 mesh) is 76 meq/100g. The extremely high plasticity index is the result of the high activity of the montmorillonite component of the bentonite.

Prior to mixing, a sample of sodium bentonite is placed in a stainless steel mixing bowl and stored in a 104^{o} C oven for at least 48 hours. On the mixing day, the bowl is removed and sealed with plastic wrap and an elastic band to allow thermal equilibration with the surrounding environment but to limit moisture absorption from the laboratory air.

3.2.2 Silica Sand

The silica sand component of BSB is mixed to a standard grain-size distribution specified by AECL (Figure 3.1). The silica sand used in this study is an angular material and the resulting sand mixture is well graded in terms of grain size distribution. Procedures for silica sand preparation described by Dixon et al. (1994) were followed. Dixon et al. (1994) allows for a grain-size distribution of 6% above or below the specified target values. Figure 3.1 displays the average grain-size distribution from all batches, completed in general accordance of ASTM D 422, as part of this study as well as the upper and lower limits specified. The average falls within the limits throughout the distribution.

The properties of the ideal mixture are C_u = 4, C_c = 0.84, d_{10} = 0.12 mm and d_{50} = 0.38 mm.

Prior to mixing triaxial specimens, a sample of silica sand was placed in a mixing bowl and stored in a 104^o C oven for at least 24 hours. It was removed and sealed with plastic wrap and an elastic band to allow for thermal equilibration prior to mixing.

3.2.3 Distilled De-aired Water

Water used for mixing specimens was produced on-site in the geotechnical laboratory. A distilling apparatus was used that boils tap water and then condenses the vapour into liquid form in a separate container. The distilled water was stored in a plastic container prior to use. To de-air the water, distilled water was placed in a container and subjected to vacuum pressure overnight.

3.3 Specimen Preparation and Compaction

3.3.1 Mixing Bentonite Sand Buffer (BSB) Specimens

All BSB specimens were mixed using a procedure based on Dixon et al. (1994) to ensure consistent material properties based on. The sodium bentonite and silica sand components were removed from the oven, sealed to prevent absorption of moisture, and allowed to equilibrate with the temperature in the laboratory. Prior to mixing the required masses of sand and distilled de-aired water were placed in a stainless steel mixing bowl and sealed with plastic wrap.

Masses were calculated on a spreadsheet in Excel where selected calculations were checked with hand calculations. An equal mass of sodium bentonite was placed in a glass beaker and sealed. Both containers along with the mixing tools were taken into a cold room where the mixing occurs. Figure 3.2 is a photograph of a mixing bowl, glass beaker and mixing tools.

The mixing timing begins at the time the sodium bentonite is placed into the steel mixing bowl with the silica sand. The entire process took 15 minutes and incorporates six (6) steps including light mixing, grinding, tamping, scraping, a second grinding step and finally placement in sealed bags. For the first two (2) minutes the clay, sand and water were lightly mixed together to wet the clay particles that are initially in powder form. Throughout the mixing process any particles that became stuck on the mixing tool were removed with the scraping knife directly back into the mixing bowl. At two (2) minutes, the mixture was lightly tamped into the base of the bowl and then ground using a scraping action with the mixing tool. The time for the first light tamping and grinding step was four (4) minutes. The larger clumps of clay were broken down during this step. After six (6) minutes from the beginning, the mixture was again tamped into the bottom of the mixing bowl using the flat end of the mixing tool. Tamping occurred for a total of two (2) minutes. More intense tamping was used during this step to ensure combination of the water and the clay particles. At the end of the tamping step the clay-sand mixture was in a relatively blocky form at the bottom of the mixing bowl. At the eight (8) minute mark, the mixing tool was turned over and

used to scrape the mixture off the base using the 'toe'. This was immediately followed by another grinding step where the large clumps of material were ground against the side of the mixing bowl. The goal was to have a homogeneous mixture at the end where the sand particles were coated with clay. After 14 minutes from the beginning, the mixture was poured into a sealed plastic bag and placed inside another plastic bag. The second bag was taped shut and labelled with the specimen number and date of mixing. The double bagged mixture was placed in cold storage for a moisture equilibration period of 48 hours as specified by Graham et al. (1995). After the moisture equilibration period, two (2) water content samples were taken to determine the water content of the mixture (ASTM D 2216). The water content was used to calculate the required mass for each layer. After another 24 hours, the mixture was ready for compaction.

3.3.2 Specimen Compaction with Internal Suction Sensor

All specimens were compacted to the parameters described in section 3.2. The process for compacting BSB specimens was originally developed by Yarachewski (1993). It was later modified to allow compaction of internal psychrometers as described by Blatz (2000) and further modified for this program to allow compaction with the Xeritron sensor.

To allow compaction of a Xeritron sensor at the center of compacted triaxial specimens the ram was modified by drilling a hole at its center to allow the

sensor wire to come directly out the top of the specimen. The hole had a small screw inserted in it when not being used for the wire.

Before beginning the compaction process the drill press was set up to be ready the hole for the sensor. Figure 3.3 is a photo of the drill press used. The press was used to drill a hole in the center of the specimen where the Xeritron sensor was placed before compaction of the fifth and final layer. Setting up the drill press involved centering the mold on the press as well as setting the drill bit height. First the drill bit was inserted into the drill chuck. To locate the center of the mold a circular Lucite disc that has a hole at its center was placed inside the mold. The compaction mold with Lucite disc was locked into the adjustable base. The adjustable base was moved until the drill bit was located at the exact center of the compaction mold. Then the base was screwed down so that it could not move. Later once the first four (4) layers had been compacted the mold could be placed back into the base at the same location and the hole was drilled. A compacted specimen with a hole drilled in the middle is shown in the inset of Figure 3.3. Next the elevation of the drill was adjusted to ensure that enough distance could be covered to complete the hole. The guide on the press was located to allow drilling of at least 120 mm. Following compaction of the first four (4) layers a hole was drilled through the center of the specimen that is 3 mm longer than the Xeritron sensor.

All triaxial specimens were compacted to nominally 50 mm diameter and 100 mm height in five (5) layers using the one-dimensional compaction mold and piston apparatus shown in Figure 3.4. Before assembling the compaction mold its interior was lightly coated with silicon oil to minimize disturbance when the specimen was removed from the mold. All excess oil was wiped off of the mold prior to assembly.

Using the water content measurement from the mixture following 48 hours of equilibration the required mass per layer was calculated. A strain-based criterion was used to compact specimens so that results are comparable with previous research. For each layer the mass of clay-sand mixture was placed in a glass beaker and then deposited into the one-dimensional compaction mold. The mold was placed on top of the base in the compaction apparatus. The hydraulic ram was operated by hand until the layer is compacted to 0.01 inch smaller than 20 mm and held for ten (10) seconds. The pressure was released, and then reapplied for another 10 second increment. Then the ram was allowed to rise back to its original position and the mold removed from the base. Between layers the surface was scarified using a Phillips screwdriver so that adjacent layers were bonded adequately. This process was repeated for four (4) layers and then the mold was covered with plastic wrap and sealed with a rubber band and taken to the drill press. The length of the Xeritron sensor was measured from the end of the mesh to the end of the copper tube. This length was added to the distance from the top of the mold to the top of the fourth layer. A hole

three (3) mm longer than the sum of these two (2) values was then drilled through the center of the specimen to ensure adequate length for the sensor. Cuttings were collected from the drill for water content measurement. Then the mold was covered with plastic wrap sealed with a rubber band and taken back to the compaction ram for compaction of the fifth layer. The tiny screw was removed from the compaction ram to allow the sensor wire out. Soil for the fifth layer was again measured into the glass beaker. The plastic wrap was removed from the mold and the Xeritron sensor was placed into the hole and held in place. The top of the fourth layer was scarified and then the soil for the fifth layer was deposited into the mold. To make sure the sensor wire lines up with the hole in the compaction ram, the loose soil was lightly tamped into place carefully making sure the sensor wire was located at the center of the top of the specimen. The wire was marked with a felt tip pen at an elevation even with the mold top so that after compaction it could be determined if the wire was pushed down into the specimen. The mold is placed on the compaction base and the wire is fed through the hole and out the side of the ram. The fifth layer is then carefully compacted while holding onto the wire to ensure it runs down the center axis of the specimen and was not crushed. Once the fifth layer had been compacted twice, the wire was fed back down through the hole and the mold removed from the compaction base. The top of the mold was covered with plastic wrap and its bottom removed. The six (6) hexagonal bolts along the side of the mold were loosened slightly and then the mold was placed upside down on the base in order to separate the specimen from the mold. The compaction ram was brought

into contact with the bottom of the specimen and then used to push the specimen approximately 5 mm. The mold was removed from the base and the bolts now completely removed from the mold. The two (2) halves were separated and finally the specimen was removed from the mold.

Prior to compaction the Xeritron sensor's mass was recorded and following compaction the specimen and sensor's combined mass was measured and recorded. The difference between the two (2) measurements was taken as the specimen's initial mass. Four (4) measurements were taken of its height and ten measurements of its diameter (two (2) on each layer) were taken and recorded using dial callipers. A photo of a compacted specimen with internal Xeritron sensor is shown in Figure 3.5. Following compaction a water content measurement was completed on the remaining soil in the sealed bag.

3.4 Specimen Designation

Specimens were designated according to the author's initials and the number of specimens mixed. They were designated as GS-XXX where the X's are number of specimens prepared.

3.5 Quality Control Testing

Before initiating the formal testing program, quality control specimens were mixed to ensure the author was comfortable with the process and the water

contents and densities were consistent with previous researchers. Also, a strength testing program was completed by the author using a similar material so there was considerable experience gained in BSB specimen preparation. Figure 3.6 displays the gravimetric water content and dry density measured for all specimens tested for this program. Consistent control of water content and dry density was observed for all specimens.

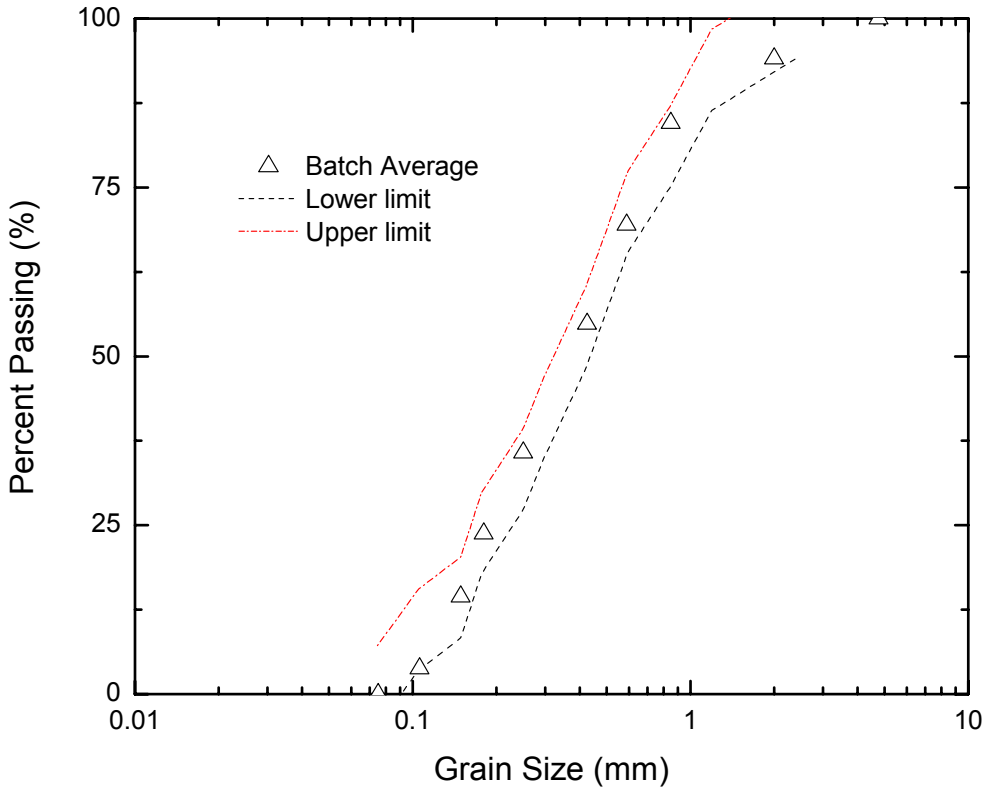

Figure 3.1. Average silica sand grain-size distribution and allowable limits.

Figure 3.2. Photograph of mixing bowl, glass beaker and mixing tools.

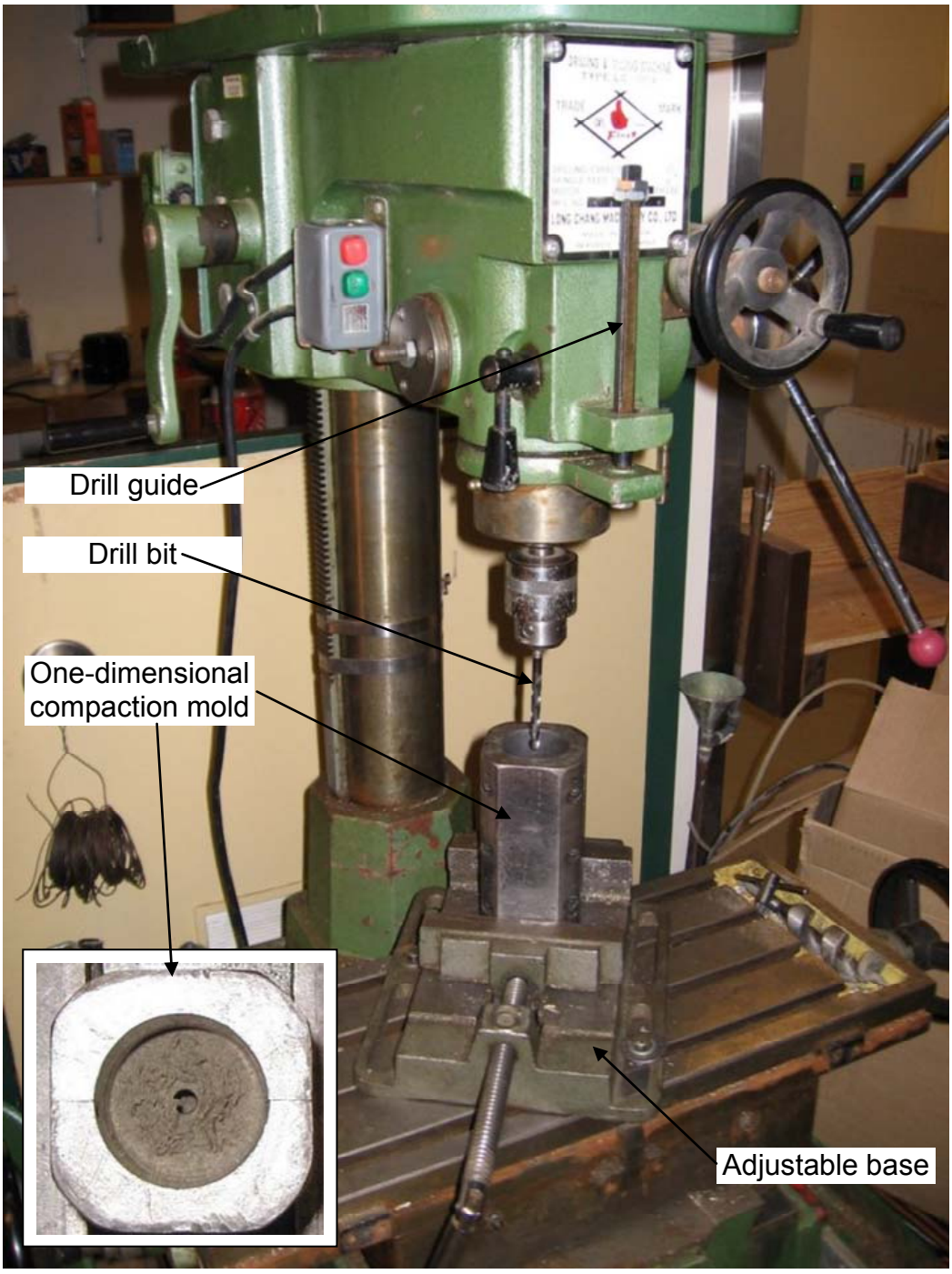

Figure 3.3. Photograph of drill press with one-dimensional compaction mold secured in adjustable base.

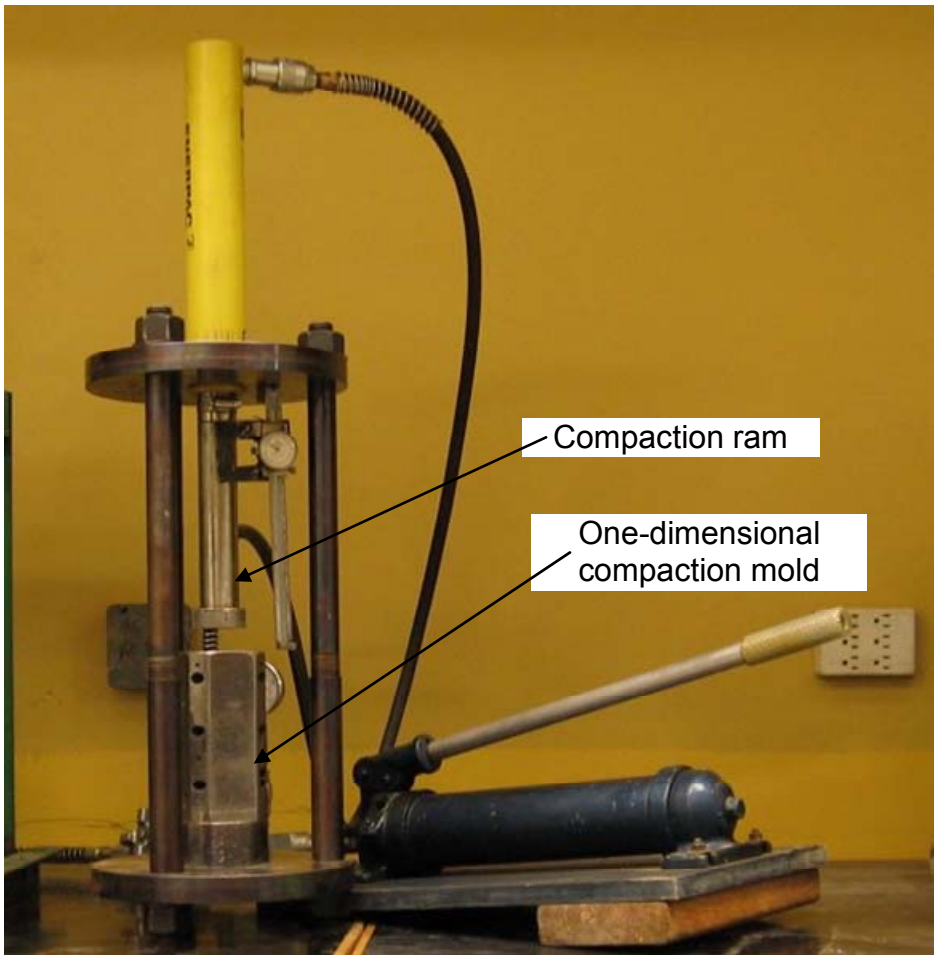

Figure 3.4. Photograph of one-dimensional compaction mold and ram.

Figure 3.5. Photograph of compacted specimen with internal Xeritron Sensor.

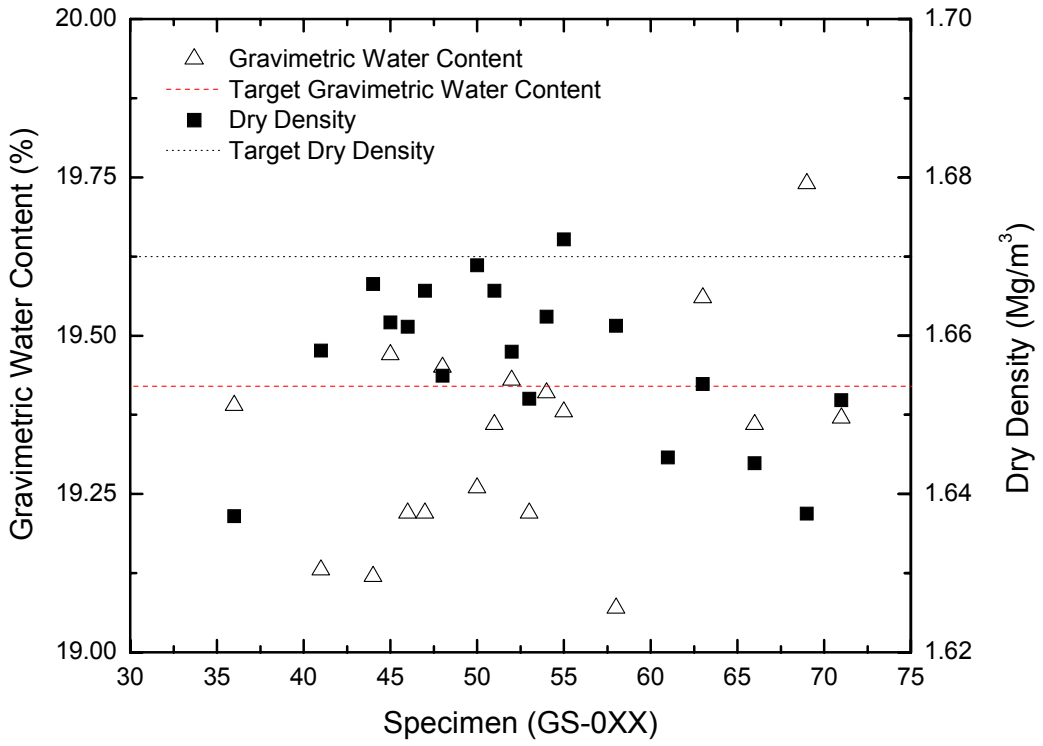

Figure 3.6. Gravimetric water content and dry density of compacted specimens.

CHAPTER 4: EQUIPMENT FOR LIQUID INFILTRATION TESTS UNDER CONTROLLED BOUNDARY CONDITIONS[2]

4.1 Introduction

This chapter describes the equipment used for infiltration tests and hydraulic conductivity tests performed for this research program. The primary piece of lab equipment used was the high temperature high pressure (HITEP) triaxial apparatus. The laboratory program for this research includes three (3) series of

---

[2] Sections of this chapter have been published as:
Blatz and Siemens (2004, 2005, 2006) – Ontario Power Generation Reports.

Siemens, G.A. and Blatz, J.A. 2006. A triaxial apparatus for applying liquid infiltration under controlled boundary conditions with internal suction measurement. ASCE Geotechnical Journal of Geotechnical and Geoenvironmental Engineering to be considered for publication. *In Review*.

Siemens, G.A. and Blatz, J.A. 2006. Development of a new hydraulic conductivity apparatus for deformable low permeability materials. Canadian Geotechnical Journal. *In preparation*.

Siemens, G.A., Blatz, J.A. and Priyanto, D.G. 2006. Results of Long-Term Infiltration Tests on Unsaturated Swelling Clay. Geotechnical Special Publication No. 147: Proceedings of the Fourth International Conference on Unsaturated Soils, Carefree, Arizona, 2-6 April 2006. **1**: 939-950.

tests including constant mean stress, constant stiffness and constant volume infiltration tests. These are used to apply simulated field conditions, as shown in Figure 1.2, in order to understand the influence of boundary conditions on the hydraulic-mechanical behaviour of unsaturated compacted swelling clay soil.

The HITEP triaxial cell was designed at the University of Manitoba (Lingnau 1993) and a schematic is shown in Figure 4.1. The cell was designed to examine behaviour of soil at cell pressures and temperatures up to a maximum of 10 MPa and 100 ^{o}C respectively. The HITEP cell was later modified to control and independently measure suction using the vapour equilibrium technique (Blatz and Graham 2000). A custom data acquisition system was also added to apply general stress paths in isotropic and shear loading (Anderson 2003, Blatz et al. 2003). The triaxial system reported here includes the addition of a liquid infiltration apparatus, automatically controlled boundary conditions during infiltration and enhanced suction measurement using a new sensor.

4.2 Infiltration Test Apparatus

A new laboratory apparatus was developed to apply liquid infiltration with control and/or measurement of stress and volume states including mean stress, deviator stress, suction and volume (void ratio). The apparatus includes automatic control of mechanical boundary conditions during infiltration. Using algorithms that apply feedback control based on volume response to increasing water content,

specimen volume is controlled by adjusting cell pressure (mean stress). The Xeritron sensor is also developed and is a new suction measurement instrument. It measures relative humidity of air in equilibrium with the soil to infer total suction. The Xeritron sensor was chosen because of its wide range of measurement, accuracy, small size and durability.

The liquid infiltration apparatus is based, in concept, on the apparatus reported by Blatz (2000) with significant differences. Blatz (2000) developed a system that applied suction control using the vapour equilibration technique. Although that apparatus worked well in the higher suction range using vapour, wetting paths using liquid could not be applied. The triaxial cell was further modified to apply liquid infiltration while retaining the ability to apply suction control using vapour equilibrium (gas phase). The apparatus can apply controlled increase and decrease of suction in the triaxial cell with independent suction measurement (using the embedded sensor).

A schematic of the triaxial specimen and a photograph of the apparatus are shown in Figure 4.2 and Figure 4.3 respectively. As shown in Figure 4.2, hydraulic boundary conditions are controlled by enforcing radial flow of water applied from the periphery of the specimen. The triaxial specimen is surrounded with a non-woven geotextile fabric (Amoco Propex 4553) that overlaps the top and bottom filter stones providing direct hydraulic connection to the water supply. Lucite discs were placed between the filter stones and the specimen to prevent

axial flow of water and limit the flow field for interpretation. Plastic wrap was attached with a thin film of vacuum grease to the faces of the Lucite discs that contact the specimen. Plastic wrap minimizes end friction and ensured a proper seal was developed at the interface between the Lucite discs and the specimen. The top Lucite disc had a bevelled hole allowing the Xeritron sensor wire to pass through to the top cap. The annulus between the sensor wire and the hole in the Lucite disc was sealed with hot glue during specimen installation. The components along the center axis of the triaxial cell from the pedestal base to the top cap were a layer of filter paper, filter stone, Lucite disc, layer of plastic wrap, triaxial specimen with Xeritron sensor, layer of plastic wrap, Lucite disc, filter stone and filter paper. Water was supplied to the specimen using separate pressurized burettes for the top and bottom water pressure.

The infiltration apparatus applies pure radial flow of water using external pressure. Drying paths may also be applied to the specimen before or after infiltration paths by removing the liquid infiltration apparatus and connecting the vapour equilibrium apparatus (Blatz and Graham 2000) which are interchangeable. Controlled hydraulic boundary conditions provide for straightforward interpretation of the results and are noted as important considerations for numerical modeling.

4.2.1 Suction Measurement

Previous studies of the material used in this work have used thermocouple psychrometers to measure total suction (Wan 1996, Blatz 2000). The

measurement range of the psychrometer has limited these studies to the 1-8 MPa total suction range (Blatz and Graham 2003). As such, at the beginning of this work a new suction sensor was developed that has a wider range of measurement and was small enough to be installed in 50 mm diameter by 100 mm tall specimens without significantly affecting their performance. The final choice was the Xeritron RH1018 sensor produced by Hygrometrix Incorporated (Xeritron 2002). It is a relative humidity measurement instrument and therefore is used to measure total suction. Although it was developed mainly for Heating, Ventilating and Air Conditioning Systems, its wide range of measurement, accuracy, and small size qualities were seen as being ideal for use as a suction measurement device. Its dimensions are 6.4 mm diameter and 25.4 mm in length. The Xeritron sensor indirectly measures relative humidity using a cellulose crystallite strain beam. It uses a similar principle to a thermostat except the sensor has a small cantilever beam connected to the xeric element that deforms with changes in relative humidity (Xeritron 2002). A strain gauge attached to the beam measures the deformations and infers relative humidity.

The Xeritron sensor measures total suction and the individual suction constituents (matric and osmotic) were considered together. The osmotic suction in a material using the exact same preparation procedures with only a different type of bentonite component was 1.5 MPa (Wan 1996). In the study reported here, Wyoming Bentonite was used, while in many of the previous studies at the University of Manitoba, Saskatchewan bentonite was used. The affect of

bentonite mineral was found to be quite small in the range of 10 - 130 MPa total suction under isotropic and shear loading (Anderson 2003, Blatz et al. 2006). Total suction in the Wyoming bentonite mixture was consistently lower compared to the Saskatchewan mixture at similar water contents. It is anticipated that during increases in water content, the Wyoming bentonite has notably different behaviour due to its higher activity. The best prediction that can be made at this time is that the osmotic suction is likely lower than 1.5 MPa and is probably in the 0.5-1.0 MPa range in the Wyoming bentonite specimens. Osmotic suction was not measured explicitly during the tests but would likely decrease during liquid infiltration since it is a function of the salt concentration of the fluid. Since the permeant is distilled water, the mass of salt was constant during the tests. Therefore, the salt concentration would decrease with increasing water content and osmotic suction would also decrease.

The WRC for the material used in this study is shown in Figure 4.4 (Blatz et al. 2006). This WRC was obtained by preparing specimens in the standard manner and then subjecting them to drying paths under zero stress. Following compaction, total suction is in the 3.5 - 4.0 MPa range. Tests in the present study include increasing isotropic stresses as well as infiltration. Both of these conditions result in decreasing suction (Blatz and Graham 2003). As such, this work extends the existing WRC in the lower suction range. It should be noted that even at full saturation the osmotic component of suction is still present.

4.2.2 Volume Measurement

Volume change in the HITEP triaxial cell is calculated from point measurements of radial and axial strain using Linear Variable Displacement Transformers (LVDTs). The LVDTs used in the apparatus are manufactured by Intertechnology. Both radial and axial measurements of displacement were monitored during the entire length of tests. Radial LVDTs had a 5 mm range of measurement and the axial LVDT had a 20 mm range. Volume change measurements were improved in this program with the addition of two (2) radial LVDTs located at the mid-height of the specimen. This provided a total of four (4) point measurements of radial strain to improve the calculated total volume strain. Mid-height of the specimen was chosen as this represents the farthest distance from the top and bottom boundaries and best represents triaxial behaviour. Since radial flow was applied making the test axisymmetric, measurements of radial strain at the mid-height are considered representative of the entire specimen. Axial displacements were measured using a single LVDT located on a platform connected to the top cap of the specimen as shown in Figure 4.3.

Due to the significant compressibility of the geotextile, LVDTs were located to avoid direct bearing on the geotextile fabric (Figure 4.5). Holes were cut in the geotextile at the LVDT contact points. Before application of the geotextile, a strip of filter paper was placed around the specimen at mid-height to provide hydraulic connection at all locations of the LVDT measurement points. This allowed LVDT

bearing points to be located at positions with no geotextile fabric under the membrane thereby avoiding the compressibility of the geofabric having an affect on the measurements.

4.2.3 Cell and Water Pressure

Cell pressure and water pressure in the top and bottom burettes were measured using traditional pressure transducers. The transducers are manufactured by Enercorp Instruments Limited and were located in cavities along the lines outside the cell. The transducers record pressure from 0-7000 kPa.

4.2.4 Axial Load

Axial load was measured using a submersible load cell. During tests reported here, no additional axial load was applied in addition to the cell pressure but shearing paths could be easily applied along any stress path using algorithms developed by Anderson (2003).

4.2.5 Water Flow

Water flow into specimens was measured using two (2) differential pressure transducers (DPTs) attached to the top and bottom burettes. The DPTs used in this research are Model PX751 from Omega Engineering Incorporated. DPTs have a membrane between two (2) chambers. One (1) chamber was connected to the air pressure supplied to the top of the burette while the other chamber was connected to the water lines exiting the bottom of the burette. A strain gauge was attached to the membrane to measure deformations. The membrane responds to the difference between the pressure applied at the top of the burette

and the pressure at the bottom; namely the water pressure from the height of water in the burette. As water flows out of the burette the height decreases thus resulting in membrane deformation decrease and the strain gauge deforms. DPTs are calibrated to burette increments and these particular ones could measure burette level over approximately 160 mm range of water height. Depending on the radius of the burette this corresponds to different volumes of water. In this apparatus the DPTs read burette level over a 21 mL range.

The DPTs measure total water flow into the plumbing, geotextile, and specimen and must be corrected to determine the in test inflow into the specimen. To calculate the mass of water added to the specimen, the initial specimen mass is subtracted from the final. This value is subtracted from the last measurement of total water added to the system (plumbing, geotextile, and specimen) to calculate the quantity of water in the plumbing. Finally, the 'in test' measurements are then corrected by subtracting the water in the plumbing from all values to calculate the water added to specimen throughout the test.

4.2.6 Load Frame

The triaxial apparatus was mounted in a strain controlled ELE 100 kN load frame. Figure 4.6 is a photograph of the complete set-up.

4.3 Data Acquisition/Stress Path Control System

To impose generalized stress and volume paths in q-p-V-S space, automated real-time data collection and stress path control are necessary. To the author's knowledge the custom data acquisition/stress path control system developed at the University of Manitoba is unique. The system includes a Rockwell Programmable Logic Controller (PLC) and associated interface devices, a computer running the software interface (RSView32 1999) and a motor assembly attached to the pressure regulator. The programmable logic controller uses the software application to record raw measurements, calculate engineering parameters and provide feedback algorithms for the automation processes. This section describes the data acquisition/stress path control system by detailing the user interface, automated stress control, feedback algorithms and on-line access to the system. Previously the unmodified base system was used for isotropic compression and shearing tests completed by Anderson (2003) and reported in Blatz et al. (2006).

4.3.1 User Interface

The customized data acquisition/control application provides a user-friendly interface for each type of triaxial test. The user selects the type of test which could include isotropic compression, triaxial shear or isotropic saturation. Figure 4.7 is a typical image of the software user-interface taken during an isotropic infiltration test. A schematic of the triaxial cell with all measurement devices and their current readings appears on the upper right hand side of the

screen. Engineering parameters such as volume strain and mean stress are displayed on the upper left hand side of the screen. These are calculated from the initial specimen dimensions inputted by the user at the beginning of the test and sensor readings during the test. At the bottom of the screen three (3) real-time graphs with plots of volume strain versus mean effective stress, suction versus time and volume strain versus time are displayed. Each test type has its own separate screen with the triaxial schematic but displays unique engineering parameters and graphs consistent with the specific test type being conducted.

The data acquisition/control application provides data protection and measurement updates at regular specified intervals. All data are recorded as they are measured or calculated. This protects against software/hardware malfunctions that can occur during tests and possibly result in loss of information. Commonly, data acquisition applications record all data at the end of a test and if a shutdown occurs during the test, all data may be lost. This application also refreshes the sensor measurements and calculations on the monitor approximately every second. Standard data acquisition applications commonly refresh the displayed data at the data record rate. The data record rate can be in the order of ten minutes for extended tests to limit the amount of data stored (tests reported in this paper require up to 41 days). For monitoring test progression, rapid display refreshing is extremely helpful for the user.

4.3.2 Automated Stress Control

The data acquisition/control system automatically applies triaxial stress and volume paths by controlling cell pressure and axial load. The cell pressure regulator is attached to a motor assembly and is driven by the control system. The desired stress path is selected by the user and the system calculates the desired cell pressure from the feedback algorithms which incorporate monitored real-time data. The control system operates the motor assembly until the cell pressure is within a user-specified tolerance (generally 15 kPa). For safety purposes, maximum and minimum pressures are limited by motion sensors located on the cell pressure regulator.

4.3.3 Feedback Algorithms

Feedback algorithms for calculating desired cell pressure for each test were developed at the University of Manitoba. The user can choose the desired stress path and the system controls the test to follow the path within the tolerance specified.

For isotropic compression tests two (2) different modes may be used: manual entry and recipe. For the manual entry mode, the user inputs the desired cell pressure and the control system operates the motor assembly to achieve it. In recipe mode, desired cell pressures and durations are inputted into a table of times and pressures. The control system achieves the desired cell pressure within tolerances for each specified time duration.

To perform triaxial shearing tests, the user inputs the desired stress path (q/p) and then engages the constant strain-rate load frame. The control system regulates cell pressure to achieve the desired stress path in response to the axial load measured by the submersible load cell. Any ratio of deviator stress to mean stress (q/p) as well as constant mean stress (constant p) shearing tests may be performed.

During infiltration tests, three (3) different boundary conditions may be automatically applied. These include constant mean stress, constant volume and constant stiffness boundaries. A schematic of the paths was shown in Figure 2.9. Constant mean stress tests use the same algorithm as the isotropic compression tests. Initial cell pressure is recorded at the beginning of the test and the control system regulates cell pressure to this value within the specified tolerance during infiltration with water.

Constant volume infiltration tests are conducted by recording initial volume strain of the specimen at the beginning of the test and maintaining that volume during infiltration. Swelling soils attempt to increase in volume as their water content increases. Every ten minutes, the program compares the current volume strain to the initial volume strain as infiltration continues. If the difference is greater than a specified tolerance (generally 0.03% volume strain), the program increases desired cell pressure to compress the specimen back to its initial volume. A rate of cell pressure increase versus change in volume strain

(generally 85 kPa/% volume strain) is inputted by the user and can be altered at any time during the test. The rate was developed during initial testing. The goal is to bring the specimen back to original volume during each increment. Raising the rate too high results in over-compression and later decreasing of cell pressure. Having a lower rate could result in extended periods where the specimen has expanded past desired tolerances.

For the constant stiffness boundary condition, test specimens are allowed to swell along a user-specified slope as shown in Figure 2.9. Real-time volume strain is compared to the initial volume strain and the desired cell pressure is altered to maintain the stiffness relationship defined by the user.

All infiltration tests continue until flow of water into the specimen, volume change, mean stress, and suction equilibrate to a user-specified condition. Due to the transient nature of the infiltration tests, the end of test criterion is not unique but soil specific. Tests reported in this study are continued until the change per day is less than 2% of the total change throughout the infiltration phase for each criterion including water flow, volume change, mean stress and suction.

The system allows for isotropic compression, triaxial shearing, infiltration and drying tests using vapour equilibrium tests to be performed in succession on one (1) specimen. Stress history and environmental states can be applied in any order. This provides the framework for evaluating soil behaviour under different

stress and volume paths. Anderson (2003) evaluated yielding during automatically controlled isotropic compression and triaxial shearing tests performed using this system.

4.3.4 On-line Access

Remote control software (RealVNC http://www.realvnc.com/winvnc.html) has been installed on the lab computer running the data acquisition/control application. RealVNC is available as freeware and allows remote access to any computer running the RealVNC server over the Internet. The remote computer can view and interact with the lab computer using the specific software control application. A window appears on the remote computer and displays the screen output of the lab computer. While connected the remote computer controls the lab computer. Triaxial tests running in the lab may be monitored and altered over the Internet from anywhere in the world using this application. This includes both checking the progress of triaxial tests as well as changing test parameters such as cell pressure, tolerances and volume-mean stress slopes. It is important to note the on-line access capabilities because of the length of tests reported in this paper can be as long as 41 days.

4.4 Hydraulic Conductivity Test Apparatus

The liquid infiltration apparatus is modified further to measure radial and vertical hydraulic conductivity. Radial flow tests are quite similar to infiltration tests except drainage is provided at the center of specimens and no suction sensor is

included. Vertical flow tests retain suction measurement at the center of specimens but remove the Lucite discs and geotextile from the apparatus. Both flow apparatuses use a bubbler to measure outflow of air and a burette to measure outflow of water.

4.4.1 Radial Flow Apparatus

A schematic of the radial flow apparatus is shown in Figure 4.8. It is very similar to the infiltration apparatus described above except the suction sensor is removed and a 0.47 mm hole is drilled down the entire length of the specimen following compaction as shown in Figure 4.9. A mesh is inserted into the hole to keep it open. The basic configuration remains the same including radial flow from the perimeter to the center of specimens. Flow paths are therefore approximately symmetric about the specimen's center axis. Axial flow is not applied in order to provide a consistent flow regime throughout specimens, aiding interpretation.

To allow center drainage out of the triaxial cell, a hole is drilled through the triaxial pedestal base. A copper pipe is placed through the hole and extends through the base, bottom filter paper, filter stone and Lucite disc to approximately 35 mm inside the mesh at the center of the specimen. The lower filter stone and Lucite disc have holes drilled through them to allow the copper pipe through. During installation the annulus between the Lucite disc and copper pipe is sealed with 5 minute epoxy produced by Lepage. The copper pipe is sealed at the

bottom of the pedestal base and then connected to a bubbler to measure downstream flow out the center of the specimen.

Beyond suction measurement, the apparatus uses the same instruments as described above. In addition, the copper pipe that is inserted into the base of the triaxial cell and a bubbler is also attached. The hose from the copper pipe is placed into an upside down burette filled with paraffin oil sitting in a bowl of the same oil. Air pushed out of the center of the specimen exits the tube, rises to the top of the upside down burette and is measured by hand throughout tests. Once water outflow reaches the end of the tube, it is connected to a burette to measure water outflow. The time of water breakthrough out the center of the specimen is back calculated by measuring the volume of the hose and copper pipe.

4.4.2 Vertical Flow Apparatus

The vertical flow apparatus does not include the geotextile nor Lucite discs from the infiltration apparatus. Suction is still measured at the center of specimens which is now at the middle of the flow path from bottom to top. Water pressure is applied at the base of specimens and a bubbler is attached to the plumbing connected to the top cap. The other change is the location of the radial LVDTs. Previously all four (4) LVDTs were placed at mid-height of the specimen to measure volume change. Since this apparatus does not apply axisymmetric flow paths two (2) LVDTs are placed each at one-third and two-thirds of the specimen height. Although displacements occurring at other heights of the specimen are ignored, this was considered the best option.

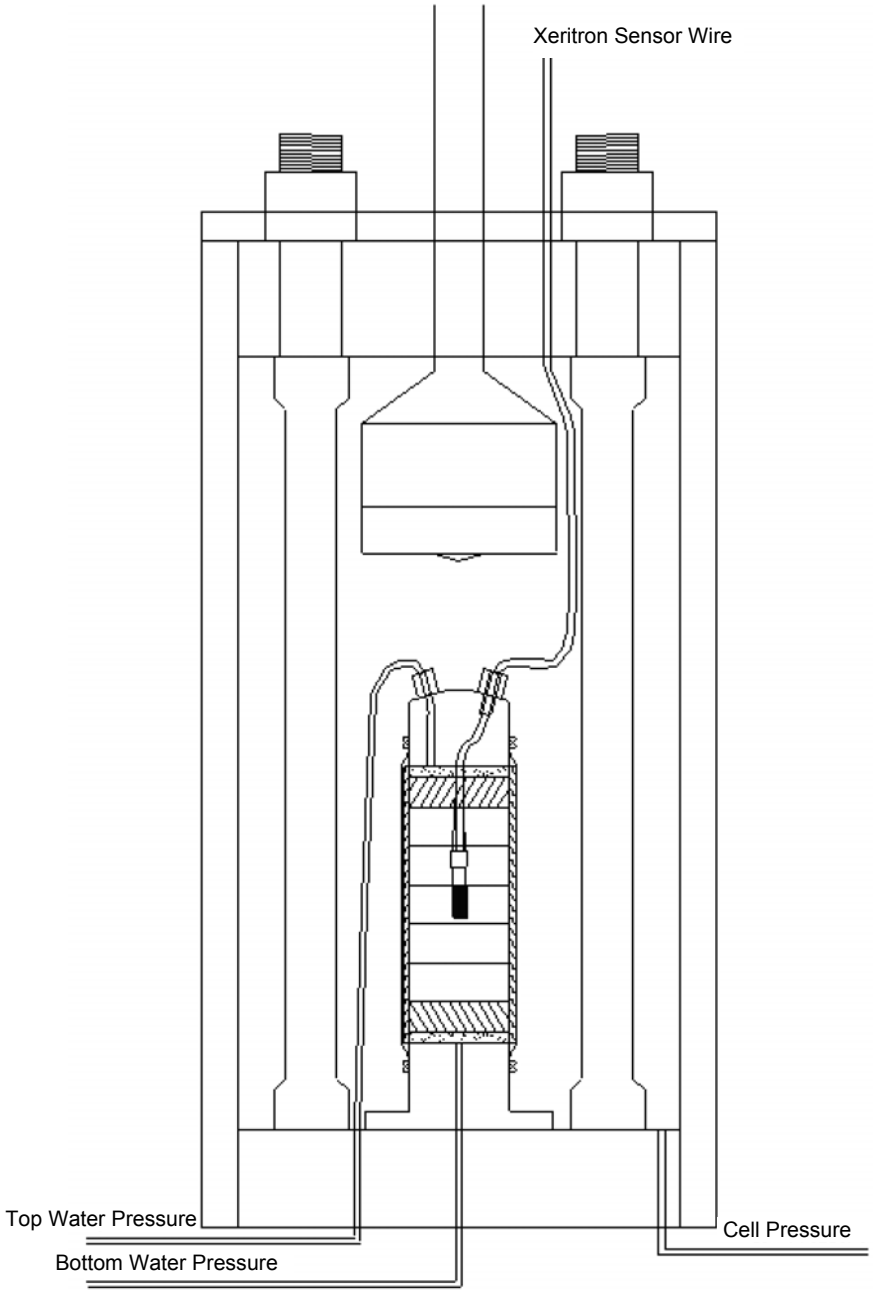

Figure 4.1. Schematic of the triaxial cell (Blatz and Siemens 2004).

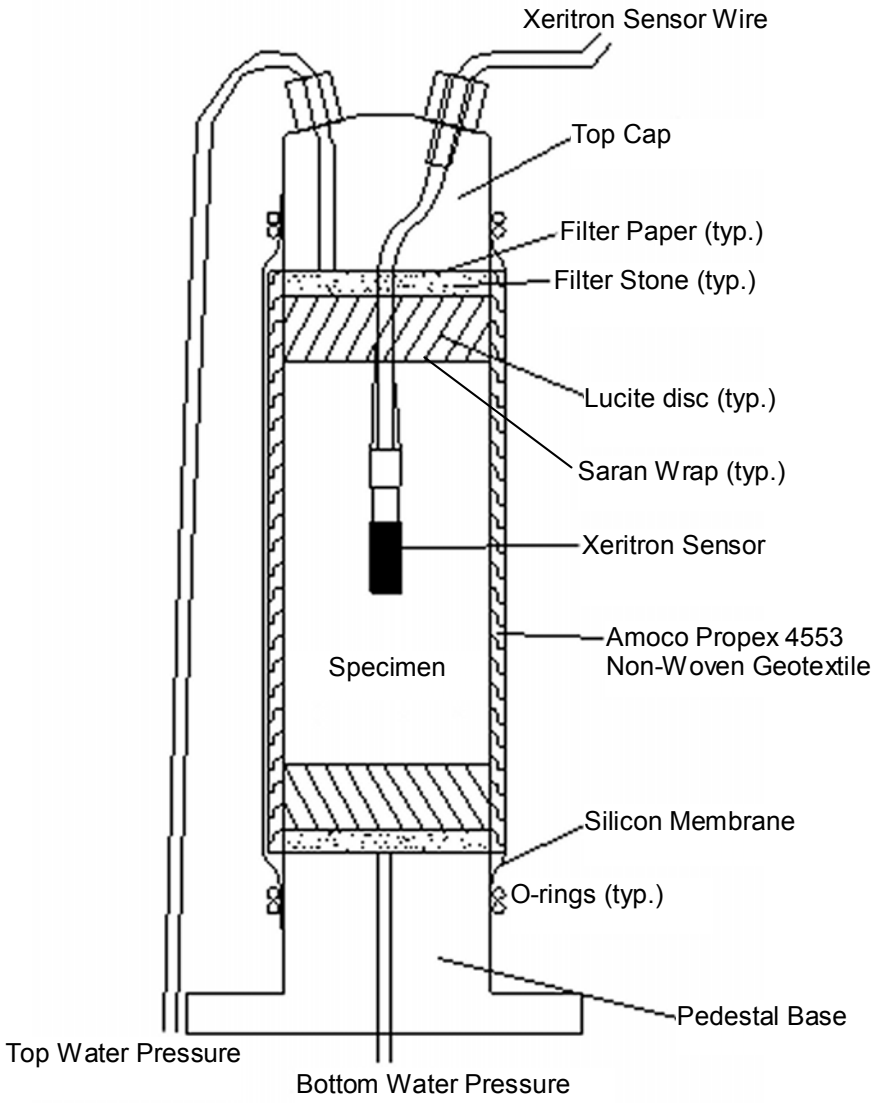

Figure 4.2. Schematic of infiltration apparatus with embedded Xeritron sensor (after Blatz and Siemens 2004).

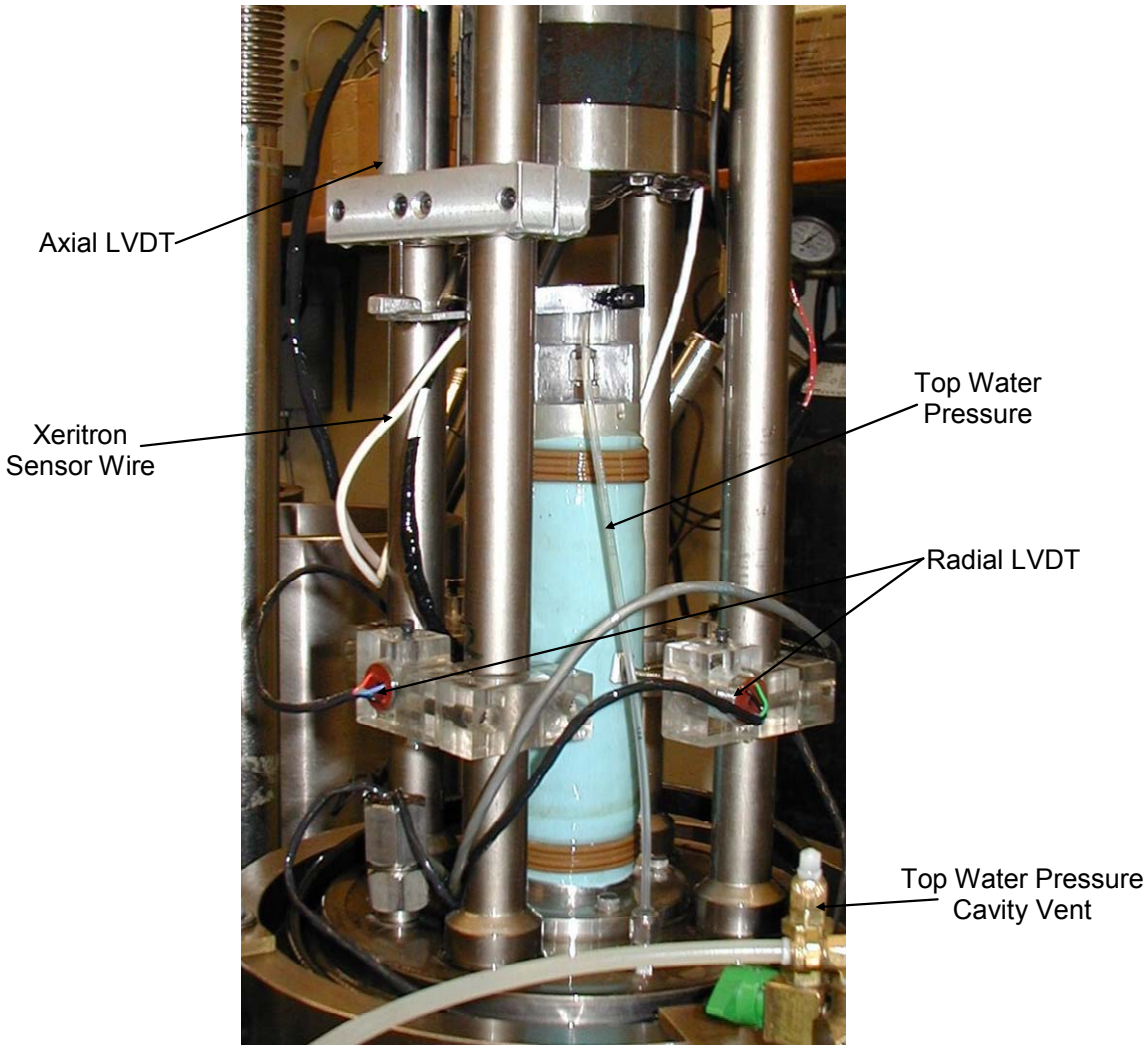

Figure 4.3. Photograph of specimen following installation in the triaxial cell (Siemens and Blatz 2006).

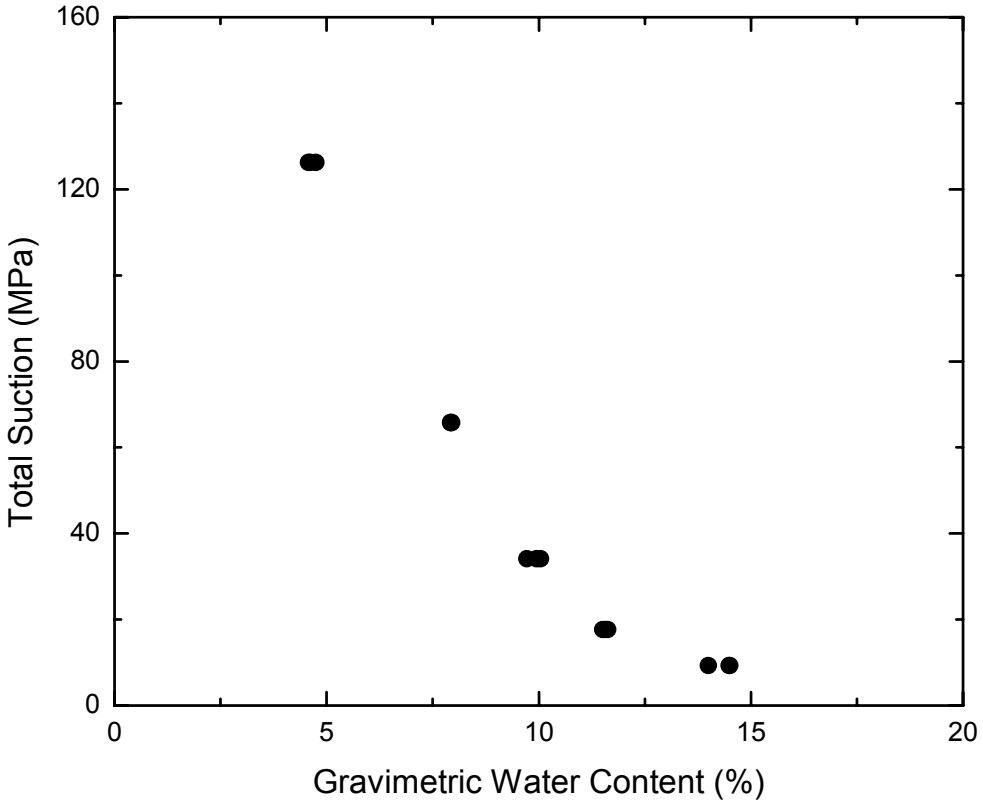

Figure 4.4. Water retention curve (WRC) for Wyoming bentonite sand buffer (BSB) specimens (after Blatz et al. 2006).

Figure 4.5. Specimen wrapped with geotextile showing holes for radial LVDT bearing locations.

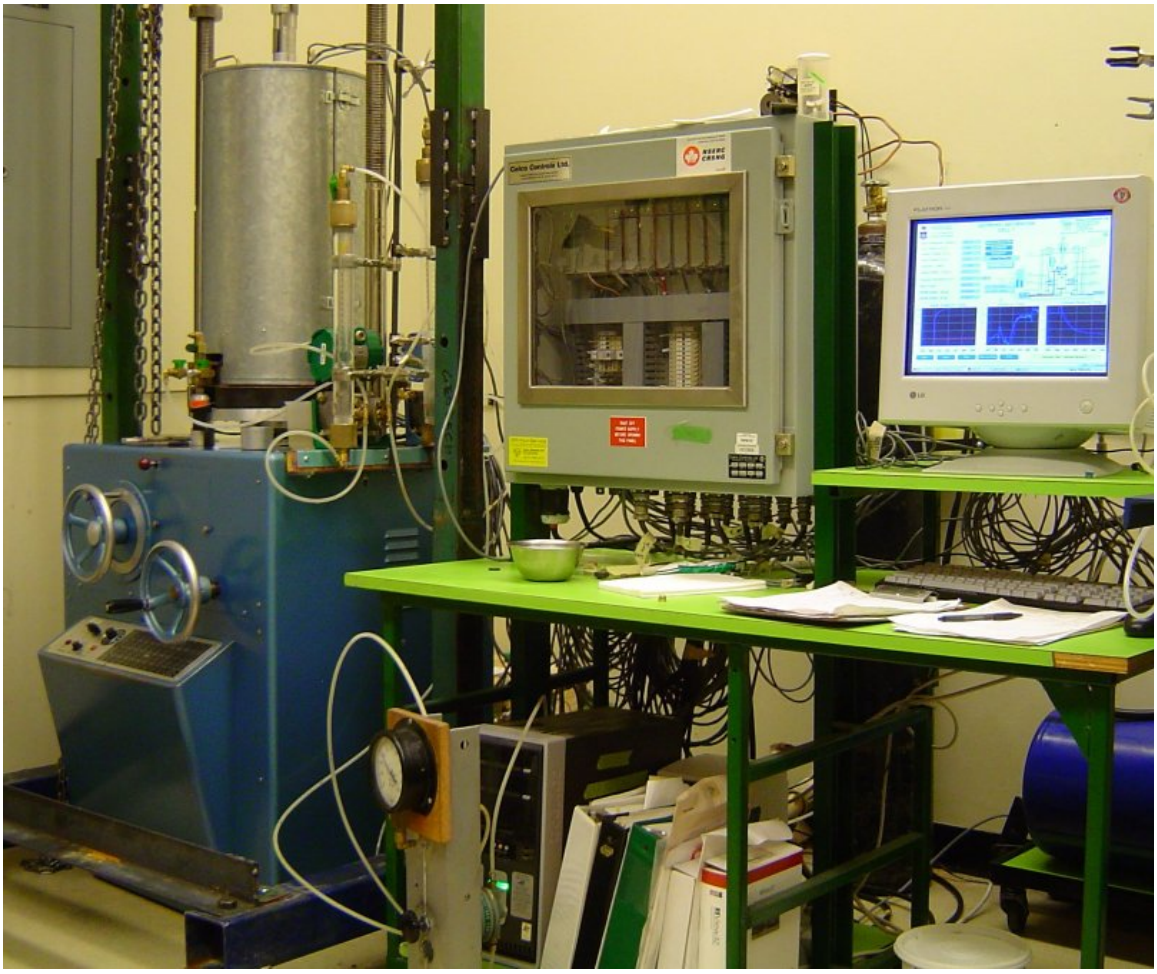

Figure 4.6. Photograph of the triaxial apparatus mounted in load frame and data acquisition/control system.

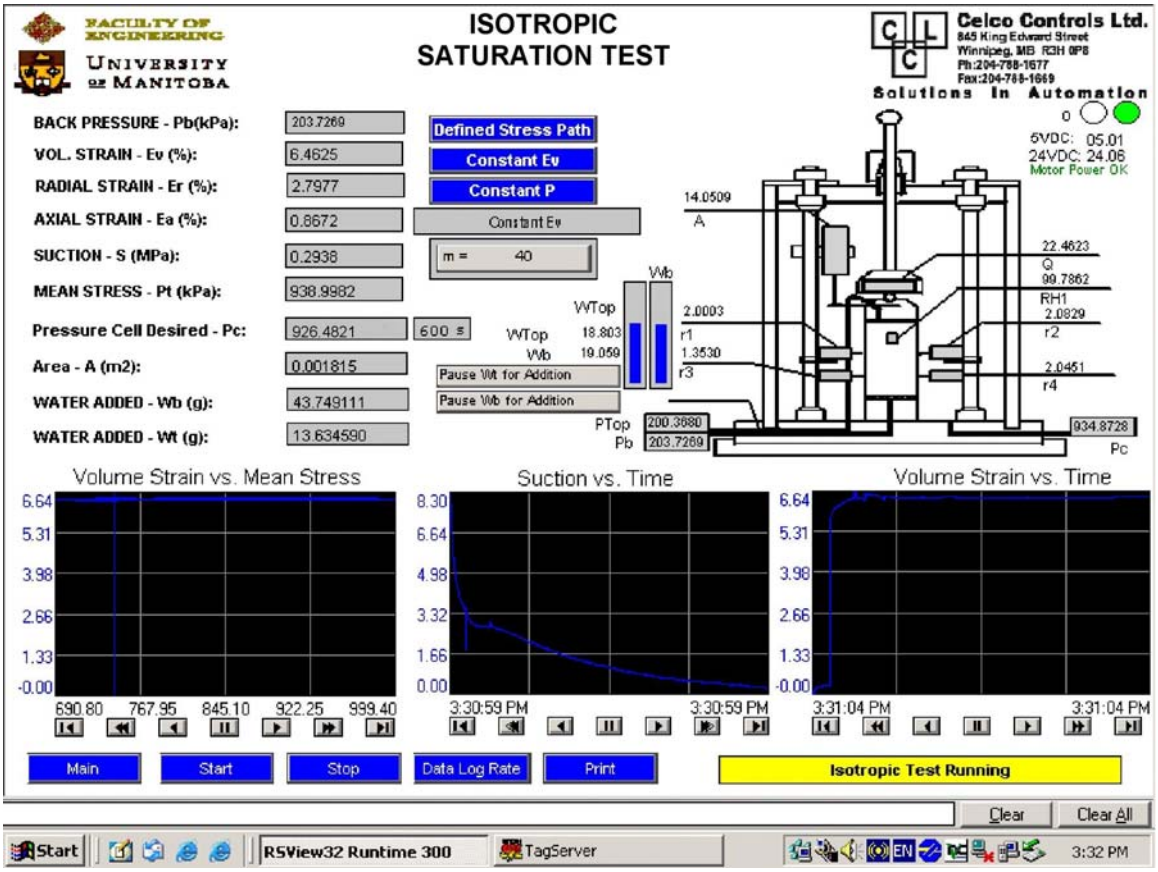

Figure 4.7. Screen shot from isotropic saturation page (after Blatz and Siemens 2004).

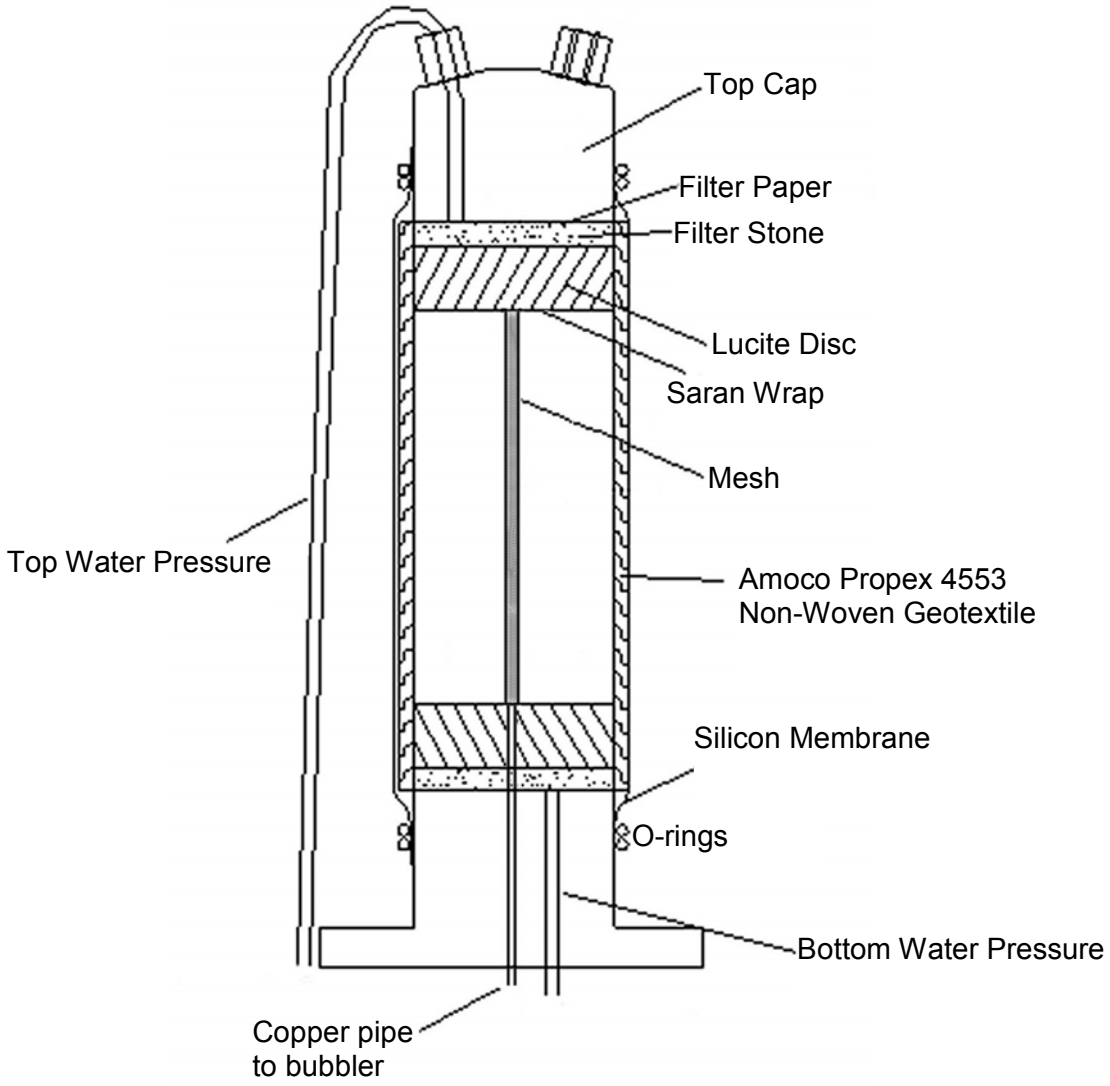

Figure 4.8. Schematic of new hydraulic conductivity apparatus (Siemens et al. 2006).

Figure 4.9. Photographs of a hydraulic conductivity specimen.

CHAPTER 5: DEVELOPMENT OF INFILTRATION SYSTEM UNDER CONTROLLED BOUNDARY CONDITIONS WITH SUCTION MEASUREMENT[3]

5.1 Introduction

This chapter describes the development of a modified triaxial apparatus to apply liquid infiltration with automatically controlled boundary conditions while using the new Xeritron sensor to measure suction at the center of specimens. Three (3) different infiltration boundary conditions of interest including constant mean stress, constant volume and constant stiffness are automatically applied as shown schematically in Figure 2.9. Constant mean stress and constant volume

---

[3] Sections of this chapter have been published as:
Blatz and Siemens (2004, 2005, 2006) – Ontario Power Generation Reports.

Siemens, G.A. and Blatz, J.A. 2006. A triaxial apparatus for applying liquid infiltration under controlled boundary conditions with internal suction measurement. ASCE Geotechnical Journal of Geotechnical and Geoenvironmental Engineering to be considered for publication. *In Review*.

tests form the limits of infiltration boundary conditions while constant stiffness represents a spring type boundary condition between the extremes. This discussion includes a detailed description of the Xeritron sensor, liquid infiltration apparatus, post-test measurements, test interpretation and finally validation and calibration of the testing system. The intent of this chapter is to provide other researchers with all the necessary details of this research program to be able to reproduce the results for verification of the methodology and apparatus. This allows other researchers to then extend or modify the approach to lead to new studies.

5.2 Xeritron Sensor

The Xeritron sensor (Xeritron XN1018 relative humidity sensor) has been incorporated in the triaxial apparatus to measure suction at the center of specimens. Water pressure applied at the perimeter and measured suction at the center of specimens form the upstream and downstream boundary conditions (radially) during testing. A wetting front migrates from the periphery of the specimen towards the center through the specimen. Pore pressure (positive and negative), gravimetric water content, density and saturation vary along the flow path as the process continues from initiation to the end of test condition.

The Xeritron sensor, compacted at the center of specimens, measures total suction in the area around the specimen. During equilibration and isotropic mean stress increments, this is representative of the entire specimen (Blatz et al.

1999). During liquid infiltration, the sensor measures total suction at the center of the specimen, which is the downstream end of flow paths during undrained tests.

The Xeritron sensor was selected because of its wide range of relative humidity measurement, accuracy, small size, durability and flexibility. It functions on the basis of vapour equilibrium within the specimen pore space to provide measurement of relative humidity that allows suction to be calculated from thermodynamic principles. The sensor uses a cellulose crystallite cantilever beam that deforms with changes in relative humidity (Xeritron 2002). The crystallite beam is protected by an open-ended stainless steel tube that prevents total stress increments from impacting sensor response.

To make the Xeritron sensor suitable for installation in triaxial specimens, the sensor is modified by shortening the wires at the back of the steel cover, soldering them to thicker stranded wire, surrounding the connection in a copper cylinder and then embedding the connection in epoxy. A wire mesh covers the open end of the stainless steel tube allowing free movement of vapour but preventing soil from directly impacting the crystallite beam. A photograph of the modified sensor which is 7.7 mm in diameter and 37.5 mm long is shown in Figure 5.1.

The Xeritron sensor's output can be set to correspond to a specific suction range if desired. Potentiometers on the sensor's signal conditioning board are

fine-tuned so that the minimum and maximum electronic signal (4-20mA) recorded by the data acquisition system corresponds to a specified relative humidity range. This makes the Xeritron sensor extremely flexible for different applications.

The effect of a compacted sensor on soil behaviour must be considered. Blatz et al. (1999) reported that compacting psychrometers at the center of triaxial specimens did not notably affect either their mechanical or suction behaviour during isotropic or shear loading. During these infiltration tests water is flowing toward the sensor and the majority of swelling is occurring in the radial direction. The sensor only makes up 2.4% of the cross-sectional area and less than 1% of the total volume of a typical 50 mm diameter by 100 mm height cylindrical specimen and is also located at the end of the flow path. Finally the Xeritron sensor is not fixed in the specimen as it is only attached with a flexible wire. For these reasons the sensor is not expected to have any significant affect on hydraulic or deformation behaviour of specimens during these infiltration tests. Any effect that the sensor does have on specimen behaviour is far outweighed by the benefit of internal suction measurement throughout testing.

5.2.1 Xeritron Sensor Calibration

The Xeritron sensor measures relative humidity from 0-100%, covering the entire theoretical range of suction. The manufacturer reports its accuracy is ±3% including linearity, repeatability and hysteresis (Xeritron 2002) but the accuracy of the instrument has been found to be far better than that specified by the

manufacturer, which is likely given as conservative. To establish individual instrument accuracy for testing, sensors are calibrated using controlled relative humidity environments before and after tests. An example calibration plot and linear regression is shown in Figure 5.1 and a magnified view in the area of 90-100% RH is shown in Figure 5.2. Calibration results indicate an R^2=0.9999 and σ^2=0.05663 over a wide range of relative humidity.

The calibration procedure begins at RH=100% then RH=33.6% followed by points of increasing relative humidity in the area of interest for the next test. In this way hysteresis in the sensor is examined during every calibration process. As shown on Figure 5.1 and Figure 5.2, the 100% relative humidity point plots directly on the best-fit line indicating low hysteresis in the sensor. The calibration procedure is also consistent with a decreasing suction response anticipated during infiltration tests. It should be noted that at low values of suction (0-1 MPa) significant non-linearity exists between the relative humidity-suction relationship (Ridley and Wray 1996) as shown in Figure 2.5. In the tests reported here, suction measurements are given to 0.1 MPa resolution. Error bars have been added on Figure 5.2 to show a standard deviation confidence interval for relative humidity measurement.

For calibration, constant humidity environments are created using unsaturated salt and acid solutions in Erlenmeyer flasks. Relative humidity environments of 90% and greater are generated using potassium chloride mixed with distilled

de-aired water. Lower relative humidity values (higher suctions) are generated with sulphuric acid solutions. The first relative humidity values are chosen based on expected suction measurements during tests. BSB specimens have an initial total suction of approximately 3 to 4 MPa. During infiltration tests, suction is anticipated to decrease in response to increasing water content and increasing mean stress (Blatz and Graham 2000, Blatz and Graham 2003). From thermodynamics shown in [2.2], 3.5 MPa suction corresponds to 97.5% relative humidity. Therefore calibration points are concentrated around higher relative humidity values. Points selected include 100.0%, 97.5%, 95.0%, 92.5%, 90.0% 59.0% and 33.6% relative humidity. The calibration procedure is also chosen to represent conditions during testing of decreasing suction (increasing RH) as described above.

The chemical solutions were mixed based on relationships provided by Young (1967) for potassium chloride and Stokes and Robinson (1948) for the sulphuric acid solutions. Following mixing flasks are placed inside an insulated box. Prior to use in calibration, a period of 72 hours is allowed for thermal and relative humidity equilibration of the mixtures. Calibration occurs in the same room as testing to ensure no temperature changes are applied. The impact of small fluctuations in room temperature is reduced by the insulated box.

5.3 Liquid Infiltration Apparatus

The High Temperature, High Pressure (HITEP) triaxial cell was designed at the University of Manitoba (Lingnau 1993) for cell pressures and temperatures up to a maximum of 10 MPa and 100 ^{o}C respectively. Previously the apparatus was modified to control and independently measure suction using vapour equilibrium and a thermocouple psychrometer (Blatz and Graham 2000).

The HITEP triaxial apparatus was further modified to apply liquid infiltration while retaining the ability to control suction using vapour equilibrium (gas phase). A schematic and photograph of a triaxial specimen installed in the apparatus were shown in Figure 4.2 and Figure 4.3 respectively. As displayed in Figure 4.2, water pressure is applied to the periphery of the specimen and water flows radially towards the center. The test geometry can be considered a small scale version of the isothermal experiment (ITT) with the exception of preventing flow into the bottom of the test specimen. The Lucite discs prevent axial flow along the specimen thereby limiting the flow field for interpretation. Flow paths are approximately symmetric about the longitudinal axis of the specimen. Hydraulic and mechanical swelling behaviour under controlled boundary conditions can be examined reliably using the modified apparatus.

5.3.1 Apparatus Development

Development of the liquid infiltration system consisted of several iterations before finalizing the apparatus and procedure. Early tests used a flow pump to cycle

water through the geotextile using the same method in which air was cycled through the woven geotextile in the apparatus described by Blatz and Graham (2000). Monitoring water uptake by the specimen was difficult using this procedure. Also, the geotextile surrounding specimens clogged with bentonite from the specimens resulting in extremely slow circulation rates.

Later water pressure was applied through a single burette to both the top and bottom cavities. During one (1) test using the single burette configuration, air bubbles were noted exiting the top cavity resulting in water being pushed out of the burette. Specimen expansion was still occurring at the time so it was known that water was being taken up by the specimen. The single burette could not measure both inflow through the bottom cavity and air bubbles moving out the top burette. Future tests used the two (2) burette system.

Burette readings were initially taken manually but it was not practical to get enough readings over the long duration of the tests to properly capture non-linear flow rates during tests. Also, due to the extended nature of the tests many manual readings were required. Differential Pressure Transducers (DPTs) were added to provide continuous electronic recording of burette levels throughout tests to ensure all water movements were measured and non-linear flow behaviour was captured.

The specimen configuration was also altered during development. Initially the top and bottom Lucite discs were not included. This allowed water infiltration to occur both radially through the geotextile and axially through the top and bottom filter stones. Interpretation and modeling of test results was difficult since not all layers were subjected to the same flow regime. Adding the top and bottom Lucite discs resulted in overall longer tests since the average drainage path was increased. This configuration provides a consistent flow regime for the entire specimen. The radial flow regime allowed averaging of the end of test spatial measurements to be taken since all layers were theoretically subjected to the same water flow. Since natural density and water content variations occur within compacted specimens and some errors can occur during water content and bulk density measurements, averaging the measurements results in increased confidence for interpreting hydraulic and mechanical behaviour.

Measuring volume change using Linear Variable Displacement Transformers (LVDTs) was recognized as a limitation of the apparatus. Previous tests in the HITEP cell used two (2) radial LVDTs and one (1) axial LVDT. A DPT was attached to a burette connected to the cell fluid in order to measure overall volume change of the specimen through cell fluid movement. This has been used on other triaxial apparatuses in order to infer specimen volume change. The main issues that did not allow use of the DPT in the HITEP apparatus were trapped air inside the cell and non-constant cell fluid leakage. During filling, a finite volume of air is still present in the cell although the exact amount is not

known. Due to the number of internal sensors and wiring within the HITEP cell, there are many locations in which air can be trapped. During increases in cell pressure the trapped air compresses and is measured as volume change by the external burette. Numerous attempts were completed in order to calibrate the volume change resulting from air compression. Air volumes inside the cell were not consistent during consecutive tests so the error in measurement exceeded the acceptable tolerance levels specified. Finally, the cell fluid leaks at a slow rate through cup seals in the top and bottom of the cell. Again attempts to calibrate the leakage rate for selected cell pressures were made but consistent rates were not found.

During development of the apparatus, water pressure to be used during infiltration was determined through testing at different pressures. Tests were completed using water pressures of 100 kPa, 200 kPa and 300 kPa respectively. Results showed that increasing water pressure during the infiltration phase increased end of test water content, lowered dry density and increased degree of saturation. It was decided that 200 kPa water pressure would be used for the remainder of the tests. This provided high enough pressure to allow reasonable completion of tests but meant that lower mean stresses (cell pressures) such as 250 kPa could still be applied. This is an important variable that should be examined in more detail in further testing.

5.3.2 Test Procedure

Following installation in the HITEP cell, the Xeritron suction sensor is allowed to equilibrate under nominal cell pressure (hydrostatic pressure of the cell fluid with no additional pressure added). This phase is followed by isotropic compression to an initial target confining pressure. Mean stress is increased incrementally until the level desired at the beginning of infiltration is reached. Isotropic compression increments last at least 24 hours. Sometimes longer durations are required for suction sensor equilibration.

Liquid infiltration begins by filling the apparatus plumbing with water. A valve connected to the top pressure transducer cavity is opened to serve as a vent. Water is pushed from the bottom burette through the plumbing, filter stones and geotextile until the top pressure cavity is filled and water flows out the vent (Figure 4.2 and Figure 4.3). The valve is closed and the top and bottom burettes are pressurized to the selected water pressure. Liquid infiltration under controlled boundary conditions continues until the rate of change in suction, total volume change or mean stress increase (depending on boundary condition) and infiltration reduces to less than 2% per day of the total changes.

The data acquisition system measures water added to the specimen by recording initial burette level and real-time burette readings for the remainder of the test. Prior to refilling a burette a button is pushed on the computer screen and the current water added to the specimen is saved. Following refilling, the button is

pushed again and the counter continues at the current value. The system measures total water added to the apparatus including plumbing during initial filling. To determine actual water flow into the specimen, the difference between the end of test and initial specimen mass is used.

Three (3) different boundary conditions, constant mean stress, constant volume and constant stiffness, are applied during liquid infiltration as illustrated in Figure 2.9. Constant mean stress boundary conditions allow specimens to deform (swell) as water infiltrates. Constant volume tests maintain original specimen volume during infiltration by increasing mean stress following extremely small (~0.03% volume strain) deformations. Increasing mean stress counteracts the specimens desire to swell. Constant stiffness tests apply infiltration while controlling a target volume strain-to-mean stress relationship (Figure 2.9). These boundary conditions represent simulated field conditions as shown in Figure 1.2.

5.4 Post-Test Measurements

Following testing, spatial distribution of gravimetric water content and bulk density are measured to calculate dry density and degree of saturation. Later in the testing program, Mercury Intrusion Porosimetry (MIP) and Scanning Electron Microscope (SEM) photographs were also performed on selected bulk density samples from an as-compacted specimen as well as some liquid infiltration specimens. These measurements are extremely valuable in order to understand

internal density and water content changes that occur during infiltration. The specimen is sliced along compacted layers and then circular cutting tools are used to divide each layer into radial regions. Figure 5.3 shows an example distribution of gravimetric water content, the circular cutting tool and radial regions. Also shown on the figure for comparison are the water content at the beginning of the test, after isotropic compression (assumed equal) and the average end of test water content from test results. Due to imposed radial flow, each layer's region should be equal and the results show little variation (i.e. at all heights the radial distribution of water content and density should be equivalent).

5.4.1 Post-Test Measurement Development

Post-test measurements also were developed during preliminary testing. Initially only two (2) spatial measurements of gravimetric water content were taken at each layer. These showed increasing water content from the center to perimeter of specimens but non-linearity could not be observed since only two (2) measurements were taken. Two (2) new cutters were made by the technician and also wax density measurements were added. This allowed determination of internal non-linear changes of water content, bulk density, dry density and degree of saturation that occur during infiltration tests.

After initiation of the post-test measurements and periodically during the testing program a series of specimens were broken up following compaction in order to establish initial conditions and gain confidence in the measurements. Results from the three (3) specimens GS-038, GS-043 and GS-067 are shown in

Figure 5.4, Figure 5.5, Figure 5.6 and Figure 5.7 including gravimetric water content, bulk density, dry density and degree of saturation. Gravimetric water content measurements show consistent water content distributions throughout the specimen. Bulk density measurements also are similar especially the outside measurement in Figure 5.5. The as-compacted dry density distribution shown in Figure 5.6 also shows consistent distributions from specimens and only small changes from the center to the perimeter. Finally, the degree of saturation distribution (Figure 5.7) is also consistent between different specimens and little gradient is observed from the center to perimeter.

5.4.2 Sample Preparation for MIP and SEM

Samples for MIP and SEM testing were the wax covered radial sections that were used for bulk density measurements. Following bulk density determination, the wax was carefully removed and specimens were placed on a tray inside a desiccator containing pure sulphuric acid. The acid created a low relative humidity environment inside the air space of the desiccator that dried the MIP and SEM specimens. Specimens were dried in the desiccator until constant mass was achieved. Both the MIP and SEM test apparatuses used in this research required dried specimens. Previous MIP tests (Wan 1996) on a similar material used specimens that had been prepared in the same manner. The same method of preparation was selected to ensure results would comparable with previous work. MIP testing was completed at the Geotechnical Laboratory at Dalhousie University and SEM photography was performed at the Geological Laboratories at the University of Manitoba.

5.5 Validation/Calibration of Liquid Infiltration System

The final test configuration, apparatuses, procedure and post-test measurements are the result of numerous attempts. They include checks and balances to ensure test specimens are subjected to consistent conditions. For validation and calibration of the liquid infiltration system two (2) comparisons are provided. The first is a comparison of two (2) 500 kPa constant mean stress infiltration tests shown where water pressure was applied at 100 kPa and 200 kPa. These preliminary tests were completed at these selected water pressures to determine the water pressure to be used for the program. The second comparison investigates the influence of the compacted sensor on the volume change, water inflow, and end of test mean stress during infiltration tests. In this comparison, 500 kPa constant mean stress and 500 kPa constant volume infiltration tests with and without a Xeritron sensor are presented.

5.5.1 Water Pressure Comparison

Results from the 100 kPa and 200 kPa water pressure tests, presented as mean stress, volume strain, suction, and water added to specimen versus time, are shown in Figure 5.8, Figure 5.9 and Figure 5.10 respectively. In general, similar modes of behaviour are observed giving confidence that the system is working properly. Volume response (Figure 5.8) shows similar behaviour observed during isotropic compression. This is expected since the specimens were compacted, installed and isotropically loaded using the same procedure. During constant mean stress infiltration, the 200 kPa water pressure specimen shows

greater expansion (negative volume strain) compared with the specimen with 100 kPa water pressure. Expansion also occurs at a greater rate during initial stages of infiltration in the higher pressure specimen. In the suction response comparison (Figure 5.9), again relatively similar responses are generated during isotropic compression. Suction decrease with increasing mean stress is observed.

During liquid infiltration, the 200 kPa water pressure specimen shows an end of test suction value lower than the 100 kPa specimen. The 100 kPa specimen shows some unexpected response with increasing suction measurement even though water content is increasing. At the end of the test, an overall decrease in suction is observed. Finally the water added to specimen comparison (Figure 5.10) displays the reason for the observed differences in behaviour, that being the 200 kPa specimen takes in more water than the 100 kPa water pressure specimen. This is anticipated due to the higher water pressure value while holding mean stress constant at 500 kPa. Greater water contents result in further expansion (Figure 5.8) and a greater decrease in suction (Figure 5.9).

Post-test spatial measurements reinforce observed behaviour during the test as shown in Figure 5.11, Figure 5.12, Figure 5.14 and Figure 5.13. Again similar shapes of the post-test distributions are observed and give confidence that the test apparatus is applying anticipated conditions to the test specimens examined. Comparing the results shows the 200 kPa test specimen has higher gravimetric

water content throughout. Bulk density results (Figure 5.12) show increasing bulk density from the center to the middle measurement and then approximately constant bulk density to the perimeter of the specimen. Dry density distribution shows a peak in the middle measurement for both specimens. The 200 kPa water pressure specimen has lower dry density for the outer two (2) measurements. These end of test measurements are anticipated since more water is taken into the specimen with higher water pressure. Increased water intake could also be a result of greater ability of water to dissolve more pore air at higher water pressure from Henry's law. Henry's law states the mass of air that can be dissolved by water at constant temperature is directly proportional to its absolute pressure (Sisler et al. 1953). This resulted in higher water content and degree of saturation as well as more swelling measured as lower dry density. Bulk density predictions are difficult but the consistent measurements give higher confidence. Finally degree of saturation increases from the center to the perimeter as shown in Figure 5.14 with the 200 kPa water pressure specimen having higher saturation throughout.

Following completion of the two preliminary tests, 200 kPa water pressure was selected for the remaining tests. This represents a balance between a high enough water pressure that tests can be completed in a reasonable time frame and low enough pressure that a wide range of isotropic mean stresses can be used during tests.

5.5.2 Influence of Compacted Xeritron Sensor

Test results from 500 kPa constant mean stress and constant volume tests with and without the compacted sensor are illustrated in Figure 5.15, Figure 5.16, Figure 5.17, Figure 5.18 and Figure 5.19 including volume strain, axial strain, radial strain, mean stress and water added to specimen versus time respectively. During the isotropic compression phase, the no sensor tests show approximately 3.1-3.3% volume strain while the tests with the compacted sensor has volume strains between 5.4% and 6.4%. During infiltration volume control is maintained for both constant volume tests. In the constant mean stress tests, increased volume expansion is observed over a longer period of time in the test without a compacted sensor. The relative difference is that -4.7% volume strain is observed for the specimen that included a sensor while the non sensor specimen expanded -10.5%, which is a difference of 55% less expansion. Comparing the axial and radial strains (Figure 5.16 and Figure 5.17) shows that observed axial strain behaviour including expansion and compression is almost identical. On the other hand, radial strain compression during isotropic compression is greater and expansion is less when the specimen has a sensor compacted at the center.

Mean stress versus time data for constant mean stress and constant volume tests with and without a compacted sensor are shown in Figure 5.18. The constant mean stress tests show control of mean stress was maintained throughout isotropic compression and infiltration. Constant volume infiltration

results show similar increases in mean stress (less than 6%) required to maintain pre-infiltration volume.

The water added to specimen plot confirms earlier mean stress and volume change results. The constant mean stress specimen without a compacted sensor was able to take in more water (33.8 mL compared with 26.0 mL or 24% less) since it experienced further expansion. The constant volume specimens experienced similar water infiltration (13 mL and 16 mL or 23% more for no sensor and sensor respectively) and is consistent with similar increases in mean stress.

The post-test distributions including gravimetric water content, bulk density, dry density and saturation are shown in Figure 5.20, Figure 5.21, Figure 5.22, and Figure 5.23 respectively. Gravimetric water content is greatest in the constant mean stress specimen without sensor followed by the other constant mean stress test and then the two (2) constant volume tests. Interestingly, comparing the two (2) constant volume tests, the specimen with sensor has greater perimeter water content while the specimen with no sensor has greater water content at the center. Relative bulk density comparisons show the greatest overall bulk density in the constant volume specimen without sensor. The other three (3) specimens had similar bulk density at the perimeter measurement with decreasing bulk density in the constant mean stress and constant volume specimens with sensor and increasing bulk density in the specimen without

sensor. Dry density is greatest in the constant volume specimen with no sensor followed by the constant volume specimen with sensor and the two (2) constant mean stress specimens having similar dry density. Saturation distributions show both specimens without sensor having the greatest overall distributions. The constant mean stress specimen without sensor has the least saturation gradient from perimeter to center while the other three (3) specimens show decreasing saturation.

Isotropic compression and infiltration results under constant mean stress and constant volume boundary conditions show that the sensor has limited affect on soil behaviour. Blatz et al. (1999) showed that compacting psychrometers had little to no effect on suction and volume change behaviour under isotropic and triaxial loading following suction change through the application of vapour drying. Under constant mean stress infiltration conditions, when no sensor is included, increased expansion is observed and leads to greater water infiltration. During constant volume infiltration, the affects are minimal as mean stress increases and water infiltration is similar. The likely cause of the change in behaviour is the inclusion of the sensor in the top half of the specimen resulting in changes of behaviour between the top and bottom halves and the annulus between the sensor and surrounding soil. Below the sensor in the bottom two (2) layers, there is only soil from perimeter to center. In the third and fourth layers (from the bottom) between the sensor and specimen the non-homogeneous conditions affect overall measured behaviour. During the preparation procedure a hole is

drilled in the third and fourth layers (from the bottom) to allow insertion of the sensor. The drilled hole must be of a nominally greater size than the sensor to allow insertion. This creates a small annulus that does not appear in the top layer nor in the first two (2) compacted layers. During isotropic compression greater compressive strains could occur due to compression of the annulus between the specimen and sensor. During constant mean stress infiltration it appears expansion is somehow restrained. This is likely due to inward expansion to fill the annulus thereby reducing density. The reduced density material would have less ability to expand and allow further water content increase.

Boundary conditions applied during infiltration include constant mean stress, constant volume and two (2) slopes of constant stiffness. During constant volume infiltration little observed difference is noted in behaviour while in constant mean stress infiltration observed increased affects of the compacted sensor. During constant stiffness tests which include expansion as well as increases in mean stress, less effect is expected especially in the test that is closer to constant volume conditions. Constant mean stress volume change behaviour observed during these infiltration tests is seen as a lower bound on expansion that would be measured with no sensor.

Despite these limited effects, the benefit of measuring suction at the center of triaxial specimens during isotropic compression and infiltration is important and

provides new insight to behaviour of high plastic swelling materials. The original goal of this apparatus is to control and/or independently measure all stress and volume states. Since suction behaviour is measured, suction changes do not have to be assumed to occur at the same time as volume change as is sometimes done although known not to be the case. Regardless, the trends in behaviour are consistent and although the impact of the sensor is noted, the value provided by the measurement with the embedded sensor far outweighs the influence of the sensor on the magnitude of the measurements. As such it was felt beneficial to continue use of the sensor in the testing program to explore the behavioural mechanisms.

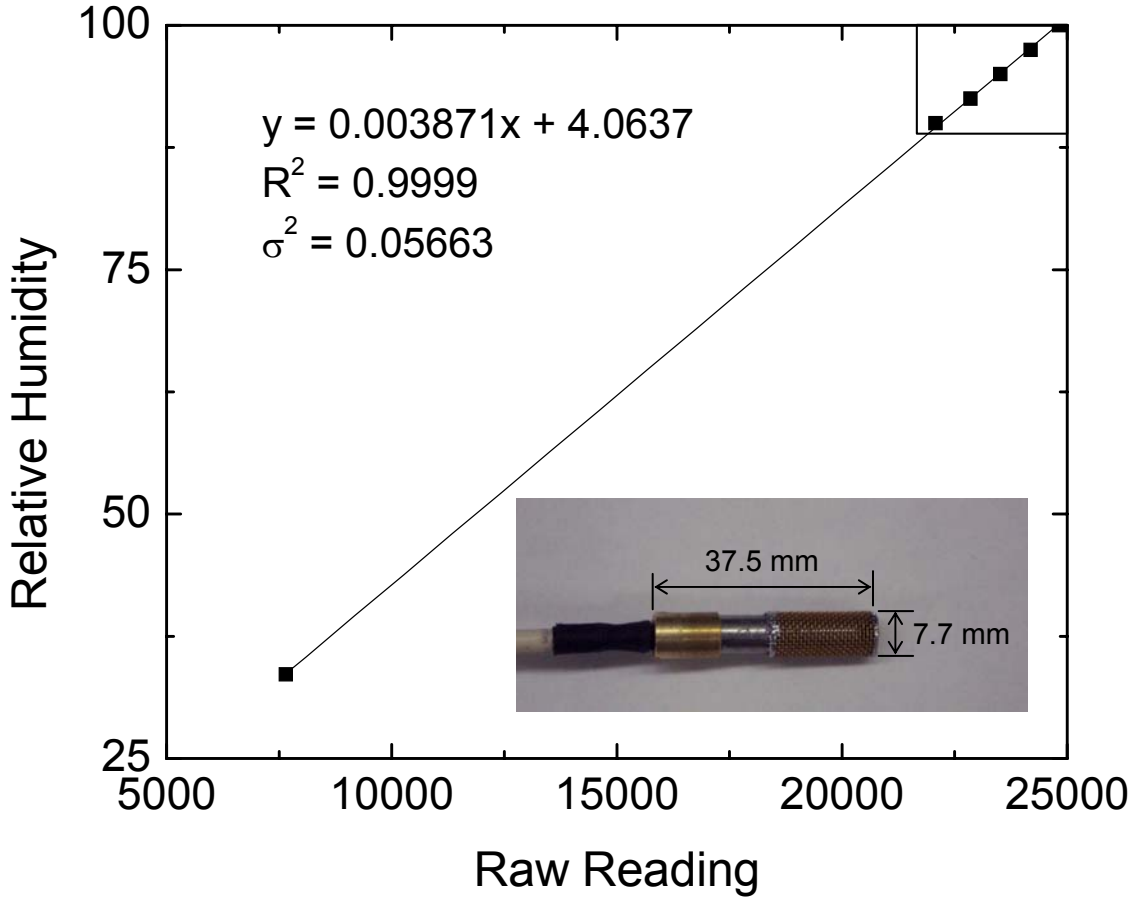

Figure 5.1. Xeritron sensor and calibration plot (Siemens and Blatz 2005).

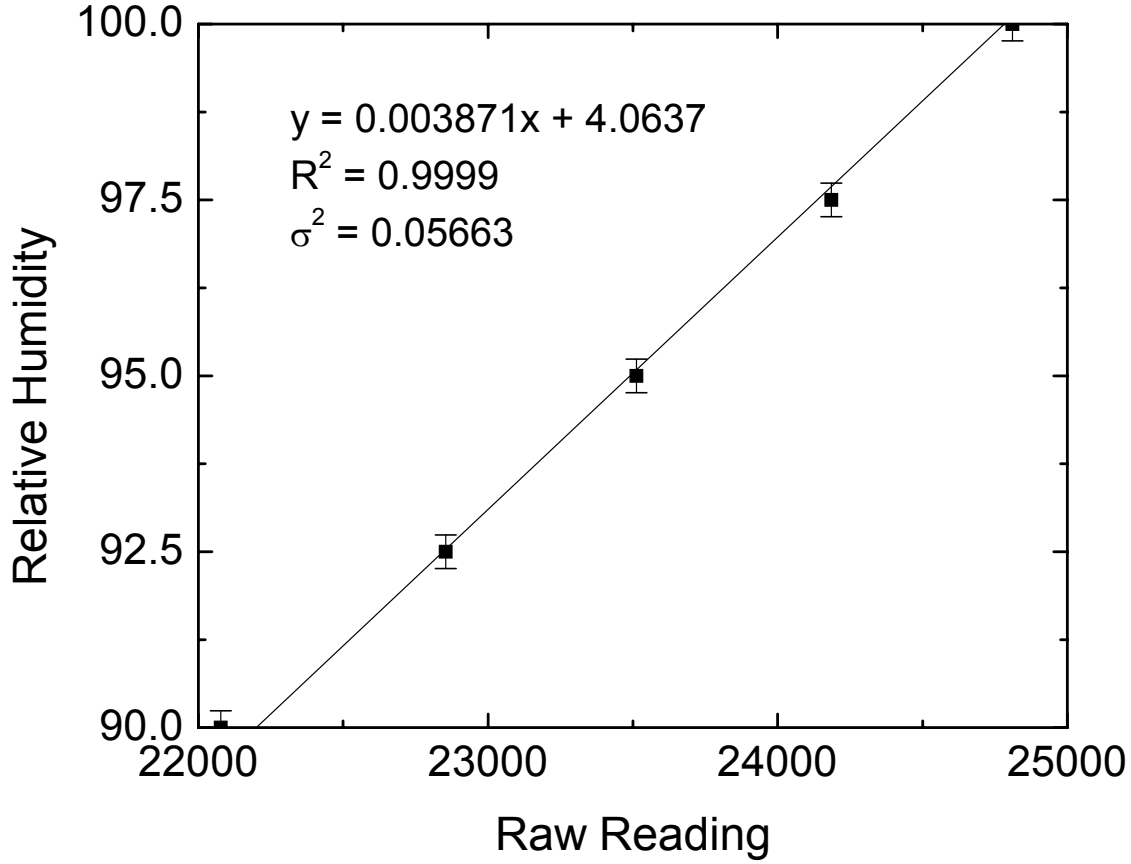

Figure 5.2. Xeritron sensor calibration with error bars (one standard deviation) for 90-100% relative humidity (Siemens and Blatz 2005).

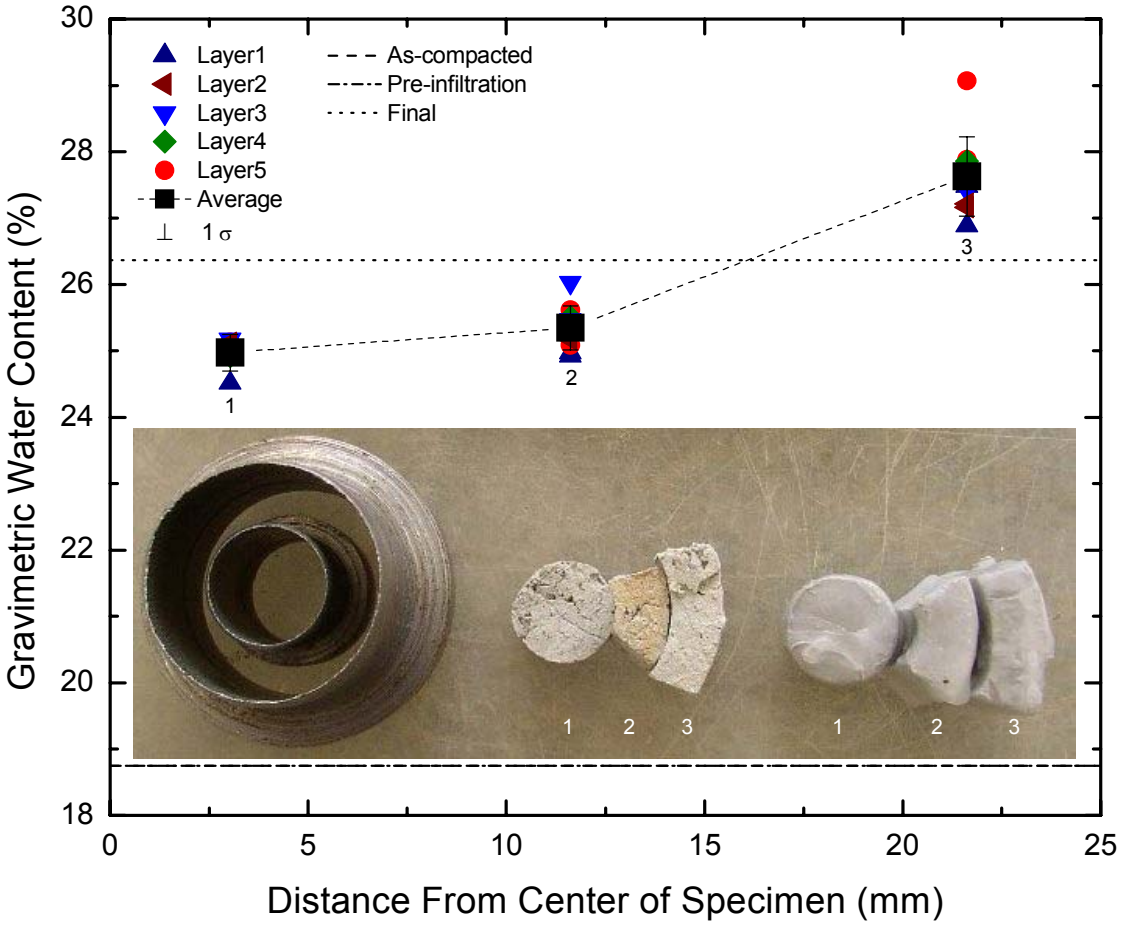

Figure 5.3. Example end of test spatial distribution of gravimetric water content, circular cutting tool and radial regions (Blatz and Siemens 2006).

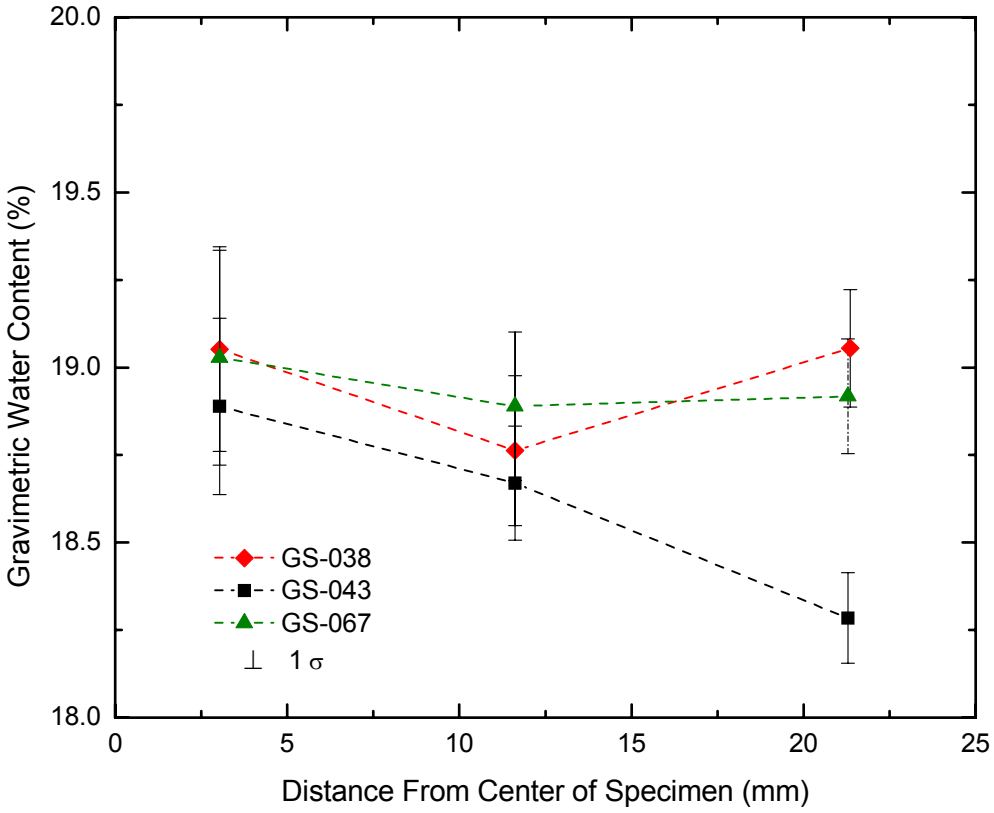

Figure 5.4. Initial breakup comparison – average initial water content distribution.

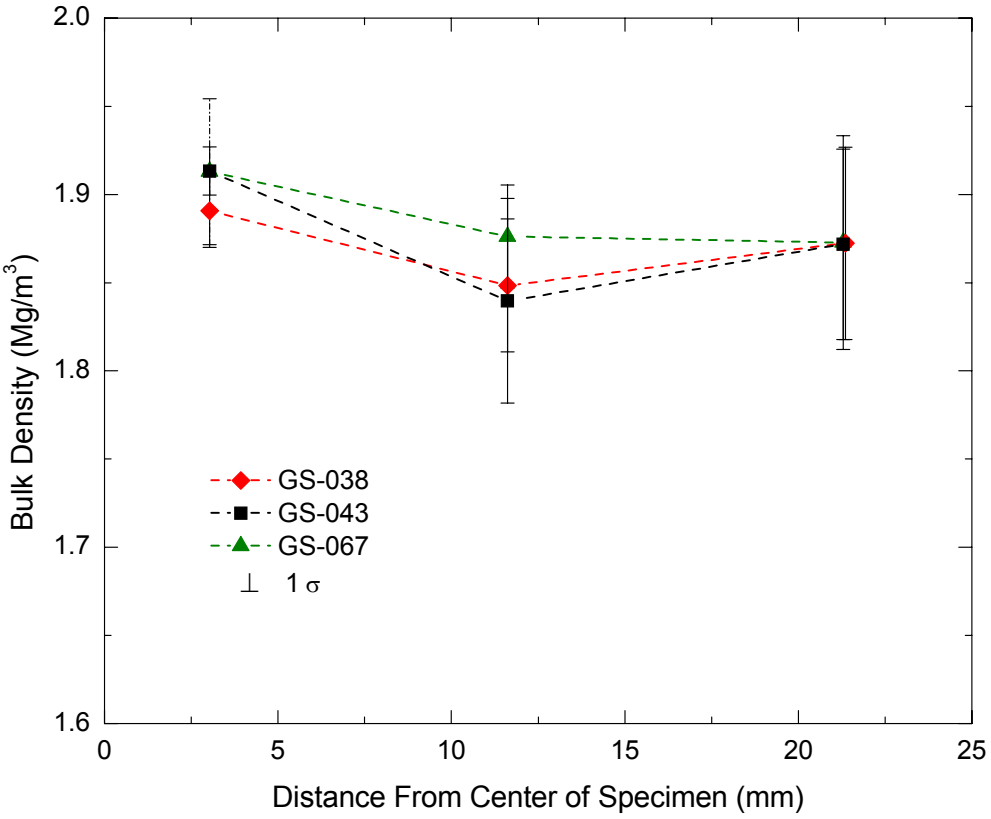

Figure 5.5. Initial breakup comparison – average initial bulk density distribution.

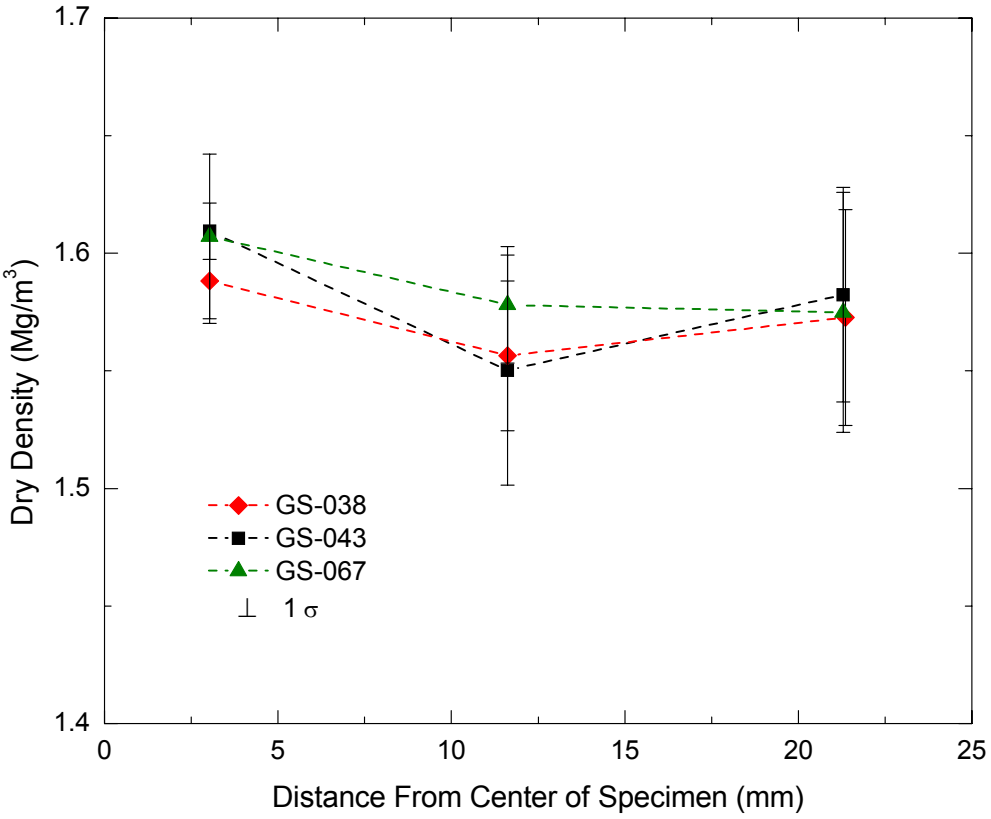

Figure 5.6. Initial breakup comparison – average initial dry density distribution.

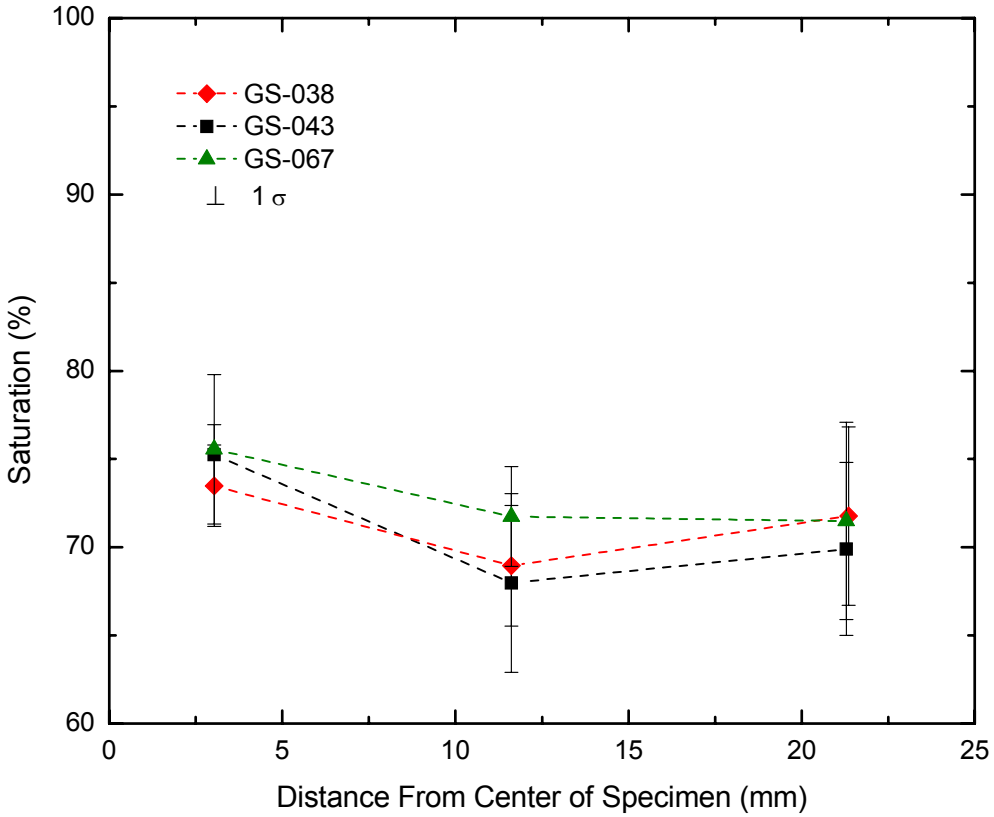

Figure 5.7. Initial breakup comparison – average initial degree of saturation distribution.

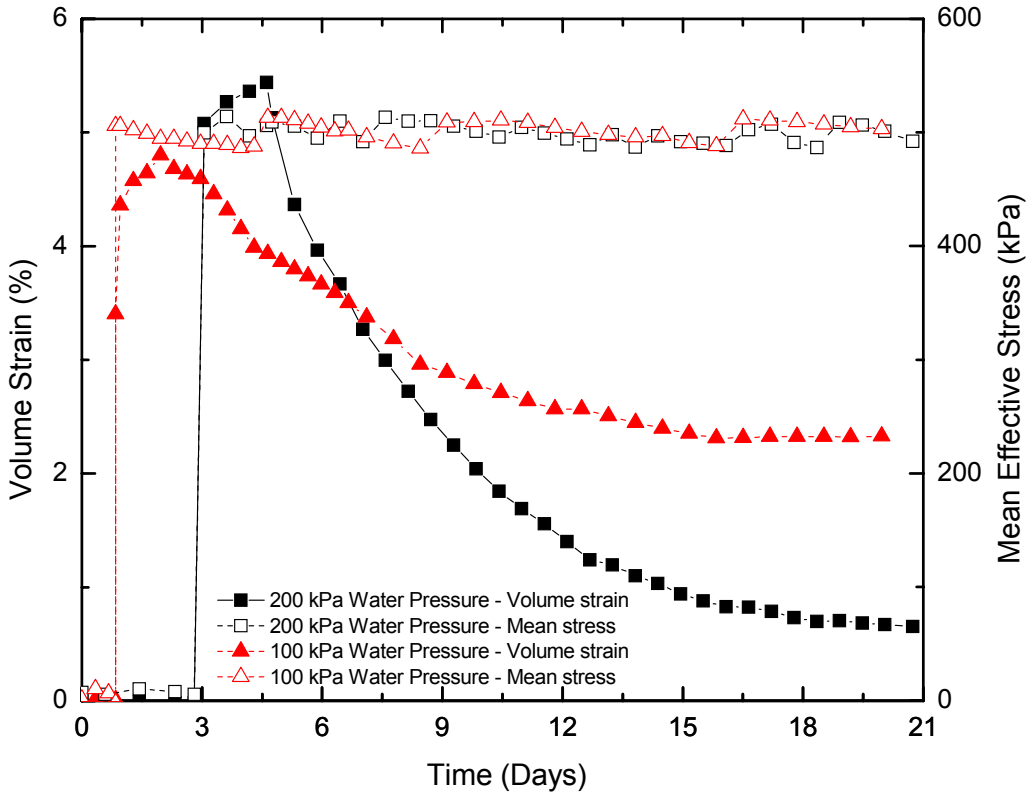

Figure 5.8. Water pressure comparison – volume strain and mean stress versus time.

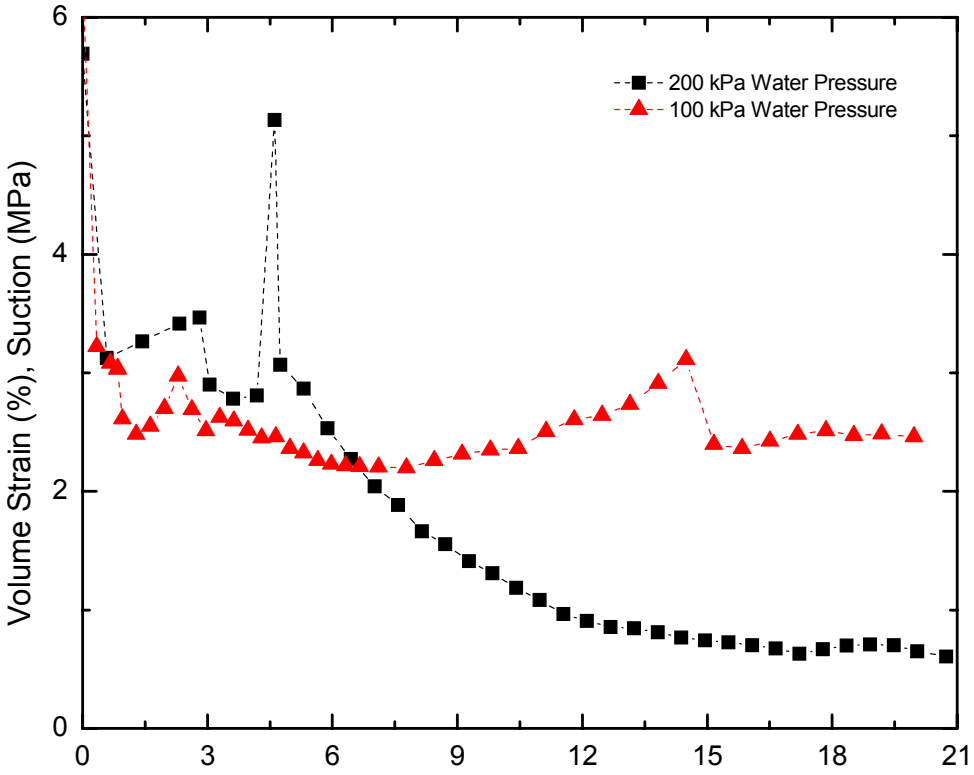

Figure 5.9. Water pressure comparison – suction versus time.

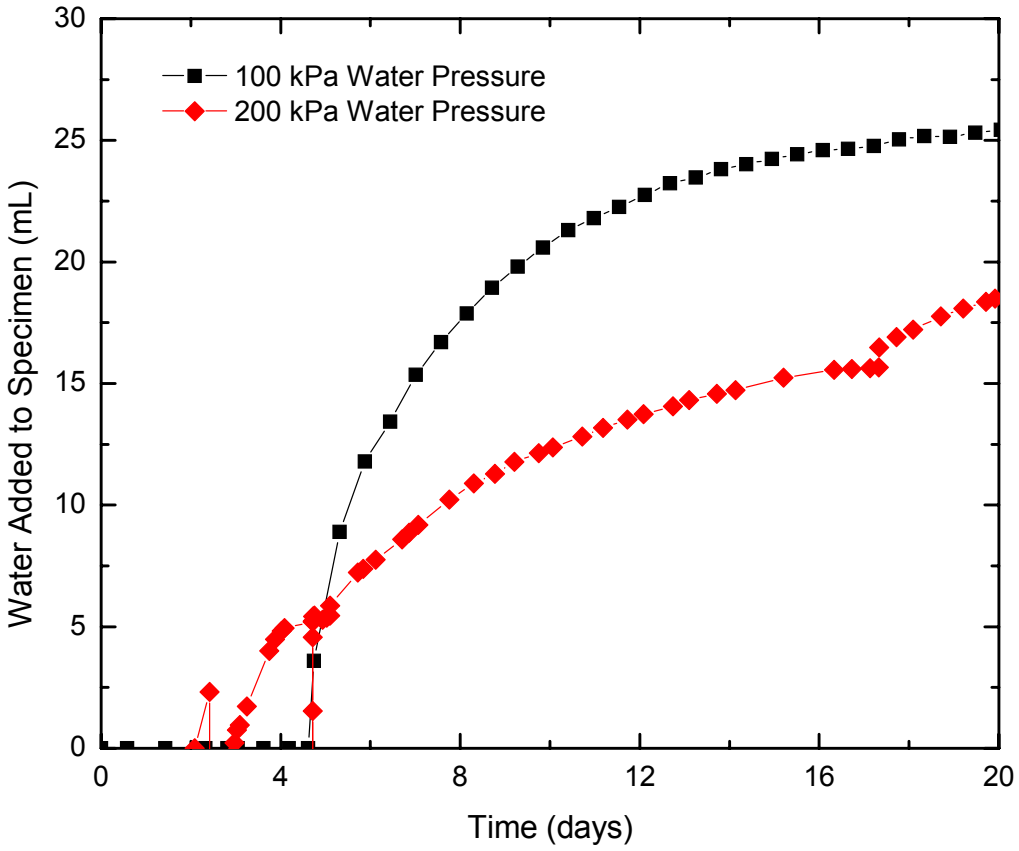

Figure 5.10. Water pressure comparison – water added to specimen versus time.

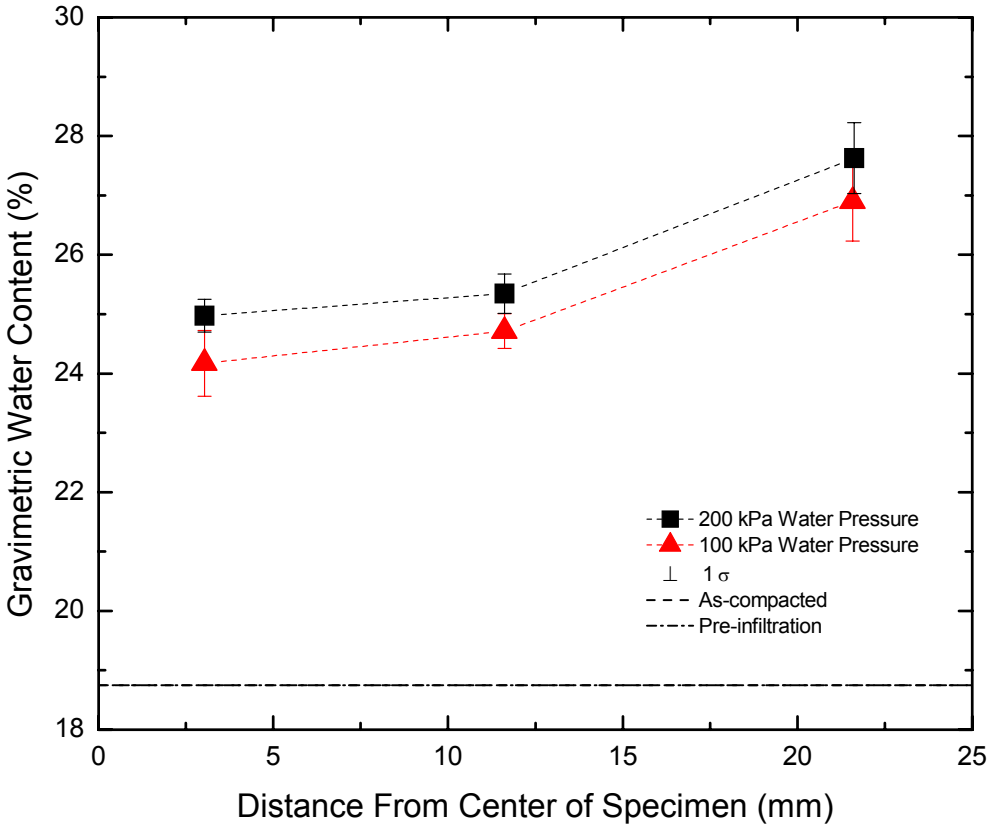

Figure 5.11. Water pressure comparison – distribution of average end of test gravimetric water content.

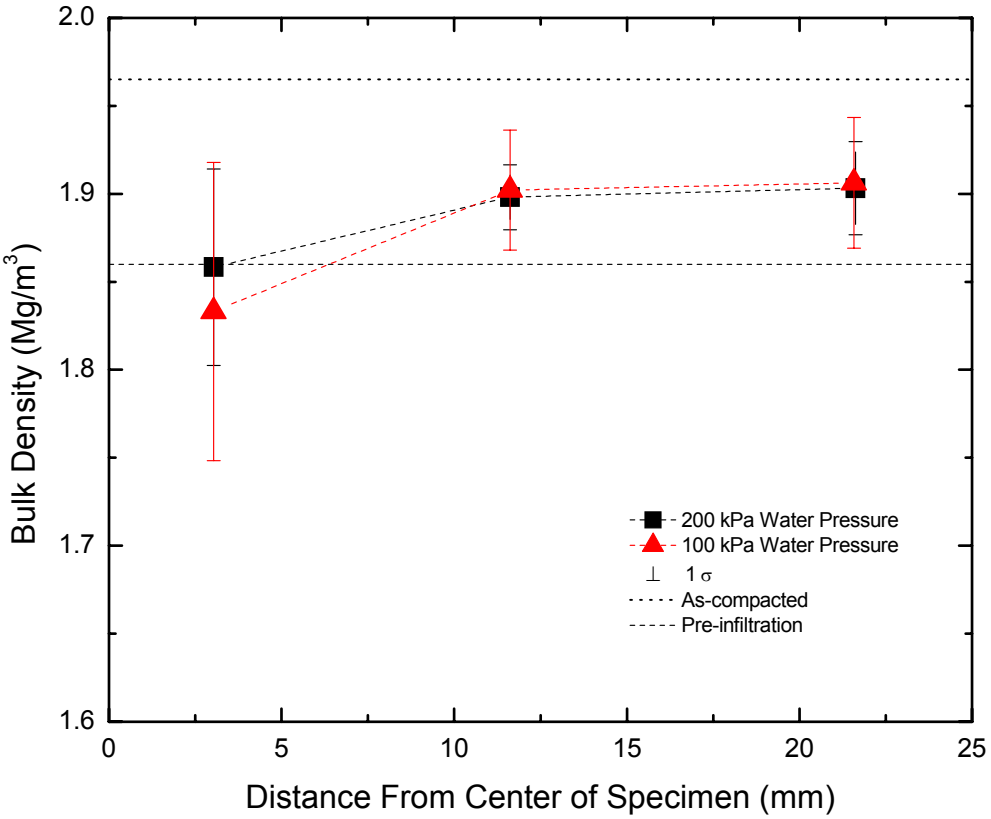

Figure 5.12. Water pressure comparison – distribution of average end of test bulk density.

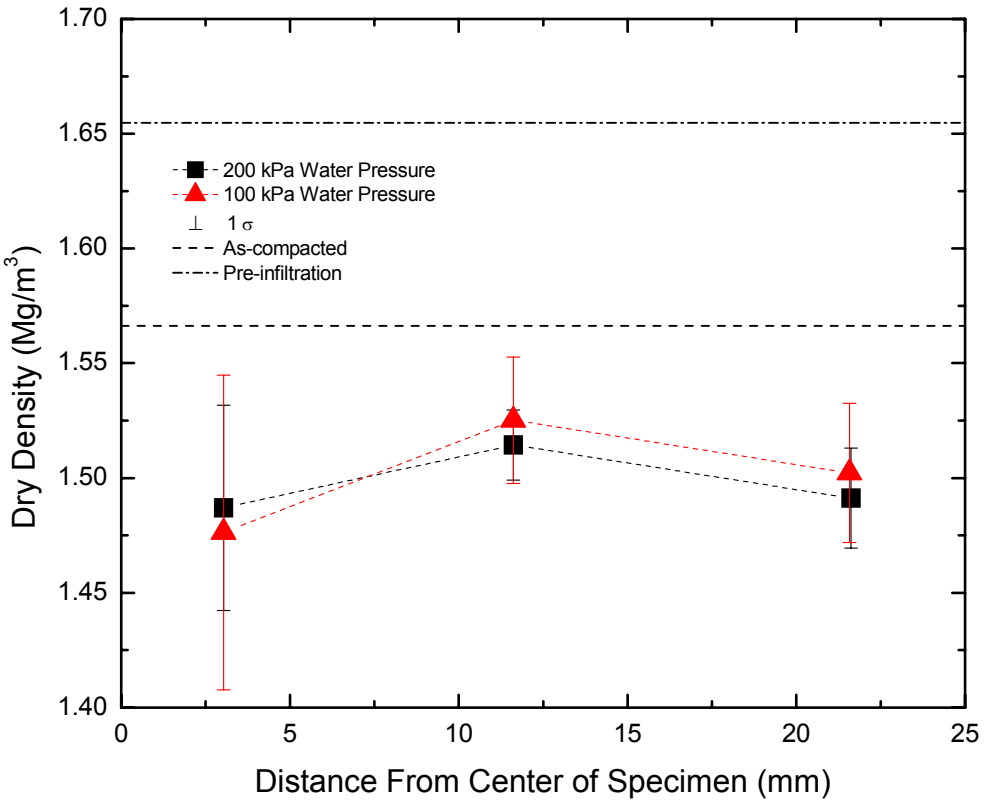

Figure 5.13. Water pressure comparison – distribution of average end of test dry density.

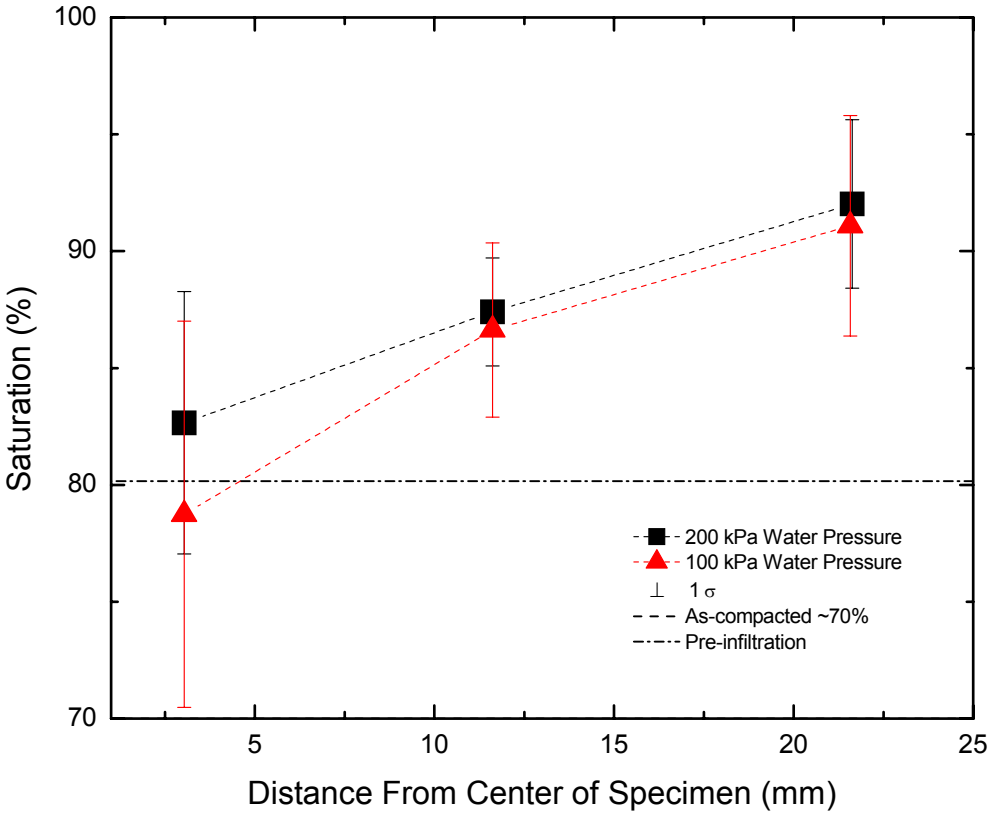

Figure 5.14. Water pressure comparison – distribution of average end of test degree of saturation.

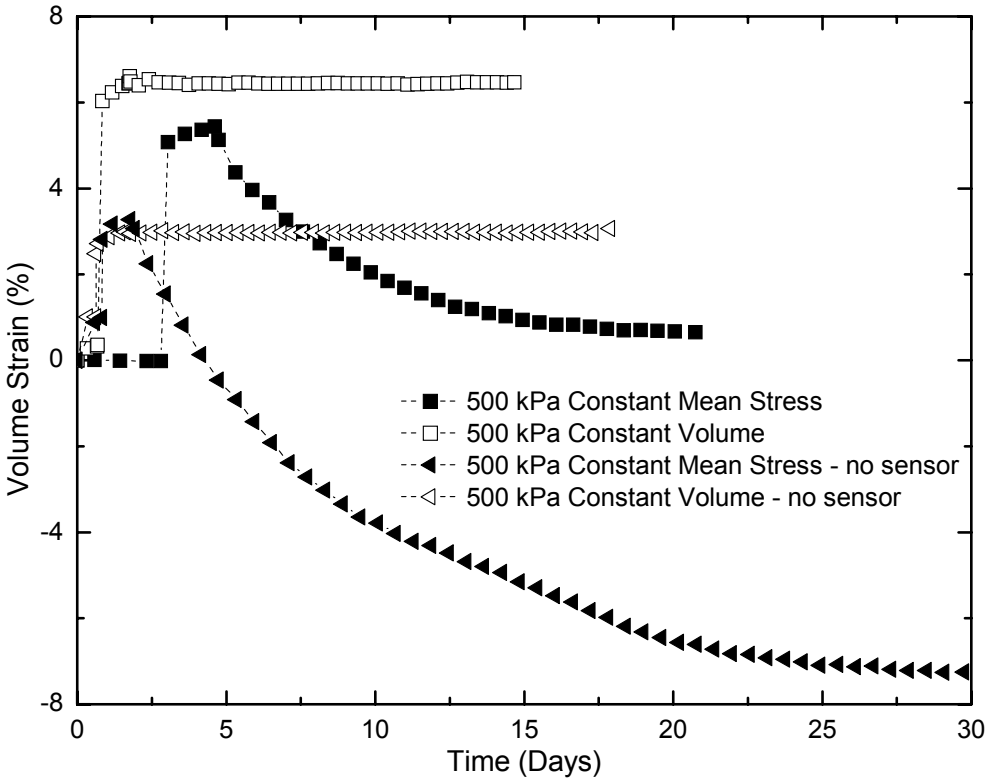

Figure 5.15. Influence of Xeritron sensor comparison – volume strain versus time.

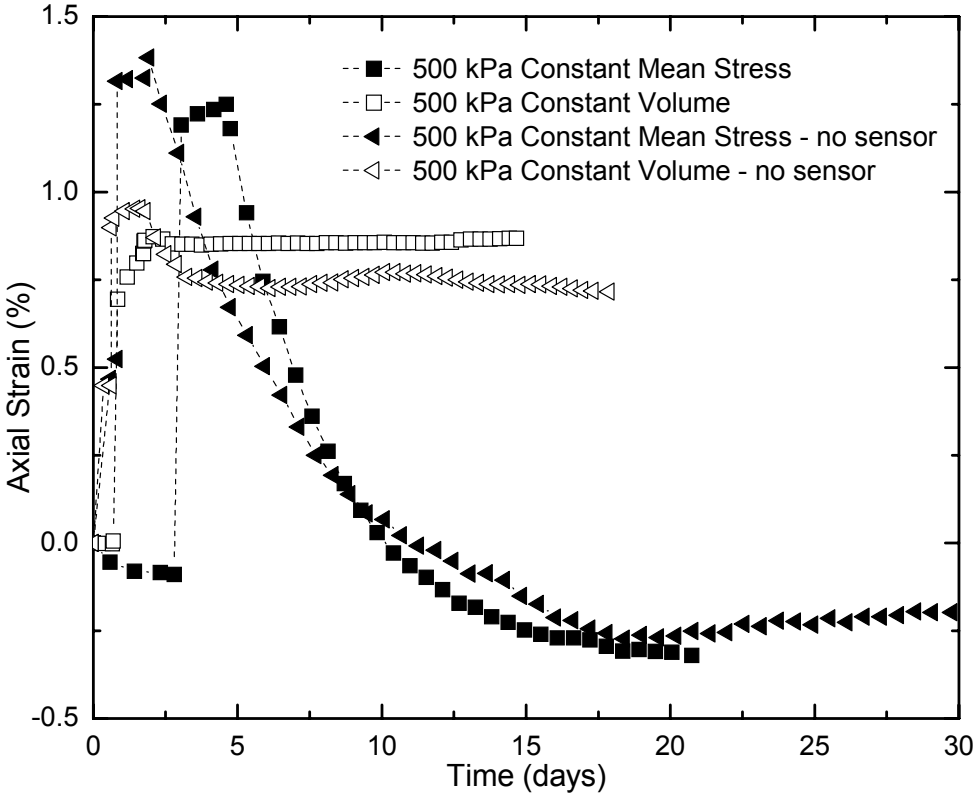

Figure 5.16. Influence of Xeritron sensor comparison – axial strain versus time.

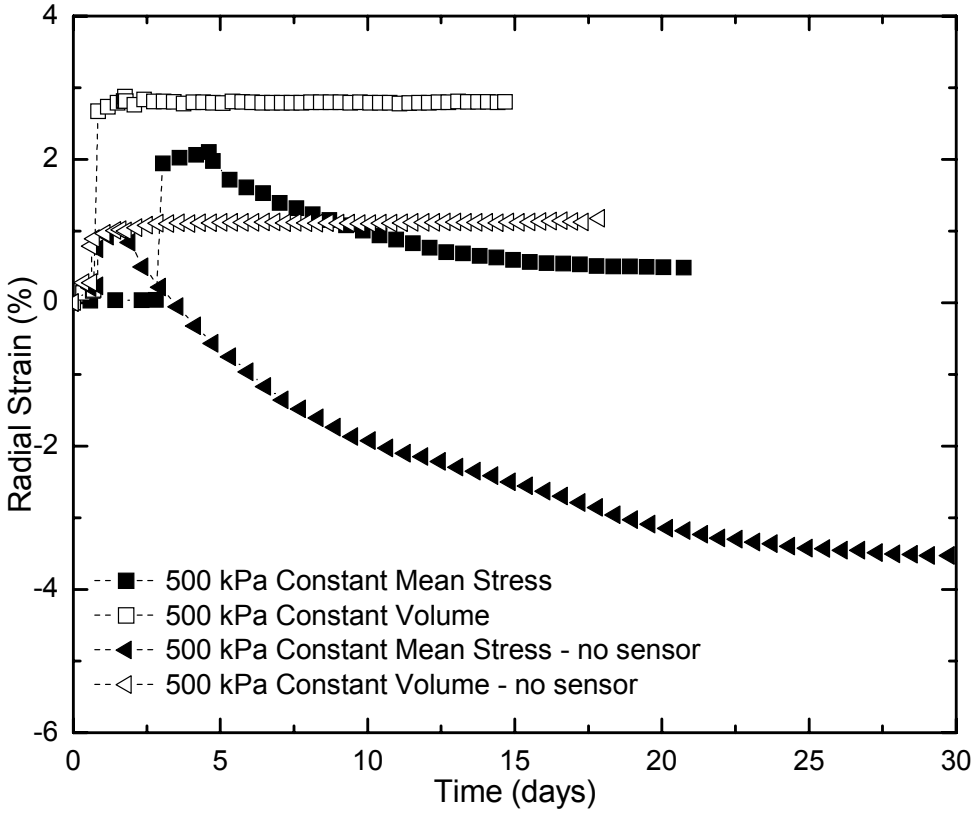

Figure 5.17. Influence of Xeritron sensor comparison – radial strain versus time.

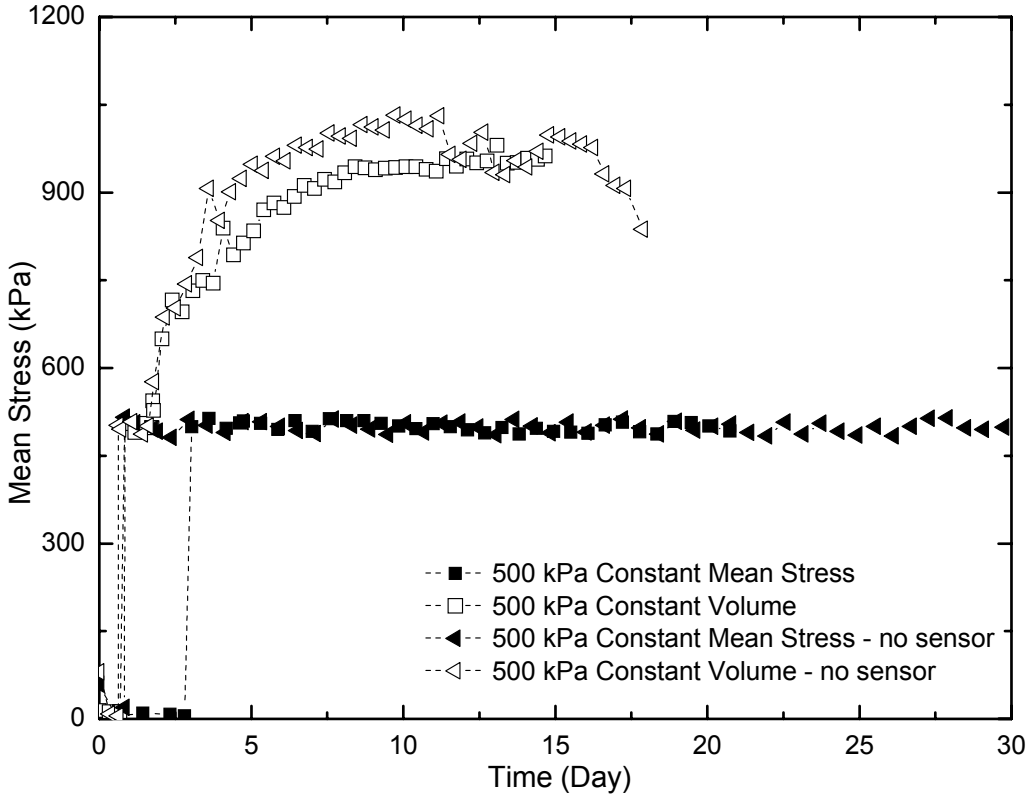

Figure 5.18. Influence of Xeritron sensor comparison – mean stress versus time.

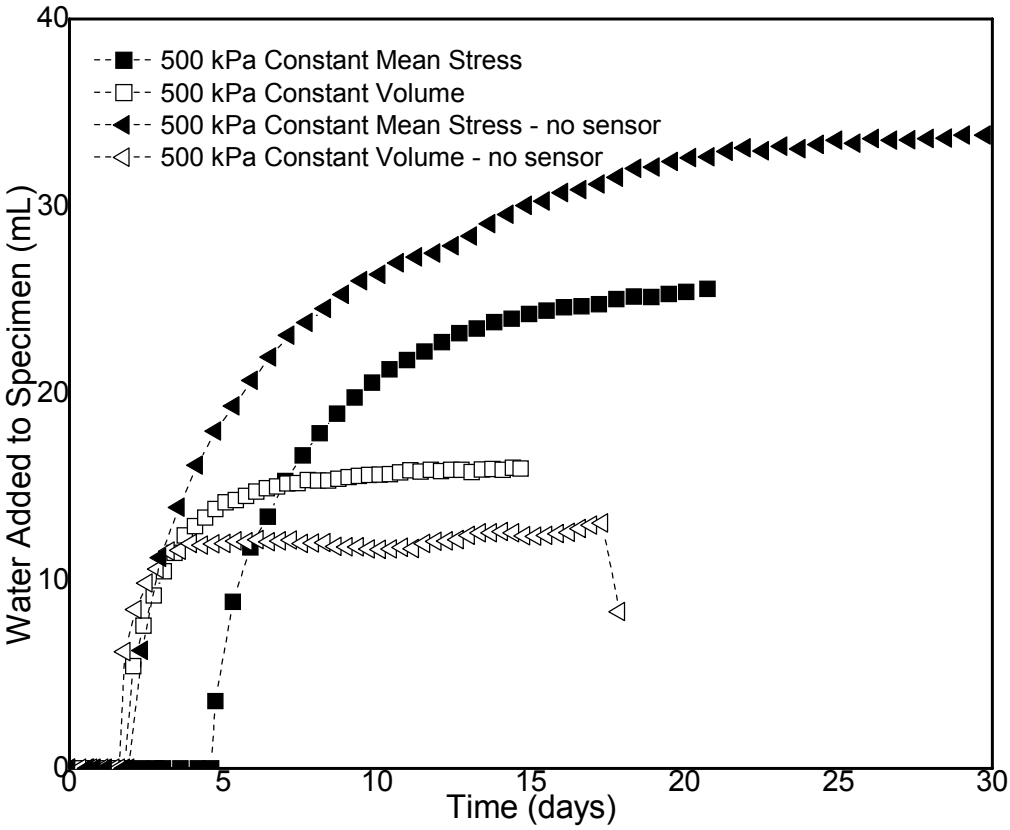

Figure 5.19. Influence of Xeritron sensor comparison – water added to specimen versus time.

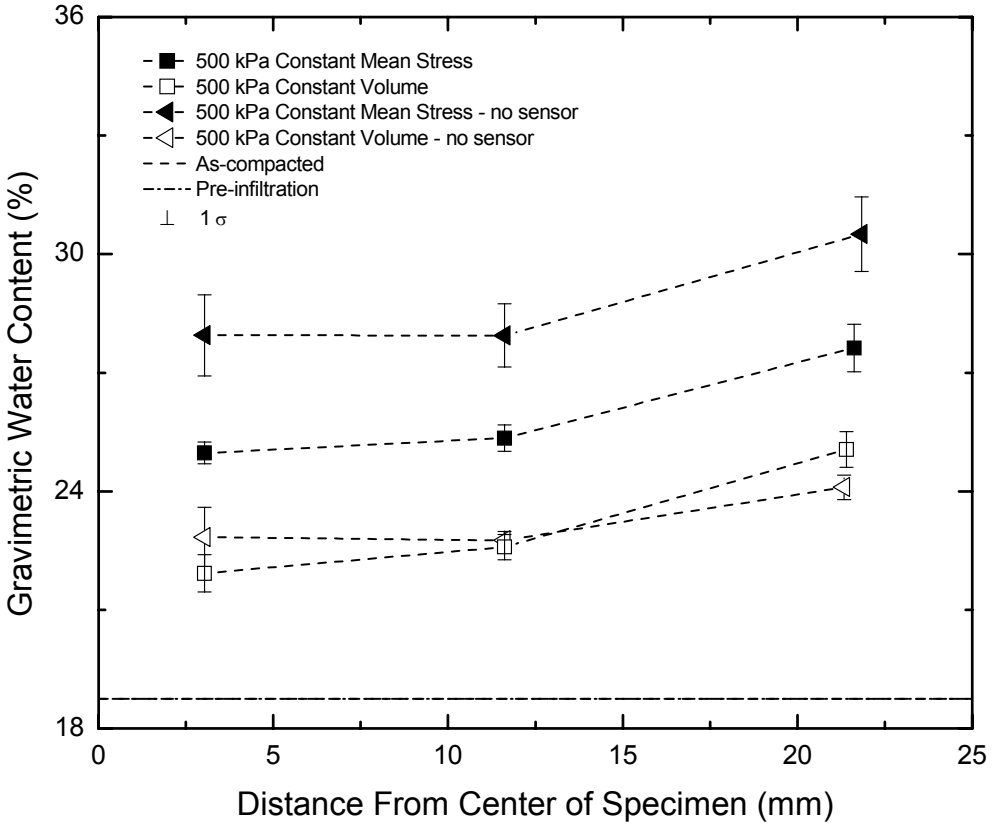

Figure 5.20. Influence of Xeritron sensor comparison – distribution of average end of test water content.

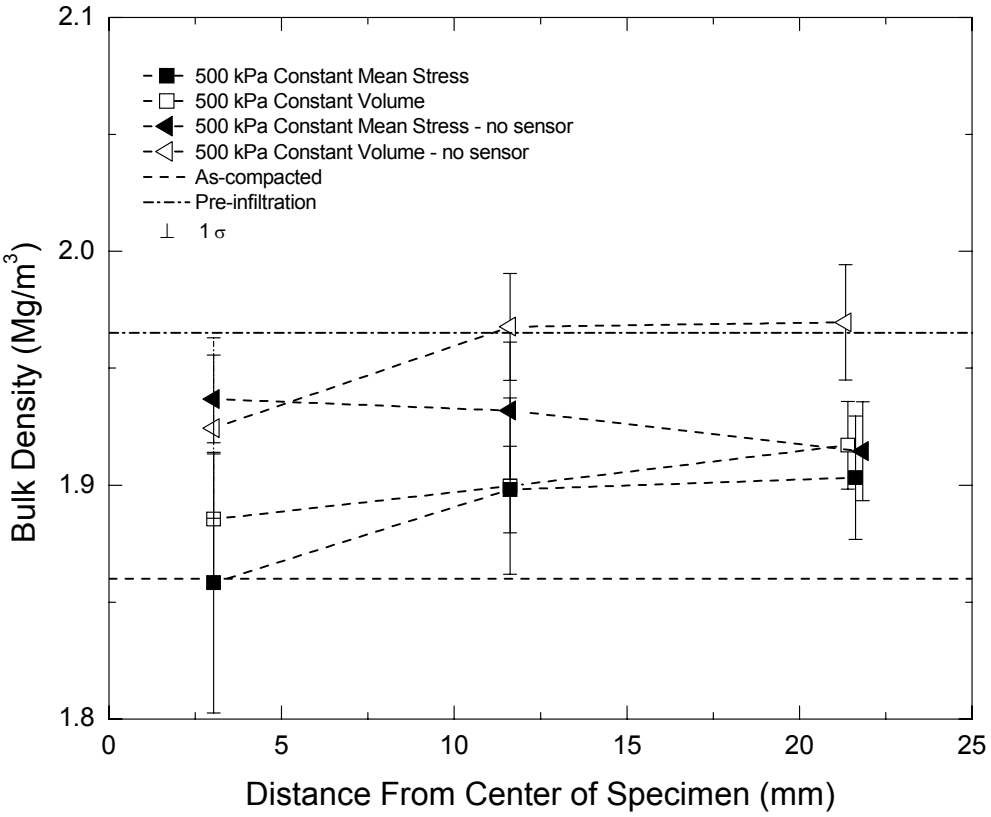

Figure 5.21. Influence of Xeritron sensor comparison – distribution of average end of test bulk density.

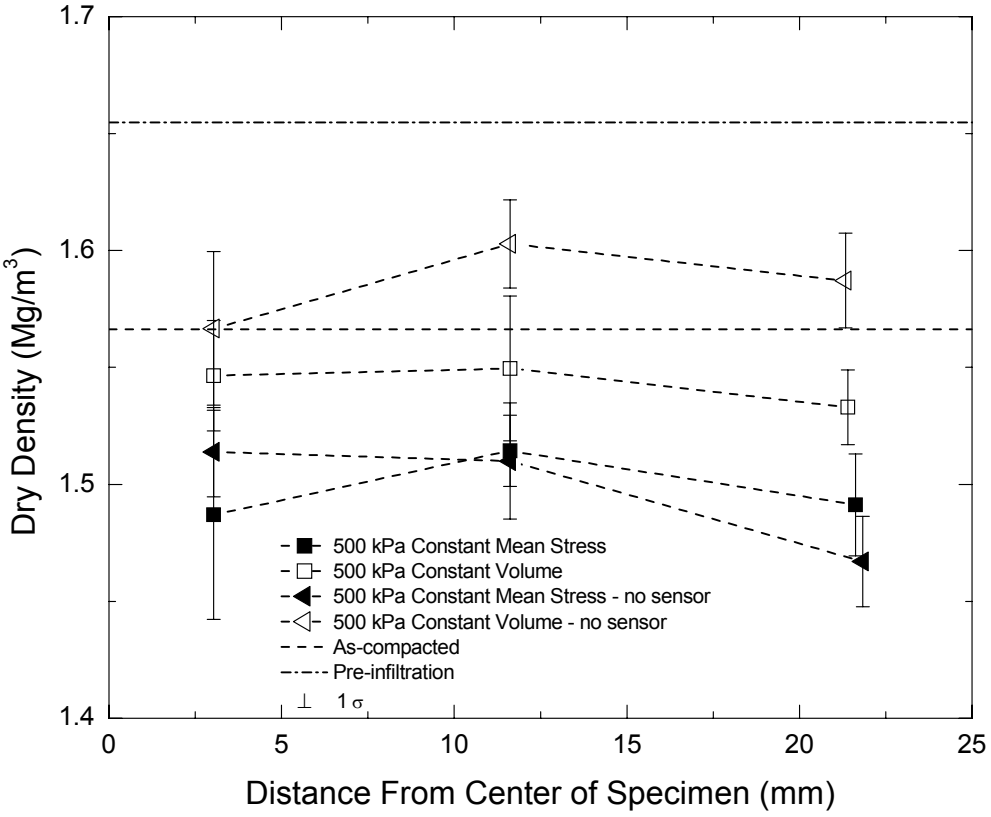

Figure 5.22. Influence of Xeritron sensor comparison – distribution of average end of test dry density.

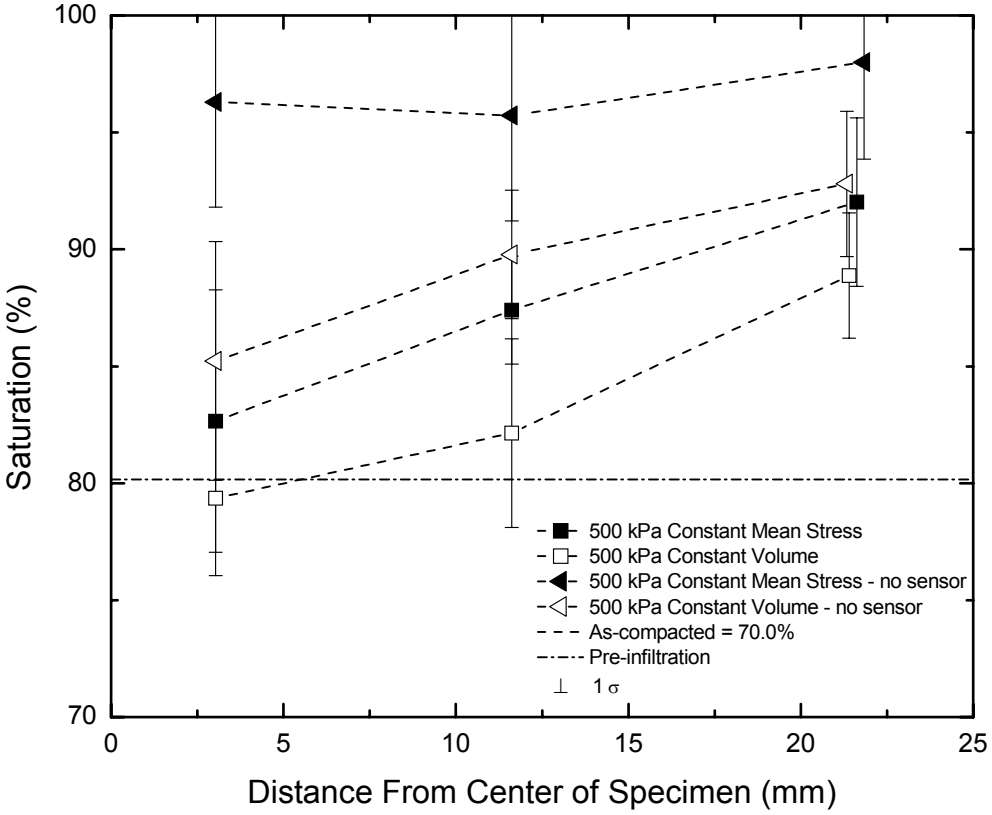

Figure 5.23. Influence of Xeritron sensor comparison – distribution of average end of test degree of saturation.

CHAPTER 6: RESULTS OF INFILTRATION ON SWELLING CLAY SPECIMENS UNDER CONTROLLED BOUNDARY CONDITIONS[4]

6.1 Introduction

Results from the laboratory infiltration tests under controlled boundary conditions are presented in this chapter. The laboratory apparatus, as described in Chapter 4 and Chapter 5, applies radial flow conditions to triaxial specimens while boundary conditions of constant mean stress, constant volume, and constant stiffness are automatically applied by the data acquisition/control system. The complete laboratory testing program is summarized in Table 6.1

[4] Sections of this chapter have been published as:
Blatz and Siemens (2004, 2005, 2006) – Ontario Power Generation Reports.

Siemens, G.A. and Blatz, J.A. 2006. A triaxial apparatus for applying liquid infiltration under controlled boundary conditions with internal suction measurement. ASCE Geotechnical Journal of Geotechnical and Geoenvironmental Engineering to be considered for publication. *In Review*.

with isotropic mean stresses ranging from 250 kPa to 1500 kPa and water pressure held at 200 kPa except as noted below Table 6.1. The laboratory testing program includes three (3) series including constant mean stress, constant stiffness, and constant volume boundary conditions. A subset of the constant mean stress series is the drained tests. All specimens were prepared to the same nominal water content and dry density and then installed directly in the test apparatus. A wide range of isotropic mean stresses have been applied in this program to assess the influence of initial conditions on hydraulic-mechanical behaviour. At each isotropic level the influence of boundary conditions during infiltration is investigated.

One (1) selected infiltration test is discussed in detail for each infiltration boundary condition examined. The remaining test results are presented together in a summary form for each type of boundary condition to give confidence the test apparatus is applying consistent conditions for all tests and to show the influence of initial density on behaviour. This provides for direct evaluation of behaviour under constant mean stress, constant stiffness, and constant volume boundary conditions for specimens prepared at the same initial state.

6.2 Constant Mean Stress Infiltration Tests

Constant mean stress infiltration tests investigate the hydraulic-mechanical behaviour of swelling clay under constant total stress. As water infiltrates into the swelling clay specimen, the total stress surrounding the material is held constant

throughout. In addition to the example provided in Chapter 1, a practical application of this boundary condition would be a shallow foundation. Following construction the soil under the footing would be required to support a relatively constant applied pressure. Increases in water content could also occur at depth due to drainage through the weeping tile resulting in constant mean stress infiltration.

6.2.1 500 kPa Constant Mean Stress Infiltration Test

Test results from the constant mean stress liquid infiltration test (GS-036) are shown in Figure 6.1 as volume strain, suction, mean stress, and water added to specimen versus time. Sensor equilibration lasts three (3) days followed by isotropic loading to 500 kPa. The specimen compresses (positive volume strain) and suction decreases as anticipated (Blatz and Graham 2003). A constant mean stress liquid infiltration test is initiated after 4.5 days. As the specimen is given access to water, it swells (decrease in volume strain). Water added to the specimen initially increases, but then levels off. At the beginning of the infiltration phase, suction at the center of the specimen increases sharply and then decreases. The increase is postulated to occur due to compression of the pore air affecting the Xeritron sensor but is not representative of an actual suction increase within the specimen. The sensor beam is likely compressing due to the increase of pore air pressure and not deforming due to changes in relative humidity. Within half a day suction decreases to the equilibration level and then decreases relatively smoothly for the rest of the test. In another preliminary specimen that was removed soon after initiation of liquid infiltration, a distinct

wetting front was observed. This would be associated with a sharp decrease in suction at the location of the wetting front although was not observed in the suction measurements from any of the liquid infiltration tests. Evaporation could be occurring ahead of the wetting front, which would decrease suction. Evaporation would not necessarily increase specimen water content although would decrease suction as shown in the Kelvin equation in [2.2]. The 500 kPa constant mean stress infiltration test was completed after 21 days when 25.6 mL of water was added to the specimen, volume strain had decreased to 0.66%, and suction had decreases to 0.6 MPa.

End of test spatial distributions including gravimetric water content, bulk density, dry density, and saturation are illustrated in Figure 6.2 and Figure 6.3. Individual measurements from the five (5) compacted layers and average measurements of gravimetric water content and bulk density are shown on Figure 6.2 as well as error bars of one (1) standard deviation. Three (3) other horizontal lines are plotted that combine measurements on the initial break up specimens presented in Chapter 5, as well as volume change and water content increase measurements of the individual test. As shown on Figure 6.2a, water content is highest at the perimeter of the specimen and decreases towards the center. Bulk density (Figure 6.2b) also is greatest at the perimeter and combines increases in both volume and water content. Dry density (Figure 6.3a) peaks at the midpoint between perimeter and center but the center measurement shows large error

bars and likely is near the higher end. Degree of saturation (Figure 6.3b) increases to the perimeter.

6.2.2 Constant Mean Stress Results

Summaries for all constant mean stress tests are shown in Figure 6.4 through Figure 6.9. Mean stress versus time, volume strain versus time, suction versus time, water added to specimen versus time, specific volume versus mean stress, suction versus mean stress, axial strain versus volume strain, radial strain versus volume strain, and end of test average distributions are displayed respectively.

Following sensor equilibration good control of mean stress is observed throughout (Figure 6.4a). Specimen expansion during the infiltration process was dependant on isotropic compression level (Figure 6.4b) with the 250 kPa specimen expanding the most and volume strain during the infiltration phase of tests decreased as mean stress increased. For the 250 kPa test, volume strain decreased 14.6% indicating expansion ($\Delta V = 0.240$) during the infiltration phase but for the 1500 kPa test, volume strain only decreased by 0.9% ($\Delta V = 0.013$). In all cases, initial specific volume, V, was calculated using initial water content and volume measurements. Volume change measurements were used to calculate specific volume during the test. Prior to infiltration during the isotropic compression phase, air volume was reduced as the specimen compressed. This reduces the volume of air that can be replaced with water as well as increases the stress boundary the swelling soil has to push against.

Suction response for constant mean stress tests were in agreement as shown in Figure 6.5a and Figure 6.6b. Initial suction readings following the equilibration phase are between 1.9 and 3.5 MPa. In all cases, during the isotropic compression phase, suction decreased with increasing mean stress as shown in Figure 6.6b. Suction decreased for the entire infiltration phase in both the 1000 and 1500 kPa constant mean stress tests. The 500 kPa test showed a sharp increase in suction followed by a steady decrease throughout the remainder of the test. This aspect is understood as a sensor issue and not representative of suction change during initial stages of water infiltration. Also, suction behaviour during the 250 kPa test was not as clear as the sensor only read intermittently due to damage occurring during installation. Due to the extended time required for recalibration of the Xeritron sensor and installation, the test was continued. For relative comparison with the other tests, assumed suction readings were added, based on results of other tests, and are plotted as dashed lines. A point was added at the end of the dashed line to identify the test which the assumed suction readings refer to.

Considering inflow to specimens (Figure 6.5b) water added is greatest at the lowest mean stress and the least at the highest mean stress as expected. The initial flow rate at the beginning of the infiltration phase is also the greatest for the 250 kPa test and decreases with increasing mean stress.

Anisotropic behaviour during the water infiltration is evident from Figure 6.7. The 500 kPa test specimen expanded axially the most during the infiltration phase followed by the 1000, 250 and 1500 kPa specimens. On the other hand, radial expansion during water infiltration decreased with increasing mean stress with the 250 kPa specimen increasing 6.9% and the 1500 kPa specimen just 0.21%. During water infiltration, change in axial versus volume strain is curved while radial versus volume strain slopes are approximately linear. Average slopes of axial strain versus volume strain increase with increasing mean stress while slopes of radial stain versus volume strain decrease. Comparing overall changes in strain during water infiltration, the 250 kPa test specimen had 6.9% decrease in radial strain and just 0.9% decrease in axial strain. The 500 kPa specimen expanded about the same axially and radially (1.6%). The 1000 and 1500 kPa specimens expanded greater in the axial direction than radially.

Average post-test results and as-compacted values for all constant mean stress tests are shown in Figure 6.8 and Figure 6.9. In general, anticipated trends of increasing bulk and dry density increase with increasing mean stress are noted in the plots. The one exception is in the bulk density measurement from the middle of the 1000 kPa specimen. This results in anomalous calculations of both dry density and saturation. During isotropic compression, dry and bulk density increase due to bulk volume reduction. During constant mean stress infiltration, specimen expansion reduces dry density. The outer measurement usually has the lowest value for dry density with the highest occurring at the second

measurement. This is somewhat unexpected as dry density is thought to increase from the perimeter to the center for this type of test. This could be due to the small amount of soil used for the middle measurement along with the fact that only one (1) measurement is taken instead of an average of two (2) measurements in the other reported values.

Saturation increases with increasing distance from the center of the specimens (Figure 6.9b). Based on the configuration of this experiment, the perimeter of the specimen is likely to be at the residual saturation of air for the material, which could be near full water saturation. Even if the specimen is saturated at the perimeter, this front may not extend far into the specimen. Nofziger and Swartzendruber (1976) report bulk density and gravimetric water content measurements taken during one-dimensional constant volume unsaturated hydraulic conductivity tests, on a 50:50 mixture of Wyoming Bentonite and silica silt. In their 24.1 cm steel column, saturations of 100% were not reported for any distance greater than 0.6 cm from the upstream end. Compared to the tests reported here they did not apply positive water pressure and the soil was air dry to start the test. Considering the undrained nature of axisymmetric infiltration tests, the saturation values reported are reasonable in spite of these differences. Some relaxation during specimen removal is also possible prior to post-test measurements. This would decrease density and saturation measurement values.

6.3 Constant Volume Infiltration Tests

Constant volume tests investigate the behaviour of specimens where volume is controlled throughout the infiltration phase. As the specimen attempts to expand with increasing water content, mean stress is increased isotropically to maintain constant volume throughout. Examples of exact constant volume conditions in geotechnical engineering applications are hard to find because some finite displacements are always required to mobilize strength. Although near constant volume conditions are evident in applications such as behind a tie-back retaining wall. Constant volume along with constant mean stress forms the extreme boundary conditions shown in Figure 2.9 so examination of constant volume infiltration gives a bound on behaviour. An example constant volume infiltration test is presented in this section followed by a discussion of all constant volume infiltration tests.

6.3.1 250 Constant Volume Infiltration Test

Test results for the 250 kPa constant volume test (GS-045) are shown in Figure 6.10. Following suction sensor equilibration, cell pressure was increased to 250 kPa. The specimen compressed (positive volume strain) and suction decreased as a result. At 2.7 days, the constant volume infiltration phase was initiated with water being pushed into the specimen from the perimeter. Initially water infiltrated rapidly but the infiltration rate levelled off at about 6.3 days as shown in Figure 6.10. After this point only limited infiltration occurred; however, cell pressure continued to increase until about 10 days. The suction response

was smooth throughout the infiltration phase and decreased until end of test equilibration. Axial and radial strain increased during the compression phase as expected. The test was complete after 21 days. A total of 16.1 mL of water was absorbed, an end of test mean stress of 915 kPa was observed and suction reduced to 1.6 MPa.

Post-test results for the 250 kPa constant volume test are shown in Figure 6.11 and Figure 6.12. The water content and saturation showed the lowest values in the center and increased values towards the perimeter with significant non-linearity noted. The middle measurements showed some difference in water content while the outer section of the specimen showed greater increase. The saturation increased due to isotropic compression of the sample and further increased due to water infiltration. Figure 6.11b and Figure 6.12a show increases in both bulk and dry density from the perimeter of the specimen to the second measurement as was observed in the constant mean stress tests.

6.3.2 Constant Volume Infiltration Results

Summaries from all constant volume tests are shown in Figure 6.13 through Figure 6.18. Mean stress versus time, volume strain versus time, suction versus time, water added to specimen versus time, specific volume versus mean stress, suction versus mean stress, axial strain versus volume strain, radial strain versus volume strain, and end of test average distributions are plotted.

Figure 6.13a shows the control of mean stress throughout testing. Following Xeritron sensor equilibration mean stress was increased incrementally to the desired level. During the infiltration phase, mean stress was increased to maintain constant volume. Interestingly, the 250 and 500 kPa tests both equilibrated to approximately the same equilibration mean stress level at the end each respective test. Also, both the 1000 and 1500 kPa tests underwent increases in mean stress of 500 kPa during the infiltration phase.

Volume strain measurements and specific volume calculations for all tests are shown in Figure 6.13b and Figure 6.15a. During infiltration, constant volume conditions are maintained. All tests showed a small jump in volume strain (compression) at the beginning of infiltration. This may be due to the initial total stress application of water around the specimen. As water later infiltrates the pore space, the specimen expands back to its original volume, which is maintained for the rest of the test. One unanticipated result is that the end of test volume strain for both the 500 and 1000 kPa tests are equal following the isotropic compression phase. This is likely an overestimation of the 500 kPa specimen volume strain. The specific volume versus mean stress plot shows a consistent slope during isotropic compression phases. During the infiltration phase constant specific volume is observed.

Suction responses during infiltration showed consistent trends (Figure 6.14a and Figure 6.15b). During the isotropic compression phase, suction decreased with

increasing mean stress as anticipated. At the initiation of the infiltration phase, a jump in suction reading was observed for all constant volume tests. Similar to the volume strain response, this jump is a function of the sensor and is not seen as being representative of suction at the center of the specimen. Suction response following the jump was consistent as suction was dissipated throughout the rest of all tests. Assumed suction readings are added to the plot where the Xeritron sensor malfunctioned due to soil pushing through the mesh and stressed the sensor beam or in the case of calibration changes during the test. Similar slopes of suction versus mean stress during the isotropic compression phase are shown on Figure 6.15b. During constant volume infiltration, steeper slopes are observed because suction was being reduced due to both increase in mean stress and addition of water to the specimen.

Summaries of water added to specimen are shown in Figure 6.14b. As shown, both the 250 and 500 kPa tests took in the same amount of water (16.0 mL). Although the specimens were isotropically compressed to different mean stress levels, the quantity of water uptake under constant volume boundary conditions is the same. This combined with the equilibration mean stresses achieved shows that the specimens were behaving similarly. As in the constant mean stress tests, initial water flow rate decreased with increasing isotropic compression level. For all tests, flow rate into the specimen decreases throughout their duration until no flow or extremely small flow rates are observed at the end of tests.

Axial strain and radial strain versus volume strain are shown in Figure 6.16a and Figure 6.16b. The 250, 1000 and 1500 kPa tests show consistent results with specimens expanding axially and compressing radially during water infiltration. This is further evidence of anisotropic behaviour of bentonite sand buffer (BSB). The magnitude of radial strain increase during water infiltration is the same for these three (3) tests. The 500 kPa test does not show this same behaviour but this could be due to a couple of factors. First, there is some small loss of volume control at the beginning of infiltration in this particular test. Also, this test was completed early on in the program and instead of filter paper placed underneath the geotextile, small filter stone tabs were placed at specimen mid-height to allow direct contact with LVDTs. Some compression of the tabs into the specimen was observed and this could affect volume measurement during the test.

Average post-test results for all constant volume tests are shown in Figure 6.17 and Figure 6.18. Spatial distribution of gravimetric water content, bulk density, dry density, and saturation are plotted. Non-linear results are observed in most cases. Gravimetric water content (Figure 6.17a) increased from the center of the specimen to the perimeter as expected. Total average water content for the 250 and 500 kPa tests is equal and agrees with the water flow into specimen test results. For stress levels greater than 500 kPa, end of test average water content decreases with increasing mean stress. Bulk density results

(Figure 6.17b) show increasing average bulk density with increasing isotropic compression stress level except for the 500 kPa test. The 1500 and 1000 kPa tests show decreasing end of test bulk density from the center of the specimens to the perimeter while the 250 kPa shows increasing bulk density. The 250 kPa level shows an increase from the center to the second measurement followed by a decrease to the perimeter. Average dry density spatial distributions (Figure 6.18a) show overall decrease from the center to the perimeter. As water infiltration occurs from the perimeter under constant overall volume, expansion likely occurs around the outside of the specimen while the center of the specimen experiences compression. The 250 and 500 kPa tests show decreasing dry density from the second measurement to the center. The change is greater for the 250 kPa than the 500 kPa test. The 500 kPa test results are unexpectedly less than the 250 kPa test. This is due to comparable gravimetric water content measurements combined with higher bulk density measurements for this calculation. Finally saturation results show an interesting trend (Figure 6.18b). At the center of the specimen, the 1500 and 1000 kPa tests have the highest saturation while at the perimeter the highest saturation is observed at the perimeter for the 250 and 500 kPa tests. In the 1500 and 1000 kPa tests, increase in saturation is likely due to isotropic compression (observed at the center) while in the 500 and 250 kPa tests the increase is likely due to water infiltration (perimeter of specimen). The saturation trends also show distinctive behaviour as the 500, 1000 and 1500 kPa tests show a greater increase from the second point to the outside while the 250 kPa test shows a greater increase from

the center to the second point. This is evidence for water getting the farthest into the specimen in the 250 kPa test compared to the other tests.

6.4 Constant Stiffness Infiltration Tests

Constant stiffness tests investigate the behaviour of a swelling clay soil during infiltration under a flexible spring type boundary condition. As specimen expansion occurs, mean stress increase is applied to restrict expansion but not eliminate it. As described in the previous section, many engineering applications can be represented by this test. An example would be use of swelling materials as backfill next to a vertical basement wall. The backfill would be placed in a dry state following construction of the adjacent structure and compacted into place. As rainfall infiltrates into the swelling material, expansion occurs. The boundary conditions in this application are the basement on one side and insitu material on the other side against which the material swells against. As displacements occur, the basement would undergo relatively smaller displacements compared to the insitu soil but would show increasing resistance with further expansion. This type of flexible boundary condition is represented by constant stiffness infiltration tests.

In this testing program two (2) different slopes of mean stress versus volume strain were followed as shown in Table 6.1. Determination of the slopes to be followed during constant stiffness infiltration was completed after all undrained constant mean stress and constant volume tests. First volume change and mean

stress increase during infiltration were normalized to the end of the isotropic compression phase. That is, volume strain and mean stress at the beginning of infiltration were taken as zero and the remaining data normalized to this datum as shown in Figure 6.19. In the figure, constant mean stress infiltration test results plot along the vertical axis and constant volume test results plot along the horizontal axis. The limits of mean stress increase and volume strain are also shown on the plot for comparison. Constant stiffness boundary conditions were selected to bisect this plot at 30 and 60 degrees from the horizontal. This is calculated as slopes of -75 and -25 kPa mean stress increase per percent volume strain. The numbers are negative due to the sign convention of volume expansion being negative. From here forward the tests are referred to as CS75 and CS25 tests. In this section one (1) constant stiffness infiltration test is described in detail followed by presentation of both types of constant stiffness tests completed.

6.4.1 250 kPa Constant Stiffness (x = -75kPa/%) Infiltration Test

Experimental results from the 250 kPa CS75 infiltration test (GS-058) are shown in Figure 6.20. Mean stress was increased in one (1) increment to 250 kPa following suction sensor equilibration. The infiltration phase was initiated on day four (4). Water flows into the specimen and the inflow rate decreases throughout this phase as shown in Figure 6.20. As the specimen expands (decreasing volume strain) with increasing water content the mean stress is increased in response at a rate of 75 kPa/% volume strain. Suction increases after the initiation of the infiltration phase but then decreases for the rest of the test due to

both the increase in water content and mean stress. The test was completed after 21 days when 24.0 mL of water was added to the specimen, volume strain had equilibrated to -3.3% and mean stress had been increased to 580 kPa.

Post-test distributions of gravimetric water content, bulk density, dry density, and saturation are shown in Figure 6.21 and Figure 6.22. Gravimetric water content increased to an average of 26% and shows anticipated trends increasing towards the water source. Average bulk density is approximately constant over the middle two (2) measurements and then increases to the perimeter. Dry density shows a slight decrease over the middle two (2) measurements and then is constant towards the outer edge of the specimen. Finally saturation increases from the center of the specimen to the perimeter.

6.4.2 Constant Stiffness (x = -75kPa/%) Infiltration Results

Test results for the CS75 tests are shown in Figure 6.23 through Figure 6.28. Plots of mean stress versus time, volume strain versus time, suction versus time, water added to specimen versus time, specific volume versus mean stress, suction versus mean stress, axial strain versus volume strain, radial strain versus volume strain, and end of test average distributions are shown.

Mean stress for all CS75 tests are plotted in Figure 6.23a. Good control of mean stress is observed throughout the test. Mean stress is increased incrementally to the desired isotropic level following Xeritron sensor equilibration (Figure 6.24a). During constant stiffness infiltration mean stress is increased along the

predetermined ratio until the end of test values are achieved. At the beginning of infiltration, a relatively constant rate of mean stress increase with time is observed until the equilibration stress level is reached. Following this time, mean stress is maintained constant for the remainder of tests. End of test mean stress levels of 580 kPa, 700 kPa and 1120 kPa are observed for the 250, 500 and 1000 kPa tests respectively. Relative increases in mean stress during constant stiffness infiltration decreases with initial isotropic stress level (greatest in 250 kPa test and least in 1000 kPa test).

Volume control during all tests is smooth as illustrated in Figure 6.23b and Figure 6.25a. Specimen compression is observed during the isotropic compression phase and expansion during infiltration as anticipated. The constant stiffness slope applied (x = -75kPa/%) plots as parallel lines in the specific volume versus mean stress graph (Figure 6.25a) showing consistent boundary conditions are applied for all tests. During infiltration, volume expansion is greatest in the 250 kPa specimen and least in the 1000 kPa specimen. Since volume strain and mean stress are related through the boundary conditions applied this is expected from the mean stress results.

Suction results (Figure 6.24a and Figure 6.25b) show similar trends as in the constant volume and constant mean stress series. This includes decreasing suction with increasing mean stress and increasing water content. Assumed suction readings are added as discussed earlier due to malfunctions in the

Xeritron sensor. Consistent slopes of suction versus mean stress are shown (Figure 6.25b) as expected.

The water added to specimen versus time (Figure 6.24b) verifies previously observed behaviour. The 250 kPa test takes in the most water leading to the highest swell and greatest mean stress increase. The initial flow rate of the 250 kPa test is also greatest and the 1000 kPa test shows the lowest initial flow rate. Although in the three (3) tests, flow into the specimens halts at approximately the same time relative to initiation of the infiltration phase.

The axial and radial strain versus volume strain plots (Figure 6.26) give further evidence of anisotropic behaviour during infiltration. Almost no axial expansion is observed in the 1000 kPa test while the 250 kPa test has approximately -1.4% axial strain. Radial expansion versus volume strain shows consistent slopes throughout infiltration as observed in the constant mean stress tests (Figure 6.26b).

The end of test post-test distributions shown in Figure 6.27 and Figure 6.28 agree with boundary conditions imposed during infiltration tests and give insight to internal specimen behaviour. Gravimetric water content is highest in the 250 kPa specimen and least in the 1000 kPa test. Non-linear water content distributions are noted in all three (3) tests. Bulk and dry density is greatest in the 1000 kPa test and least in the 250 kPa. This is due to the initial isotropic

compression level and even the increase in water content of the 250 kPa tests does not bring it within range of the other two (2) tests. Overall decrease in dry density is observed in the 250 kPa and 500 kPa tests while the 1000 kPa test shows an increase in dry density towards the perimeter (Figure 6.28a). This is unexpected since the water content is greatest at the perimeter. Saturation decreases from the perimeter towards the center in the three (3) tests. As in the constant volume tests, saturation at the center of specimens is greater in the higher pressure tests compared with the 250 kPa test but at the perimeter the 250 kPa test is still lower although relatively similar. In constant stiffness tests, expansion is allowed which leads to higher water contents but also increases mean stress.

6.4.3 Constant Stiffness (x = -25kPa/%) Infiltration Results

CS25 test results are presented in Figure 6.29 through Figure 6.34 with similar plots to earlier sections. The only difference between these tests and the CS75 infiltration tests is that mean stress is increased at a reduced rate which allows further swelling. This makes the CS25 tests closer to a constant mean stress test boundary while the CS75 tests are closer to constant volume. Behaviour observed in these tests is very similar to the previous section and to save repetition the previous section can be referred to with the relevant figures.

6.5 Constant Mean Stress Drained Infiltration Tests

Constant mean stress drained (CMSD) infiltration tests provide an explicit outflow location during liquid infiltration as opposed to the previously described tests. These are a select set of tests to try and better examine the influence of the lack of center drainage for the air phase imposed in the experiments described previously. Two (2) configurations were used including radial and vertical flow as described in Chapter 5. The radial flow apparatus has a mesh inserted at the center of the specimen instead of a suction sensor while the vertical flow apparatus retains the Xeritron sensor and allows drainage out the top of the specimen. Test procedure remains the same as the undrained tests except for the end of test criterion. In the undrained specimens, tests are complete when no further inflow, volume change nor suction change occurs. With drainage provided, inflow continues indefinitely and the end of test is determined when water content equilibrium is achieved as inflow equals outflow along with the volume and suction criteria. In this section, the three (3) drained infiltration tests are compared. They include a 250 kPa and 500 kPa radial flow tests as well as a 500 kPa vertical flow test.

6.5.1 Constant Mean Stress Drained Infiltration Results

Test results from the drained infiltration tests are shown in Figure 6.35 through Figure 6.41 as mean stress, volume strain, suction, and inflow and outflow versus time followed by specific volume and suction versus mean stress and axial, and radial strain versus volume strain. Figure 6.35a illustrates mean stress

was controlled throughout tests at the selected levels. Volume strain versus time plot (Figure 6.35b) shows responses from the three (3) specimens. The 250 kPa radial test expands the most with the 500 kPa vertical test showing the least expansion. The shapes of the volume strain versus time curves are also quite similar in the radial tests with sharp reduction at the beginning of infiltration followed by a reduced rate. The vertical test shows some compression at the beginning of infiltration followed by expansion but to a much smaller degree. As a reminder, the radial LVDTs on the vertical test were placed at one-third and two-thirds of the specimen height so they could not capture all displacements that occurred during the test. Post-test diameter measurements showed significant expansion in the bottom layer that was not measured with the LVDTs at their respective locations. The suction versus time plot only shows actual data from the vertical flow test since the radial tests do not include a suction sensor. Suction decreases due to isotropic compression and then has a small jump at the beginning of infiltration followed by suction dissipation. At approximately 43 days suction reading goes below zero. Since the Xeritron sensor measures relative humidity and not positive pore pressures the remainder of readings are ignored. The inflow and outflow plots (Figure 6.36b and Figure 6.37) show relatively higher inflow and outflow rates at the beginning of tests followed by reductions to constant rates. In both radial tests, inflow and outflow equilibrate to approximately the same rate. In the vertical test, inflow continues but outflow is only observed until approximately day 60 after which no further outflow is measured.

The specific volume and suction versus mean stress (Figure 6.38a and b) reflect the time dependent results in terms of state variables. Consistent deformation slopes are observed during isotropic compression for the three (3) tests. During infiltration the 250 kPa test expands the most the 500 kPa vertical test the least.

Anisotropic behaviour is evident in the axial and radial strain versus volume strain graphs (Figure 6.39a and b). Axial expansion levels off during infiltration while radial expansion continues during the two (2) radial flow tests. The vertical flow test shows some different behaviour but not all displacements were measured due to the LVDT configuration as described above. Slopes of radial versus axial strain are consistent for the radial flow specimens as observed in the undrained tests.

End of test post-test distributions are plotted in Figure 6.40 and Figure 6.41 for gravimetric water content, bulk density, dry density, and saturation. To allow for comparison, the phase relationships are plotted versus normalized distance along the flow path that is taken as the final length in each test. Since the vertical specimen is sliced into compacted layers, five (5) points are plotted compared to the three (3) sections in the radial flow tests. In-test results are reflected in the post-test measurements. The 250 kPa radial test has the highest gravimetric water content followed by the 500 kPa radial and vertical tests. Similar bulk and dry density distributions are observed in the two (2) 500 kPa

flow tests while the 250 kPa radial flow test density is lower due to expansion. The second bulk density measurement in the vertical flow test plots unexpectedly low as smooth transitions are anticipated in density and water content. Overall dry density increases from the upstream to downstream since water contents are higher in these areas. Finally, saturation plots show similar values for the downstream points in the radial tests while the 250 kPa test has a greater perimeter value. The 500 kPa vertical flow test shows significantly lower saturation although going towards the water source shows saturation trending towards the same value as in the radial flow test.

6.6 Mercury Intrusion Porosimetry and Scanning Electron Microscope Results

Results from selected SEM and MIP testing are displayed in Figure 6.42 and Figure 6.43. One SEM photograph from the as-compacted and three infiltration specimens are shown in Figure 6.42. MIP results from the three (3) radial sections are plotted in Figure 6.43.

6.6.1 Scanning Electron Microscope Results

Scanning Electron Microscope (SEM) photographs are all shown at similar magnification (2000x) and a scale is shown in the bottom left corner of each photo. The four photographs were taken to identify the macro pore mode of the specimens. The as-compacted specimen (Figure 6.42a) shows a large amount of pores that are on the 5-9 μm range. The infiltration specimens

(Figure 6.42b-d) all have less macro pores evident. Decrease in macro pore size was observed in all three (3) SEM photographs of infiltration specimens (Figure 6.42b-d). The 1000 kPa specimens (Figure 6.42c and d) show significantly less macro sized pores than the as-compacted and 250 kPa specimens. This was the result of higher mean stresses applied before as well as ped expansion during infiltration. The CS75 had greater increase in mean stress during infiltration compared with the CS25 test, which allowed less bulk expansion of the specimen. This is reflected in the photographs as smaller pores in Figure 6.42c compared with Figure 6.42d.

6.6.2 Mercury Intrusion Porosimetry Results

Pore size distributions from as-compacted and infiltration specimens agree with previous results and expected trends. The as-compacted specimen, Figure 6.43a, has a bimodal distribution with similar located modes as previously measured (Figure 2.2). The perimeter section has a higher incremental intrusion distribution compared to the middle and center specimens but with the same modes. The tails at the upper end of the diameter axis which show increases are interpreted as being due to disturbance either during preparation or drying and not representative of actual pore space during tests. On the lower magnification SEM photos that were not included in this paper, cracks were observed around sand particles. The bentonite clay likely shrank away from the sand during drying and resulted in anomalous ‘tails’ at the upper end of the pore size distributions.

Comparing the infiltration specimens to the as-compacted shows decrease in macro porosity for the three specimens, especially in pores greater than 10 μm. In the micro pore sizes, a small shift to the left is observed in the infiltration specimens compared to the as-compacted.

Internal changes in pore size distribution are evident along the flow path in the infiltration specimens. The 250 kPa specimen (Figure 6.43b) has shift to the right in micro porosity and a shift to the left in macro porosity from the perimeter to the center. For the 1000 kPa specimens, little change in micro porosity is observed from perimeter to the center. Conversely, the macro porosity is least at the perimeter increases towards the center of the specimens.

Table 6.1. Infiltration Test Summary.

Test Type	Isotropic Compression Level (kPa)			
	250	500	1000	1500
Constant Mean Stress - Drained	GS-053	GS-051 GS-052	-	-
Constant Mean Stress	GS-048	GS-034 GS-035 GS-036	GS-050	GS-047
Constant Stiffness - X = -25 kPa/%	GS-066	GS-055	GS-071	-
Constant Stiffness - X = -75 kPa/%	GS-058	GS-054	GS-069	-
Constant Volume	GS-045	GS-041	GS-046	GS-030 GS-044

Note: All infiltration tests were completed with 200 kPa water pressure except GS-034 and GS-035, which used 100 kPa water pressure.

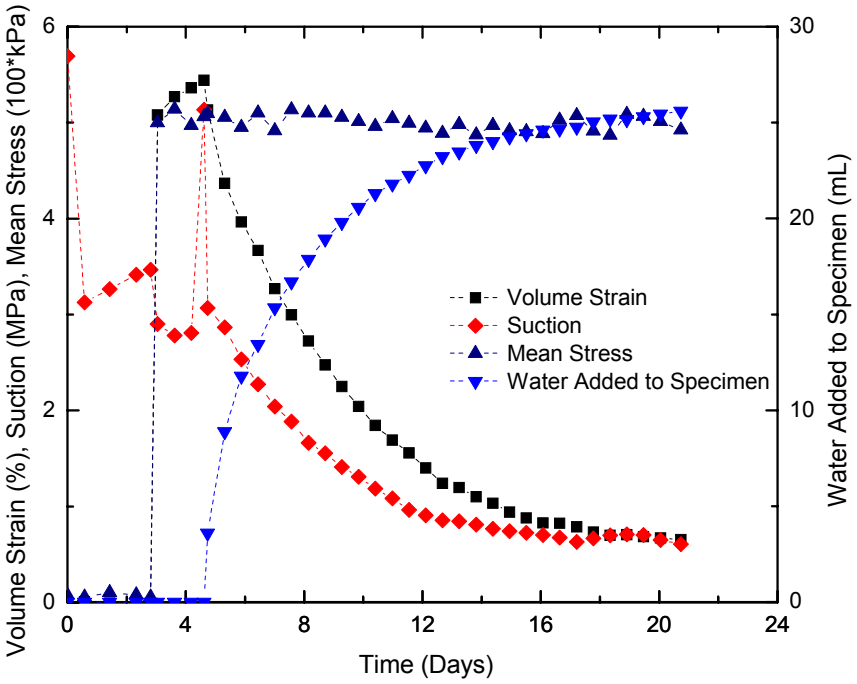

Figure 6.1. 500 kPa constant mean stress (CMS): volume strain, suction, mean stress and water added to specimen versus time (after Blatz and Siemens 2004).

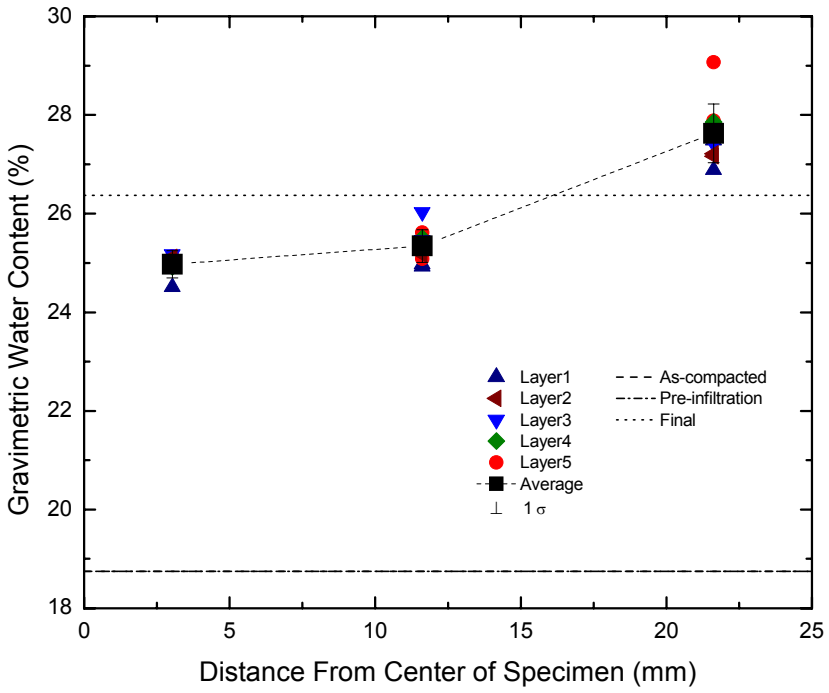

a.

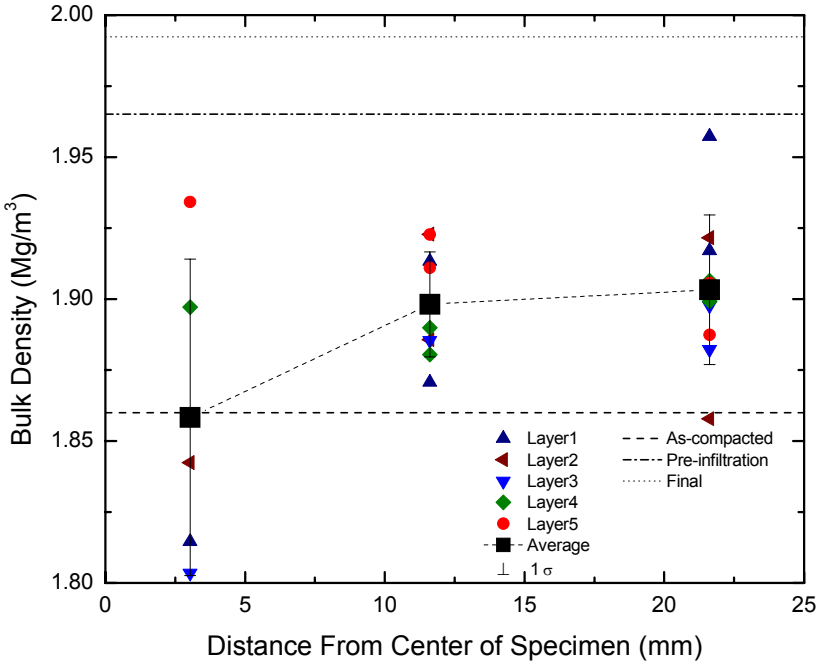

b.

Figure 6.2. 500 kPa constant mean stress (CMS): end of test distribution of gravimetric water content and bulk density (after Blatz and Siemens 2004).

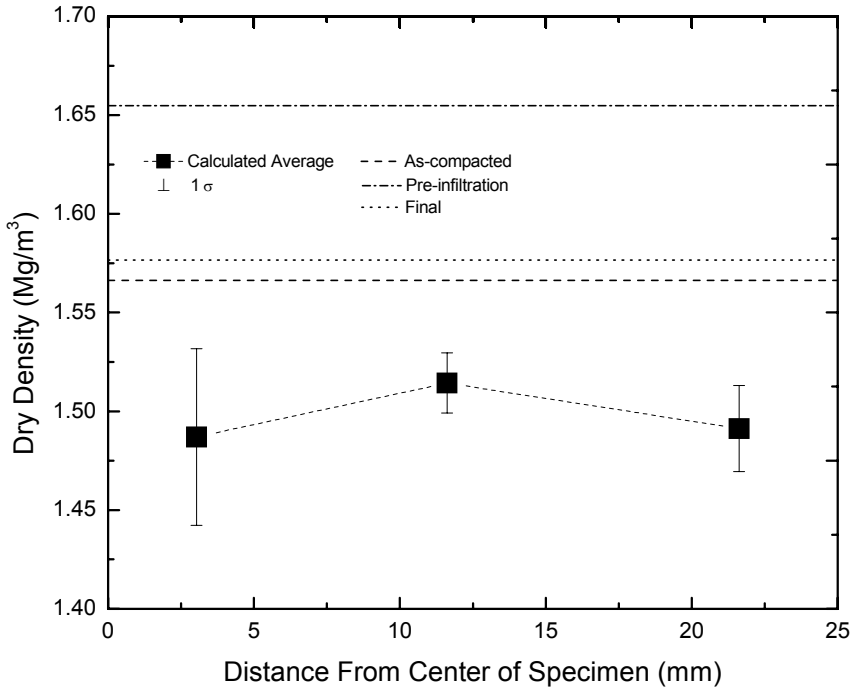

a.

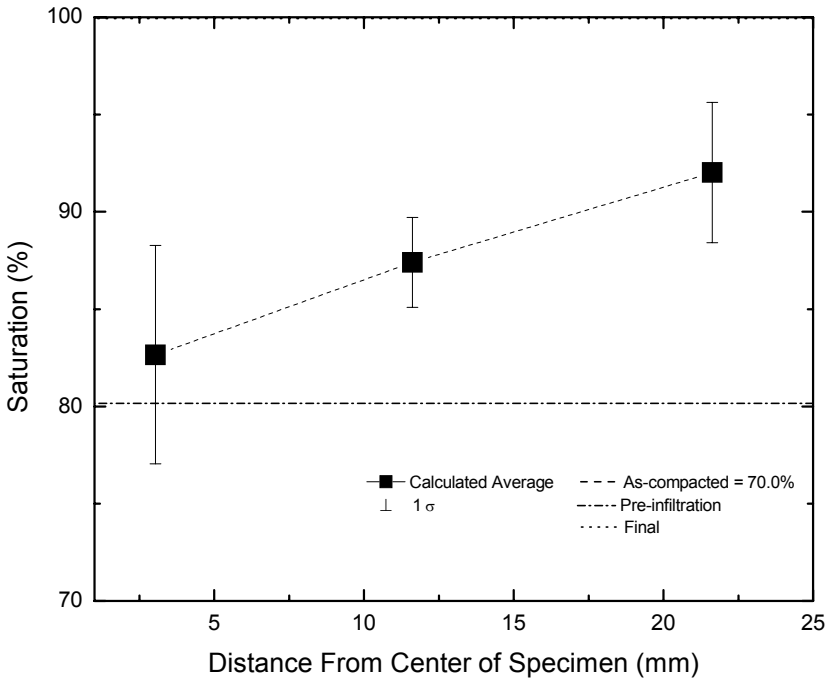

b.

Figure 6.3. 500 kPa constant mean stress (CMS) infiltration: end of test distribution of average dry density and saturation (after Blatz and Siemens 2004).

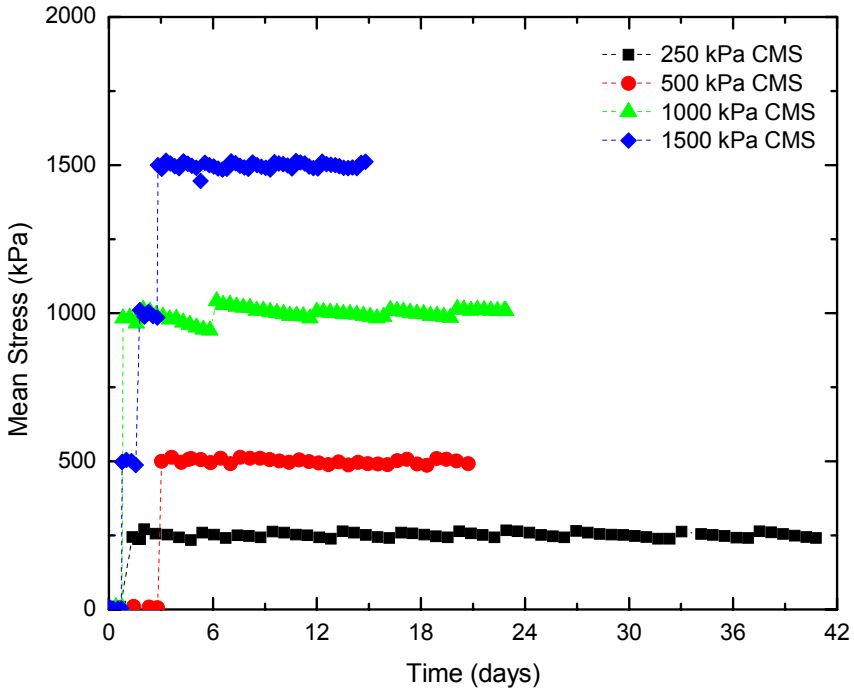

a.

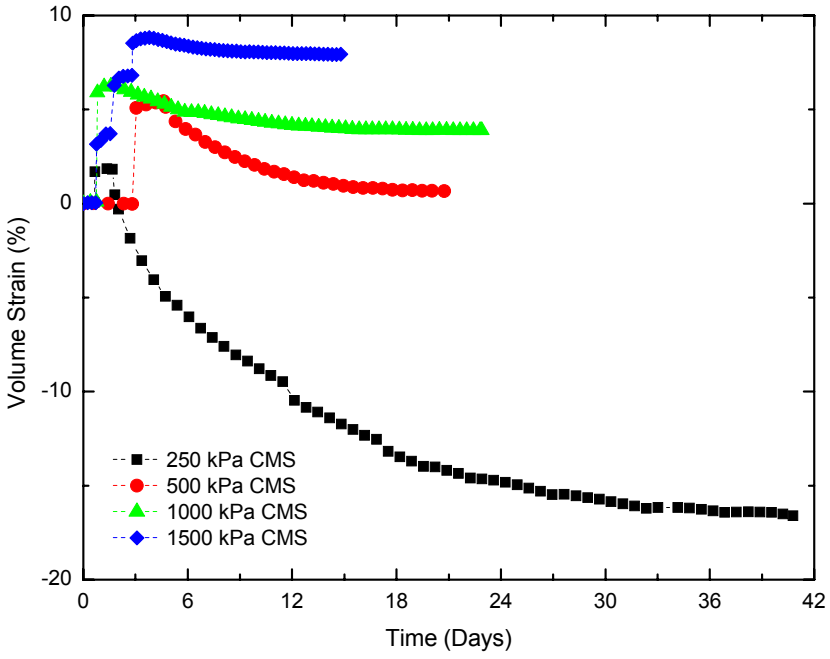

b.

Figure 6.4. Constant mean stress (CMS) summary: mean stress and volume strain versus time (after Blatz and Siemens 2005).

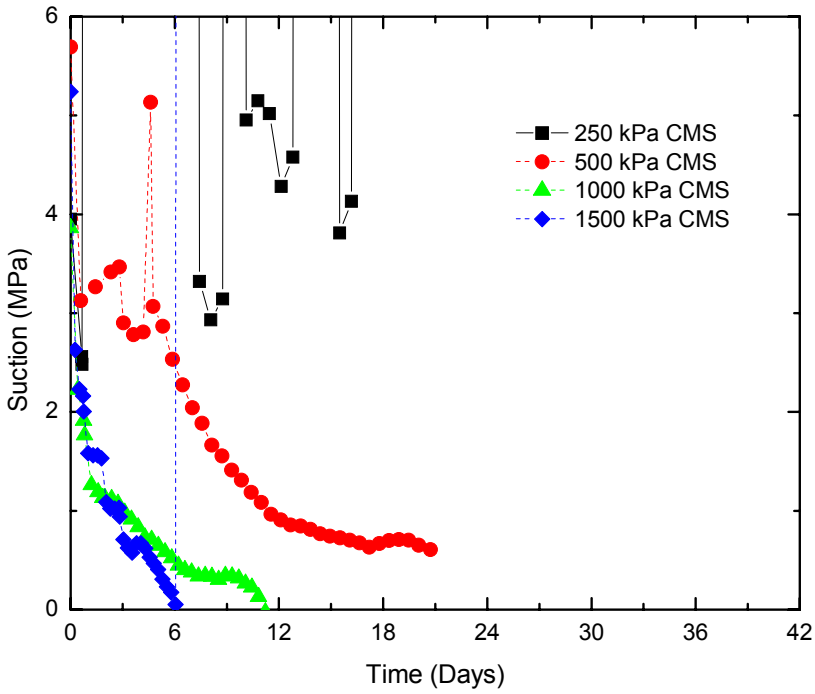

a.

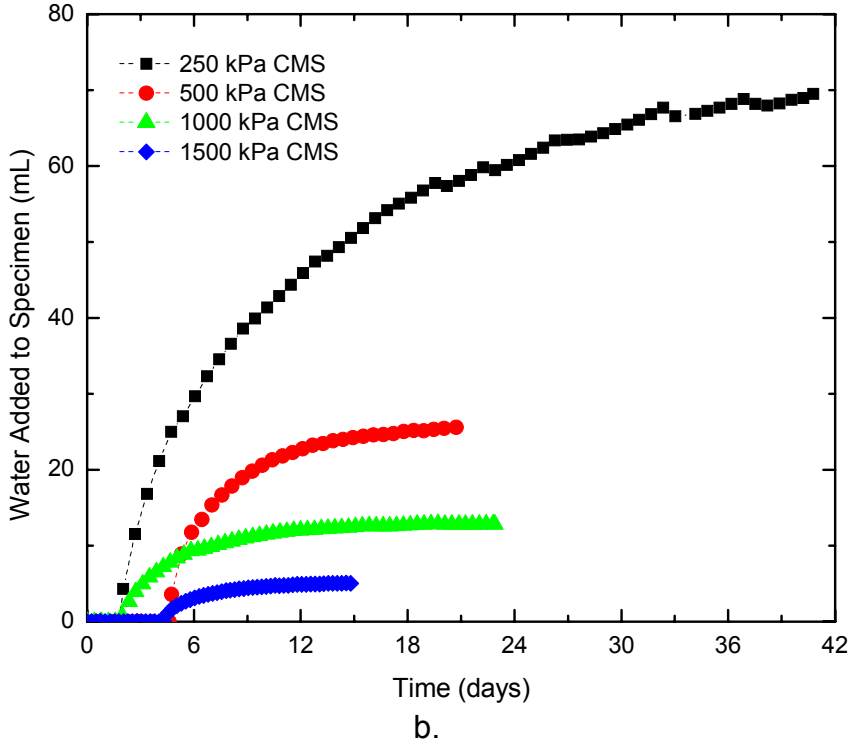

b.

Figure 6.5. Constant mean stress (CMS) summary: suction and water added to specimen versus time (after Blatz and Siemens 2005).

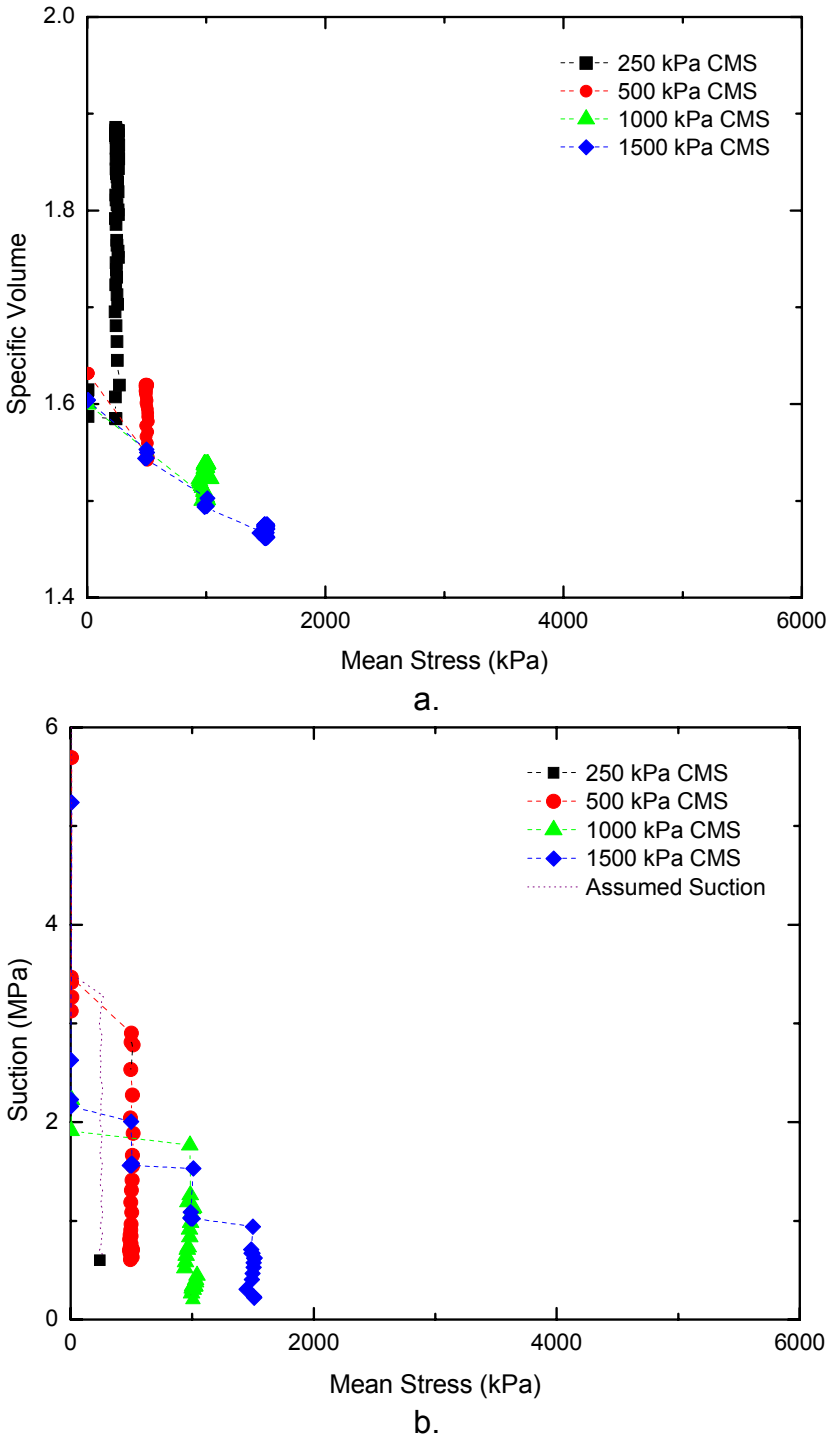

Figure 6.6. Constant mean stress (CMS) summary: specific volume and suction versus mean stress (after Blatz and Siemens 2005).

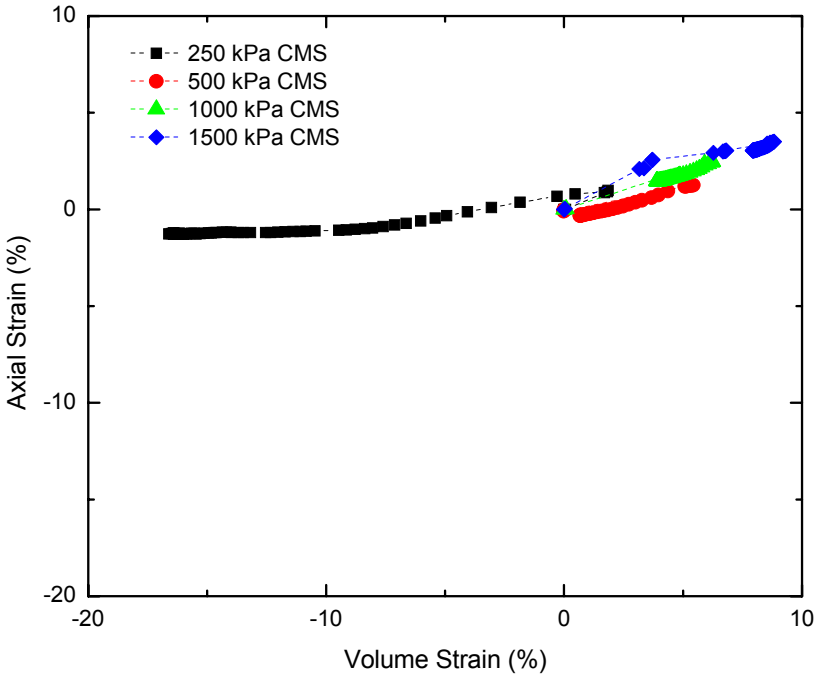

a.

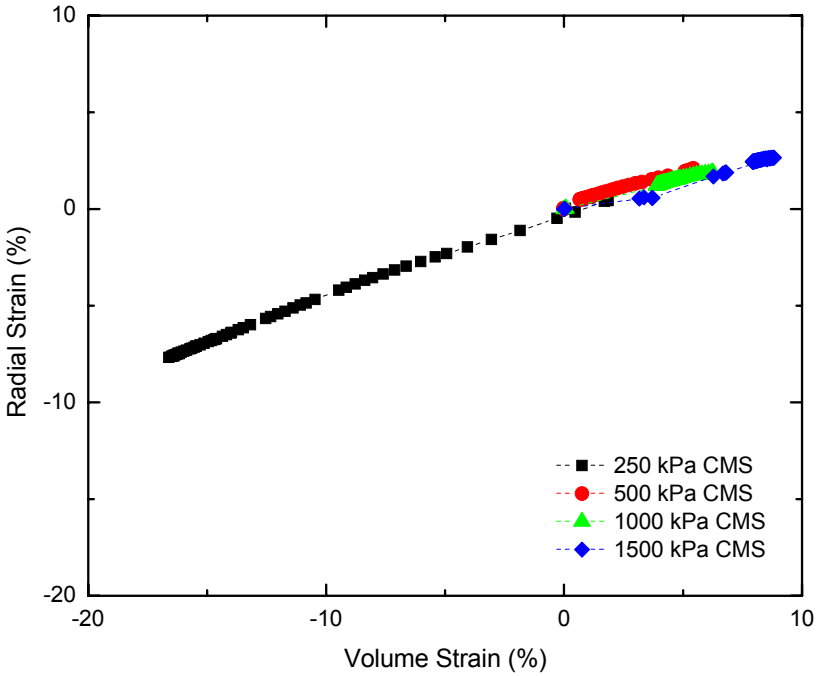

b.

Figure 6.7. Constant mean stress (CMS) summary: axial strain and radial strain versus volume strain (after Blatz and Siemens 2005).

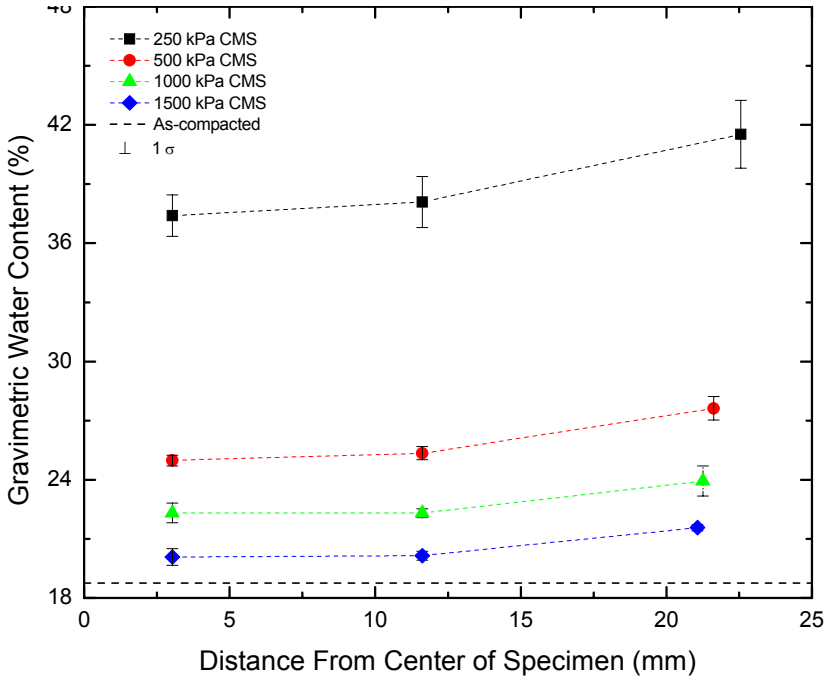

a.

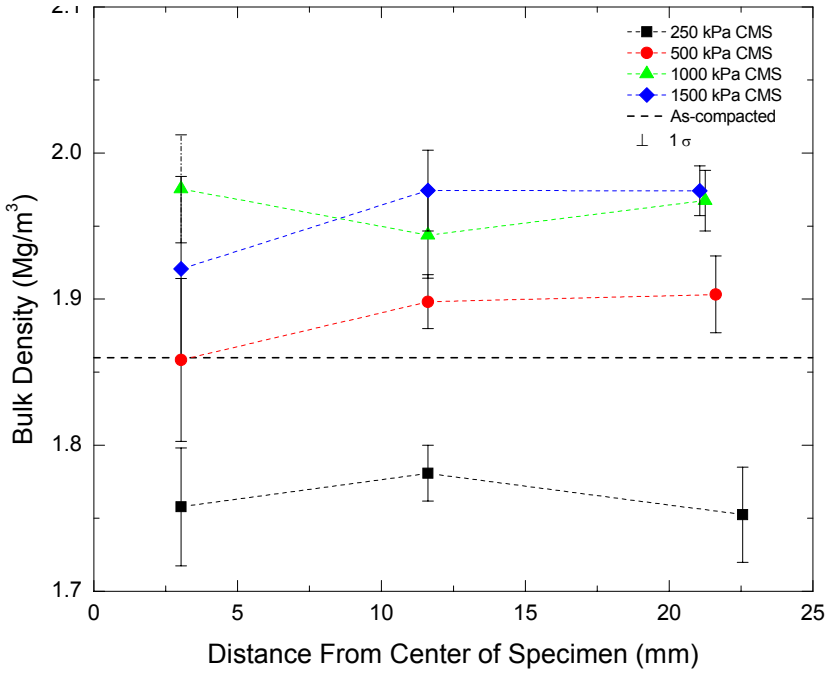

b.

Figure 6.8. Constant mean stress (CMS) summary: end of test distribution of average gravimetric water content and bulk density (after Blatz and Siemens 2005).

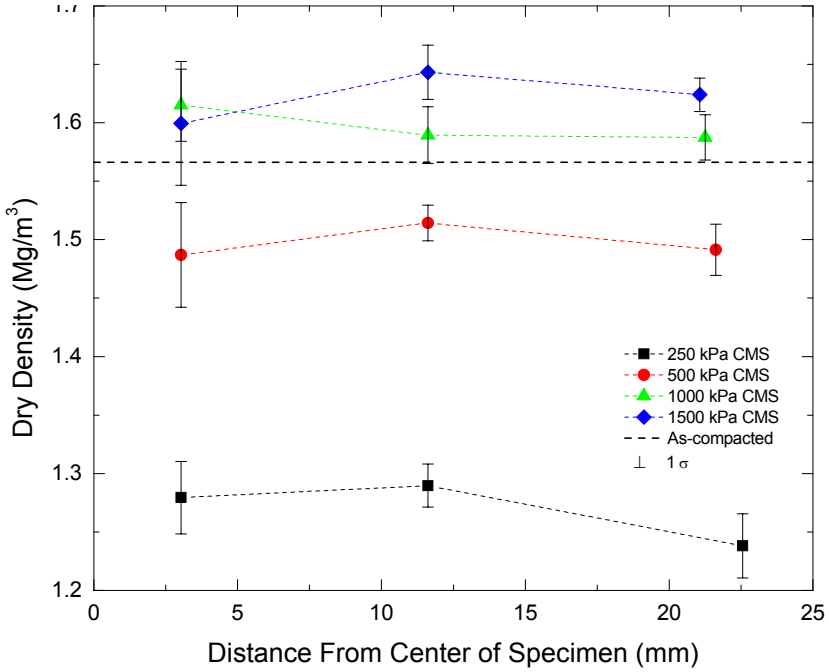

a.

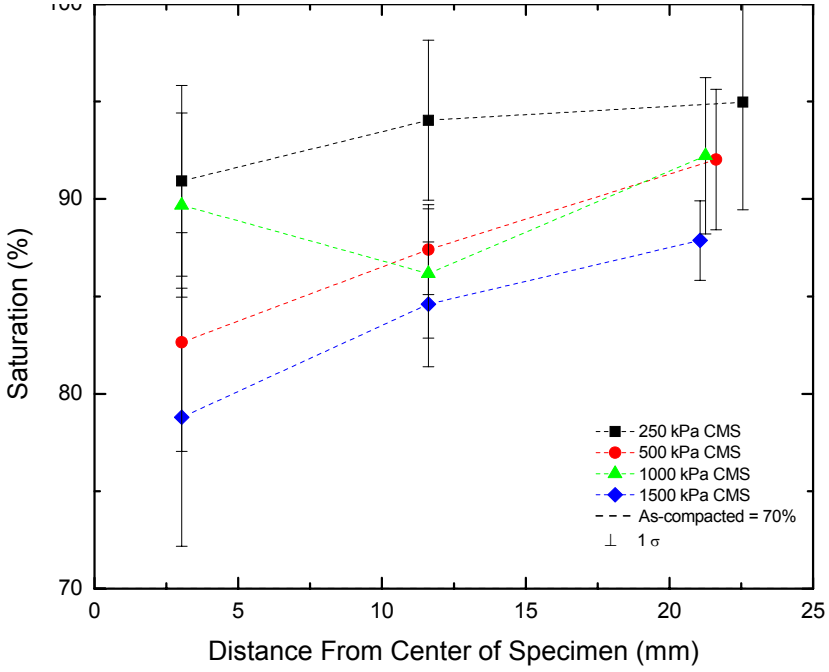

b.

Figure 6.9. Constant mean stress (CMS) summary: end of test distribution of average dry density and saturation (after Blatz and Siemens 2005).

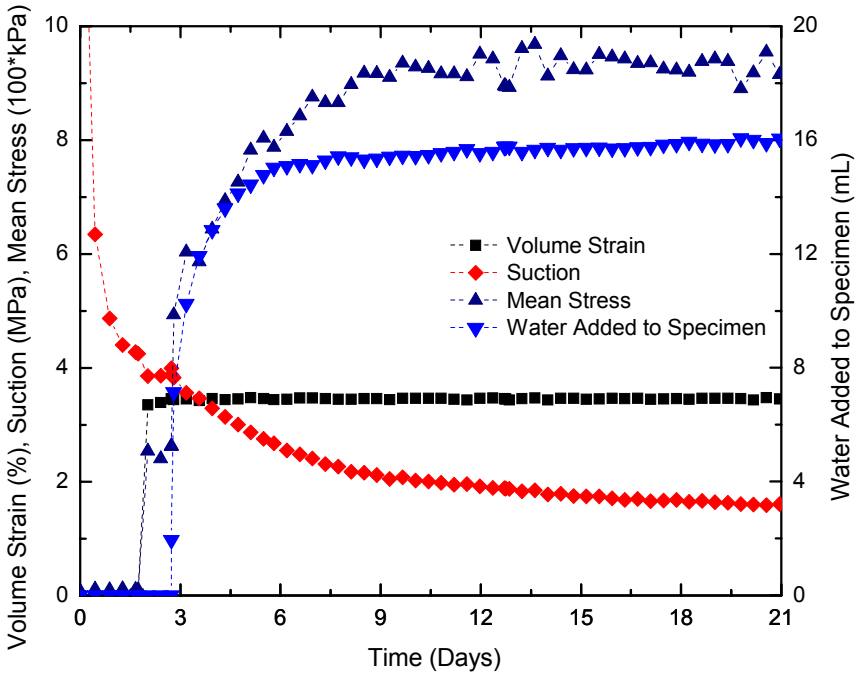

Figure 6.10. 250 kPa constant volume (CV): volume strain, suction, mean stress and water added to specimen versus time (after Blatz and Siemens 2005).

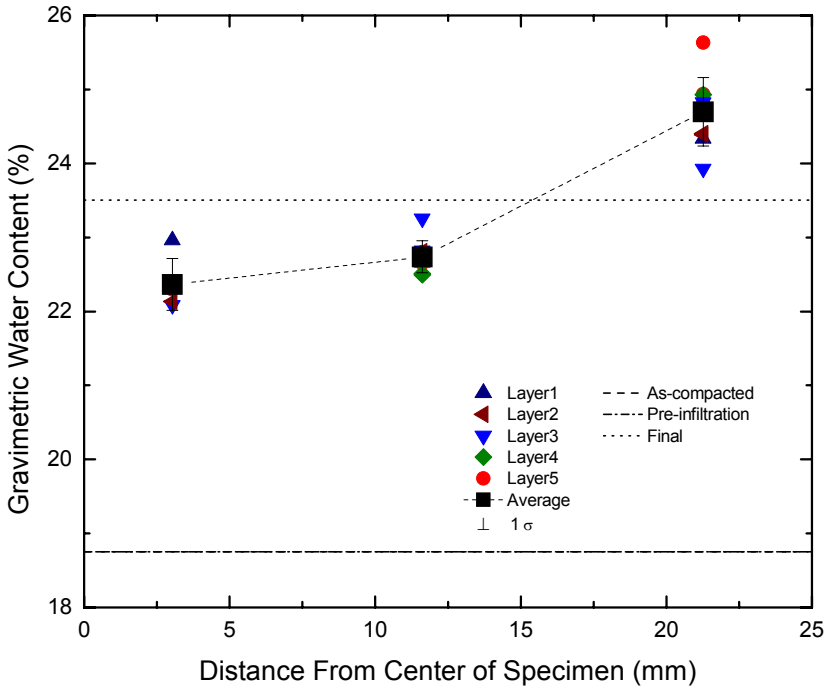

a.

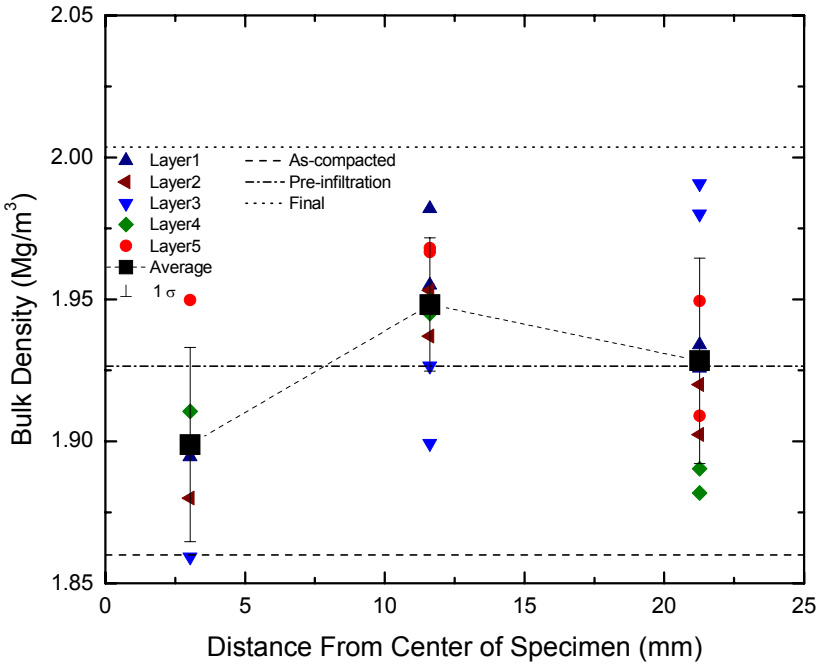

b.

Figure 6.11. 250 kPa constant volume (CV): end of test distribution of gravimetric water content and bulk density (after Blatz and Siemens 2005).

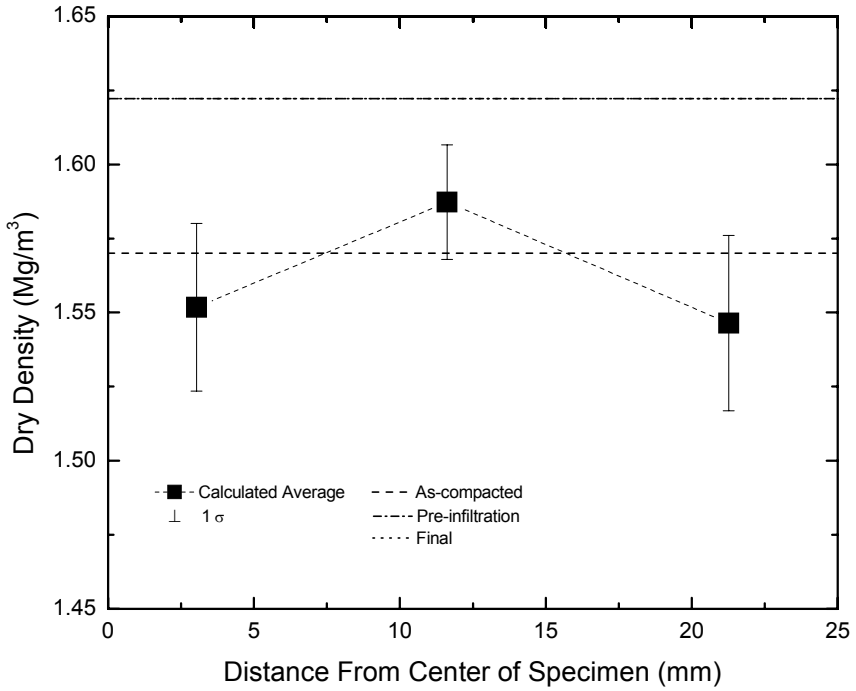

a.

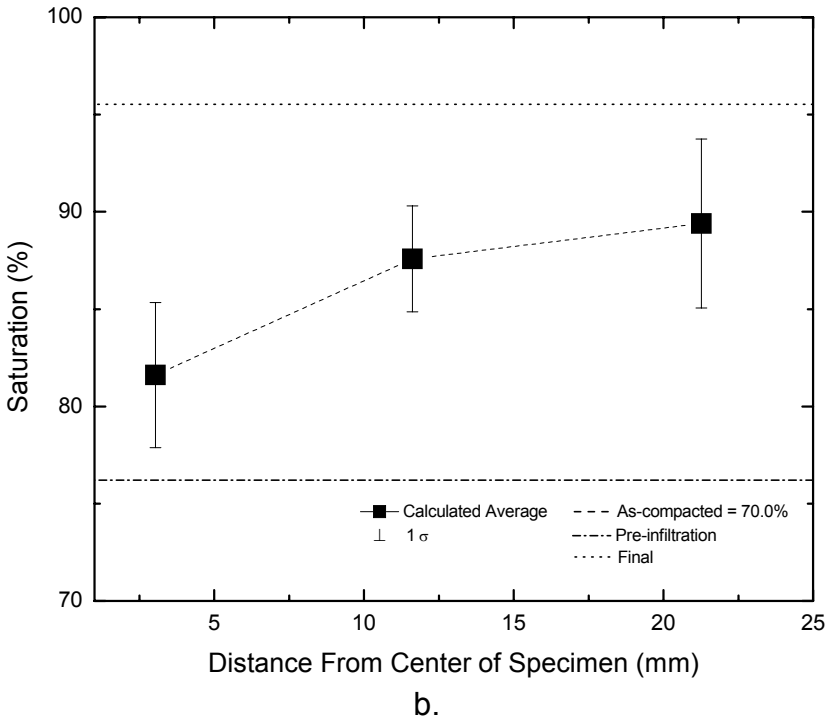

b.

Figure 6.12. 250 kPa constant volume infiltration: end of test distribution of average dry density and saturation (after Blatz and Siemens 2005).

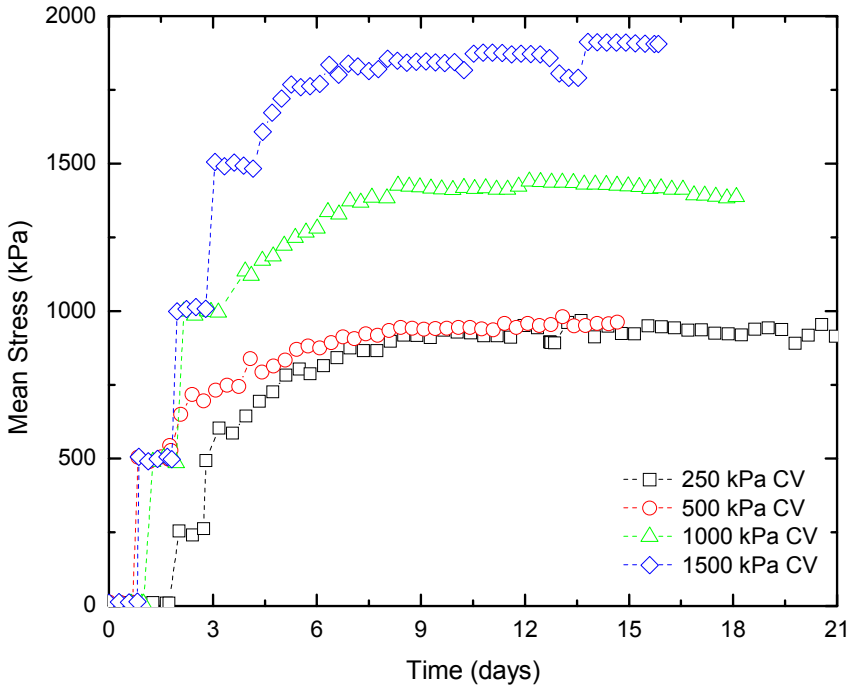

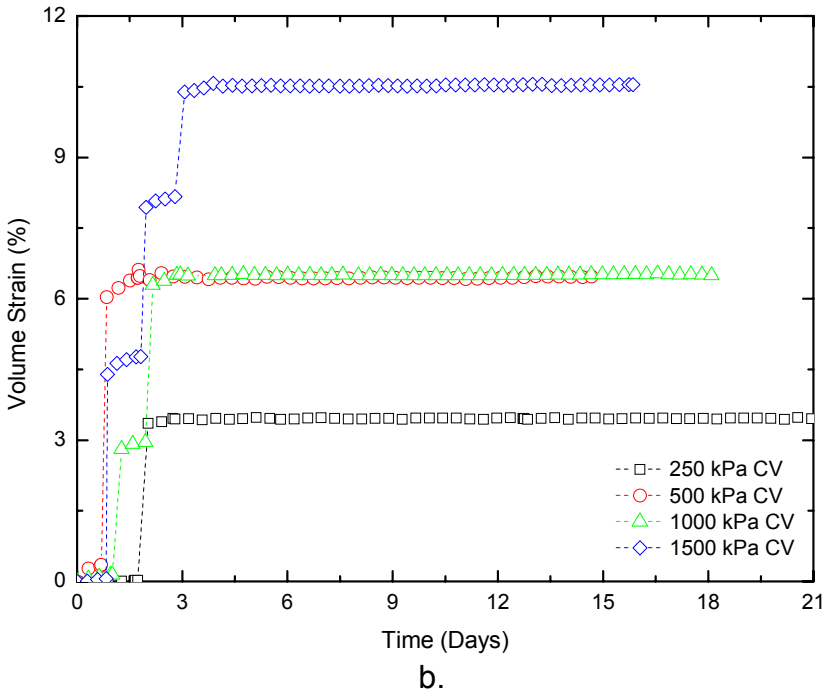

Figure 6.13. Constant volume (CV) summary: mean stress and volume strain versus time (after Blatz and Siemens 2005).

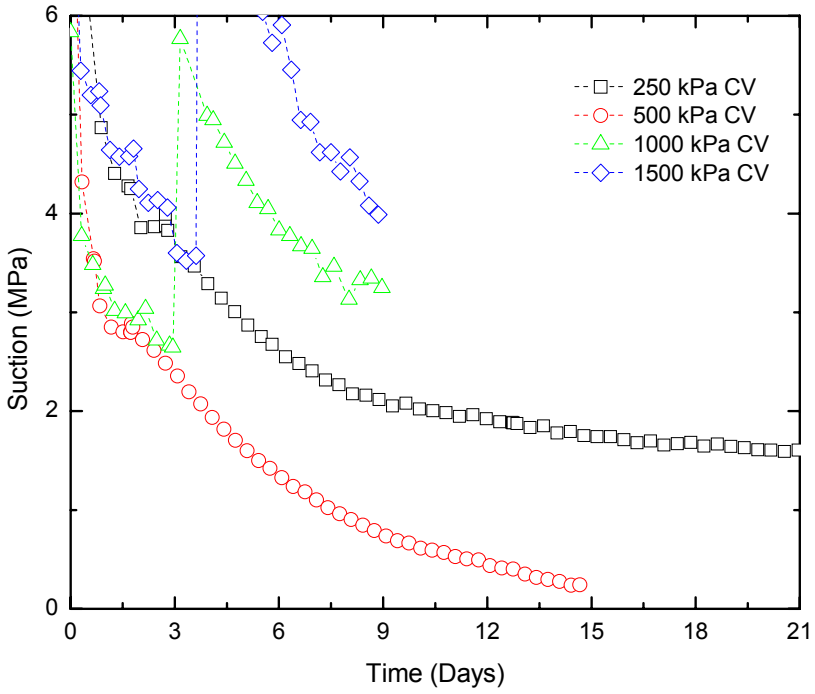

a.

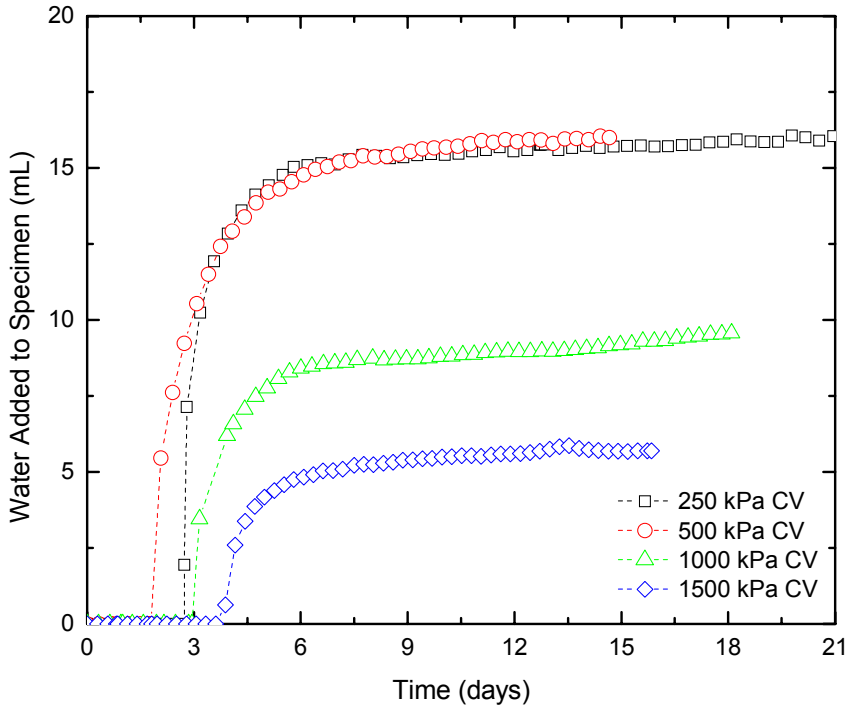

b.

Figure 6.14. Constant volume (CV) summary: suction and water added to specimen versus time (after Blatz and Siemens 2005).

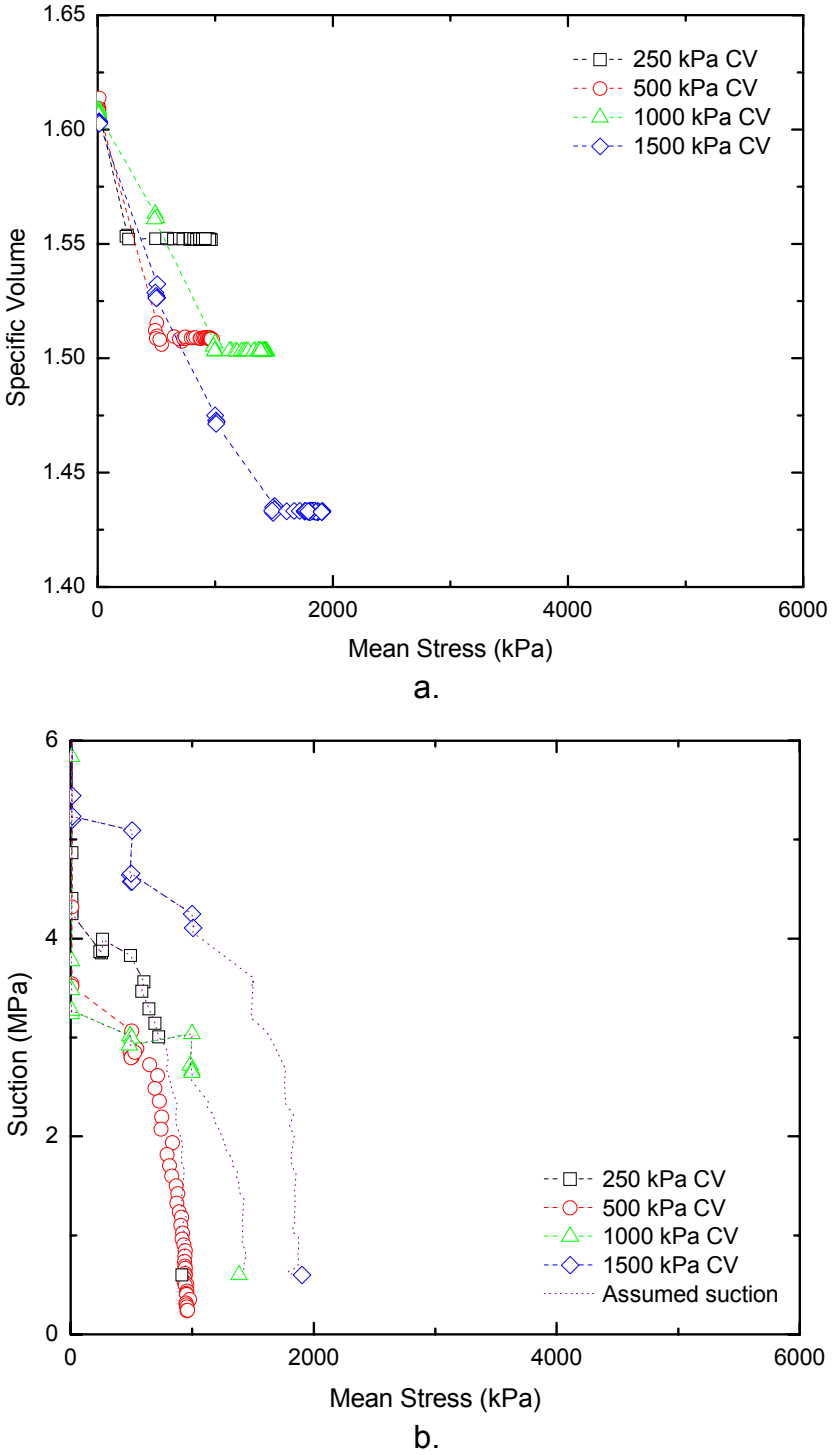

Figure 6.15. Constant volume (CV) summary: specific volume and suction versus mean stress (after Blatz and Siemens 2005).

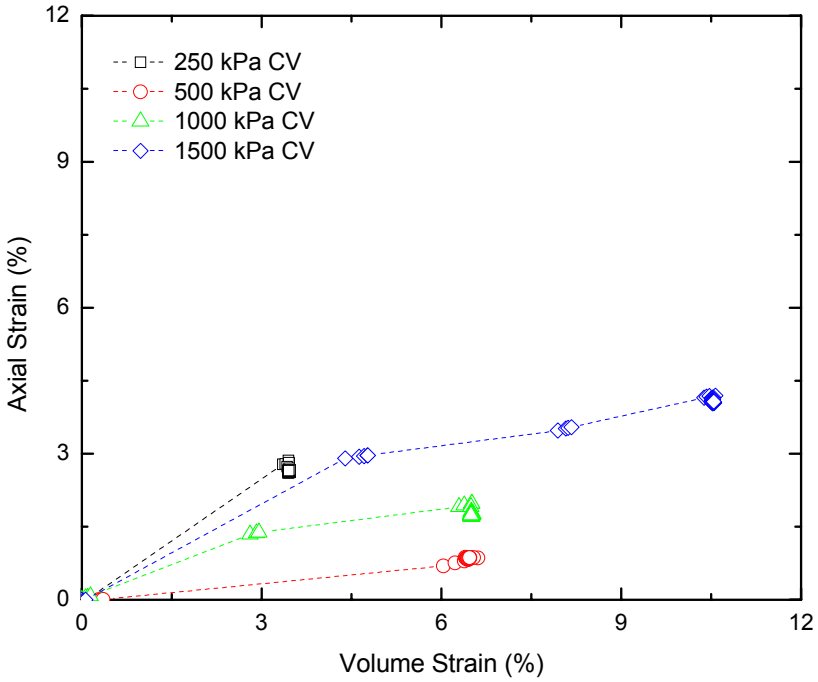

a.

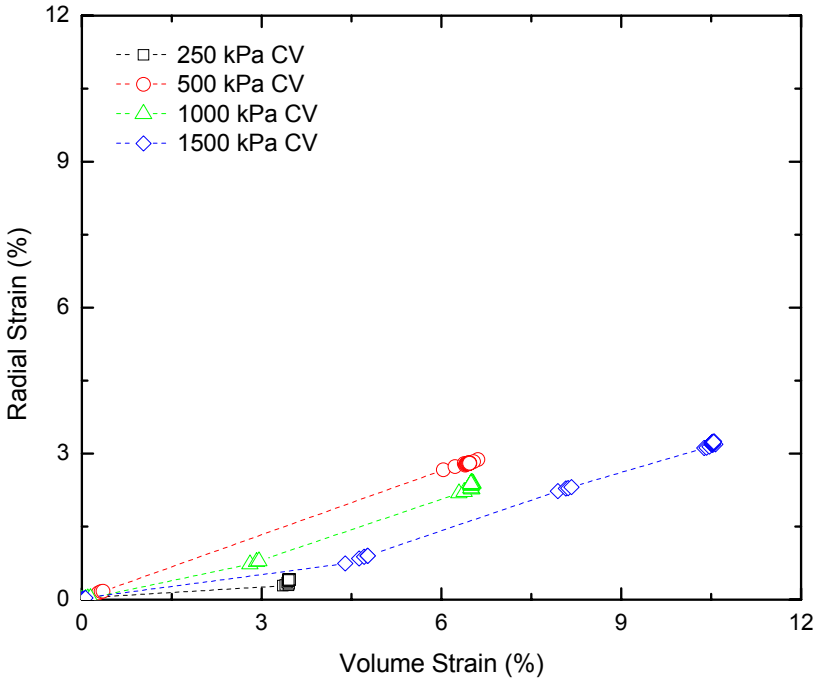

b.

Figure 6.16. Constant volume (CV) summary: axial strain and radial strain versus volume strain (after Blatz and Siemens 2005).

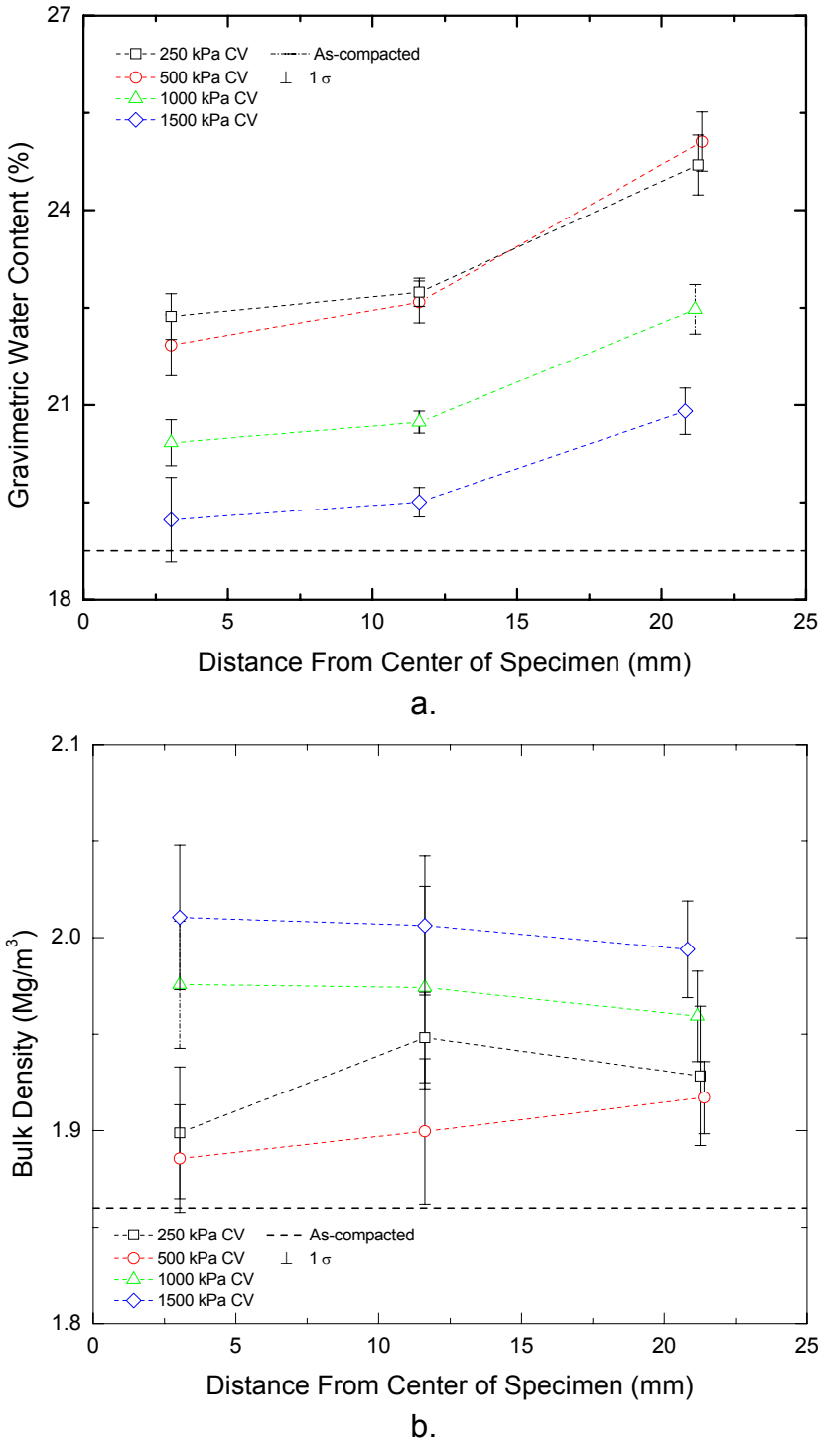

Figure 6.17. Constant volume (CV) summary: end of test distribution of average gravimetric water content and bulk density (after Blatz and Siemens 2005).

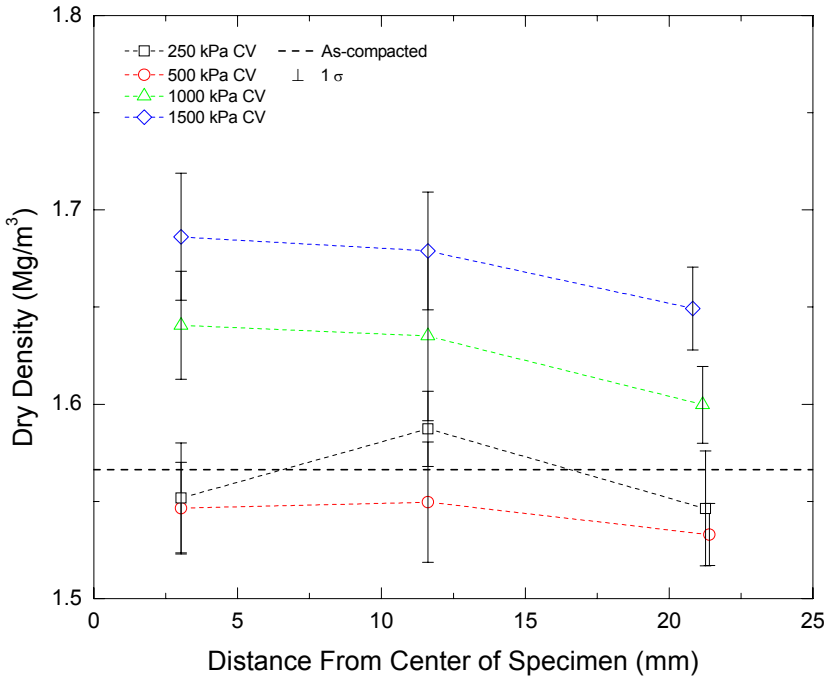

a.

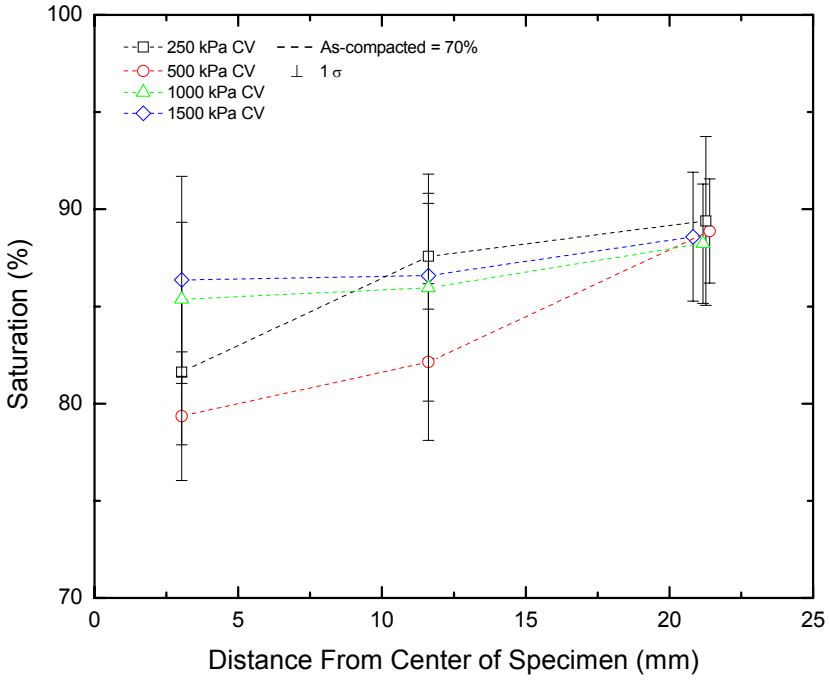

b.

Figure 6.18. Constant volume (CV) summary: end of test distribution of average dry density and saturation (after Blatz and Siemens 2005).

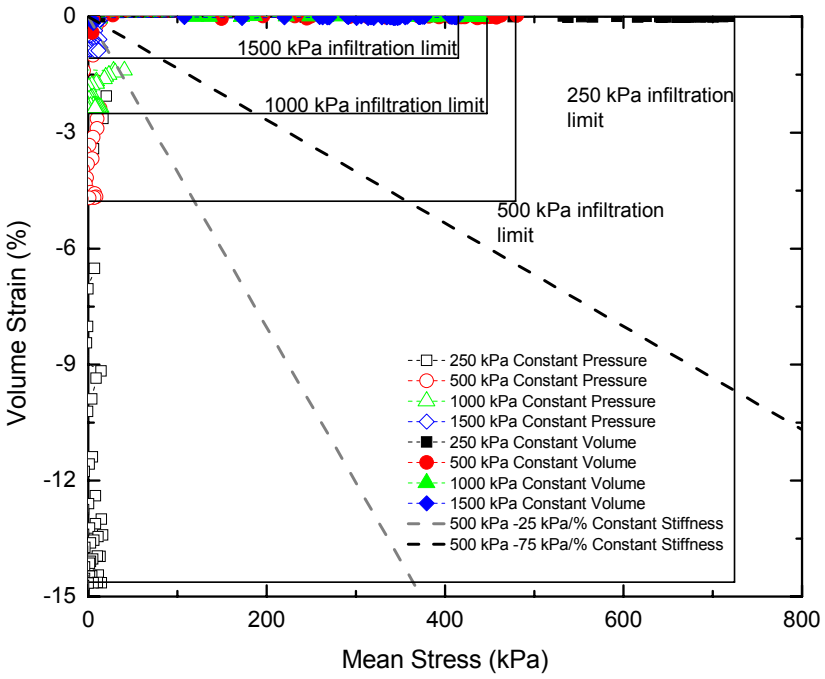

Figure 6.19. Normalized volume strain versus mean stress change during infiltration for constant mean stress and constant volume test results (after Blatz and Siemens 2006).

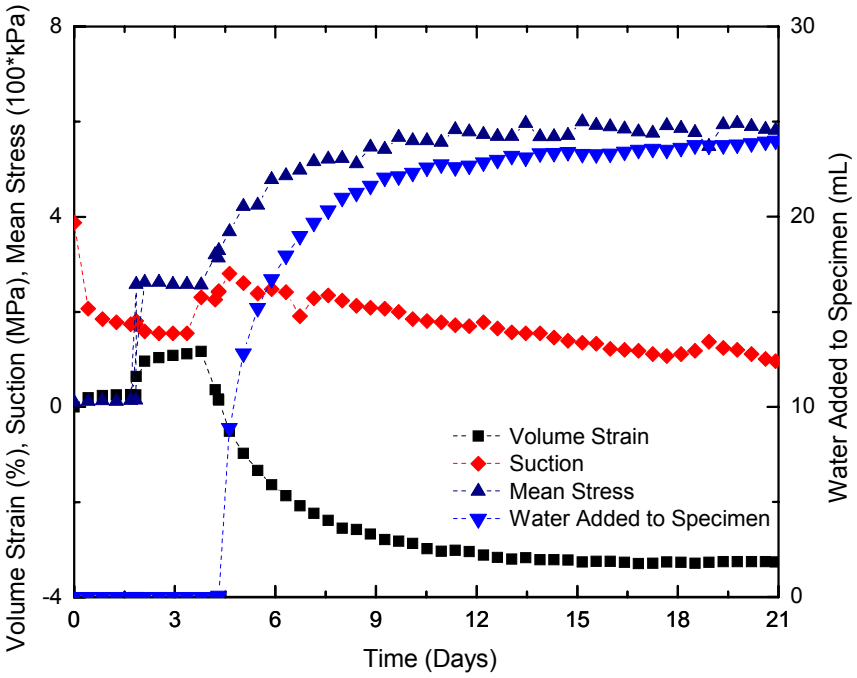

Figure 6.20. 250 kPa constant stiffness (CS75): volume strain, suction, mean stress and water added to specimen versus time (after Blatz and Siemens 2006).

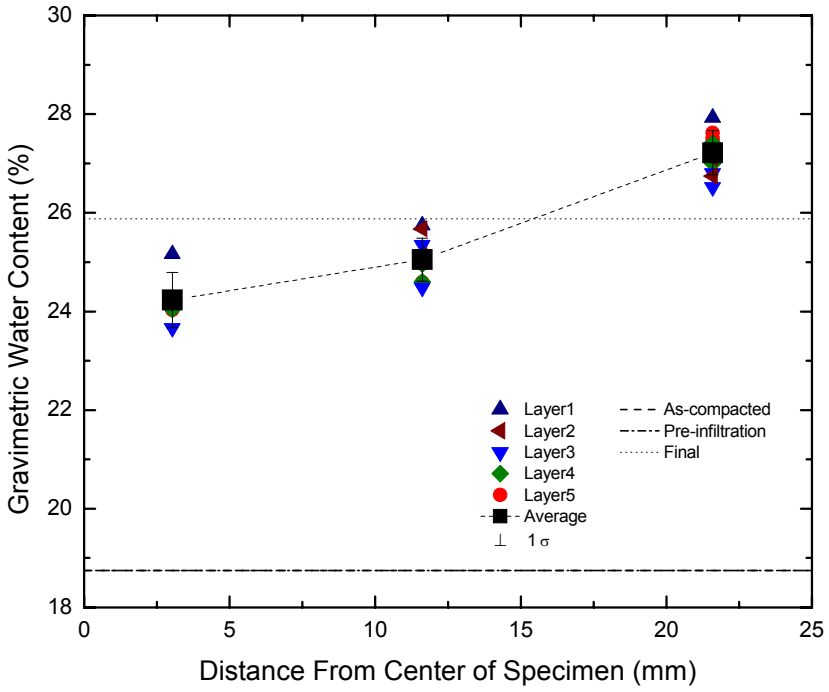

a.

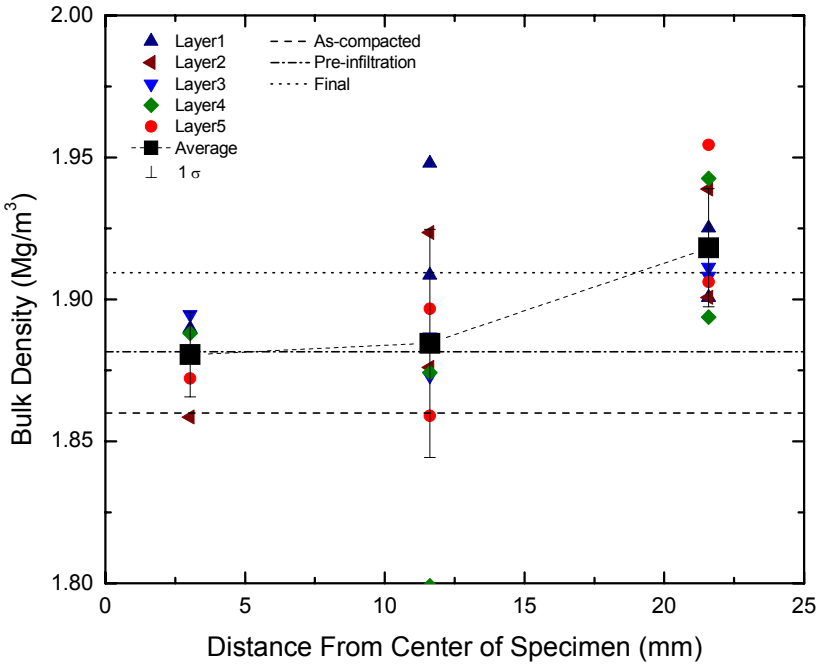

b.

Figure 6.21. 250 kPa constant stiffness (CS75): end of test distribution of gravimetric water content and bulk density (after Blatz and Siemens 2006).

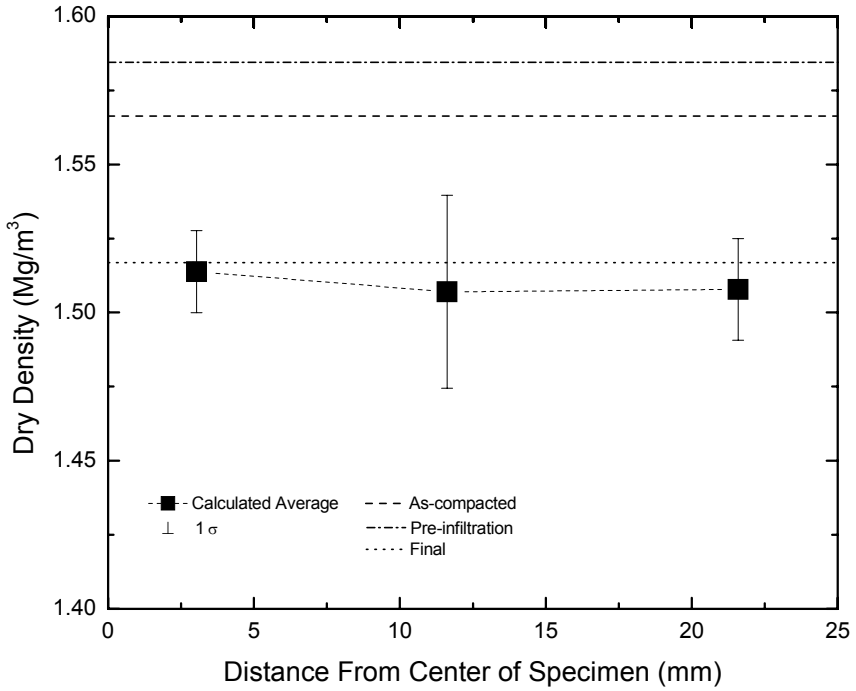

a.

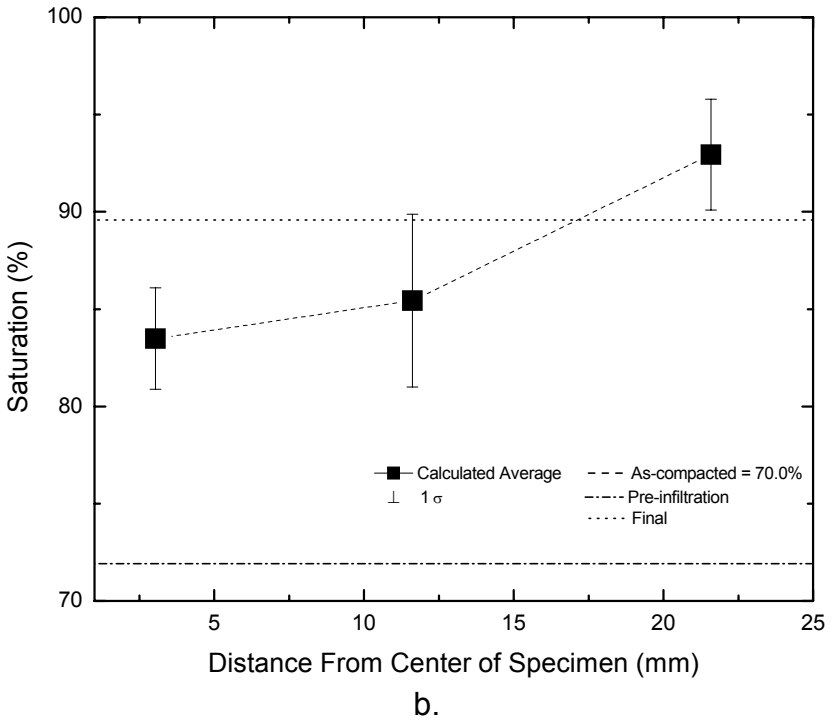

b.

Figure 6.22. 250 kPa constant stiffness (CS75) infiltration: end of test distribution of average dry density and saturation (after Blatz and Siemens 2006).

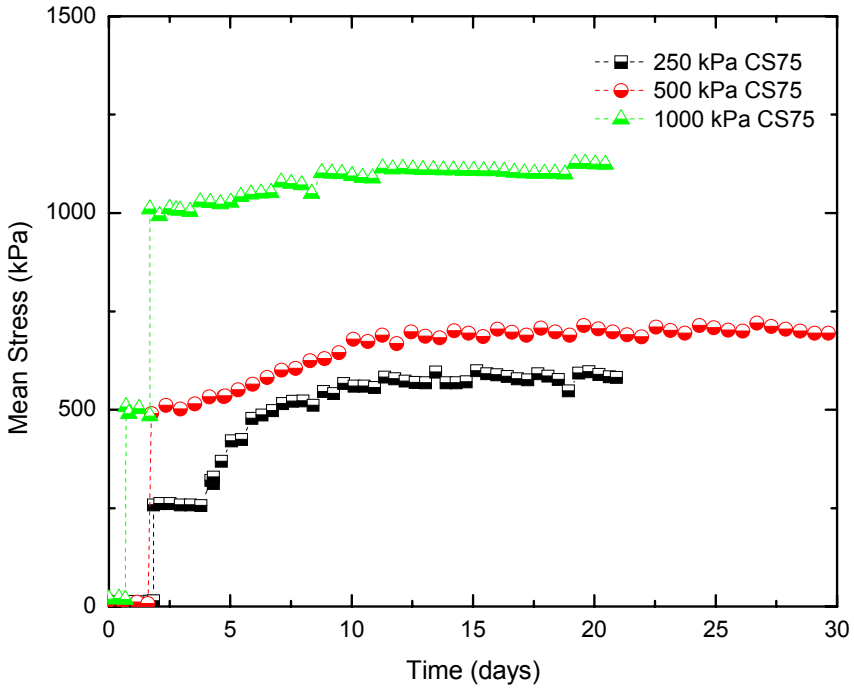

a.

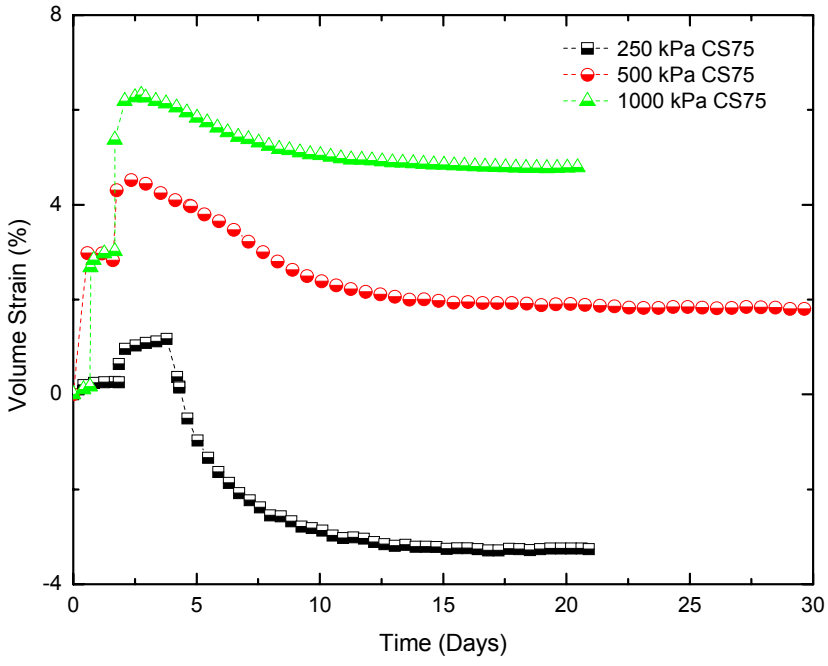

b.

Figure 6.23. Constant stiffness (CS75) summary: mean stress and volume strain versus time.

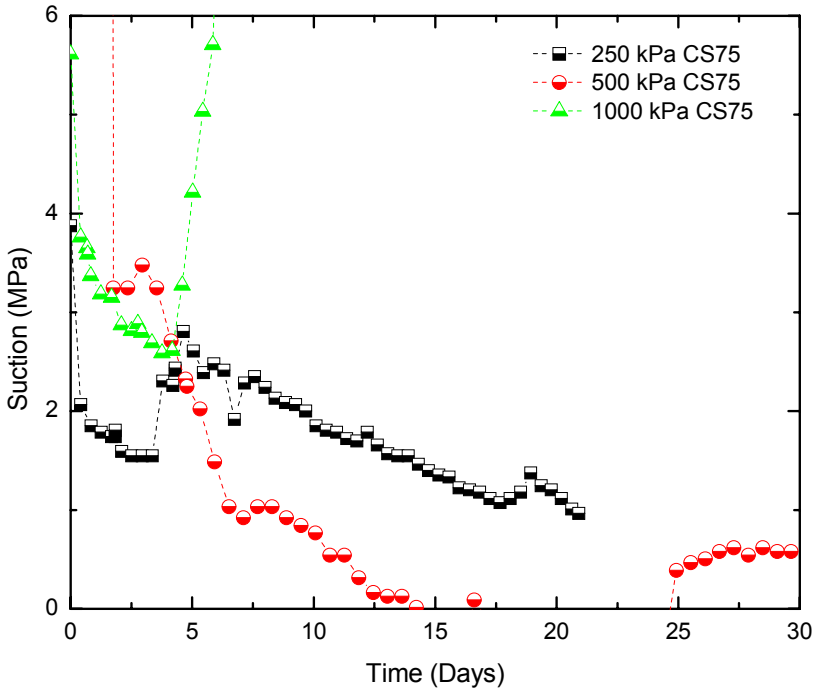

a.

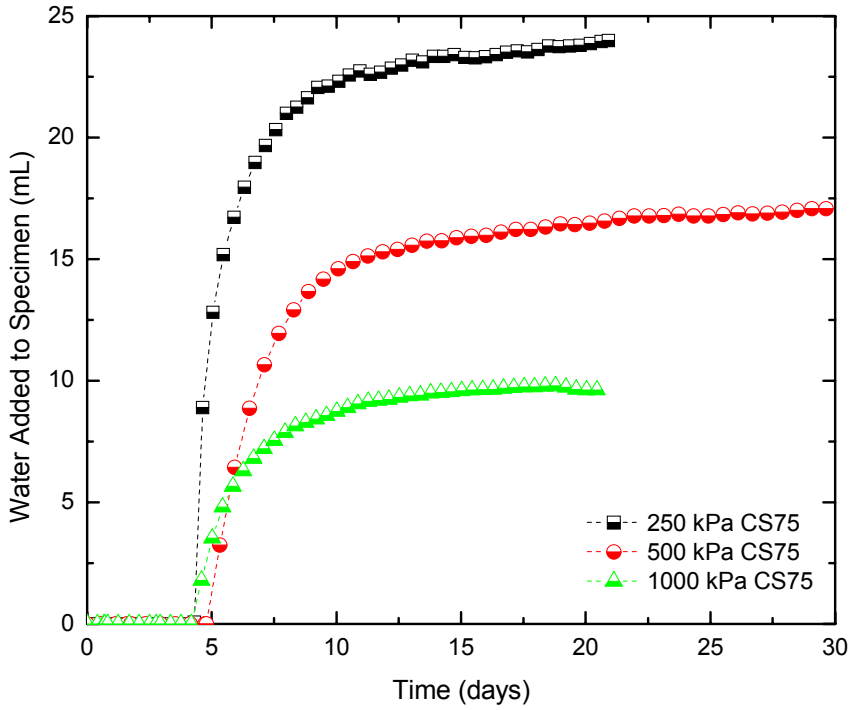

b.

Figure 6.24. Constant stiffness (CS75) summary: suction and water added to specimen versus time.

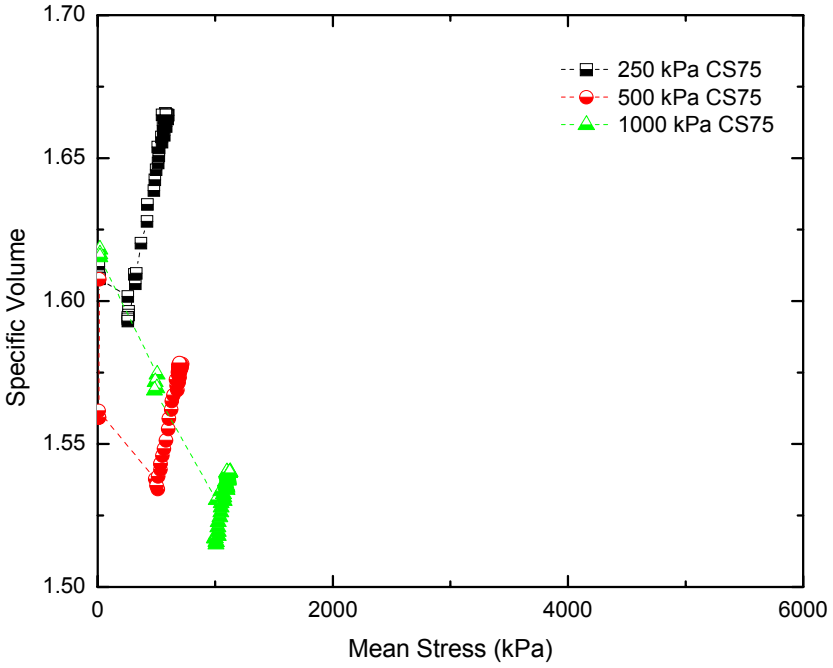

a.

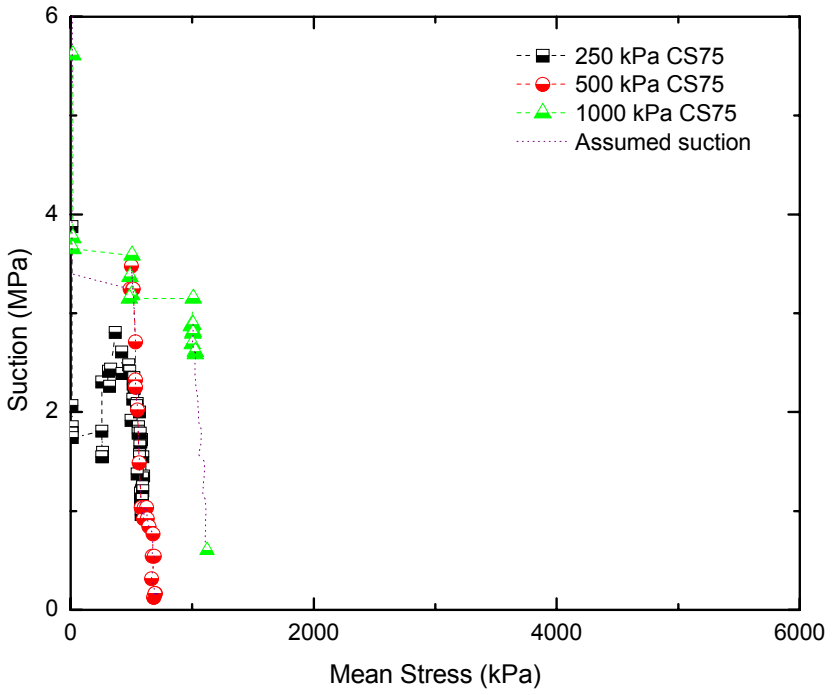

b.

Figure 6.25. Constant stiffness (CS75) summary: specific volume and suction versus mean stress.

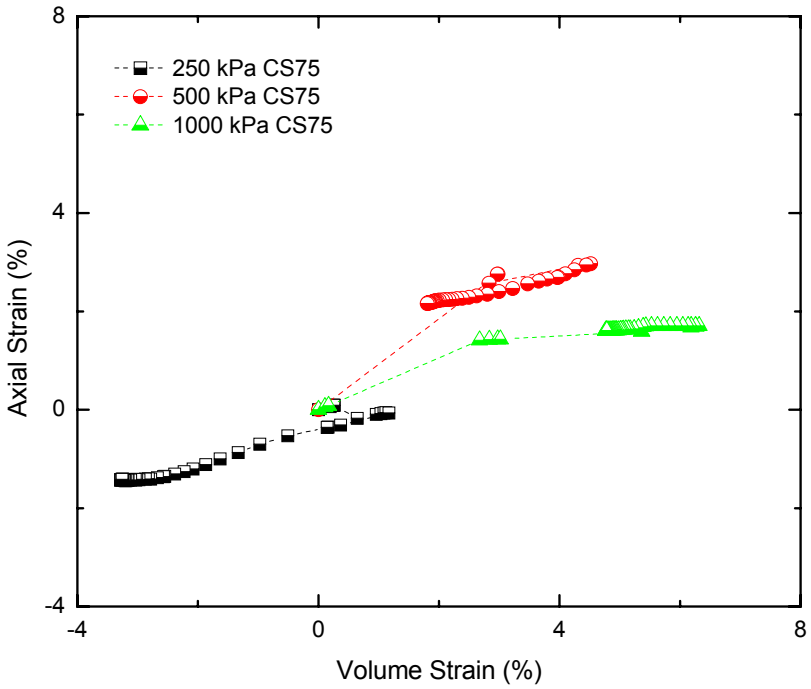

a.

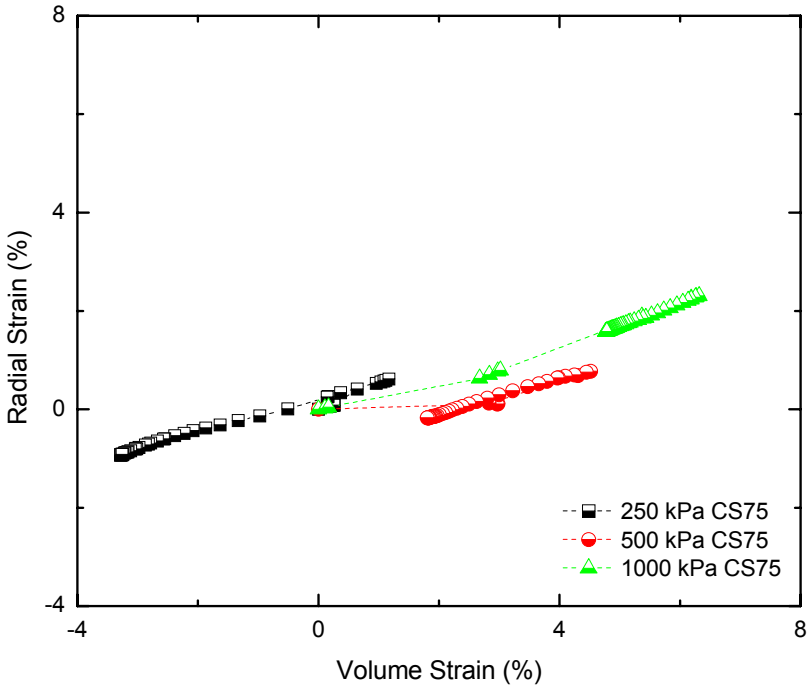

b.

Figure 6.26. Constant stiffness (CS75) summary: axial strain and radial strain versus volume strain.

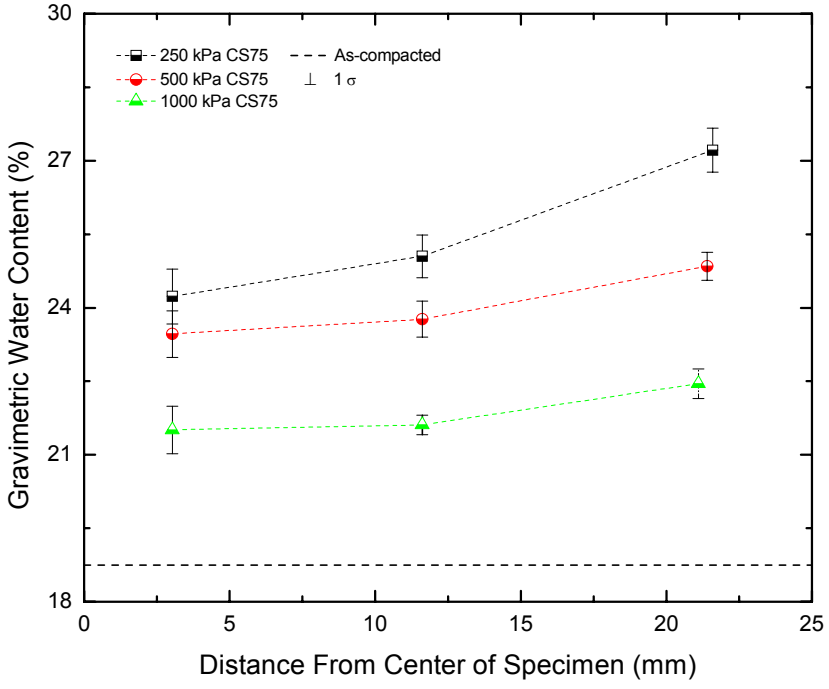

a.

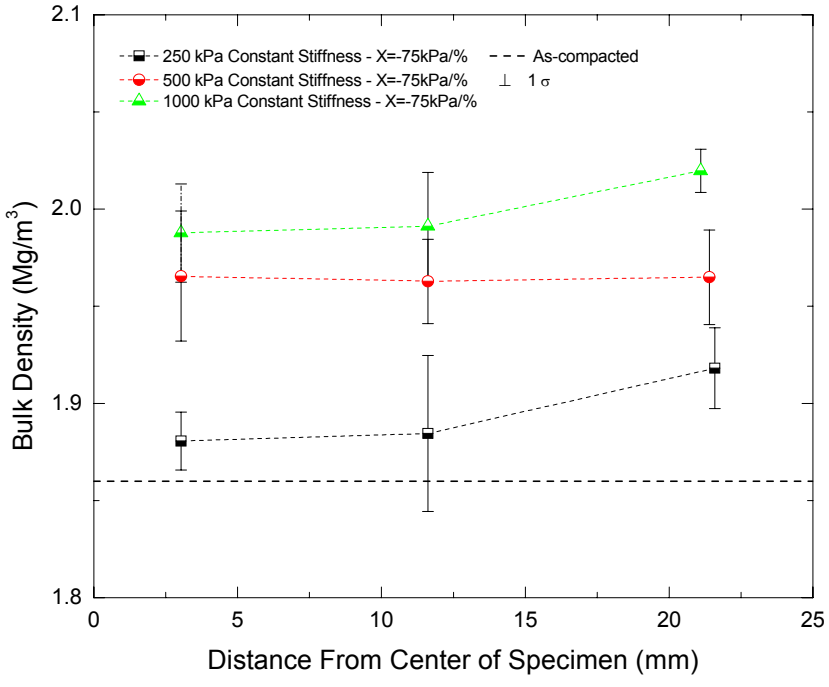

b.

Figure 6.27. Constant stiffness (CS75) summary: end of test distribution of average gravimetric water content and bulk density.

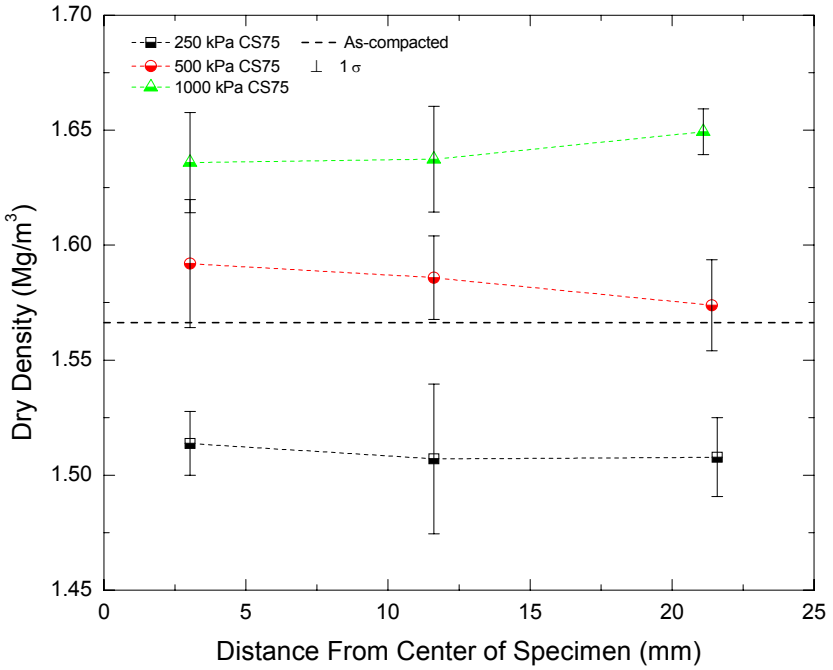

a.

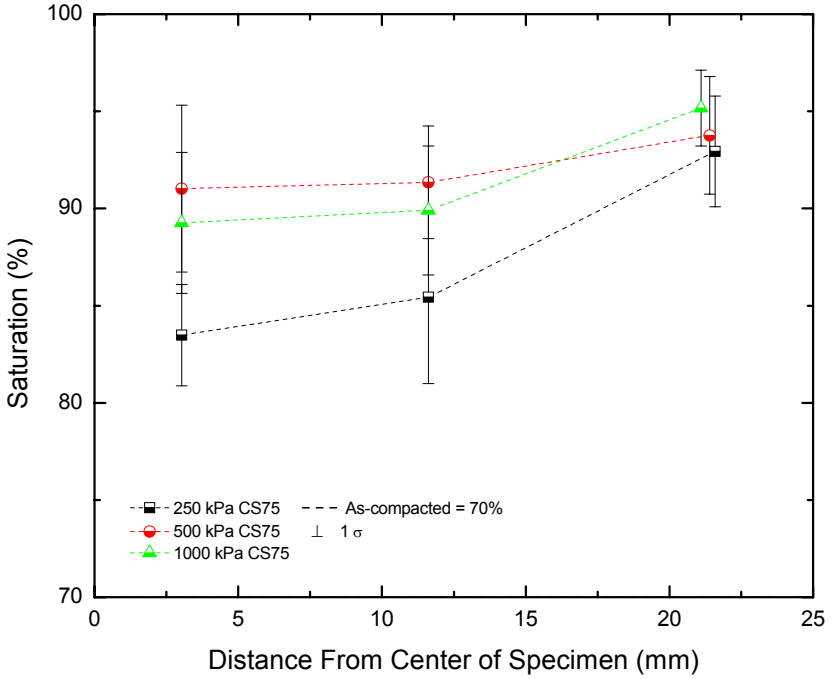

b.

Figure 6.28. Constant stiffness (CS75) summary: end of test distribution of average dry density and saturation.

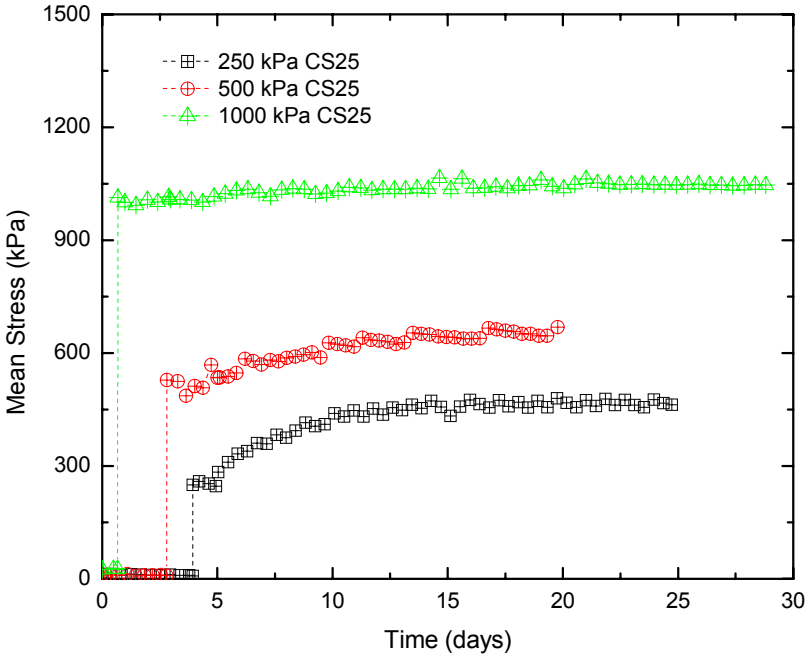

a.

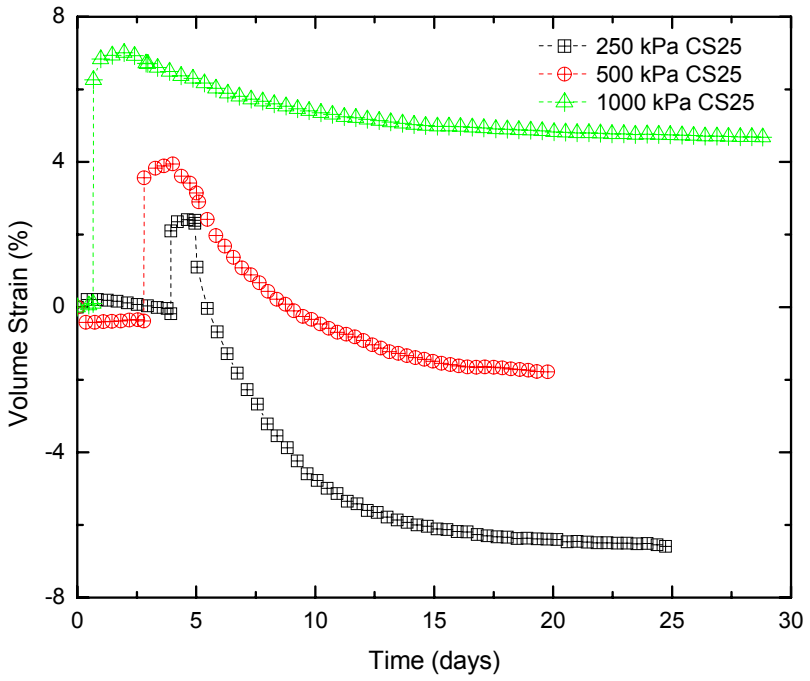

b.

Figure 6.29. Constant stiffness (CS25) summary: mean stress and volume strain versus time.

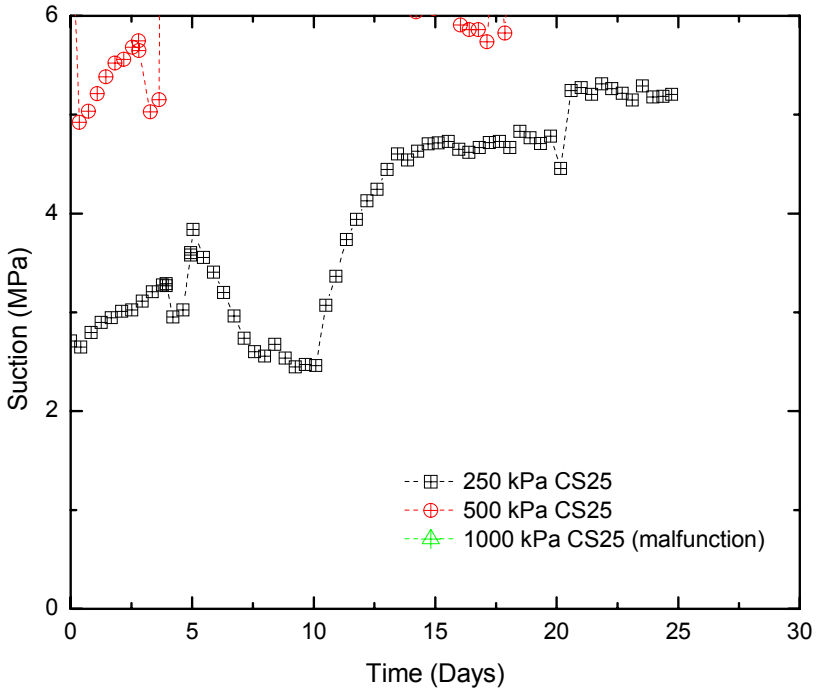

a.

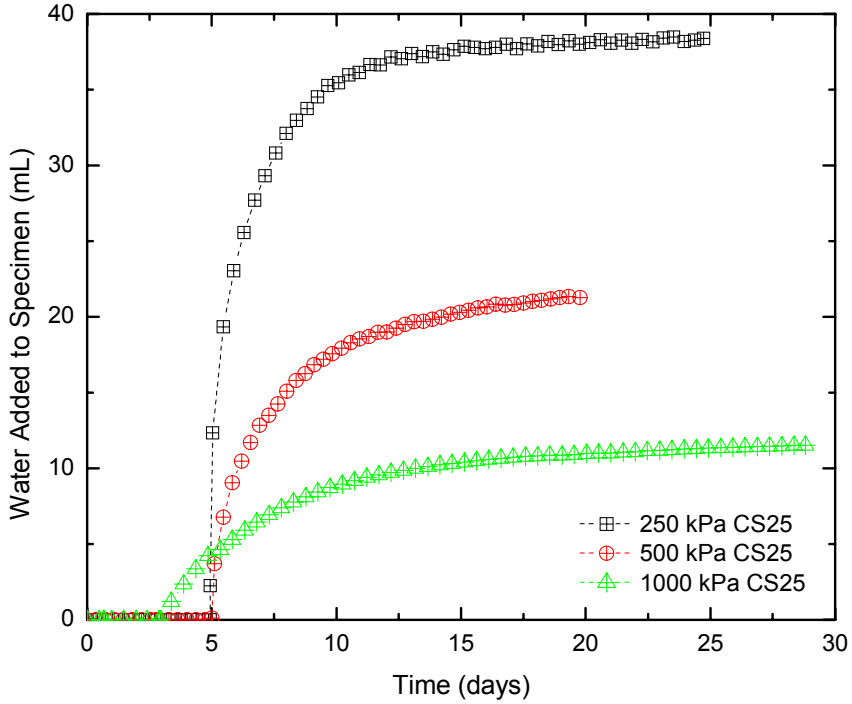

b.

Figure 6.30. Constant stiffness (CS25) summary: suction and water added to specimen versus time.

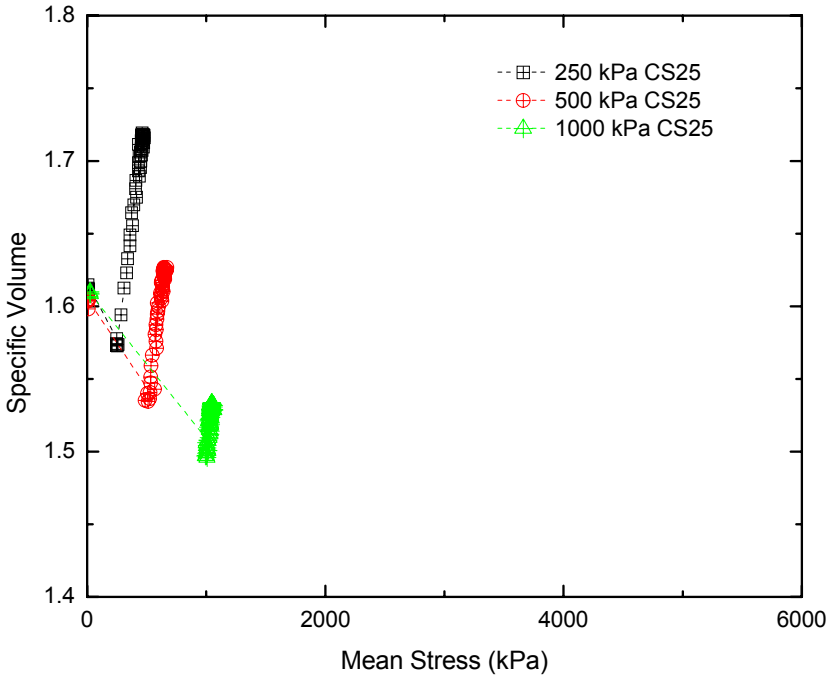

a.

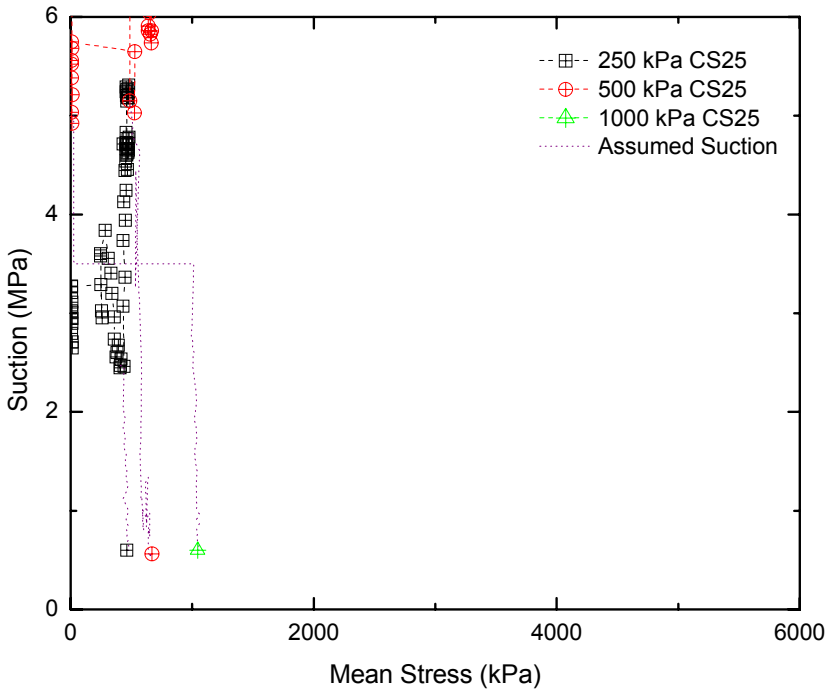

b.

Figure 6.31. Constant stiffness (CS25) summary: specific volume and suction versus mean stress.

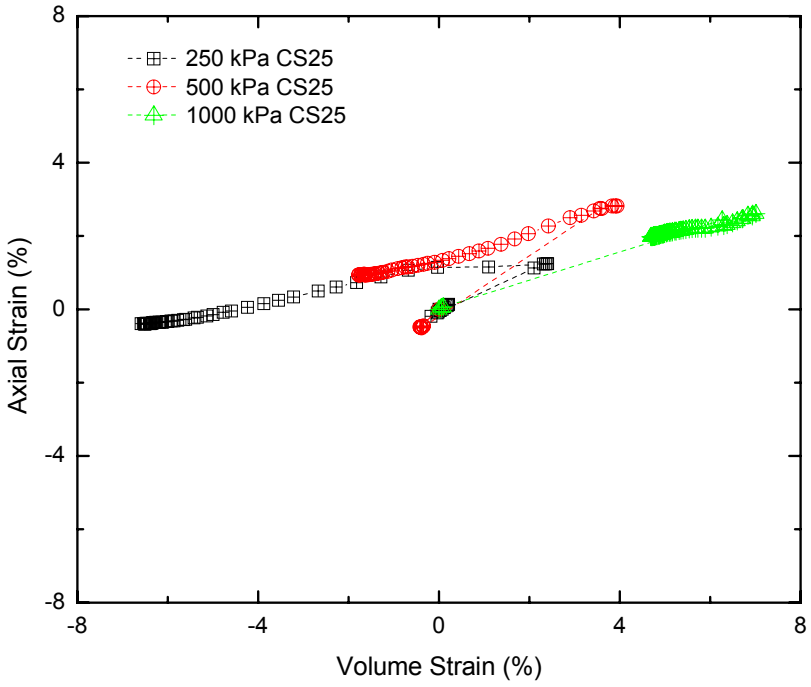

a.

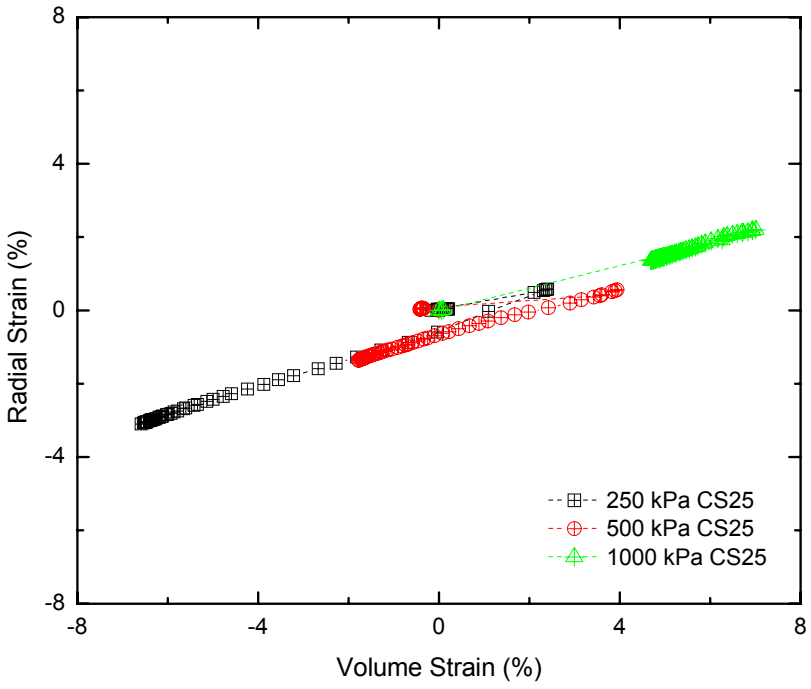

b.

Figure 6.32. Constant stiffness (CS25) summary: axial strain and radial strain versus volume strain.

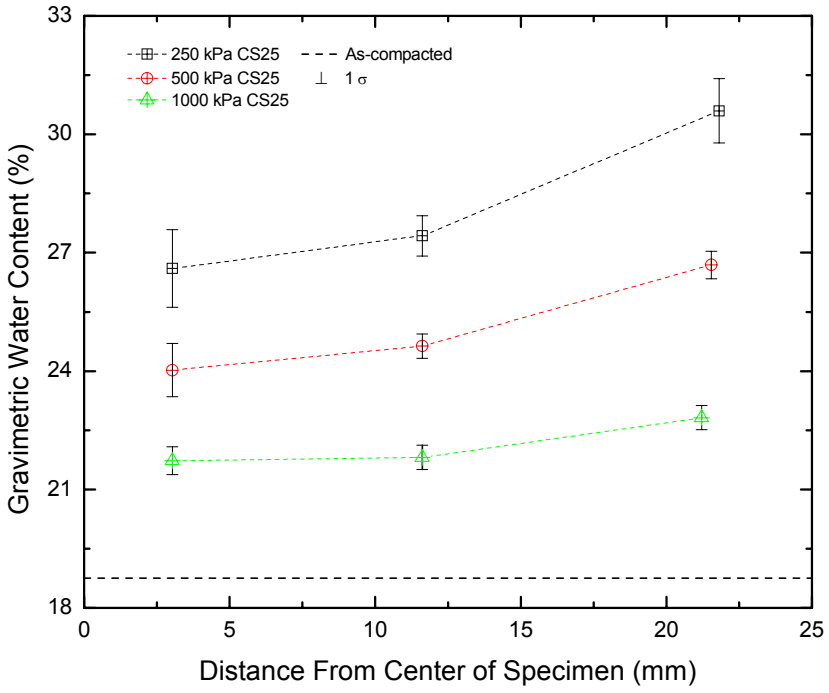

a.

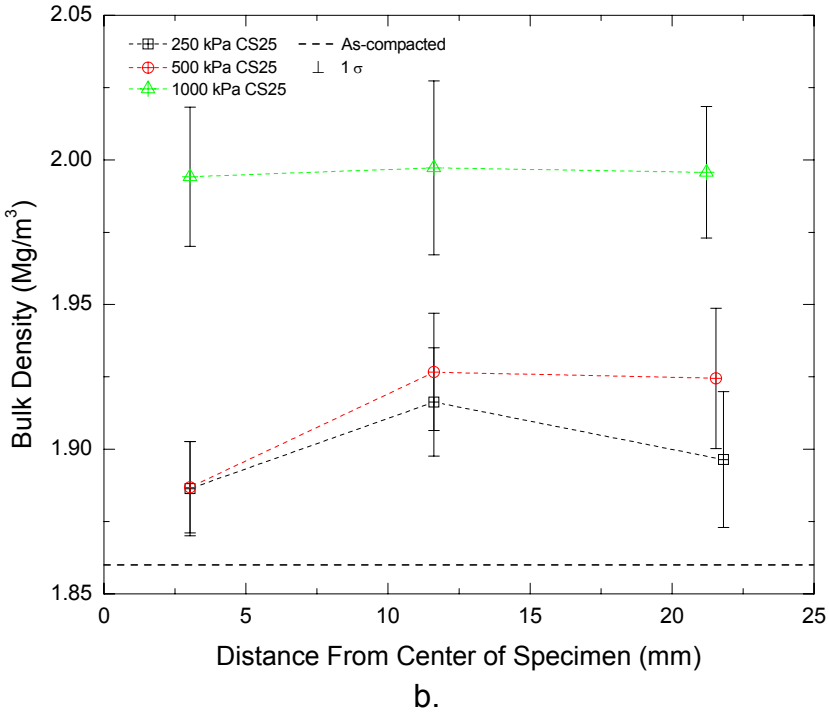

b.

Figure 6.33. Constant stiffness (CS25) summary: end of test distribution of average gravimetric water content and bulk density.

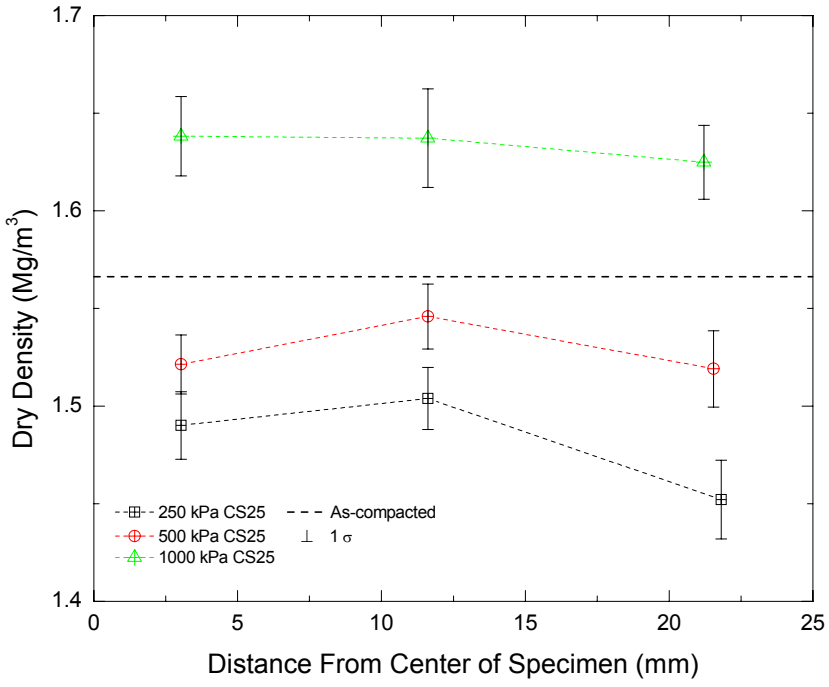

a.

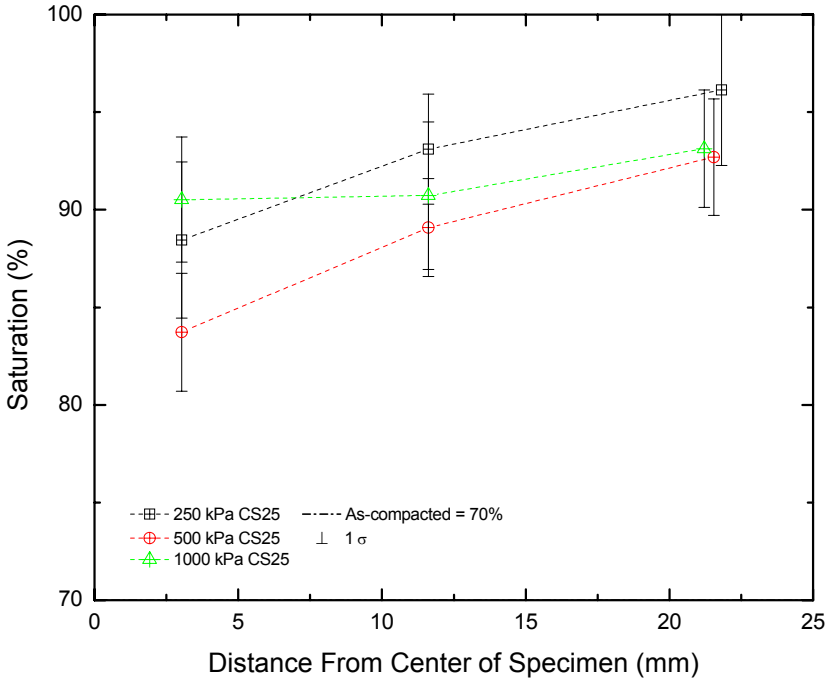

b.

Figure 6.34. Constant stiffness (CS25) summary: end of test distribution of average dry density and saturation.

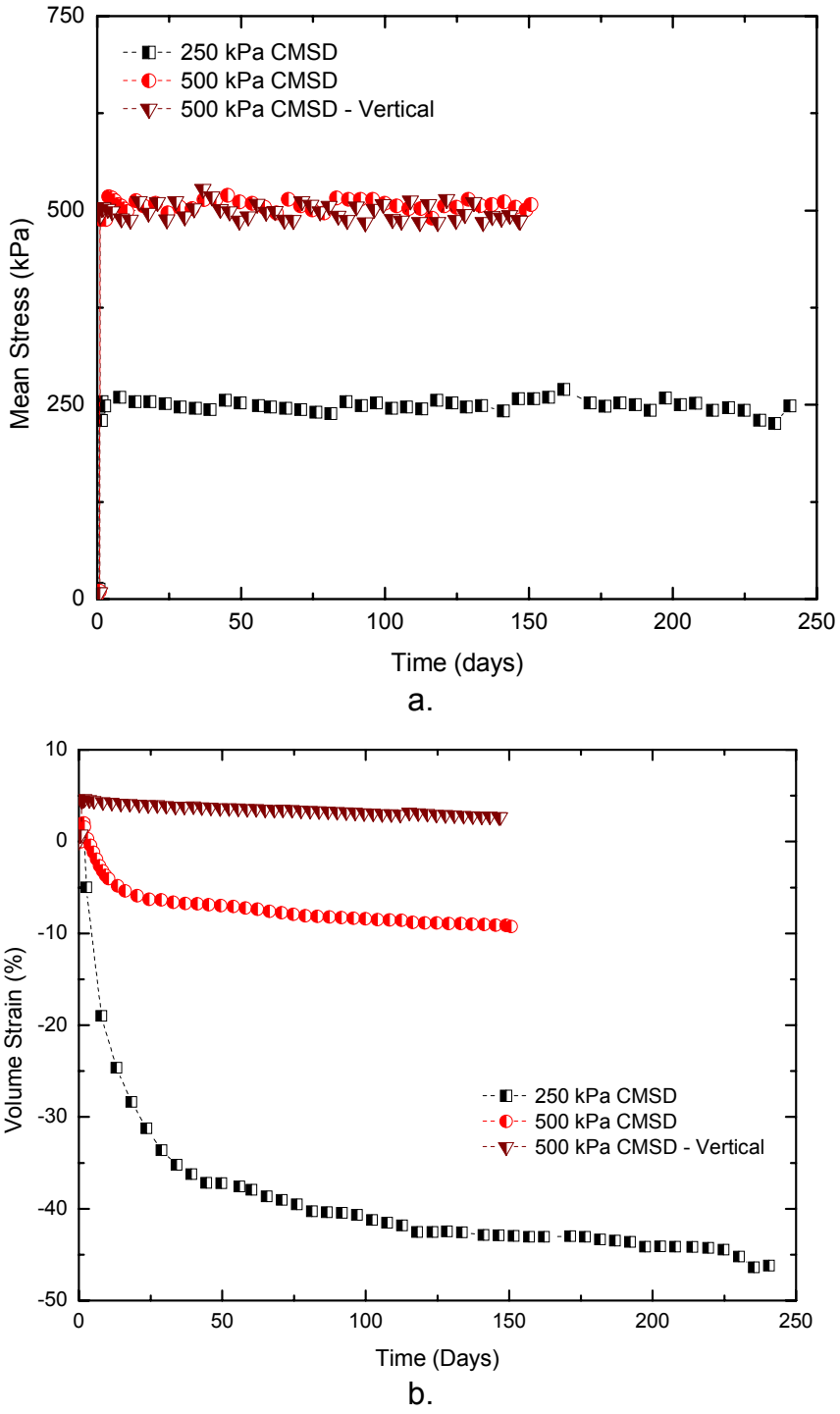

Figure 6.35. Constant mean stress - drained (CMSD) summary: mean stress and volume strain versus time (after Siemens et al. 2006).

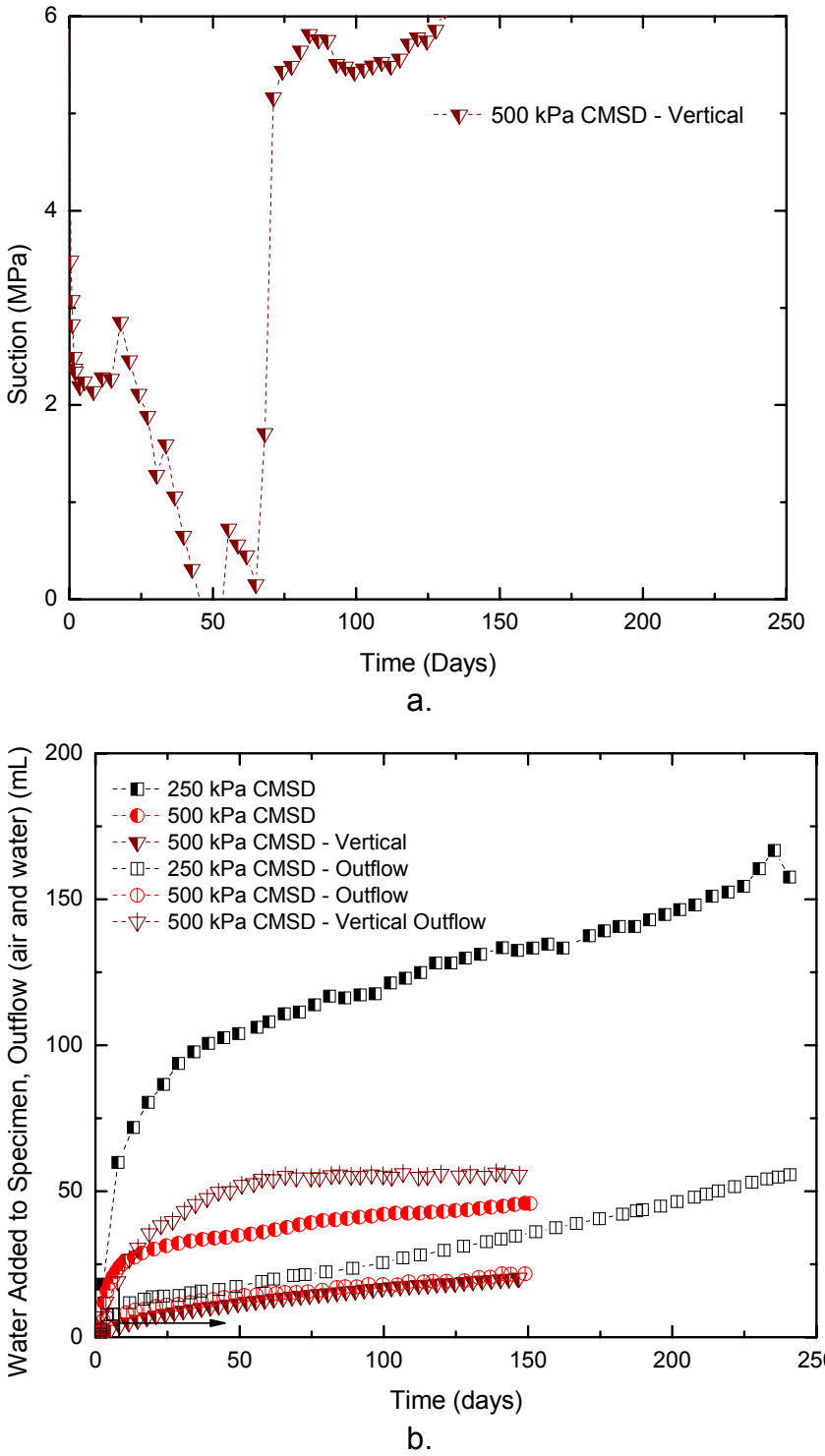

Figure 6.36. Constant mean stress - drained (CMSD) summary: suction and water added to specimen and outflow versus time (after Siemens et al. 2006).

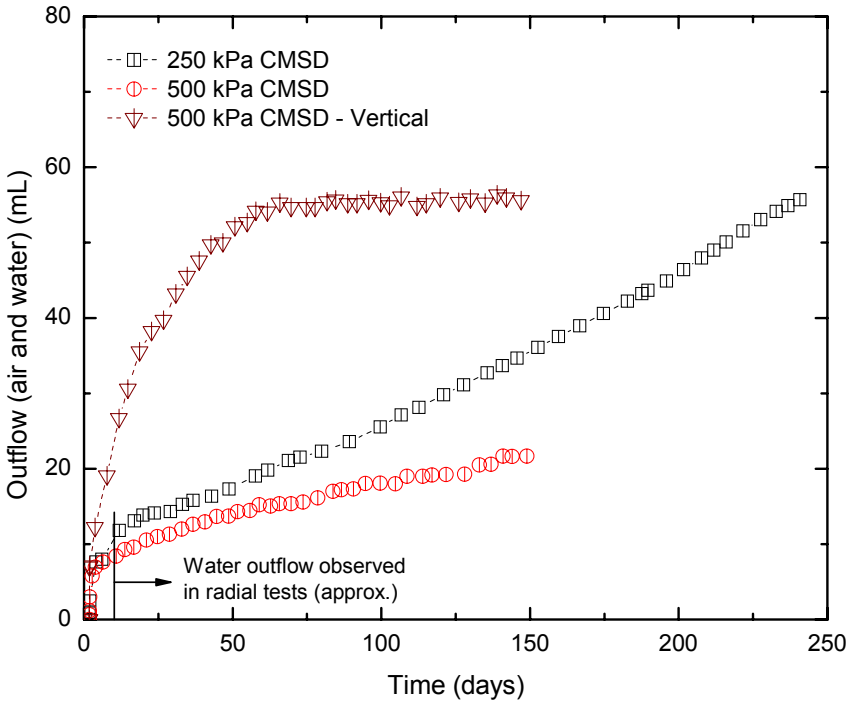

Figure 6.37. Constant mean stress - drained (CMSD) summary: outflow versus time (after Siemens et al. 2006).

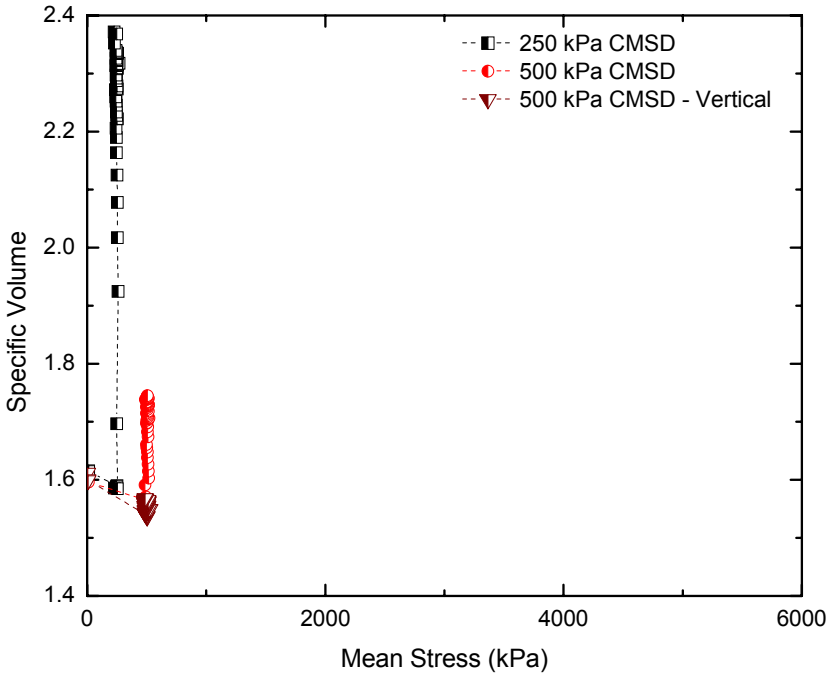

a.

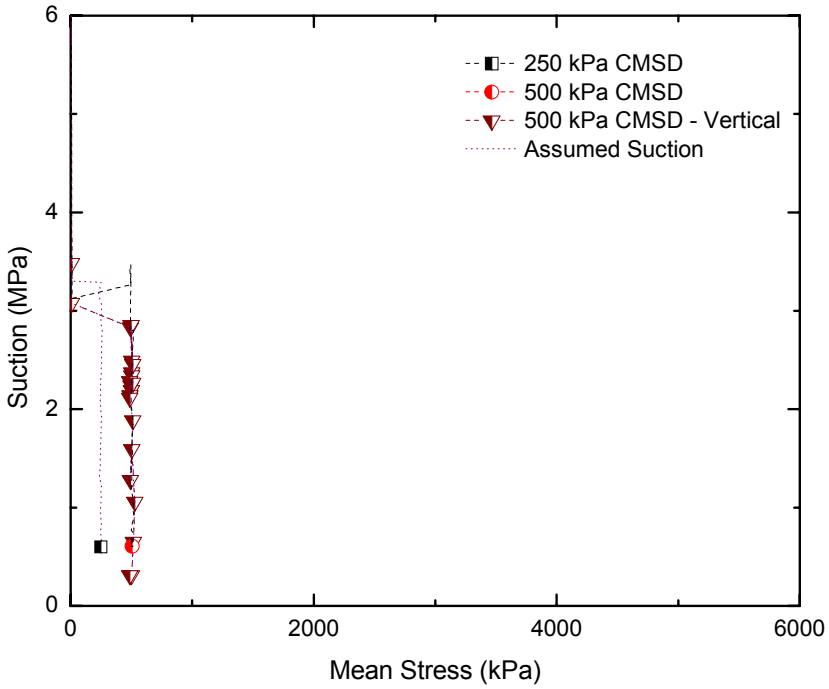

b.

Figure 6.38. Constant mean stress - drained (CMSD) summary: specific volume and suction versus mean stress.

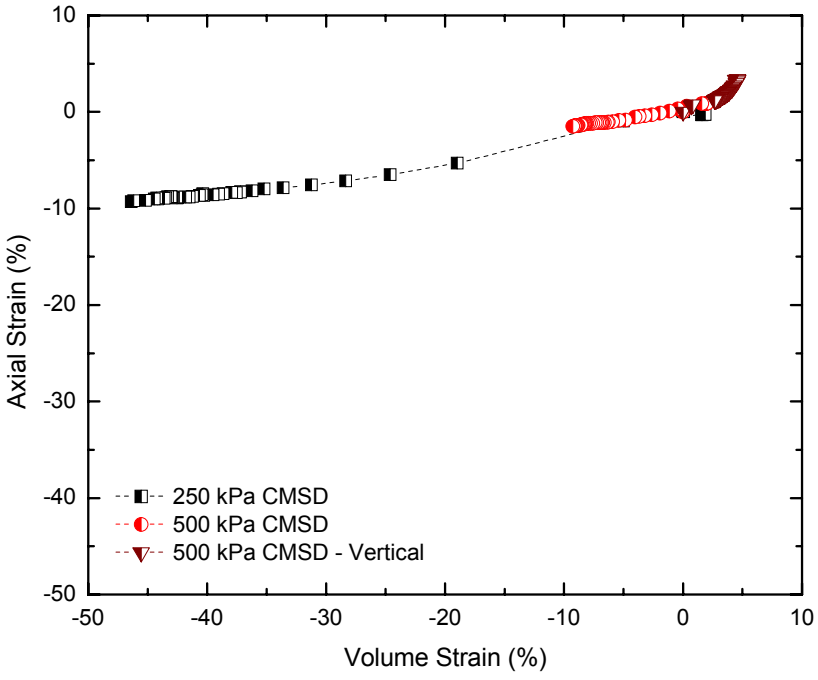

a.

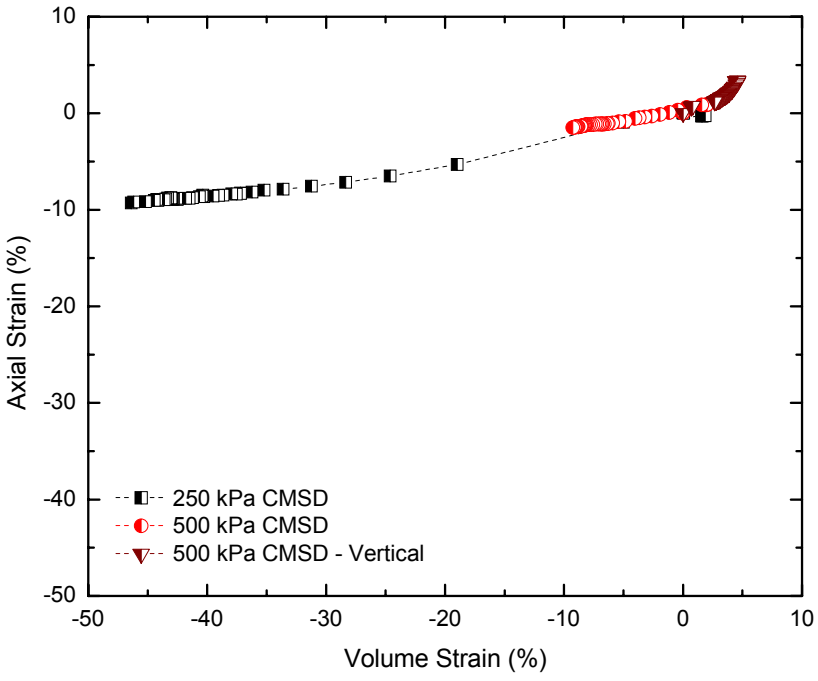

b.

Figure 6.39. Constant mean stress - drained (CMSD) summary: axial strain and radial strain versus volume strain.

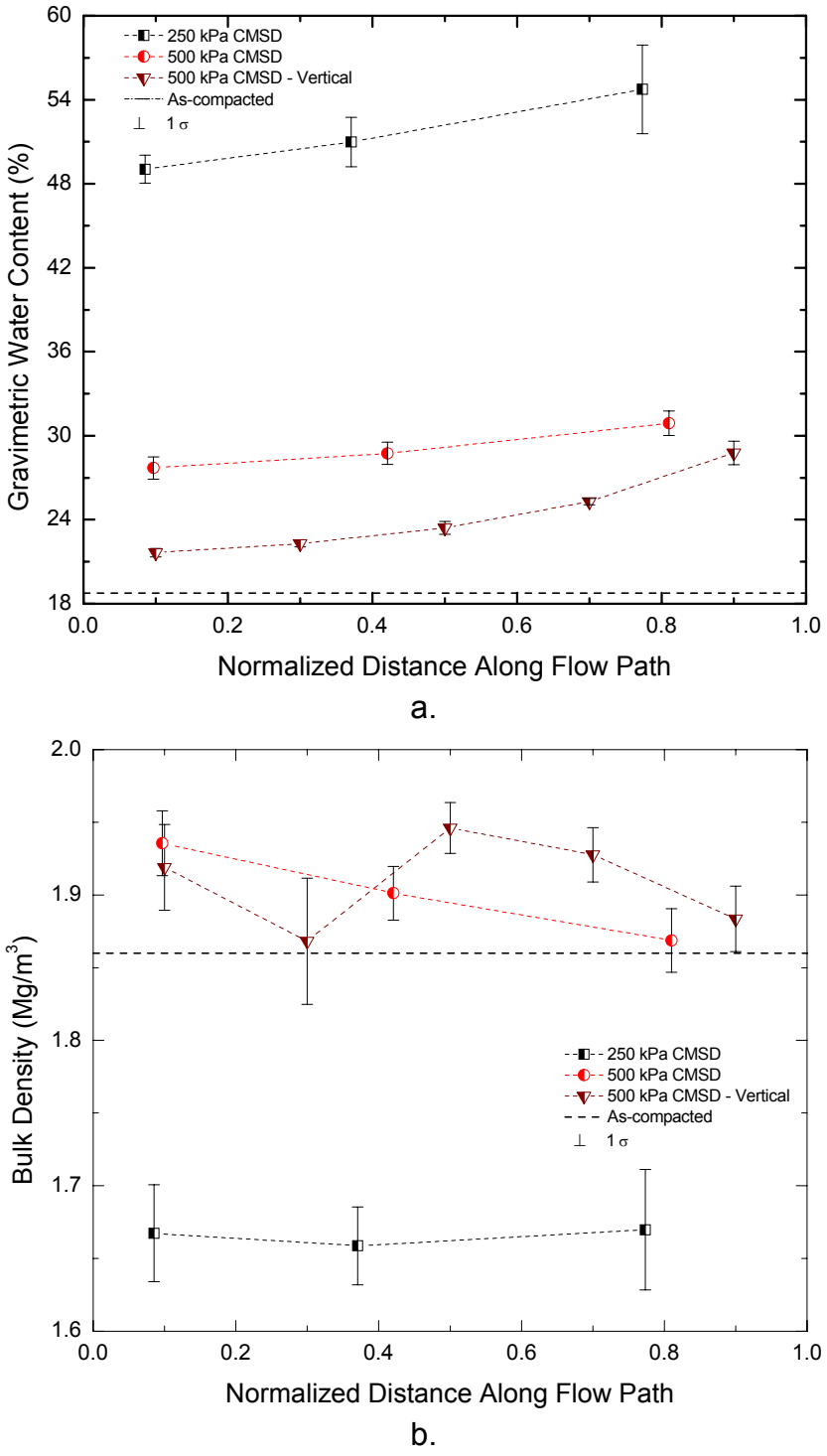

Figure 6.40. Constant mean stress - drained (CMSD) summary: end of test normalized distribution of average gravimetric water content and bulk density (after Siemens et al. 2006).

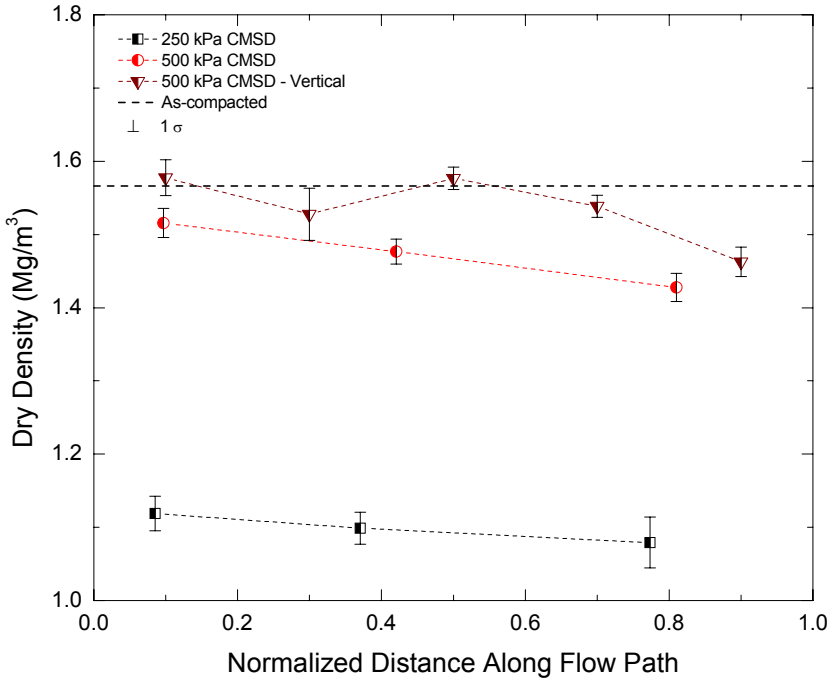

a.

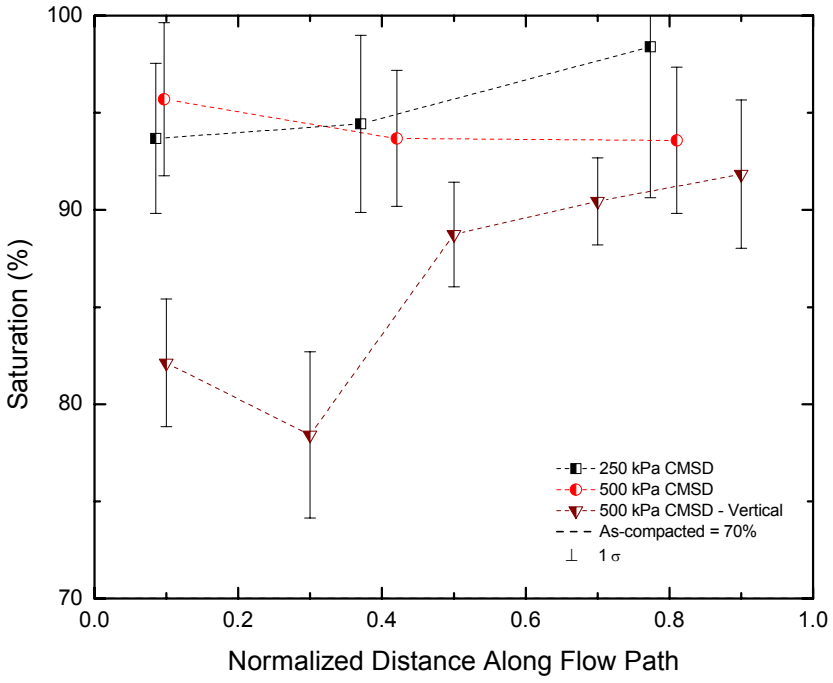

b.

Figure 6.41. Constant mean stress - drained (CMSD) summary: end of test normalized distribution of average dry density and saturation (after Siemens et al. 2006).

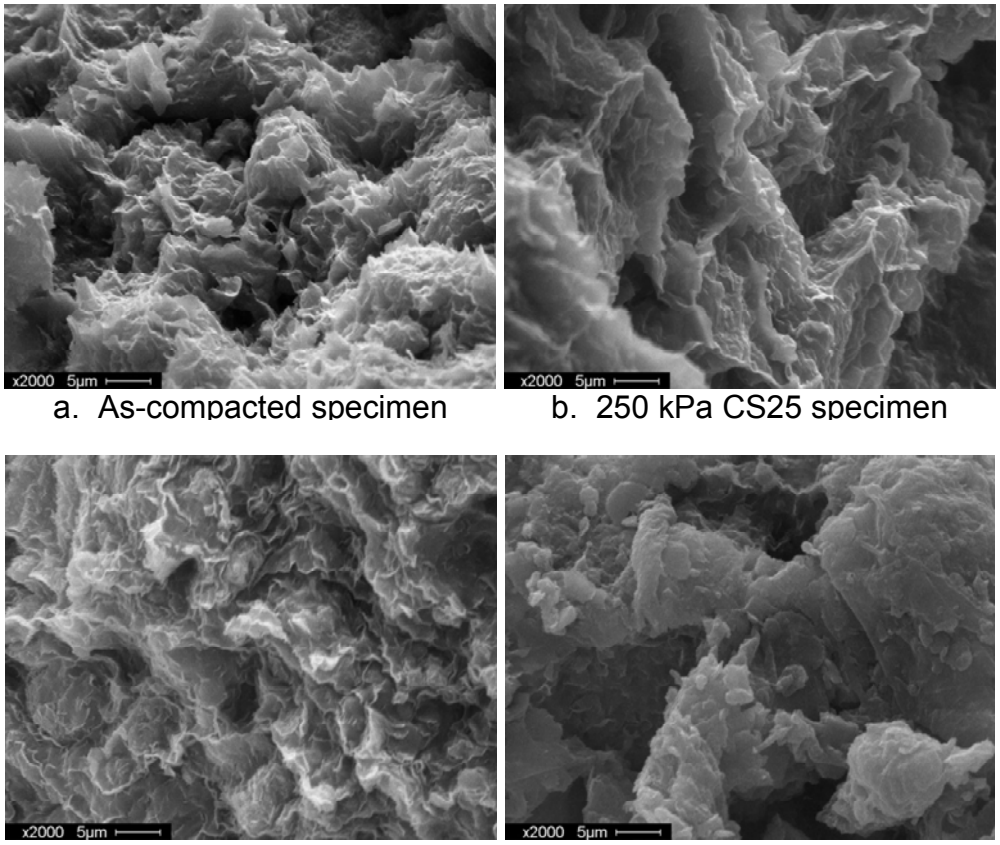

a. As-compacted specimen b. 250 kPa CS25 specimen

c. 1000 kPa CS75 specimen d. 1000 kPa CS25 specimen

Figure 6.42. Scanning Electron Microscopy (SEM) photographs of as-compacted and infiltration specimens.

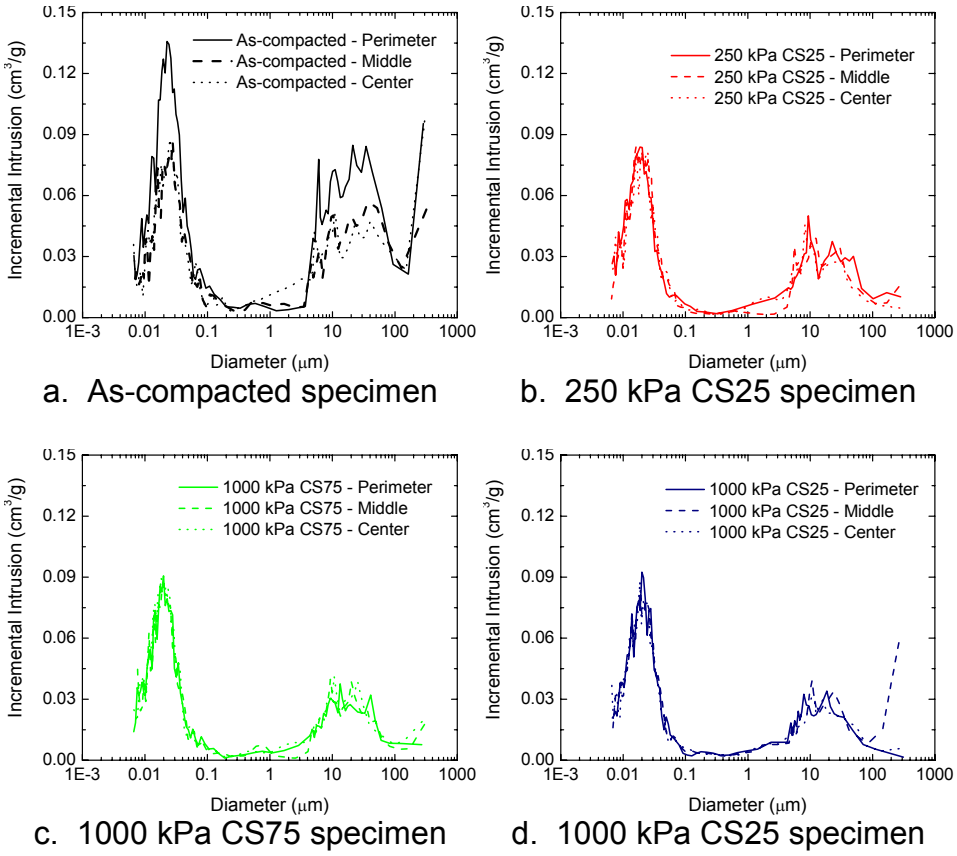

a. As-compacted specimen b. 250 kPa CS25 specimen

c. 1000 kPa CS75 specimen d. 1000 kPa CS25 specimen

Figure 6.43. Mercury Intrusion Porosimetry (MIP) results of as-compacted and infiltration specimens.

CHAPTER 7: DEVELOPMENT OF A CAPILLARY TUBE MODEL FOR FLOW THROUGH SWELLING CLAY[5]

7.1 Introduction

In compacted materials, bulk soil behaviour is the result of mechanisms and behaviours occurring at the pore scale level. Summing up the small scale occurrences results in overall soil behaviour observed at the specimen or field scale. Therefore, by considering and seeking to understand mechanisms that occur at the pore scale, greater understanding of bulk behaviour is possible. In the laboratory phase of this research, water infiltration is applied to an unsaturated swelling clay soil. Changes in water content and density occur during tests as well as alterations to the pore size distribution. Other researchers studying flow through swelling clay observed a decrease in hydraulic conductivity

[5] A combination of this chapter and Chapter 8 will been submitted as:
Siemens, G.A., Blatz, J.A. and Ruth, D. Development of a capillary tube model for swelling soil. Canadian Geotechnical Journal. *In Preparation*.

with increasing water content (Cui et al. 2001, Hoffman et al. 2006). Also, in the models performed to represent the isothermal test, the hydraulic conductivity curve had to be modified to reflect decreasing conductivity with increasing water content (decreasing suction) in order to calibrate against measured final water contents (Thomas et al. 2003). Both of these cases are contradictory to conventional understanding that hydraulic conductivity increases as an unsaturated soil increases saturation (decreases suction). Mechanisms that are occurring at the pore scale and are dominating these bulk soil behaviour mechanisms are not fully understood at this time.

Traditionally in soil mechanics, flow of water through soil is modeled using D'Arcy's Law. Conditions where D'Arcy's Law is valid are limited to those cases where flow is linearly related to the gradient. Network models for flow in porous media represent the pore space of soil with series of pipes and nodes. Laminar two-phase flow through tubes is represented using Hagen-Poiseuille's law. In these types of models, flow is a function of boundary conditions, tube size, and capillary effects. In the new model developed in this research effort, swelling behaviour of the clay is simulated by reducing cross-sectional area as water flows along a tube.

Development of a new capillary tube model is presented in this chapter. The model is used to represent behaviour observed in the laboratory infiltration results presented in Chapter 6. The new capillary tube model is initially filled with

air which is displaced by water entering the tube. Although in the compacted specimens, a water phase is present, a continuous air phase has been observed in the as-compacted state (Anderson 2003) and up to degree of saturation of 92% (Graham et al. 2002) making this initial assumption valid.

The unique feature of this model is that as water contacts the tube, the tube can reduce in cross-sectional area. The physical representation of this feature is the swelling of the clay peds into the macro pore space during liquid infiltration. Water flows both through the interconnected macro pore space and is absorbed into the clay peds. This has been reported previously and was observed in the test specimens where MIP and SEM tests were performed.

Flow area reduction is controlled by the swell rate as an input for the model. The swell rate is the one (1) fitting parameter of the model and it is used to determine the rate at which the main tube reduces in size. It represents the amount of clay particles that are adjacent to the flow path. Increasing the swell rate represents more clay particles and vice versa. A swell rate of zero is used for flow tubes that do not contract and, physically, means the soil would not have a shrink/swell potential. The influence of this parameter is investigated for each model type.

To represent laboratory-scale infiltration tests, different hydraulic boundary conditions are used in the model. This includes having the downstream end of the main tube either open or closed to represent the range of hydraulic boundary

conditions examined in the laboratory tests. A closed tube model that incorporates diffusion of air through the water phase is also investigated. A final model configuration doubles the length of the tube representing movement of water into the laboratory specimen and pushing of air out the periphery.

7.2 Capillary Tube Model Definition

7.2.1 Model Description

Capillary tube models are an application of network theory used to describe flow in porous media. In these types of models, upstream and downstream pressures are applied across a tube or series of tubes and nodes to represent the pore space of a media. A simple single capillary tube model was shown in Figure 2.10. Initially a tube is filled with one (1) fluid and subsequently a second fluid enters the tube and displaces the first. At the interface between the two (2) fluids a capillary pressure exists.

The concept for the new model is a rigid tube lined with bentonite that is initially filled with air as shown in Figure 7.1. Water enters the tube (macro pore size) and displaces the air. As water contacts the bentonite surface around the tube's periphery, the bentonite wall swells radially and reduces the cross-sectional area (to the micro pore size) of the tube to restrict flow. The bentonite is assumed to remain fixed throughout the flow process and movement of bentonite down the length of tube is not considered.

In the laboratory tests that are represented by this model (Chapter 6), radial flow occurs from the perimeter of BSB specimens to the center. The first configuration of the test simply applies water pressure at the perimeter of the specimens and is referred to as an undrained test. The other configuration provides drainage at the center of the specimen and is referred to as a drained test. The capillary tube model captures these configurations having the downstream end of the tube closed or open. In the open configuration, the upstream water pressure and downstream air pressure remain constant for the entire process. In the closed configuration, the upstream water pressure remains constant but as water fills up the capillary tube, the air component compresses and air pressure at the downstream end increases. During undrained laboratory tests, the exact movement of the air phase is unknown. Since no explicit drainage is provided for the air component, air could move through the water phase as a dissolved gas or could be pushed out the face of the specimen as water infiltrates. The second concept would have water entering some pores on the periphery of the specimen at the same time as air exits the periphery through other pores. To investigate these phenomena, two (2) other additions are made to the model. In one, diffusion of air through the water phase is considered using a closed end tube. The other configuration is a double length model that is twice as long as the other models. This model represents a flow path from the perimeter to the center and back to the perimeter of the specimen. Since the upstream and downstream ends of the long-tube model are representing the

periphery of the specimen, the same pressure is applied at both ends in the model. Forward water movement occurs due to the capillary pressure that exists at the water-air interface.

The capillary tube model created for BSB is shown in Figure 7.2. In this model, a main tube is surrounded by peripheral tubes that simulate the swelling nature of BSB. As water flows down the main tube, it also flows into the open-ended peripheral tubes. This represents water transfer through flow paths and adsorption into the surrounding clay peds in BSB (Figure 2.2). In both cases water is assumed to enter both the main tube and peripheral tubes with no restriction based on the capillary pressure at the entrance. In the laboratory tests, the initial suction of the specimens is less than that at the residual water content so water will enter the perimeter when water pressure is applied. Water is also absorbed by the clay peds, which have been reported to be saturated (Gens and Alonso 1992). Since they are previously saturated, no capillary pressure needs to be overcome for water to enter the peripheral tubes. Conservation of volume (constancy of flow) is maintained as the volume of water that flows into the peripheral tubes for a particular section equals the reduction of volume (diameter) in that same section. Reduction in cross-sectional area of the main tube is controlled by the swell rate as an input value. Swell rate is defined as the number of peripheral tubes per unit length (μm) of main tube. Increasing the number of peripheral tubes is similar to increasing the swelling clay content of a material as it provides for more area for flow into the peripheral tubes. This

corresponds to a quicker reduction in flow area down the main tube. To limit main tube size reduction, a minimum diameter of main tube is set in the model.

7.3 Capillary Tube Model Derivation

7.3.1 Two-Phase Flow Derivation

Two-phase flow in a capillary tube was derived by Bartley and Ruth (1999) and their derivation is repeated here. Figure 2.10 shows a generic tube with Fluid 'a' displacing Fluid 'b' due to a pressure drop imposed across the tube (p_a-p_b). This problem can be solved exactly using [2.7] by assuming the flow rates of the two (2) fluids are the same. That is

$$q = \frac{\pi\delta^4}{128\mu_a l_a}(p_a - p_s) = \frac{\pi\delta^4}{128\mu_b(L - l_a)}(p_s + p_c - p_b) \qquad [7.1]$$

where

q = flow rate of Fluid 'a' = flow rate of Fluid 'b',

δ = diameter of the tube,

μ_a = viscosity of Fluid 'a',

l_a = location of the Fluid 'a' – Fluid 'b' interface,

p_a = upstream pressure,

p_s = pressure just upstream of interface,

μ_b = viscosity of Fluid 'b',

L = total length of tube, and

p_b = downstream pressure.

Solving [7.1] for p_s gives

$$p_s = \frac{p_a \mu_b (L - l_a) - (p_c - p_b)\mu_a l_a}{\mu_a l_a + \mu_b (L - l_a)} \qquad [7.2]$$

Combining [7.1] and [7.2] and then solving for the flow rate results in

$$q = \frac{\pi \delta^4}{128}\left(\frac{p_a + p_c - p_b}{\mu_a l_a + \mu_b (L - l_a)}\right) \qquad [7.3]$$

To get an equation for the water-air interface, l_a, as a function of time, conservation of mass is assumed for

$$\frac{dl_a}{dt} = \frac{4q}{\pi \delta^2} \qquad [7.4]$$

Combining [7.3] and [7.4] results in

$$\frac{dl_a}{dt} = \frac{\delta^2}{32}\left(\frac{p_a + p_c - p_b}{\mu_a l_a + \mu_b (L - l_a)}\right) \qquad [7.5]$$

Because the tube is initially be filled with air, at t = 0, l_a = 0. Integrating [7.5] gives

$$2(\mu_a - \mu_b)l_a^2 + 4\mu_b L l_a = \frac{\delta^2(p_a + p_c - p_b)}{8}t \qquad [7.6]$$

and solving for l_a results in

$$l_a = \frac{-4\mu_b L + \sqrt{16\mu_b^2 L^2 + (\mu_a - \mu_b)\delta^2(p_a + p_c - p_b)t}}{4(\mu_a - \mu_b)} \qquad [7.7]$$

Substituting the following equation for capillary pressure

$$p_c = \frac{4\sigma\cos(\theta)}{\delta} \qquad [7.8]$$

where

σ = surface tension, and

θ = contact angle

into [7.5] gives an equation for the instantaneous speed of the interface of

$$\frac{dl_a}{dt} = \frac{\delta^2}{32}\left(\frac{p_a - p_b}{\mu_a l_a + \mu_b(L - l_a)}\right) + \frac{\delta}{8}\left(\frac{\sigma\cos(\theta)}{\mu_a l_a + \mu_b(L - l_a)}\right) \qquad [7.9]$$

This is the equation for a single tube and is used in this model for flow through the peripheral tubes. For flow down the main tube, a serial tube model is used so that the diameter of individual sections can change with time as they contact water. Generalizing the equation for flow in a single tube gives equations for the flow from the upstream end to the interface and from the interface to the downstream end to give

$$q = \frac{\pi}{128\mu_a}(p_a - p_s)\left(\frac{l_a}{\delta_s^4} + \sum_{l=1}^{l=N_b^-}\frac{L_l}{\delta_l^4}\right)^{-1} \qquad [7.10]$$

and

$$q = \frac{\pi}{128\mu_b}(p_s + (p_c)_s - p_b)\left(\frac{L_s - l_a}{\delta_s^4} + \sum_{l=N_b^+}^{l=N_b}\frac{L_l}{\delta_l^4}\right)^{-1} \qquad [7.11]$$

where

δ_s – diameter of the tube in which the interface is located,

L_s – length of the tube in which the interface is located,

$(p_c)_s$ – capillary pressure in the tube in which the interface is located,

N_b – total number of serial sections,

N_b^- - number of tubes upstream of the interface, and

N_b^+ - number of tubes downstream of the interface.

Equations [7.10] and [7.11] may be solved for p_s because the flow rate is constant along the tube. This results in

$$p_s = \frac{p_a D_\Sigma \mu_b - ((p_c)_s - p_b) U_\Sigma \mu_a}{\mu_a U_\Sigma + \mu_b D_\Sigma} \qquad [7.12]$$

where

$$U_\Sigma = \frac{l_a}{\delta_s^4} + \sum_{l=1}^{l=N_b^-} \frac{L_l}{\delta_l^4} \qquad [7.13]$$

$$D_\Sigma = \frac{L_s - l_a}{\delta_s^4} + \sum_{l=N_b^+}^{l=N_b} \frac{L_l}{\delta_l^4} \qquad [7.14]$$

Combining equations [7.10], [7.11], [7.12], [7.13], and [7.14] results in an equation for flow rate of

$$q = \frac{\pi}{128} \frac{\left(p_a - p_b + (p_c)_s\right)}{\mu_a U_\Sigma + \mu_b D_\Sigma} \qquad [7.15]$$

Again applying the assumption of conservation of mass [7.4] leads to the expression for the instantaneous speed of the interface as

$$\frac{dl_a}{dt} = \frac{1}{32\delta_s^2} \left(\frac{p_a + (p_c)_s - p_b)}{\mu_a U_\Sigma + \mu_b D_\Sigma} \right) \qquad [7.16]$$

This is the equation used at each time step in the model to calculate the speed of the water-air interface. It directly solves for the progression of the water-air interface (inflow) at each step based on the assumption of equal flow rates for air and water.

7.3.2 Air Diffusion Derivation

Some closed tube models incorporated diffusion of air through the water phase. The air pressure just downstream of the water-air interface is used as the boundary condition and the water is assumed to have no air dissolved in it initially. The upstream boundary condition is set to zero concentration simulating a large reservoir.

For the case of air diffusing through water, the concentration is calculated using the density of air. Therefore, [2.6] becomes

$$\frac{m}{t} = DA\Delta\rho \qquad [7.17]$$

and density is calculated by

$$\rho = \frac{P\omega}{RT} \qquad [7.18]$$

where

A – cross-sectional area,

P – gas pressure at interface,

ω – molecular mass of air,

R – universal gas constant, and

T – absolute temperature.

7.4 Model Computer Program

The computer code for this model is written in C++. The code is attached in the Appendix and the algorithm is described below. Initially the program inputs initial parameters from a text file including geometry, pressure boundary conditions and fluid properties. These parameters are used to calculate the constraints used by the model.

At each time step the program first calculates the pressure distribution along the length of the tube followed by the speed at which the interface is moving during the time step. For closed-end models, the mass of air is known as well as initial volume. Assuming constant temperature, average air pressure followed by downstream pressure is calculated. A constant displacement criterion is used to calculate the time step increment. Following calculation of the time step increment, diffusion of air through water is determined. Diffusion is modeled using a constant mass flow of free air into the water component at each time step. This process usually works on a considerably longer time scale compared

to flow of water down an open-ended tube depending on the main tube diameter. Two (2) algorithms were created to deal with the situations that arise during diffusion. The first algorithm is used when the interface velocity is positive (moving forward) and the other when it is negative. Negative interface velocity calculations occur when the downstream air pressure is greater than the upstream pressure. Sub-time steps are required because the amount of free air that moves into the water phase is relatively small compared to the total mass. When the air-water interface velocity is positive, diffusion sub-time steps are completed until they equal the total time step. When the interface velocity is negative, it is assumed that the interface can not move forward until free air diffuses into the water phase and the downstream mass (pressure) is reduced. The required mass of air to be removed for the interface velocity to be positive is calculated and diffusion sub-time steps are continued until this is achieved. Finally, flow into the peripheral tubes is determined as well as reduction in area of the main tube.

Relative magnitudes have a major impact in this model. For example, the gas removed at each gas time sub step can be less than the significant figures carried by the total mass of free gas variable. As such, the amount of free air lost at each sub time step is accounted for as a separate variable until it is substantial enough to be recorded in the total amount of free air. A similar situation occurs with diffusion time steps. During diffusion models, the length of an individual time step can be less than the last decimal place captured by the total time variable.

Again the time step lengths are accounted for using a separate variable and once their magnitude is great enough, it is added to the total time.

Output from this program includes flow in the main tube, main tube diameter, flow in the peripheral tubes, and density of air (in models considering diffusion). The model contains arrays that store the current value of each output value and periodically copied them to a matrix. After completion of the model, output matrices are copied to an Excel spreadsheet that displays the model parameters as well as distributions throughout the model. A typical output is shown in Figure 7.3.

7.5 Model Parameters

7.5.1 Properties of BSB

A capillary tube model requires relevant properties of the natural material in order to represent its pore geometry. For BSB, tube diameters were determined from Mercury Intrusion Porosimetry (MIP) tests performed on BSB specimens (Wan 1996). A plot of pore size distribution for as-compacted BSB specimens as well as a conceptual schematic of the proposed capillary model is shown in Figure 2.2. As described previously BSB has a strongly bimodal pore size distribution centered at approximately 10-20 μm (macro or inter ped pores) and 0.01-0.02 μm (micro or intra ped pores). In this material, the clay forms groups of clay particles known as peds as presented schematically in Figure 2.2 and

Figure 2.3. This is due to the mixing and compaction process during preparation. Due to the greater pore size water transfer generally occurs through the macro pores. During flow through the macro pores, water is taken up by the clay peds resulting in swelling. In a constant volume situation the overall volume remains constant. Ped expansion then reduces the distance between peds resulting in collapse of the macro porosity. Reduction in area for flow reduces the hydraulic conductivity of the material despite increases in water content (Cui et al. 2001, Hoffman et al. 2006). During liquid infiltration on BSB specimens, the bimodal distribution of pores is likely reduced to a unimodal distribution but the final pore size is unknown.

In the capillary tube model, the main tube represents flow tubes between peds. As water flows along its length, the cross-sectional area of the main tube is reduced restricting flow. Reduction in area continues until a specified diameter is reached. For the model, representative values are chosen for the macro pores, micro pores and final pore size distribution. Sensitivity analyses are summarized on all geometric parameters as well as swell rate to determine their impact on performance of the model.

The length of the main tube is taken from the configuration of the laboratory infiltration tests described in Chapter 4 and Chapter 5. In this test, specimens are subjected to radial infiltration from perimeter to center as shown in Figure 4.2. Upstream and downstream boundary conditions are known as water pressure is

applied at the perimeter and suction (negative pore pressures) is measured at the center of the specimen. For the capillary tube model, the radius of BSB specimens is 25 mm however tortuosity must also be considered. In tests, flow does not occur down a straight tube and so a reasonable factor of 1.6 (Ruth 2005, private communication) was estimated and assumed for tortuosity leading to a main tube length of 40 mm.

Peripheral tube diameter is chosen from the micro pore sizes shown in Figure 2.2. When the peripheral tubes are full, the main tube is at its minimum diameter. The length of peripheral tube in the model is a function of swell rate, peripheral tube diameter, initial main tube diameter and the minimum main tube diameter. The length of peripheral tubes is calculated by dividing the total volume reduction of the main tube by the swell rate multiplied by the area of one (1) peripheral tube. Since a wide range of swell rates and tube geometries can be analyzed by this model, it is recognized that some physically impossible scenarios can arise. When swell rate is quite low, the peripheral tubes are extremely long while with very high swell rates, that number of peripheral tubes could not physically be attached around the main tube due to its size. Another consideration is that in the physical test, radial flow is imposed occurring from the perimeter to center of specimens. Therefore total flow area reduces as the water front moves radially toward the center. Reduction in total flow area cannot be captured by a single tube of initially constant cross-sectional area and is recognized as a limitation in this model. The focus of network models such as

capillary tube models is to understand modes of behaviour that occur in physical tests (Fatt 1956) so these irregularities are accepted as a limitation. The focus of this model is to understand flow down the main tube and not attempting to represent seepage into the peds in which consideration of the physics of flow should be taken.

Other parameters required for the capillary tube model include boundary conditions and fluid properties. Boundary conditions (upstream and downstream pressures) were chosen based on the laboratory tests. Absolute pressures for upstream and downstream were imposed at 301.3 kPa and 101.3 kPa respectively (200 kPa and 0 kPa barometric pressure). For undrained tests this only represents initial conditions. As the gas is compressed the downstream pressure increases. Viscosities for water and gas at a temperature of 25 ^{o}C are 0.895×10^{-3} N-s/m^2 and 1.8245×10^{-5} N-s/m^2 (Tuma 1976) respectively. Water surface tension of 72.0×10^{-3} N/m (Kaye and Laby 1973) was also used for all models. A contact angle for BSB of 16.1^{o} was taken from Chenu et al. (2000) who studied wettability of clay as a function of organic content. The organic content of BSB was taken as zero since no organic material is added during the mixing process. The contact angle was extrapolated from a linear regression of their data. It is considered a best-estimate for contact angle and is reasonable considering the type of material.

7.6 Calibration/Validation

As each step of complexity was added to the model, calibration with standard solutions was performed. This section summarizes calibration/validation performed on the flow and diffusion calculations.

7.6.1 Flow

Flow rates for constant diameter tube models were checked with hand calculations and compared with flow predicted from [7.9] to ensure the program was performing accurate calculations. The comparison is shown in Figure 7.4 for three (3) different diameters of main tube. Theoretical movement of the water-air interface is plotted with lines and the model output is shown using symbols. As shown in Figure 7.4, the symbols plot directly on top of the theoretical predictions. This shows that the model is performing accurate calculations throughout and agreeing with theory. Flow into peripheral tubes was also confirmed through hand calculations.

7.6.2 Diffusion

Diffusion checks consisted of creating a spreadsheet that simulated diffusion of air through a column of water using [7.17] and comparing it to the capillary tube model output with constant diameter (no swell). At the boundary between the water and air a constant air density was applied equal to density of air created by the summation of the upstream water pressure and the capillary pressure. This simulates the time in the capillary tube model when diffusion dominates forward progression of the water-air interface. In the model, the time prior to building up

of air pressure is negligible compared to amount of time after. Comparison of air density versus distance to the water-air interface for the capillary tube model and the theoretical relationship is plotted in Figure 7.5. For ease of comparison, data was set so that the water-air interface is at the right side of the graph for all series plotted. As time progresses air diffuse through the water phase as shown in Figure 7.5. Similar times are plotted and comparison shows the capillary tube model is accurately calculating diffusion of air through the water component.

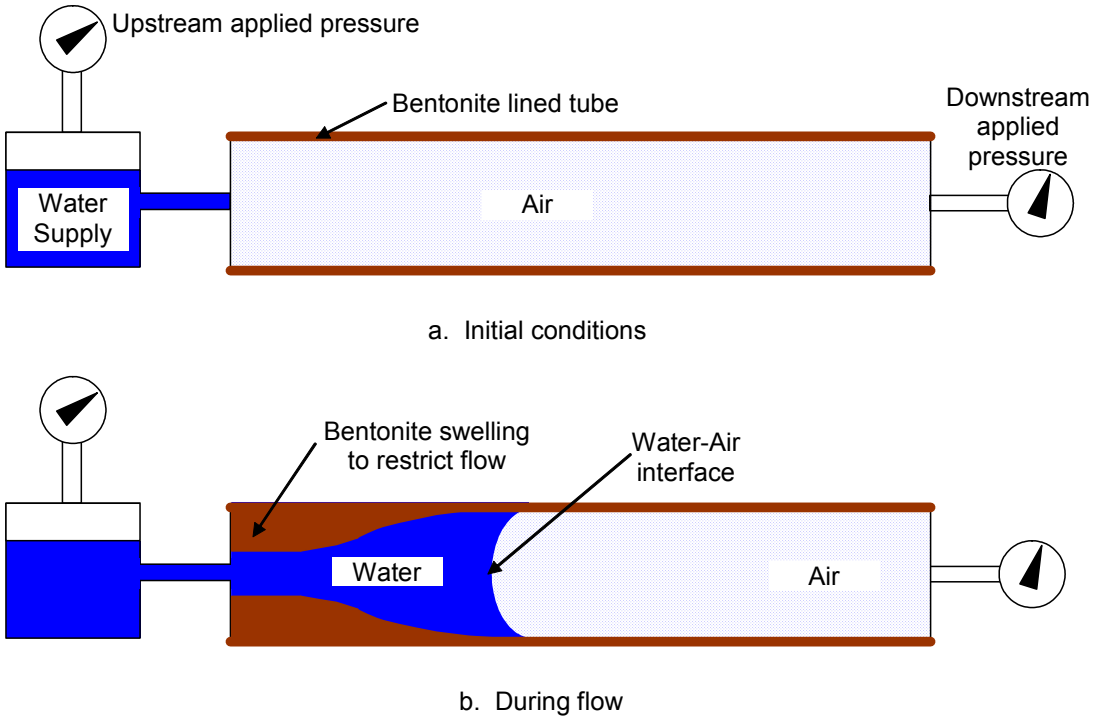

Figure 7.1. Conceptual capillary tube model for BSB.

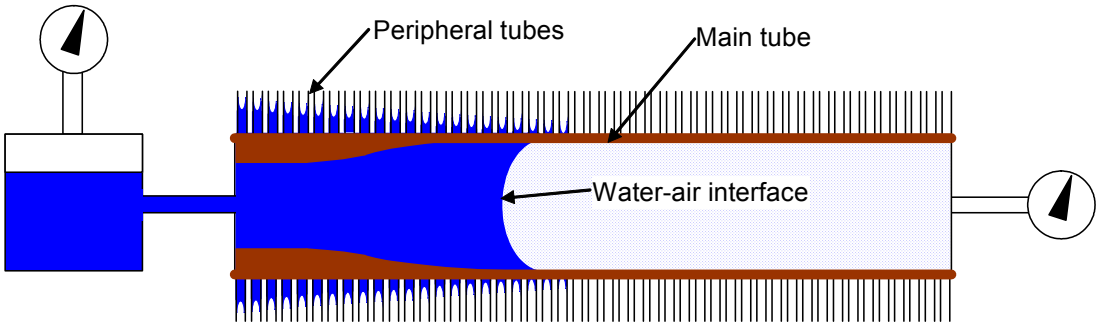

Figure 7.2. Capillary tube model for expansive soil showing swell mechanism using peripheral tubes.

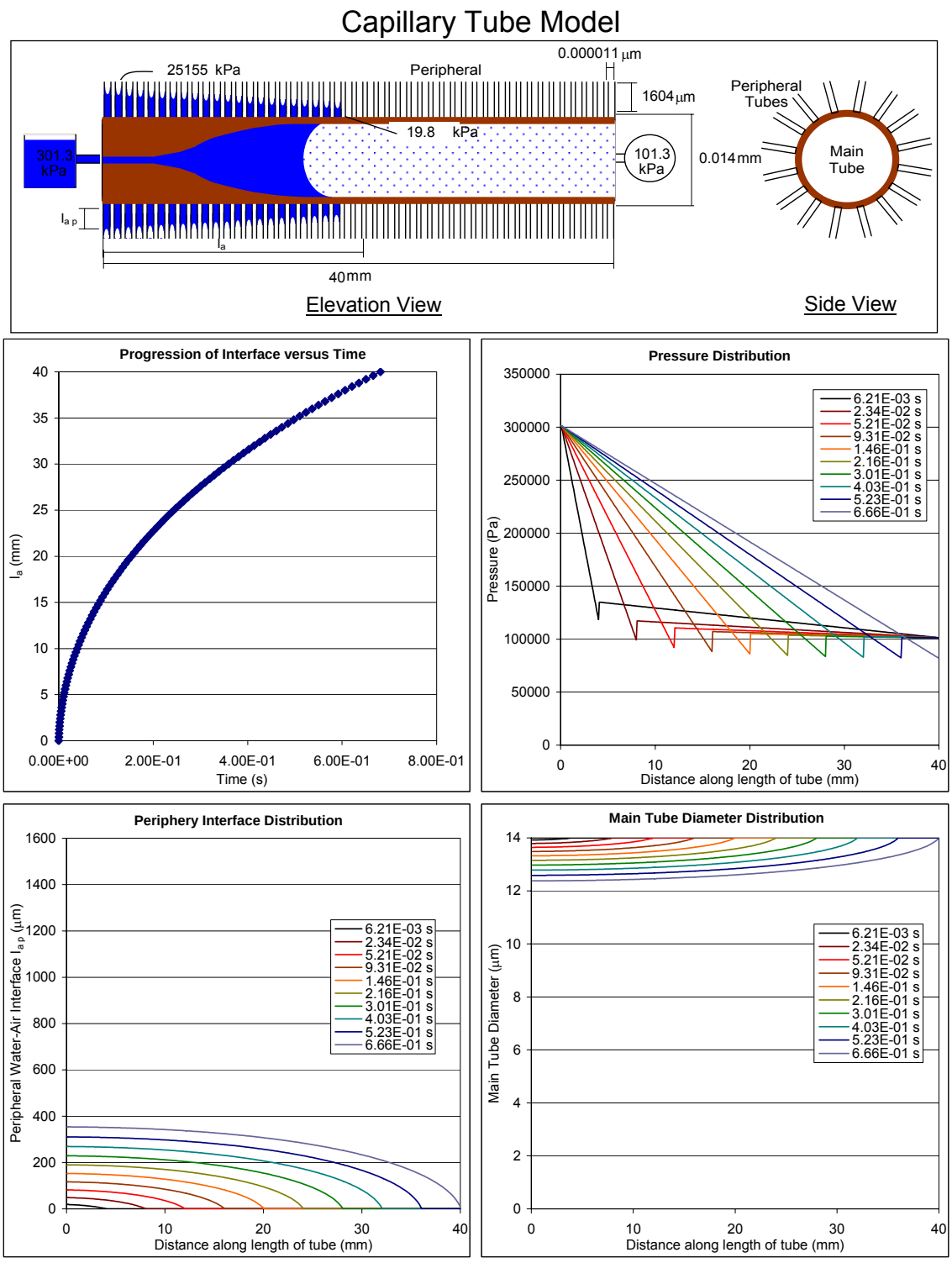

Figure 7.3: Typical output from swelling capillary tube model – open tube.

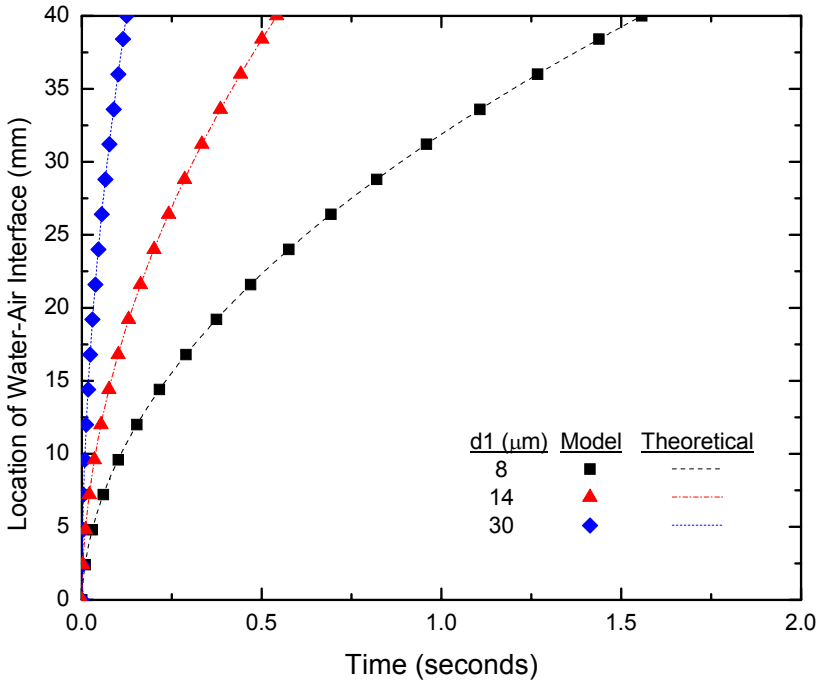

Figure 7.4: Comparison of model output to theoretical derivation.

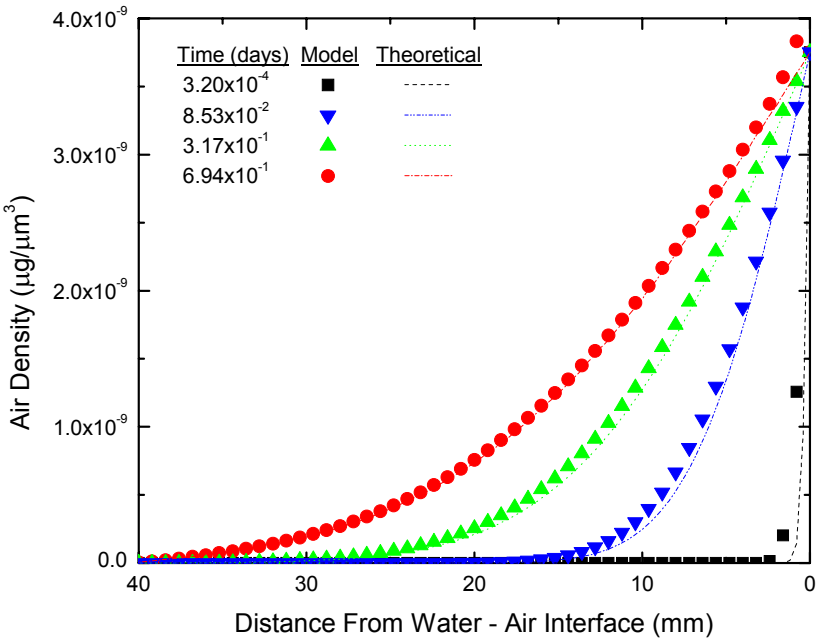

Figure 7.5: Comparison of model diffusion to theoretical derivation.

CHAPTER 8: CAPILLARY TUBE MODEL RESULTS[6]

8.1 Introduction

Bulk behaviour of high plastic compacted clay soils is in many ways dominated by mechanisms occurring at the particle level. Although groundwater flow is often modeled on a larger scale using bulk properties, consideration of flow at the pore scale aids understanding of behaviour observed at the large scale level. A capillary tube model for flow in unsaturated swelling clay was presented in Chapter 7. The new capillary tube model incorporated a mechanism to simulate swelling behaviour. As water flows down the tube, its cross-sectional area reduces to restrict flow. This represents decreasing hydraulic conductivity with increasing saturation as proposed by previous researchers (Thomas et al. 2003, Cui et al. 2001, Hoffman et al. 2006).

---

[6] A combination of this chapter and Chapter 7 will be submitted as:
Siemens, G.A., Blatz, J.A. and Ruth, D. Development of a capillary tube model for swelling soil. Canadian Geotechnical Journal. *In Preparation*.

The goal the new tube model is to understand swell mechanisms under differing boundary conditions at the particle level. Boundary conditions and model parameters are based on the laboratory apparatus presented in Chapter 4 and Chapter 5 and soil properties presented in Chapter 3. Capturing the behaviour observed in the laboratory results (Chapter 6) is the focus of this model. Several different versions of the model have been created to represent the test types including drained and undrained infiltration tests as well as to investigate possible mechanisms occurring during laboratory tests such as air diffusing through the water phase and water pushing air out the perimeter of the specimen. For each model type, numerous iterations are performed in order to determine the influence of model parameters. This chapter presents results from the capillary tube model as well as preliminary interpretations. Detailed interpretation of all models is provided in Chapter 9.

For each model type a typical output is shown followed by several graphs of the water-air interface progression versus time for all swell rates. A typical output from an open end model was displayed in Figure 7.3. A template was created in Excel to view detailed output from every model completed. This includes progression of the water-air interface with time along the main tube, as well as distributions of pressure, peripheral interfaces and main diameter at discrete points during the model as shown in Figure 7.3 although they are calculated at every time step. The bottom two (2) graphs on Figure 7.3 are related as the one

on the left is the distribution of peripheral water-air interfaces along the length of the tube while the right graph displays the main diameter distribution along its length. The limits on the graphs correspond to the physical limits placed on their individual parameters to allow the physics of the model to be understood clearly. As mentioned in Chapter 7, peripheral tube length is a function of the initial and minimum main tube diameters, peripheral tube diameter and swell rate. The length of each peripheral tube in this particular model is 1604 μm which is the upper limit on the graph. The initial main tube diameter is 14 μm which is the upper limit on the diameter distribution graph (lower right).

As water enters the main tube, it also flows into the peripheral tubes and causes a corresponding reduction in main tube diameter. This is consistent with the swell mechanism described in Chapter 7 where macro pores reduce in size during swelling of clay peds. Initially the peripheral tubes are also filled only with air and remain that way until the water-air interface passes their location. Ten (10) discrete distributions are shown on these graphs and are regularly distributed during flow although in the model they are updated at each step. Each series plotted on the graph corresponds to the elapsed time at which the distribution was recorded as displayed on the legend. At water breakthrough, the downstream end of the tube is still at its initial diameter while upstream a smooth transition to smaller diameter occurs.

For each model type several iterations are performed. This includes changing

the model dimensions including main and peripheral diameters as well as the swell rate. As noted in Chapter 7, the bimodal macro and micro porosities are centered on 10-20 μm and 0.01-0.02 μm respectively. A final pore size distribution between the two (2) initial modes has also been suggested. As such representative diameters of 14 μm and 0.011 μm have been chosen for the initial main and peripheral tube sizes respectively. A representative final minimum main tube diameter of 1.4 μm is also chosen based on the final pore size distribution being between the initial two (2) modes. For each model type, the first base case presented use these input diameters while subsequent models include a sensitivity analysis on each of the three (3) input diameters.

The main focus of the capillary tube model is to understand bulk movement of water through soil. The following sections focus on movement of the water-air interface along the length of the main tube. Main tube and peripheral tube parameters are modified and a wide range of swell rates applied. Recall the goal of the capillary tube model is to understand microscopic mechanisms occurring during flow through swelling soil. The controlling mechanism of flow through a tube that has transient changes to its cross-sectional area is determined.

8.2 Open End Tube Model Results

The goal of the open end capillary tube model is to represent the drained laboratory test. Although relatively fewer drained laboratory tests were

performed, the open end model is discussed first because it is the most intuitive to understand.

In all open end tube models upstream and downstream pressures are maintained at a constant level throughout. Upstream pressure represents water pressure applied at the periphery of laboratory specimens and is set to 200 kPa (301.3 kPa absolute pressure). Downstream pressure is maintained at atmospheric (101.3 kPa absolute pressure) representing zero back pressure applied during drained tests. Initially, the capillary tube is of constant diameter and filled entirely with air. Models continue until breakthrough occurs as water fills up the tube and pushes all the air out.

An example output from an open tube model was shown in Figure 7.3. Initially water enters the tube quickly but then progression of the water-air interface slows down to an approximate constant rate at water breakthrough. This is consistent with flow behaviour observed in the drained laboratory tests where relatively high initial flow rates steadily decreased to constant values over the remainder of tests. On the pressure distribution graph, most of the pressure drop occurs in the water phase. Upstream and downstream pressures are maintained at constant levels throughout. At the water-air interface, a jump in pressure corresponding to the capillary pressure of the tube appears. Since water is the wetting fluid the capillary pressure results in an increase in pressure. Little gradient is required to move the air forward due to its relatively lower viscosity. Upstream of the

water-air interface, the diameter of the tube reduces as water flows into the peripheral tubes. Both this reduction and diameter and the reduction of gradient in the water phase result in the flow behaviour observed in the main tube, which is a high initial flow rate that reduces to a relatively constant value.

8.2.1 Open end models – Base Case

Model flow from the base case is shown in Figure 8.1 as location of water-air interface versus time plotted on a logarithmic axis. A summary of the open end models is presented in Table 8.1. Swell rates for the base case in open end model were applied from 0 (no swell) to $1x10^{6}$. In all cases models continued until water breakthrough occurred. The model with swell rate equal to zero represents flow through a constant diameter tube. Breakthrough occurs in $6.28x10^{-6}$ days (0.543 s) through a 40 mm long tube. As swell rate increases, breakthrough takes longer since the water is pushed through a smaller cross-sectional area upstream of the interface. Little change in time to breakthrough is observed from increasing swell rate from 0-1000 but when the swell rate is increased to 2000 breakthrough time increases several orders of magnitude. Subsequent increases in swell rate again do not result in significant increases to breakthrough time and a maximum breakthrough time of $6.15x10^{-2}$ days occurs for a swell rate of $1x10^{6}$. The reason for the sudden increase in breakthrough time is that the minimum main tube diameter is reached for capillary tubes with swell rates greater than approximately 2000 for the base case of open end models. Once the minimum diameter is reached no further swelling (reduction in main tube diameter) occurs and therefore further increases

in swell rate of several orders of magnitude do not result in significant changes to breakthrough times. The total range of breakthrough times is over four (4) orders of magnitude and the transitional swell rate is between 2000 and 2400 as shown in Table 8.1.

8.2.2 Open end models – initial diameter analysis

The next set of models analyzes the influence of initial main tube diameter on open end models. Results are shown in Figure 8.2a and Figure 8.2b and summarized in Table 8.1. Again a wide range of swell rates are applied from $0 – 1x10^6$. Results are compared to the base case discussed above. Increasing initial main tube diameter (Figure 8.2a) results in shorter breakthrough times for low swell rates as the upstream pressure drives flow. Once the transitional swell rate is reached around 10000-22000, breakthrough actually increases five (5) orders of magnitude. Decreasing initial main tube diameter results in the opposite scenarios. At low swell rates, longer breakthrough times are observed compared to the base case while at higher swell rates shorter times to water breakthrough are observed. The transitional swell rate when reducing the initial main tube diameter also reduces.

Changing initial main tube diameter results in two (2) changes to the model including the capillary pressure at the water-air interface and the magnitude of reduction in cross-sectional area during flow. Increasing the main diameter corresponds to decreasing the capillary pressure at the interface and vice versa from [7.8]. In the first case initial models reduced breakthrough times as the

upstream and downstream pressures control the flow. Once the transitional swell rate is reached the difference from this model to the base case is the capillary pressure pulling at the interface. With a lower capillary pressure associated with an increased main tube diameter, the result is a relative increase in breakthrough time compared to the base model. Also, the range from maximum to minimum is over a wider range of breakthrough times for the swell rates applied. Finally increasing the main diameter also increases the volume that must be reduced during flow to get to the minimum main tube diameter. As such, increasing and decreasing main tube diameter increases and decreases the transitional swell rate one (1) order of magnitude respectively.

8.2.3 Open end models – minimum diameter analysis

Figure 8.3a and Figure 8.3b show the model results from increasing and decreasing the minimum main diameter (after swell). The minimum time to breakthrough is 6.28×10^{-6} days (0.543 s) in both cases. Increasing swell rate restricts flow and transitional swell rates of approximately 2000 are observed in both cases. Increasing the minimum main diameter results in a maximum breakthrough time of 9.24×10^{-4} days while decreasing the minimum main diameter increases the maximum breakthrough time by six (6) orders of magnitude.

Altering the minimum main tube diameter only affects flow once the swell rate is high enough to have a significant effect. Below the transitional swell rate threshold, since the minimum main tube diameter is not reached upstream of the

interface, little change in flow rate is observed. Above this swell rate threshold, significant change to the flow regime occurs and the maximum breakthrough time is affected. Increasing the minimum main tube diameter reduces maximum breakthrough time by two (2) orders of magnitude while decreasing it increases breakthrough times by two (2) orders. Although this affects the flow regime upstream of the interface, the capillary pressure remains constant since the initial main tube diameter does not change. Interestingly, the transitional swell rate is not altered by changing the final main tube diameter as in all three (3) cases it is in the 2000-2500 range despite a four (4) order of magnitude change to the breakthrough time.

8.2.4 Open end models – peripheral diameter analysis

Results from the open end models where peripheral tube diameter is modified are shown in Figure 8.4a and Figure 8.4b and summarized in Table 8.1. Increasing the peripheral diameter does not change the flow regime with swell rates less than the threshold in either case as the minimum breakthrough time is 6.28×10^{-6} days (0.543 s) for both increasing and decreasing peripheral tube diameter. Above the threshold, similar behaviour is also observed as the maximum breakthrough time is the same for all cases. The only difference between the three (3) models is the transitional swell rate that increases with increasing peripheral diameter and decreases with decreasing peripheral diameter by about one (1) order of magnitude in each case.

In the model, the peripheral diameter affects the rate of swell. Smaller diameter peripheral tubes have larger capillary pressures but are also longer for equal swell rates. In these models flow down the peripheral tube is governed by the upstream and downstream pressures. The upstream pressure is the pressure in the main tube at the location of the peripheral tube while the downstream pressure is maintained at atmospheric (101.3 kPa absolute pressure) throughout. Larger peripheral tubes that are also shorter (since total peripheral tube volume is constant) allow quicker flow leading to a faster decrease in main tube diameter and lowering the transitional swell rate.

8.2.5 Open end models – summary

The goal for open end models was to represent drained laboratory tests. In these tests, upstream and downstream pressures remain constant throughout. Water inflow and air outflow are initially relatively high but later reduce to constant values (Figure 6.36). In the model, this is a result mainly of the decrease in cross-sectional area upstream of the interface but also due to the decreasing gradient as water flows down the tube. Results from the capillary tube model show that these basic behaviours are captured with the open end model. More detailed discussion is presented in Chapter 9.

8.3 Closed End Tube Model Results

The goal of closed end tube models is to represent undrained infiltration tests. As described in Chapter 6, radial flow is applied to cylindrical specimens. Water

is applied to the entire periphery and no open drainage is provided for the air component. In the capillary tube model the downstream end of the tube is closed fixing the air component inside the tube. As water enters the tube, the air component compresses and increases in pressure. A typical output from a closed end model is presented in Figure 8.5. Water enters the tube relatively quickly but then stops abruptly at around 15 mm into the 40 mm tube. The upper left graph shows the reason for the stop in flow as the downstream air pressure increases until it equals the sum of the upstream and capillary pressures. Once pressure increase occurs, flow into the tube stops and the model is complete at 6.09 s. As in the open end models, water flows into the peripheral tubes resulting in a reduction in cross-sectional area of the main tube. In this particular model, the minimum diameter is not reached once forward progression of the interface stops.

8.3.1 Closed end models – Base Case

Model results from the closed end model base case are shown in Figure 8.6. The base case in all model types uses representative diameters for initial and minimum main tube as well as peripheral tube sizes. In this case all models stop at the 15 mm point once the downstream air pressure increases up to the sum of the upstream pressure and capillary pressure at the water-air interface. The last forward movement of the interface for each swell rate is shown with the horizontal line at the end of the model run. In the base case, the shortest time to end of flow is 8.26×10^{-6} days (0.714 s). This is greater than the time required in the open end models (6.28×10^{-6} days). Again this is due to the increasing

downstream pressure that reduces the flow rate. The transitional swell rate for the closed end model is 1000-1400 and is on the same order of magnitude as the open end model.

8.3.2 Closed end models – initial diameter analysis

Modifying the initial main tube diameter alters the mass of air in the tube. The models where initial main diameter was increased and decreased are shown in Figure 8.7a and Figure 8.7b respectively. Increasing the initial diameter of the tube actually reduces the amount of flow into the tube. It also decreases the minimum time to end of flow in the lower swell rate models. Above the transitional swell rate of 10000-14000 flow times increase to greater than the base case by an order of magnitude. Decreasing the initial main tube diameter results in further penetration into the tube prior to the end of flow as well as longer times to the end of flow to compare to the base case. The maximum time to end of flow is reduced compared to the base case as in the open end models and the transitional swell rate is also lower.

Changing the initial main tube diameter affects the mass of gas in closed end models as well as the capillary pressure. Increasing the mass of gas results in less penetration required to stop forward progression of the water-air interface. At lower swell rates increasing main diameter allows faster progression of the interface and reduced times to end of flow and vice versa. Transitional swell rate also increases with increasing initial main tube diameter. Comparing to the open

tube models shows consistent transitional swell rates are observed for similar geometries.

8.3.3 Closed end models – minimum diameter analysis

Model results in which the minimum diameter was altered are shown in Figure 8.8a and Figure 8.8b. At low swell rates flow is not affected so the minimum time to end of flow is the same as the base case. Above the transitional swell rate progression of the interface is attenuated by decrease in cross-sectional area. Decreasing the minimum main diameter increases the time to end of flow by two (2) orders of magnitude while increasing it lowers the time one (1) order. The transitional swell rate is approximately 1000-1400 regardless of the minimum main tube diameter.

As in the open end models, altering the minimum main diameter significantly affects the advancement of the water-air interface. Reducing the minimum diameter increases the time to end of flow two (2) orders of magnitude while increasing the minimum diameter reduces time to end of flow. The swell rate affect is unchanged by altering the main tube as the transitional swell rate is unchanged for all three (3) cases.

8.3.4 Closed end models – peripheral tube analysis

Figure 8.9a and Figure 8.9b show the model results from increasing and decreasing peripheral tube diameter and a summary is shown in Table 8.2. For all three (3) cases the maximum and minimum times to end of flow are equal.

The transitional swell rate is considerably affected by altering peripheral tube diameter as it changes by an order of magnitude in both cases.

Altering peripheral tube diameter has the further affect of changing the length of peripheral tubes since peripheral volume is constant. Increasing peripheral diameter shortens the peripheral tubes and allows quicker swell or reduction in main tube diameter and vice versa. This is why the transitional swell rate changes for each case. Once swell rates greater than the transitional are applied the minimum diameter upstream of the interface is reached at each step forward which is why the maximum times to end of flow are the same in all cases.

8.3.5 Closed end models – summary

Closed end models seek to model undrained laboratory tests. In the model, general flow behaviour, similar to the undrained tests, is observed with initially relative fast flow rates that decrease and then stop entirely. Interestingly the swell mechanism does not lead to complete attenuation of the flow. Flow actually stops when the downstream pressure increases to sum of the upstream pressure and the capillary pressure at the interface. In the model, the swell mechanism increases the time at which this occurs but does not stop flow itself.

Some aspects of the laboratory test results are not captured. The capillary tube model shows advancement of the water-air interface to about 15 mm into the 40 mm tube. This corresponds to an effective main tube saturation of only about 37.5%. In the laboratory tests, degree of saturations greater than 80-90% are

generally observed. To calculate the mass of gas inside the capillary tube, an assumption is made that the upstream and downstream absolute pressures are 301.3 and 101.3 kPa respectively. The average pressure is used to calculate the mass of gas in the tube which then compresses and stops flow. In the laboratory tests, these pressure boundary conditions are likely an upper bound. Following isotropic compression, air pressure in the specimens is measured at or near atmospheric (101.3 kPa). As water is applied to the perimeter this internal mass of air in the specimens is slowly compressed only when water enters the pore space. As such the mass of air calculated in the capillary tube model could be based on a flat distribution of 101.3 kPa absolute pressure across the tube. The next section investigates the influence of altering this initial condition on the flow behaviour in a swell capillary tube.

8.4 Closed End – Low Pressure Tube Model Results

The closed end – low pressure tube models investigate the influence on the initial mass of gas in the capillary tube. The difference between models in this section and the previous one (1) is that the initial mass of gas is reduced based on the assumption of atmospheric pressure in the tube instead of a gradient from 301.3 kPa to 101.3 kPa (absolute pressures) from upstream to downstream.

An example output form a closed end – low pressure model is shown in Figure 8.10. Comparing Figure 8.10 to Figure 8.5, the one described in the previous section, shows a few differences. First, progression of the interface

continues until approximately the 27 mm point instead of 15 mm in the previous models. This is almost twice as far into the main tube resulting in 67.5% of the tube filled with water. Comparing the pressure distributions at equal progressions of the interface reveals a lower pressure building up at a slower rate in Figure 8.10. Similar shapes are observed in the progression of the interface versus time plots in both figures. In both models, progression of the interface stops once the air pressure equals the sum of the upstream pressure and the capillary pressure at the interface.

Table 8.3 summarize results from the closed end – low pressure models. Figure 8.11, Figure 8.12, Figure 8.13, and Figure 8.14 show the models completed including the base case and altering of the initial main tube diameter, minimum main tube diameter and peripheral tube diameter respectively. Comparing the tables and figures to the ones discussed in the previous section shows that the same trends are observed in both models. The only difference is the increased penetration, resulting in longer flow times in the low pressure models. This is due to the reduction in gas mass and allows further progression of the interface and longer times to end of flow. The transitional swell rates for both models are similar for both types of models as well. This gives confidence that similar conditions are being applied in both cases and the only difference is the initial mass of air. Since the two (2) models behaved so similarly, detailed discussion is not repeated in this section. The previous section can be applied with similar comments. Again flow shapes are captured by this model but

saturations of 80-90% are still not modeled. The next two sections investigate mechanisms which may be occurring during undrained infiltration tests to achieve the greater observed saturations.

8.5 Closed end – with Diffusion Tube Model Results

Thus far closed end models have captured only some of the basic flow behaviour observed in undrained tests. This includes initially relative higher flow rates that reduce eventually to zero. In both previous model types flow stopped at about 15 mm and 27 mm respectively corresponding to penetration percentages of 37.5% and 67.5%. Following laboratory tests degrees of saturation greater than 80-90% are generally measured indicating that the water phase is getting farther into the specimens than is being predicted by the closed end models. The issue is removing the free air from the downstream end of the capillary tube so that water can penetrate farther. The next two sections investigate possible mechanisms that would result in the higher saturations to occur. The first mechanism is diffusion of air through the water phase. In traditional saturated soils testing, diffusion is often assumed to occur during the saturation phase of triaxial tests. As such it could also occur during the undrained radial flow tests. Diffusion of all the air downstream of the interface results in breakthrough in the capillary tube model. As a starting point, the low pressure initial condition was used to calculate initial mass of gas in the capillary tube so all models discussed in this section are compared to the closed end – low pressure models presented in Section 8.4.

An example output from a closed end model that considers diffusion is illustrated in Figure 8.15. One difference in the output configuration compared to previous example output figures (Figure 7.3, Figure 8.5 and Figure 8.10) is the lower left graph plots the air density dissolved in the water phase instead of progression of the peripheral water-air interfaces. Since diffusion is the main addition to this model, this plot is shown so that movement of air can be observed and the diameter distribution is still shown so that the swell mechanism can be also examined. As shown on the figure, breakthrough is observed in diffusion models once all the free air downstream of the interface diffuses into the water phase and down along the tube. Initially relatively quick progression of the water-air interface is observed until the 27 mm point down the length of the tube after which it slows considerably. The pressure build up downstream of the interface is similar to the one observed in closed end – low pressure models until the 27 mm point at which those models were complete. After this point the diffusion mechanism takes over and progression of the water-air interface continues slowly until breakthrough. In the lower left graph of air density distribution, early on a very steep air density gradient is observed as flow is occurring so quickly that there is little time for movement of air. Once the air pressure builds up to its maximum and interface progression slows down, air moves through the water phase and allows breakthrough to occur. Upstream of the interface the diameter reduces due to flow into peripheral tubes as shown in the lower right graph. In the model shown, a swell rate of 10 was applied and the minimum diameter is

not reached prior to breakthrough. Regular progression of the interface occurs all the way to breakthrough.

In some other models discussed later, at points extremely close to breakthrough (generally with the interface more than 39 mm through the 40 mm long tube) some numerical instability is observed due to the extremely small amount of free air remaining downstream of the interface in an incredibly small volume. Some small instability is shown in Figure 8.15 in the air density graph as the last distribution plotted at 6.27×10^4 s shows a small drop in air density at the water-air interface. As air density only builds up with progression of the interface this behaviour is not realistic. Numerous attempts were made to correct this issue but it could not be fixed. In the plots (Figure 8.16 for example) the point where instability occurs is quite clear as progression of the interface is smooth until near the end and suddenly a sharp increase in time for progression is observed. This behaviour is not representative of actual diffusion behaviour and is ignored in this discussion. To get time to breakthroughs for the summary presented in Table 8.4, flow times were extrapolated assuming progression would have been completed in a log-linear shape had numerical instability not occurred.

8.5.1 Diffusion models – Base Case

Models for the diffusion model – base case are plotted in Figure 8.16 as location of the water-air interface versus time plotted on a logarithmic scale and are summarized in Table 8.4. Comparing the figure to the base case of the closed

end – low pressure base case (Figure 8.11) shows that the exact same flow rates occur until the interface nears the 27 mm mark where diffusion takes over. In the closed end – low pressure model, flow stops but in the diffusion model flow continues until breakthrough. The difference in breakthrough times is less than an order of magnitude over the swell rates applied and no transitional swell rate is apparent. In the base case, diffusion of the downstream air is limiting inflow for all models.

8.5.2 Diffusion models – initial diameter analysis

Diffusion models for the initial diameter analysis are plotted in Figure 8.17 and summarized in Table 8.4. Comparing the diffusion models to the low pressure models (Figure 8.12) shows that the same flow behaviour is observed until downstream air pressure builds up and diffusion takes over. Comparing to the base case, increasing initial main tube diameter has the result of increasing breakthrough times for both low and high swell rates. This is due to the capillary pressure at the interface that reduces with increasing diameter. As initial main tube is increased a small transitional swell rate is observed at the 1000 level. Although the change in breakthrough time is not greater than an order of magnitude, it does increase by approximately 1.5 times. As initial main tube is increased, the swell rate has an increased affect on the flow behaviour as initial faster flow rates are slowed by high swell rates. Decreasing initial main tube diameter results in less volume required to swell and less impact of the swell rate on overall flow behaviour.

8.5.3 Diffusion models – minimum diameter analysis

Diffusion models that investigated the influence of the minimum main diameter are shown in Figure 8.18 and summarized in Table 8.4. Similar to the previous case diffusion results are the same as closed end – low pressure models until the downstream pressure builds and diffusion limits forward progression of the water-air interface. The minimum times to breakthrough shows no influence on minimum diameter since swell rates of zero are applied for these cases. The maximum times to breakthrough show the influence as decreasing minimum tube diameter increases breakthrough an order of magnitude. Increasing the main diameter showed basically no influence on breakthrough times. A transitional swell rate also becomes apparent with smaller minimum main diameters. The small tube size is dominating behaviour more than the downstream air pressure at this level.

8.5.4 Diffusion models – peripheral tube analysis

A summary of the peripheral tube diameter analysis is shown in Table 8.4 and the models are illustrated in Figure 8.19. Comparing flow times with the base case shows no influence on the minimum and maximum breakthrough times. Also no transitional swell rate is apparent. The only difference observed is the change in flow behaviour for specific swell rates such as 1000. As presented in Figure 8.19a increasing peripheral tube diameter results in the swell slowing down flow at approximately the 7 mm mark. Conversely in Figure 8.19b the model with swell rate of 1000 does not limit flow until the downstream air pressure builds and limits forward progression.

Increasing peripheral tube diameter allows faster reduction of the main tube diameter and results in the swell rate of 1000 to limit flow as shown in Figure 8.19a where it does not limit in Figure 8.19b until the build up of downstream air pressure takes over.

8.5.5 Diffusion models – summary

Diffusion models explored a proposed mechanism observed in undrained laboratory tests. Flow in closed end models generally appeared to be similar to the laboratory measured inflow behaviour but were unable to represent higher saturation levels measured following laboratory tests. All diffusion models achieved breakthrough as expected and this represents 100% saturation that although was not measured, could eventually occur given enough time. Inflow behaviour is similar to laboratory measured flow considering the shapes of the curves. Further discussion and interpretation is provided in Chapter 9.

8.6 Double Length – No Gradient Model Results

Double length – no gradient models investigate a second proposed mechanism of free air movement in the undrained laboratory tests. In this system, water is the wetting fluid and air is the non-wetting fluid. As water infiltrates from the perimeter of specimens, it could be pushing air out other pores. Instead of air diffusing through the water phase, water would simply be displacing air. In some early laboratory tests where water pressure was applied at 100 kPa air bubbles

were observed to be pushing out of the plumbing. Water needs to push to the center of the specimen but at this time air would still be filling some pores so water would have to continue pushing air out the face of the specimen. Converting this to a capillary tube model, the main tube length must be doubled to simulate water movement to the center and then back to the perimeter. This is seen as an upper limit as some water could short circuit back to the perimeter without passing through the center of the specimen. Upstream and downstream pressures would both be 200 kPa since water movement needs to continue until breakthrough at the perimeter is complete. The only driving force for flow is the capillary pressure at the water-air interface.

An example output from a double length – no gradient model is illustrated in Figure 8.20. As described above the length of this tube is 80 mm compared to 40 mm and both upstream and downstream pressures are 200 kPa (301.3 kPa absolute pressure) as compared with previous models. Considering Figure 8.20 progression of the water-air interface occurs relatively quickly to start and then the rate reduces to a constant level near the end of the tube. The shape of the curve looks very similar to the open end tube model (Figure 7.3). The pressure distribution shows the gradient that pulls the interface forward is only due to the capillary pressure. The gradient in the water component is much greater than the air component due to the viscosity difference between the two (2) fluids. Swell proceeds with smooth transitions along the length of wetted tube to restrict flow upstream of the water-air interface.

8.6.1 No gradient models – Base Case

Results from the base case of the no gradient model are shown in Figure 8.21 and a summary is provided in Table 8.5. With no overall gradient applied between the upstream and downstream pressures the capillary pressure pulls the interface forward throughout. In this model, the quickest time to breakthrough is 2.79×10^{-4} days (24.1 s). Increasing swell rate greater than 400 results in time to breakthrough of four (4) orders of magnitude.

Comparing to the base case of the open models shows that similar relative behaviour is observed. Comparing progression of the water-air interfaces shows similar shapes. Increasing swell rate past the transitional results in a jump in breakthrough times of several orders of magnitude. Differences include the magnitude of times and swell rates. In the open tubes flow rates less than one (1) second were observed while in double length models flow times are two (2) orders greater. Similarly the longest time to breakthrough is two (2) orders of magnitude greater in the double length model compared to the open. Comparing the transitional swell rates shows that in the double length models is one (1) order of magnitude less than in the open models.

8.6.2 No gradient models – initial diameter analysis

The no gradient models that altered the initial main tube diameter are shown in Figure 8.22 and summarized in Table 8.5. For low swell rates increasing initial main tube diameter results in decreased breakthrough times. Although increasing diameter reduces the capillary pressure resistance to flow is also

decreased allowing faster progression of the interface. At swell rates above the transitional, breakthrough time increases with initial main tube diameter increase. This is because the lower capillary pressure now has a much smaller diameter distribution resulting in longer time to breakthrough. Transitional swell rate increases with greater initial main diameters since more swell volume is required.

8.6.3 No gradient models – minimum diameter analysis

Minimum diameter analysis models are shown in Figure 8.23 with summaries provided in Table 8.5. With no swell, times to breakthrough are the same as the base case. Increasing swell rate increases breakthrough times and following the transitional, times increase five (5) orders of magnitude for a reduced minimum diameter. Relative to the base case this increases breakthrough times while increasing the minimum main diameter decreases breakthrough times due to the change in resistance upstream of the interface. Transitional swell rate does not change with changes to the minimum diameter.

8.6.4 No gradient models – peripheral tube analysis

Models with altered peripheral tube diameters are shown in Figure 8.24 with a summary provided in Table 8.5. Altering the peripheral tube geometry does not change minimum nor maximum breakthrough times compared to the base case. The only change to be observed is in transitional swell rate that increases with decreasing peripheral tube diameter. Flow occurs slower through smaller tubes so a higher swell rate is required so increase breakthrough times to their maximum.

8.6.5 No gradient models – summary

The goal of no gradient models is to represent a possible mechanism occurring in undrained laboratory tests. The mechanism is both inflow of water and outflow of air occurring at the perimeter of triaxial specimens. No gradient models actually behave similar to open end models. Since both model types allow outflow this is expected. The main difference is values of breakthrough times and transitional swell rates although the relative change in both these were similar. No gradient models consistently had longer breakthrough times and one (1) order of magnitude lower transitional swell rates.

Table 8.1. Summary of open end models

Case	Minimum Time to Breakthrough (Swell Rate=0) (day)	Maximum Time to Breakthrough (Swell Rate=10^6) (day)	Transitional Swell Rate
Base	6.28×10^{-6}	6.15×10^{-2}	2000-2400
1a - ↑ Initial Main	1.44×10^{-6}	2.93×10^{-1}	10000-22000
1b - ↓ Initial Main	1.81×10^{-5}	1.89×10^{-2}	100-430
2a - ↑ Minimum Main	6.28×10^{-6}	9.24×10^{-4}	2000-2500
2b - ↓ Minimum Main	6.28×10^{-6}	1.83×10^{0}	2000-2300
3a - ↑ Peripheral	6.28×10^{-6}	6.15×10^{-2}	100-200
3b - ↓ Peripheral	6.28×10^{-6}	6.15×10^{-2}	10000-11000

Table 8.2. Summary of closed end models.

Case	Minimum Time to End of Flow (Swell Rate=0) (day)	Maximum Time to End of Flow (Swell Rate=10^6) (day)	Transitional Swell Rate
Base	8.26×10^{-6}	8.04×10^{-2}	1000-1400
1a - ↑ Initial Main	2.01×10^{-6}	4.12×10^{-1}	10000-14000
1b - ↓ Initial Main	3.37×10^{-5}	3.51×10^{-2}	200-400
2a - ↑ Minimum Main	8.26×10^{-6}	1.20×10^{-3}	1000-1600
2b - ↓ Minimum Main	8.26×10^{-6}	2.38×10^{0}	1000-1500
3a - ↑ Peripheral	8.26×10^{-6}	8.04×10^{-2}	100-120
3b - ↓ Peripheral	8.26×10^{-6}	8.04×10^{-2}	7000-10000

Table 8.3. Summary of closed end – low pressure models.

Case	Minimum Time to End of Flow (Swell Rate=0) (day)	Maximum Time to End of Flow (Swell Rate=10^6) (day)	Transitional Swell Rate
Base	1.93×10^{-5}	1.92×10^{-1}	1400-2000
1a - ↑ Initial Main	3.76×10^{-6}	7.86×10^{-1}	10000-13000
1b - ↓ Initial Main	1.38×10^{-4}	1.46×10^{-1}	200-300
2a - ↑ Minimum Main	1.93×10^{-5}	2.88×10^{-3}	1400-2000
2b - ↓ Minimum Main	1.93×10^{-5}	5.68×10^{0}	1200-1300
3a - ↑ Peripheral	1.93×10^{-5}	1.92×10^{-1}	100-200
3b - ↓ Peripheral	1.93×10^{-5}	1.92×10^{-1}	6000-7000

Table 8.4. Summary of closed end – diffusion models.

Case	Minimum Time to Breakthrough (Swell Rate=0) (day)	Maximum Time to Breakthrough (Swell Rate=10^6) (day)	Transitional Swell Rate
Base	7.25×10^{-1}	7.96×10^{-1} [a]	N/A
1a - ↑ Initial Main	7.89×10^{-1}	1.10×10^{0} [a]	1000
1b - ↓ Initial Main	6.63×10^{-1}	6.86×10^{-1} [a]	N/A
2a - ↑ Minimum Main	7.25×10^{-1}	7.95×10^{-1} [a]	N/A
2b - ↓ Minimum Main	7.25×10^{-1}	2.37×10^{0}	100
3a - ↑ Peripheral	7.25×10^{-1}	7.96×10^{-1} [a]	N/A
3b - ↓ Peripheral	7.25×10^{-1}	7.96×10^{-1} [a]	N/A

[a] 'Time to Breakthrough' extrapolated due to numerical instability near end of run

Table 8.5. Summary of double length models.

Case	Minimum Time to Breakthrough (Swell Rate=0) (day)	Maximum Time to Breakthrough (Swell Rate=10^6) (day)	Transitional Swell Rate
Base	2.79×10^{-4}	2.73×10^{0}	300-400
1a - ↑ Initial Main	1.31×10^{-4}	2.70×10^{1}	2000-2500
1b - ↓ Initial Main	4.90×10^{-4}	5.10×10^{-1}	80-100
2a - ↑ Minimum Main	2.79×10^{-4}	4.11×10^{-2}	300-400
2b - ↓ Minimum Main	2.79×10^{-4}	8.10×10^{1}	300-400
3a - ↑ Peripheral	2.79×10^{-4}	2.73×10^{0}	20-40
3b - ↓ Peripheral	2.79×10^{-4}	2.73×10^{0}	1000-2000

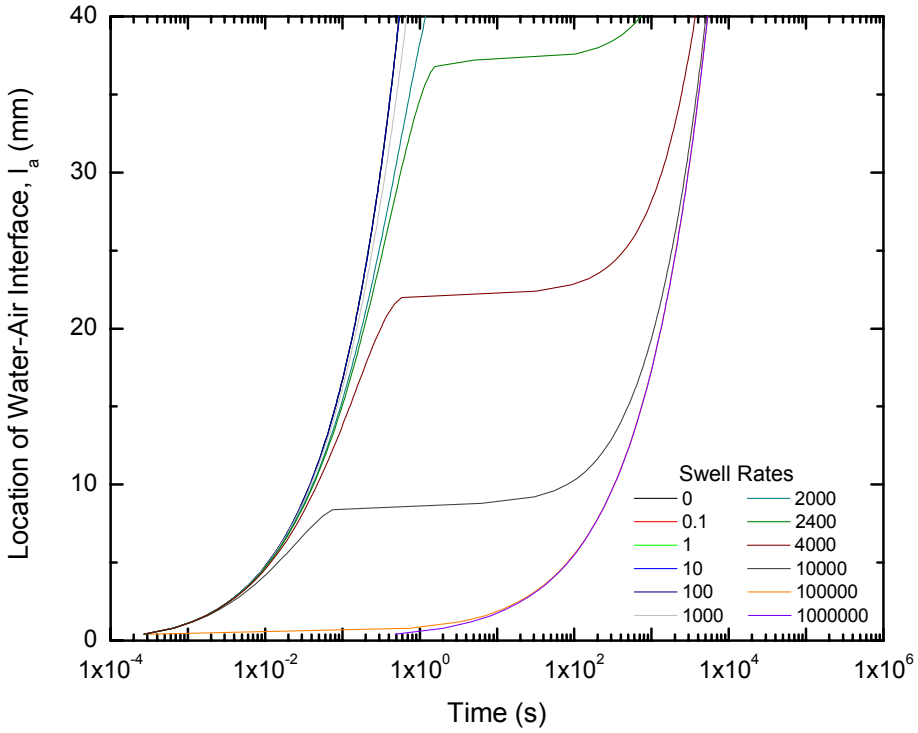

Figure 8.1. Open end model base case: initial main diameter (d1) = 14 μm, minimum main diameter (d2) = 1.4 μm and peripheral diameter (d3) = 0.011 μm.

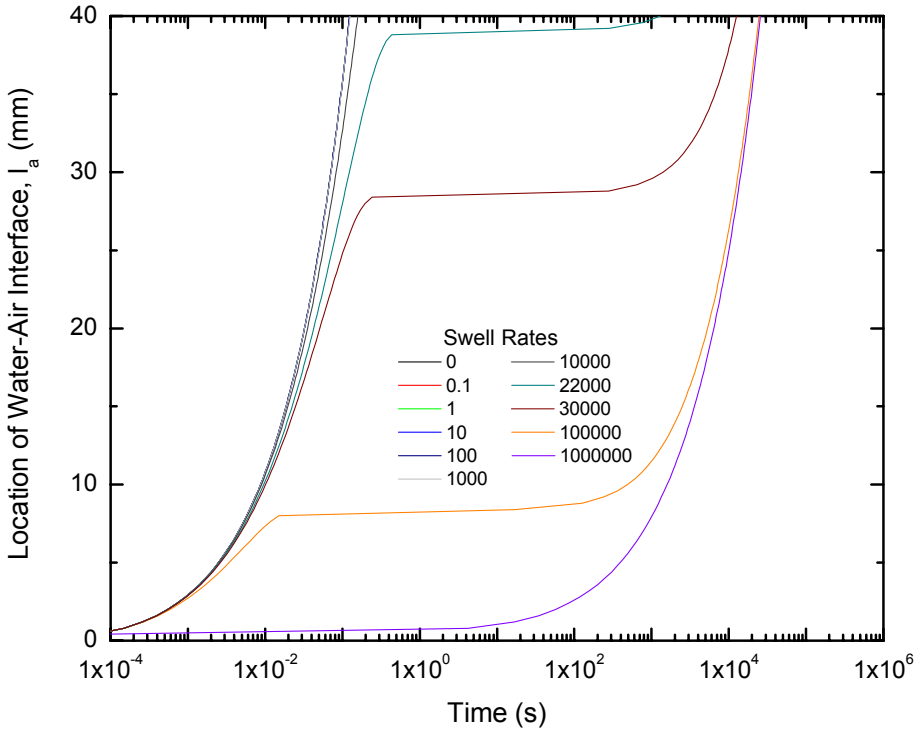

a. Increase initial main diameter (30 μm).

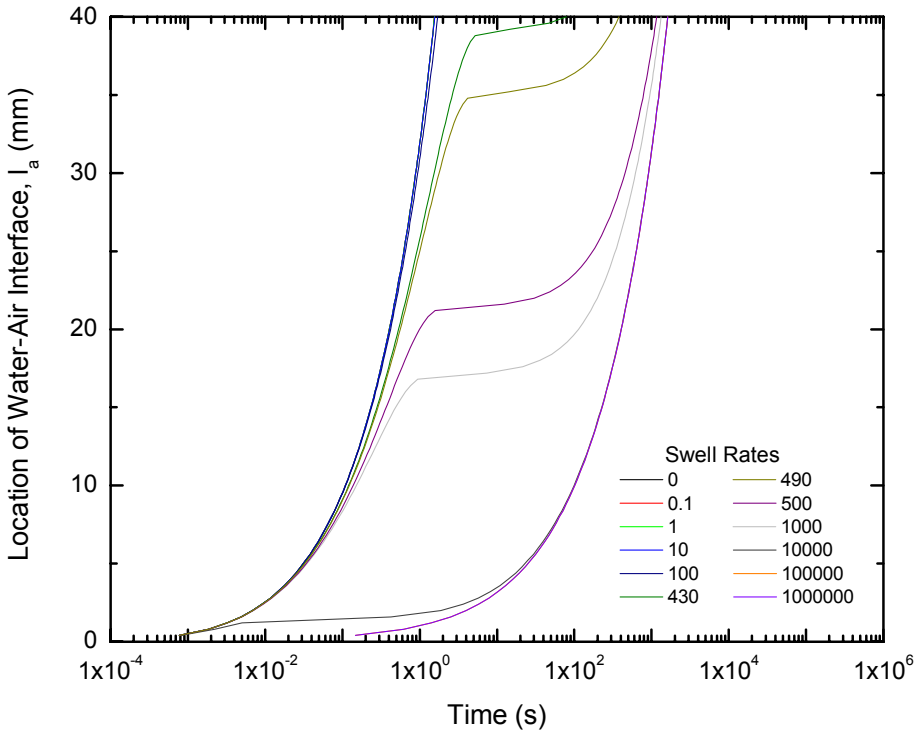

b. Decrease initial main diameter (8 μm).

Figure 8.2. Open end model Case #1 – initial main diameter (d1).

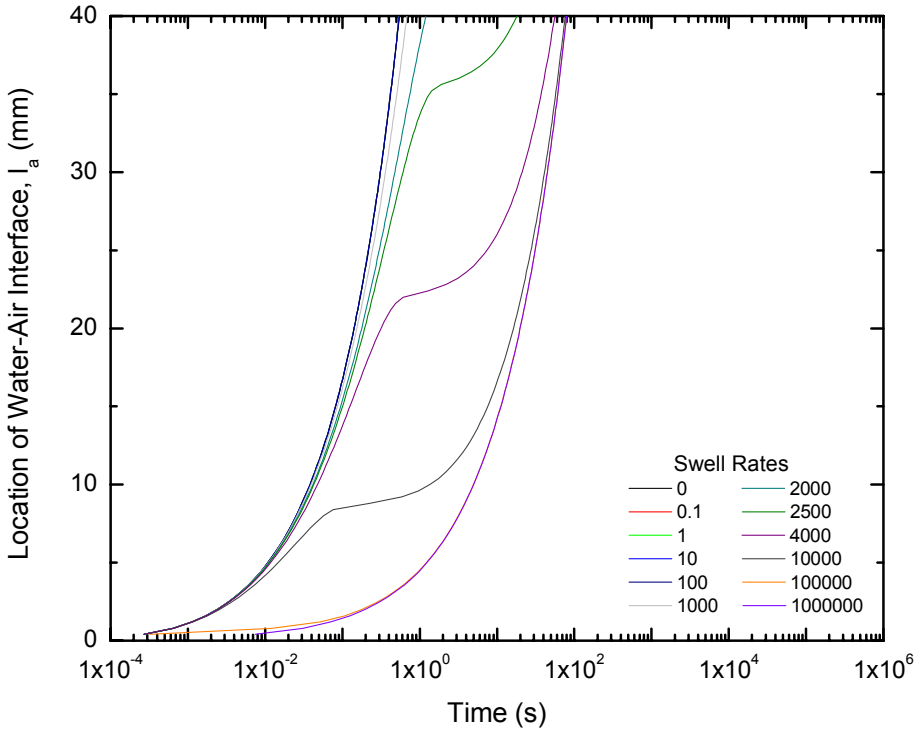

a. Increase minimum main diameter (4 μm).

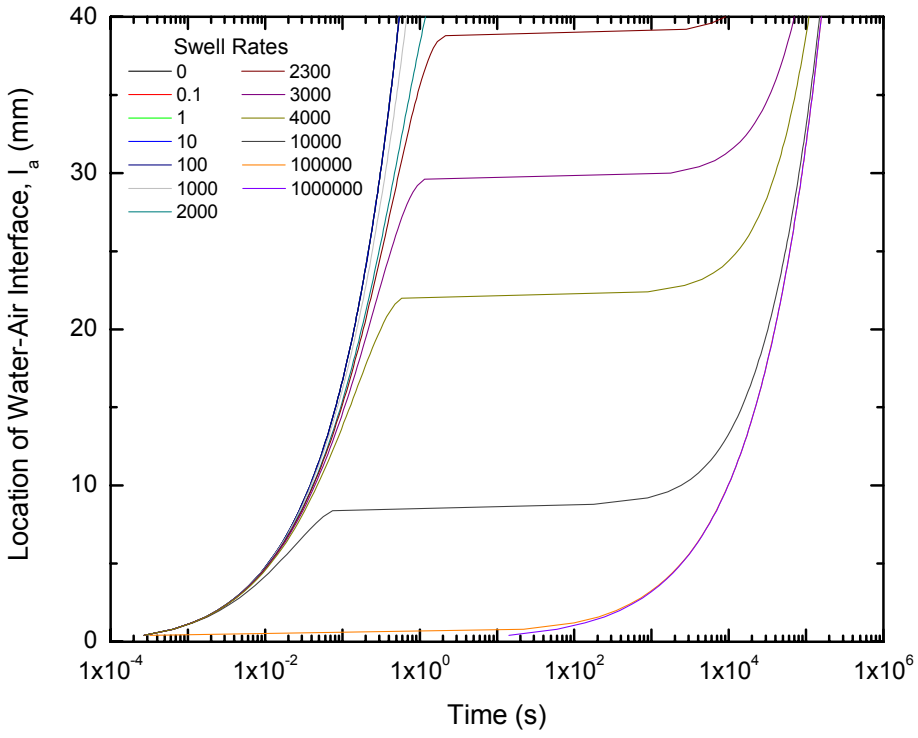

b. Decrease minimum main diameter (0.6 μm).

Figure 8.3. Open end model Case #2 – minimum main diameter (d3).

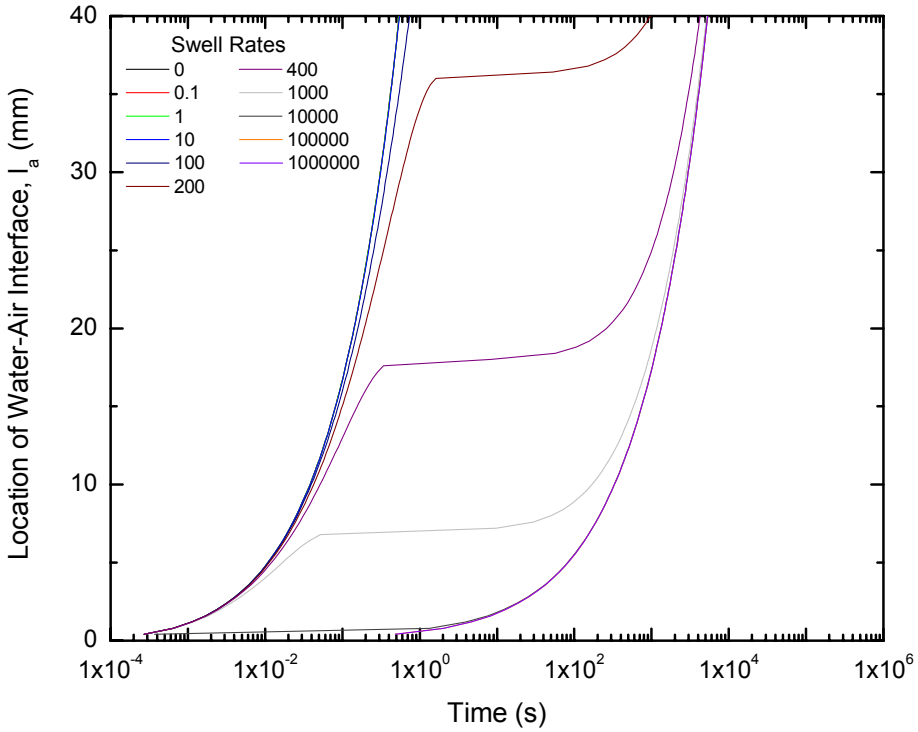

a. Increase peripheral diameter (0.03 μm).

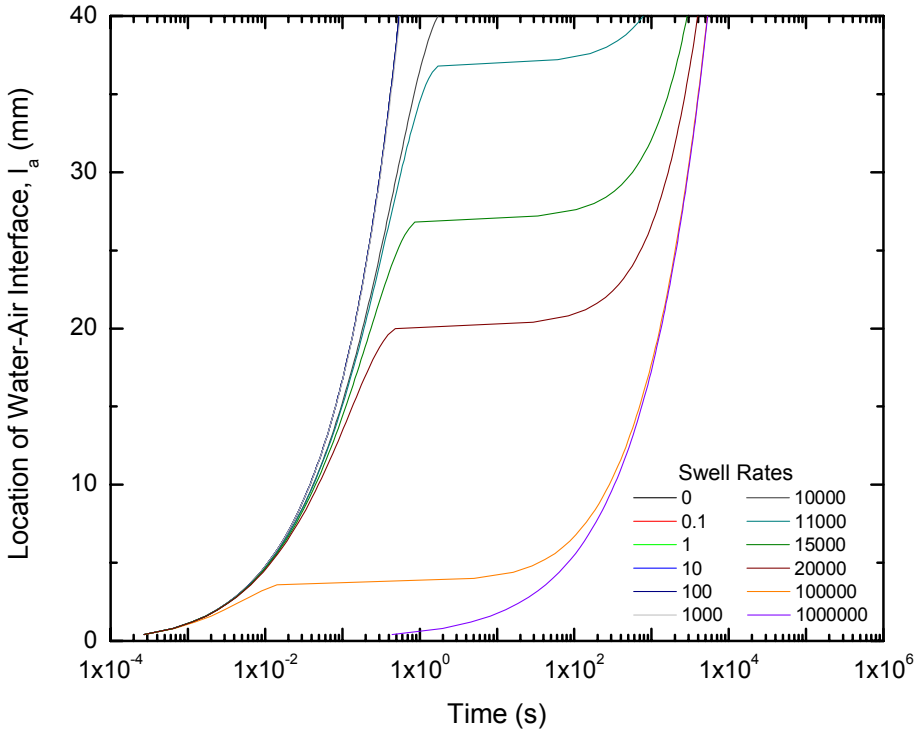

b. Decrease peripheral diameter (0.006 μm).

Figure 8.4. Open end model Case #3 – peripheral diameter (d3).

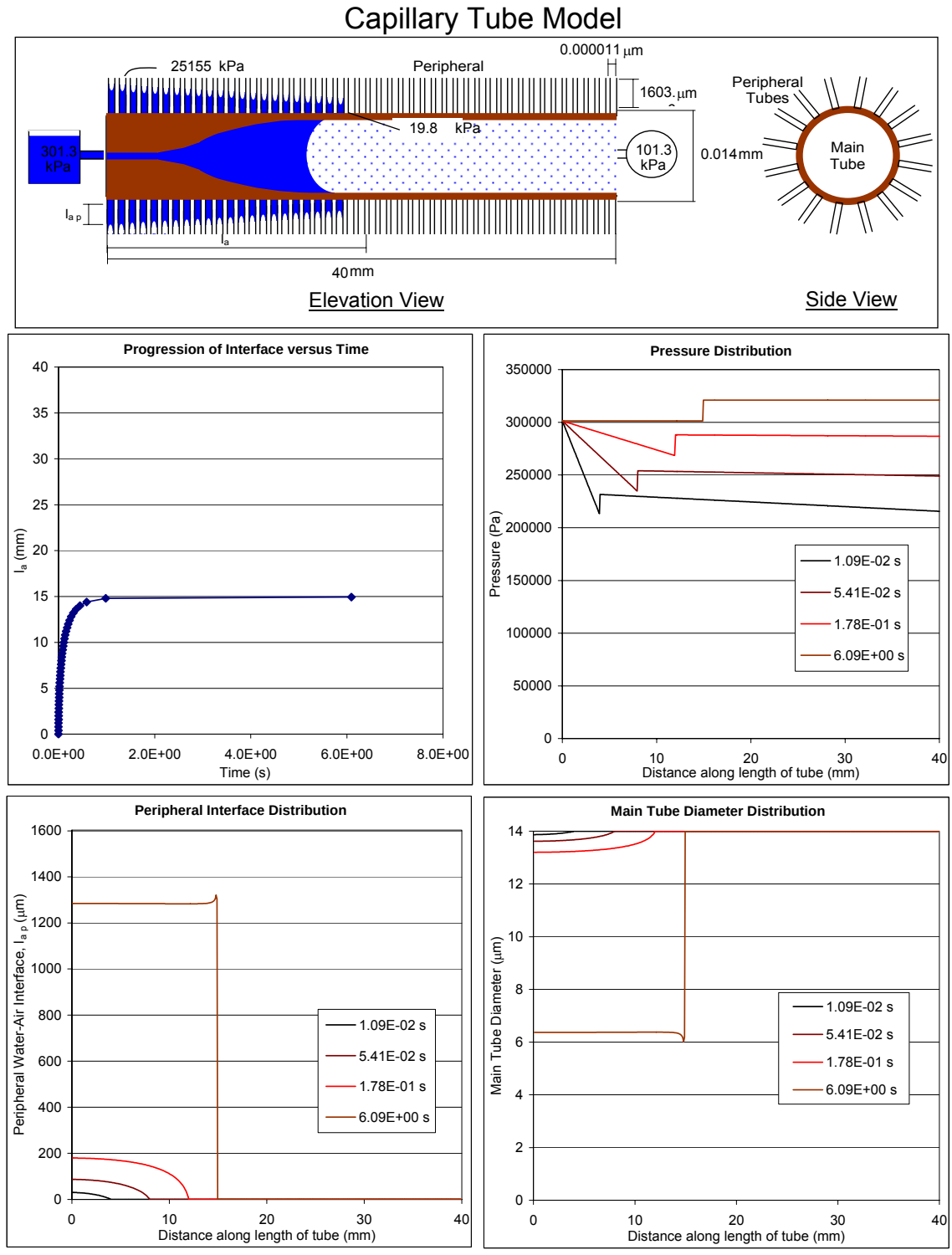

Figure 8.5: Typical output from closed end models.

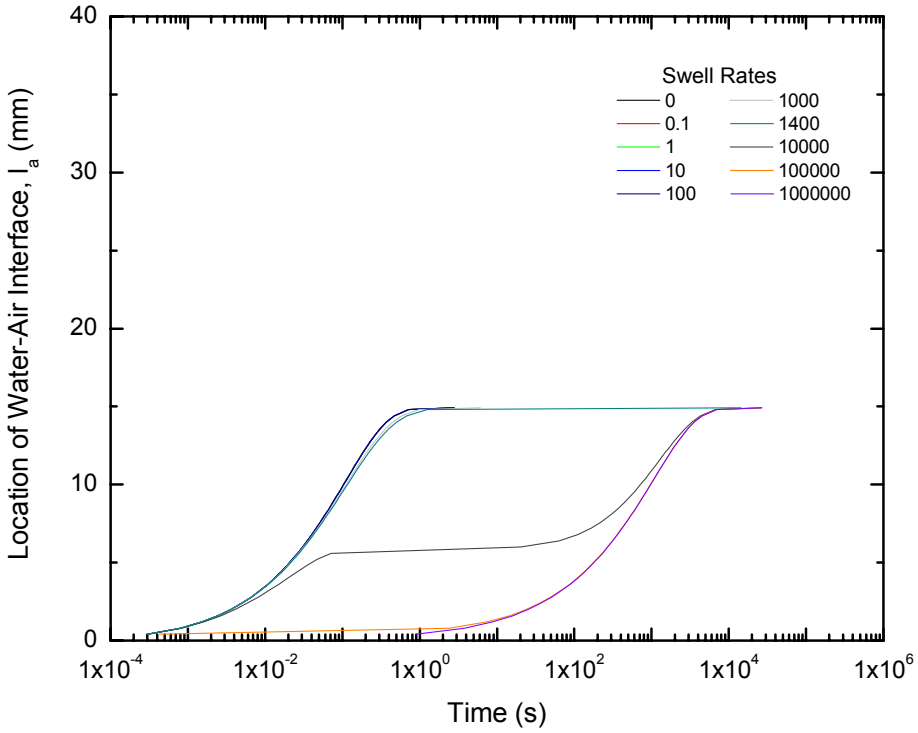

Figure 8.6. Closed end model base case: initial main diameter (d1) = 14 μm, minimum main diameter (d2) = 1.4 μm and peripheral diameter (d3) = 0.011 μm.

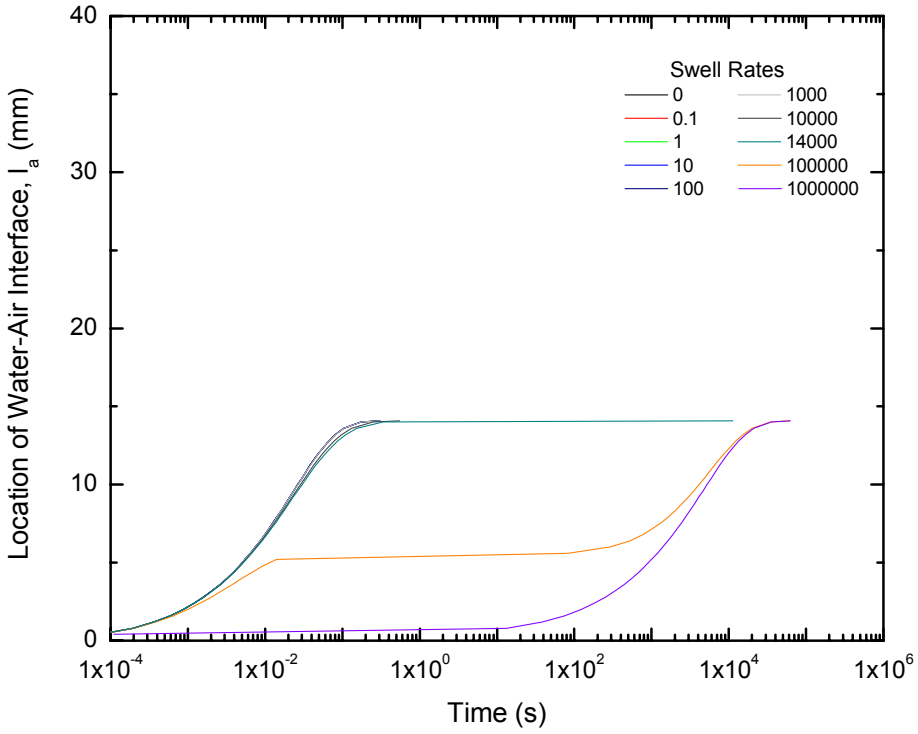

a. Increase initial main diameter (30 μm).

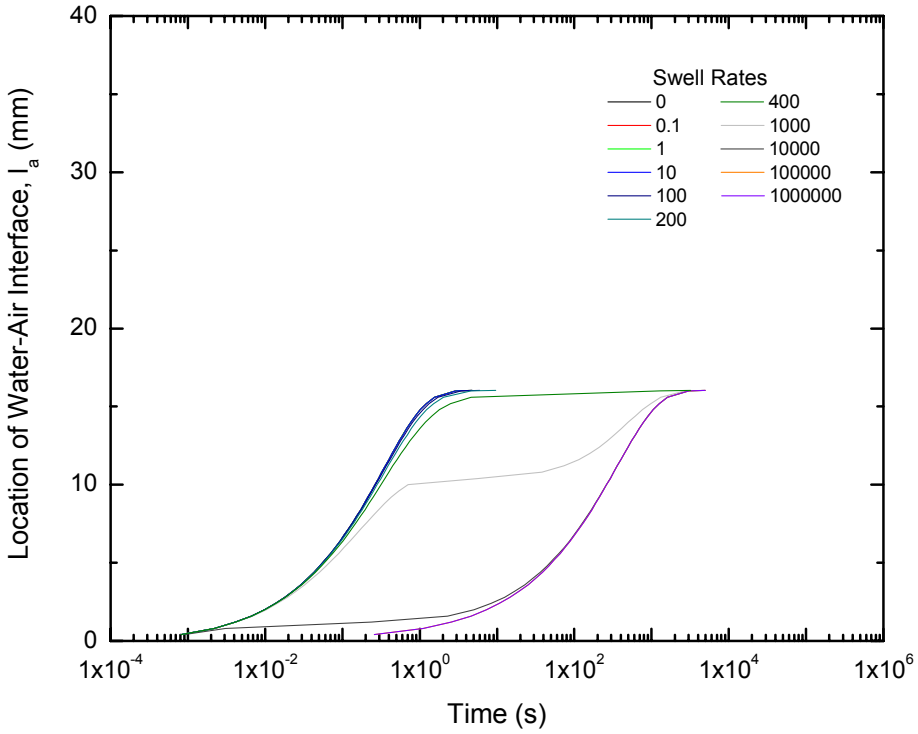

b. Decrease initial main diameter (8 μm).

Figure 8.7. Closed end model Case #1 – initial main diameter (d1).

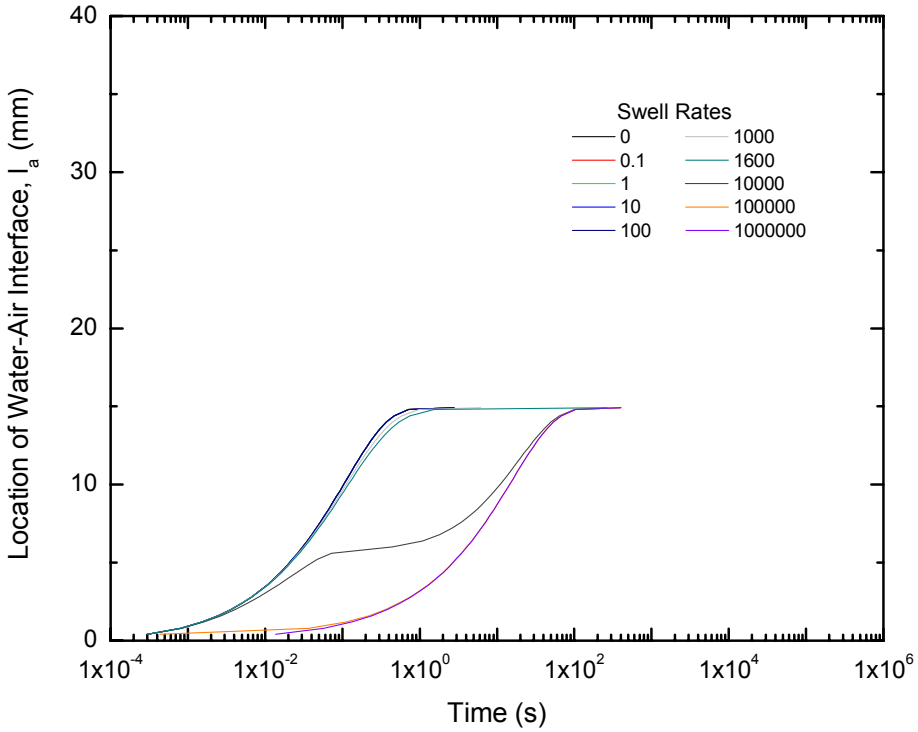

a. Increase minimum main diameter (4 μm).

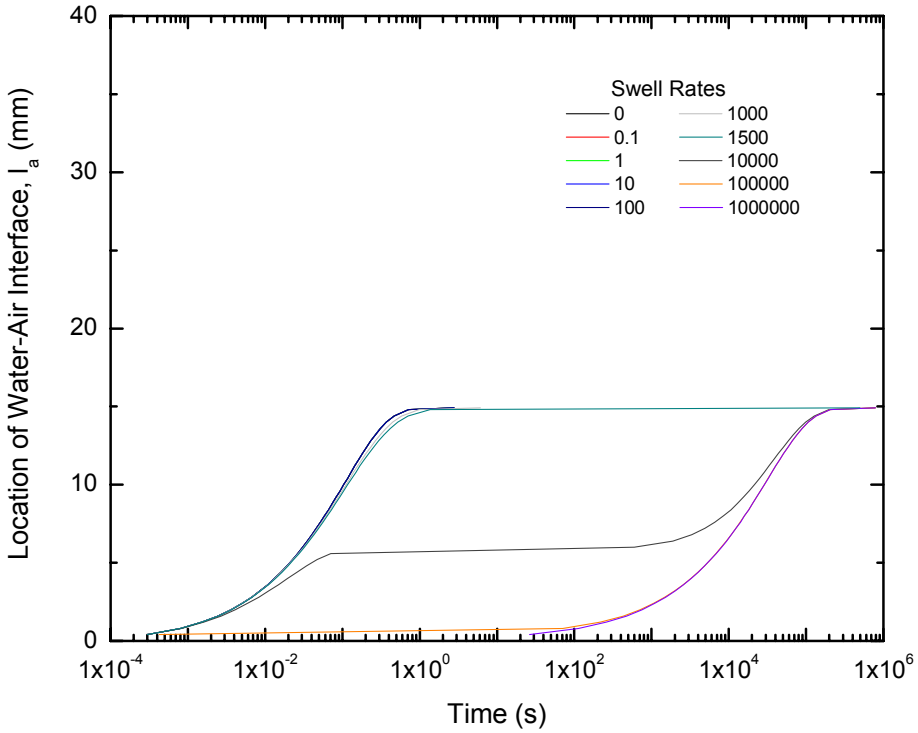

b. Decrease minimum main diameter (0.6 μm).

Figure 8.8. Closed end model Case #2 – minimum main diameter (d2).

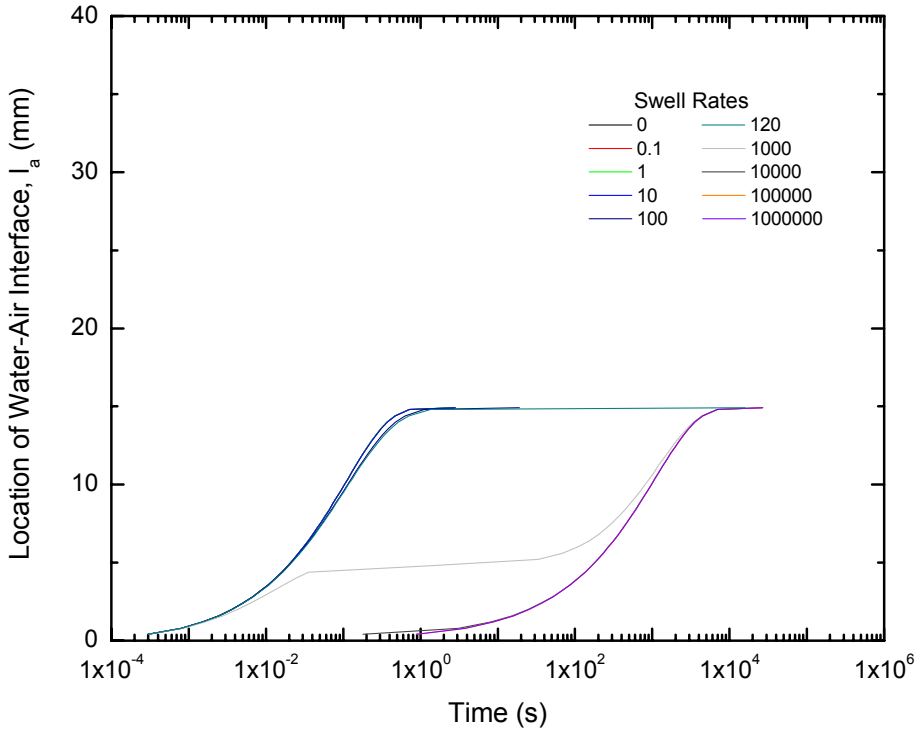

a. Increase peripheral diameter (0.03 μm).

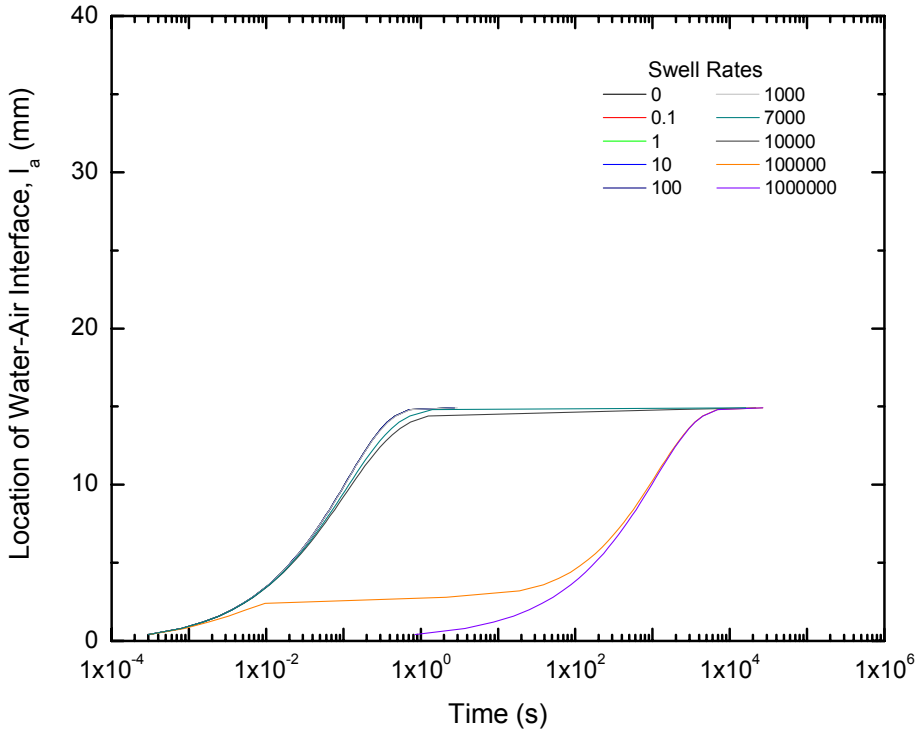

b. Decrease peripheral diameter (0.006 μm).

Figure 8.9. Closed end model Case #3 – peripheral diameter (d3).

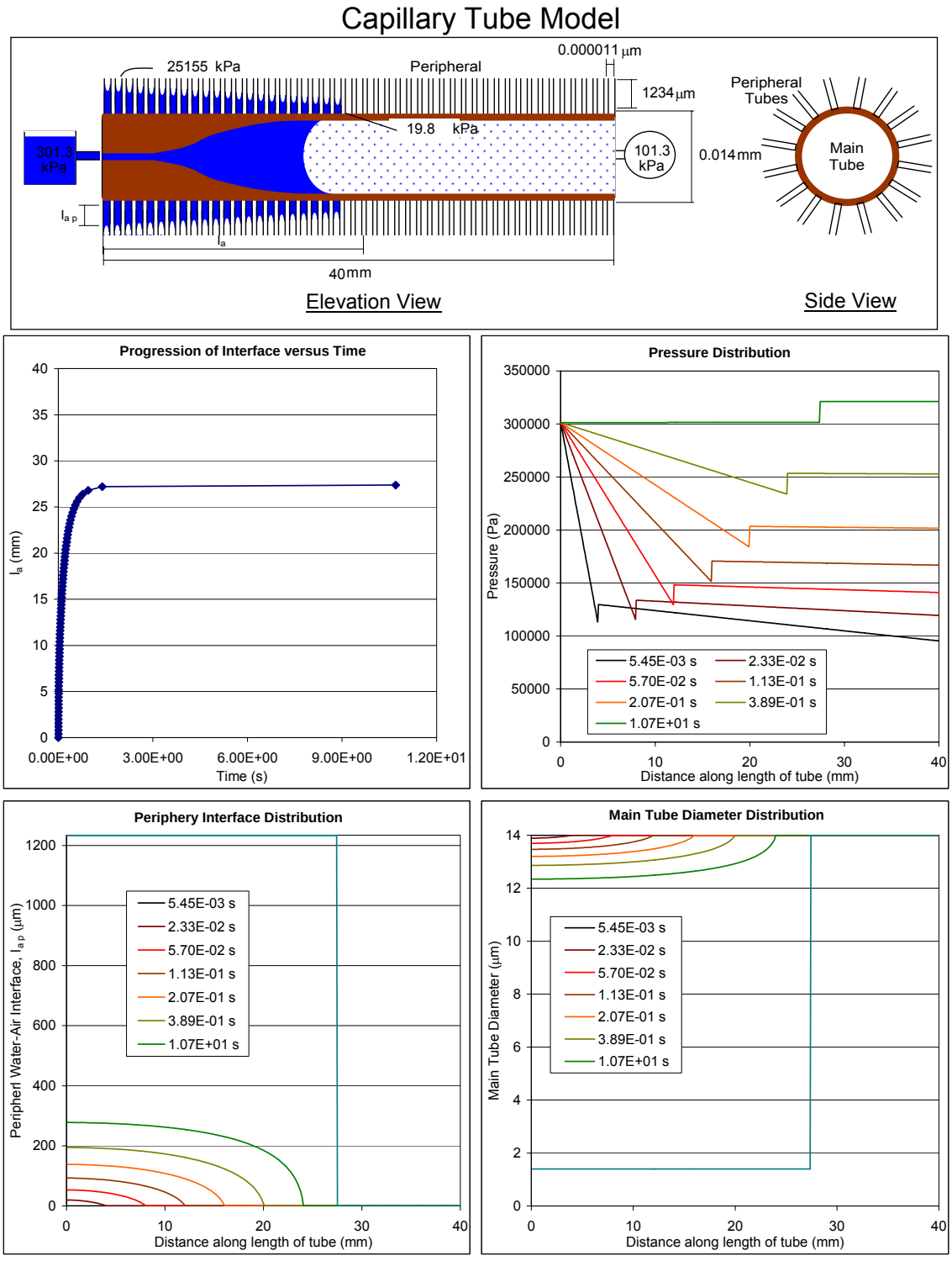

Figure 8.10: Typical output from closed end – low pressure models.

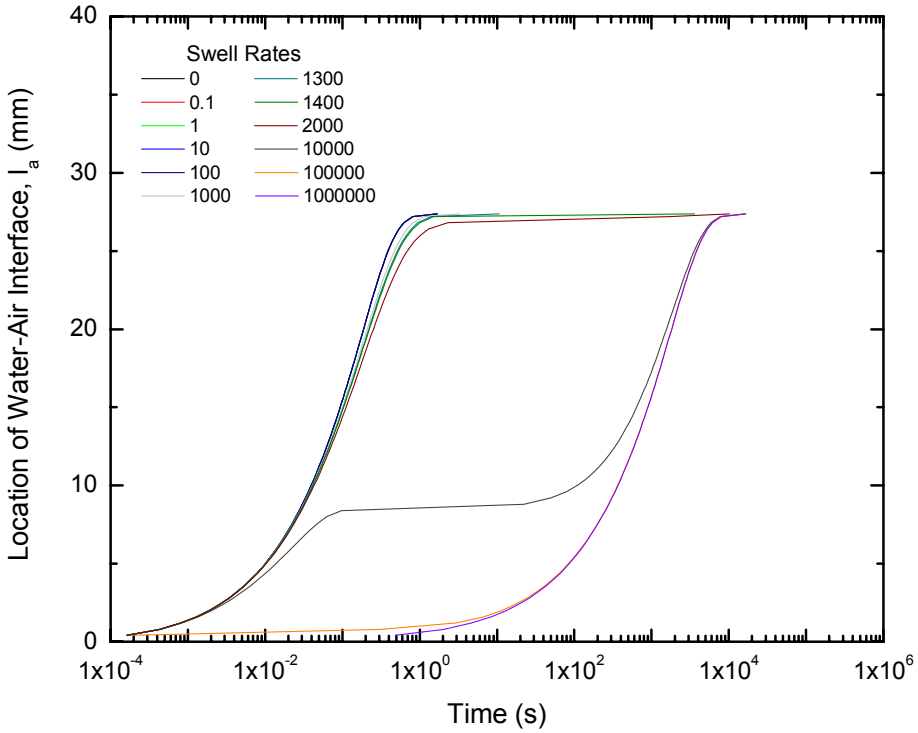

Figure 8.11. Closed end – low pressure model base case: initial main diameter (d1) = 14 μm, minimum main diameter (d3) = 1.4 μm and peripheral diameter (d3) = 0.011 μm.

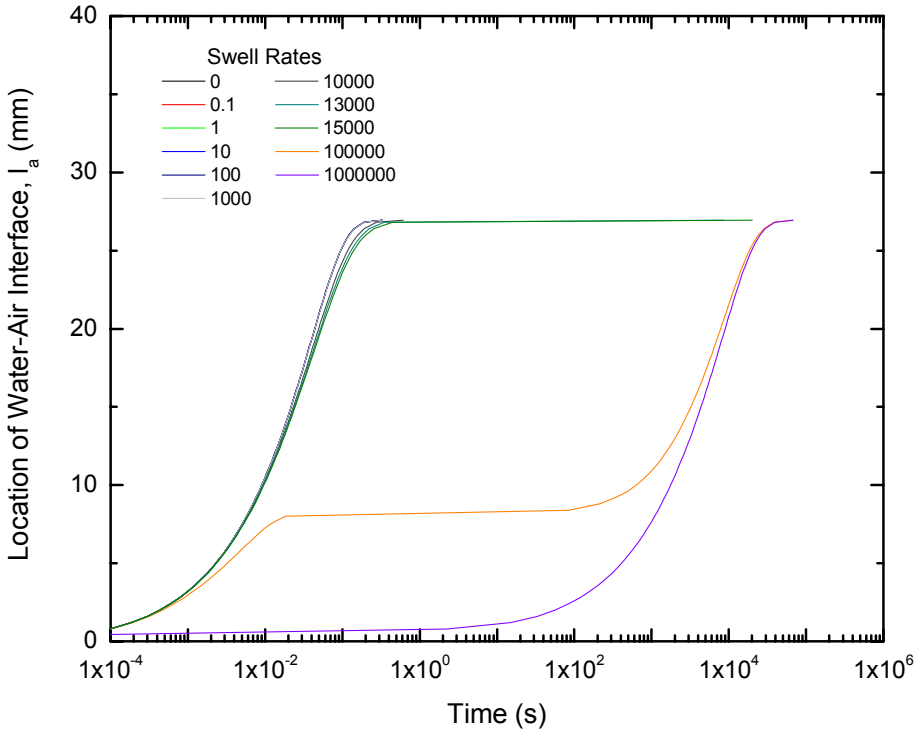

a. Increase initial main diameter (30 μm).

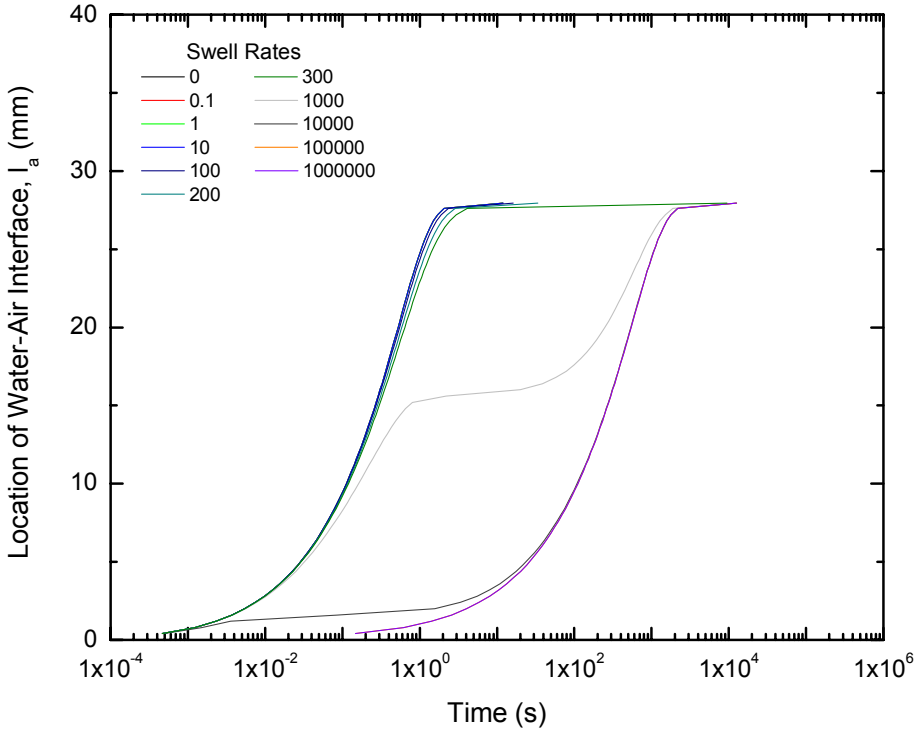

b. Decrease initial main diameter (8 μm).

Figure 8.12. Closed end – low pressure model Case #1 – initial main diameter (d1).

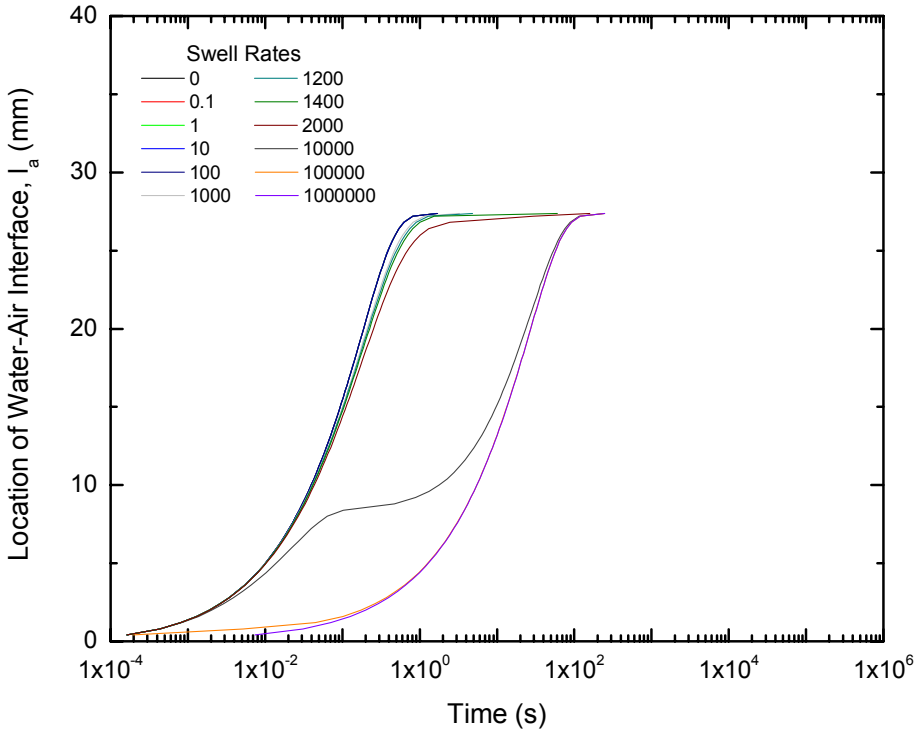

a. Increase minimum main diameter (4 μm).

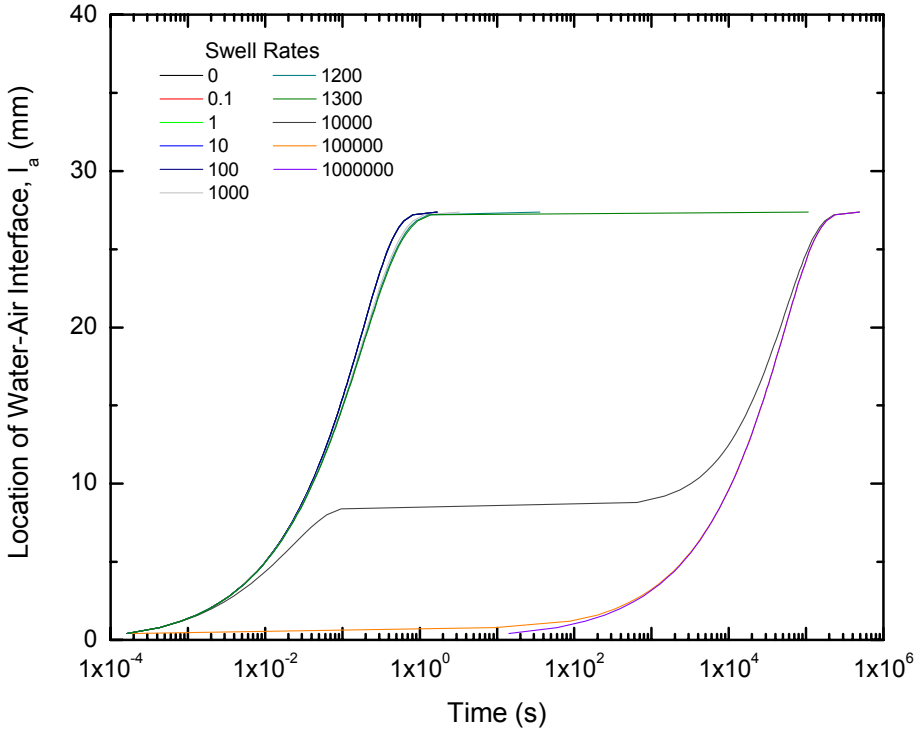

b. Decrease minimum main diameter (0.6 μm).

Figure 8.13. Closed end – low pressure model Case #2 – minimum main diameter (d2).

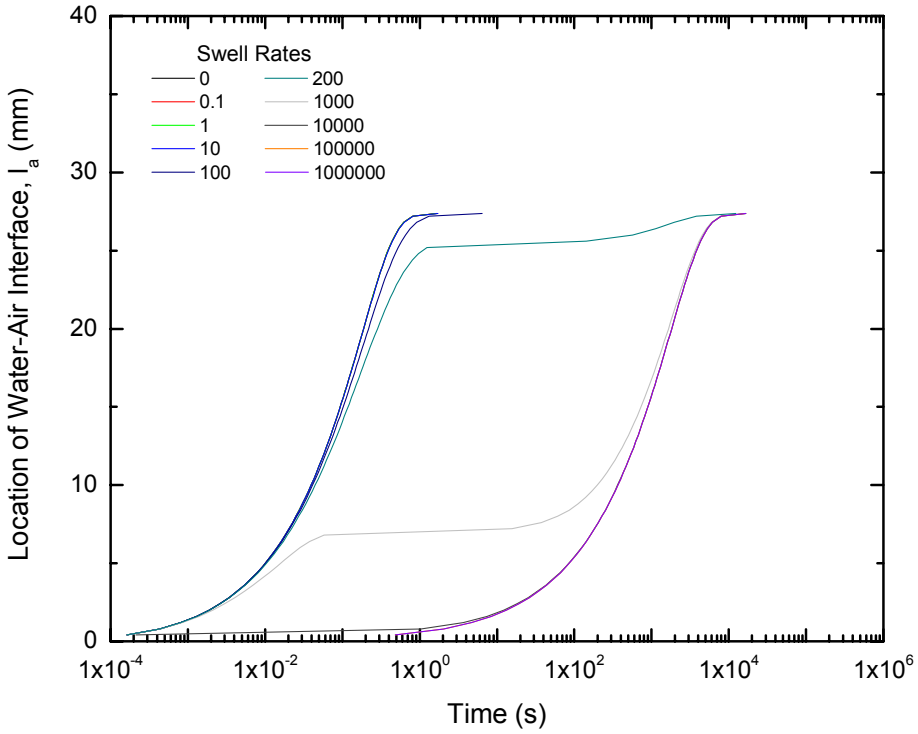

a. Increase peripheral diameter (0.03 μm).

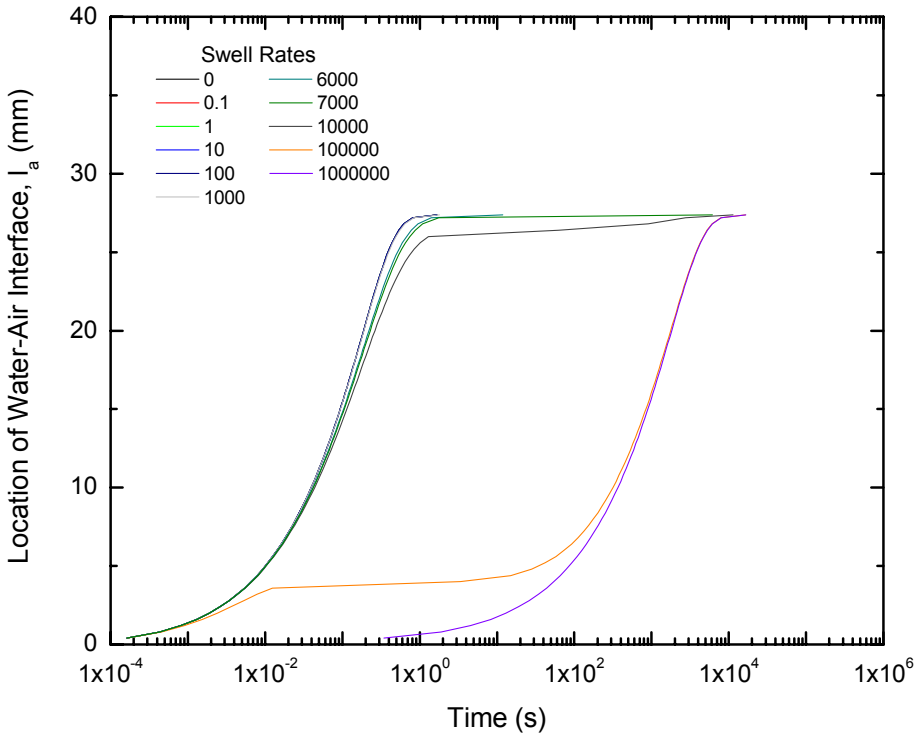

b. Decrease peripheral diameter (0.006 μm).

Figure 8.14. Closed end – low pressure model Case #3 – peripheral diameter (d3).

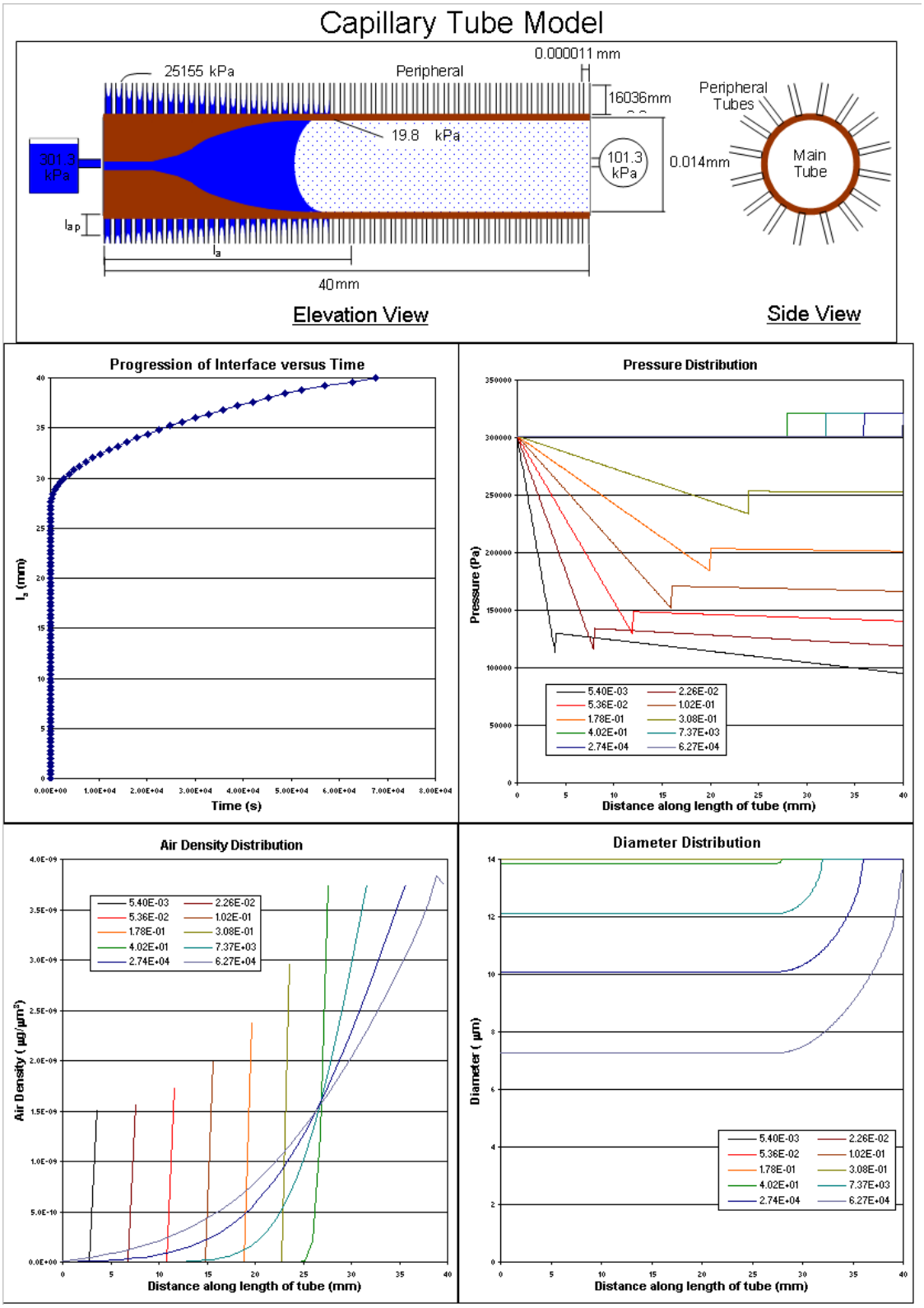

Figure 8.15: Typical output from closed end – diffusion models.

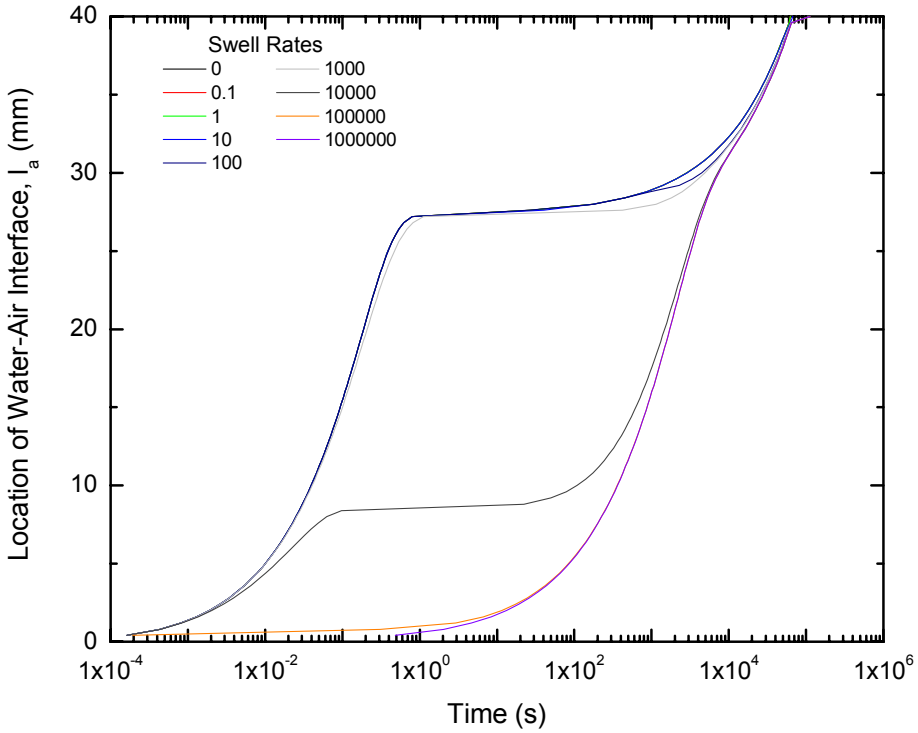

Figure 8.16. Closed end – diffusion model base case: initial main diameter (d1) = 14 μm, minimum main diameter (d2) = 1.4 μm and peripheral diameter (d3) = 0.011 μm.

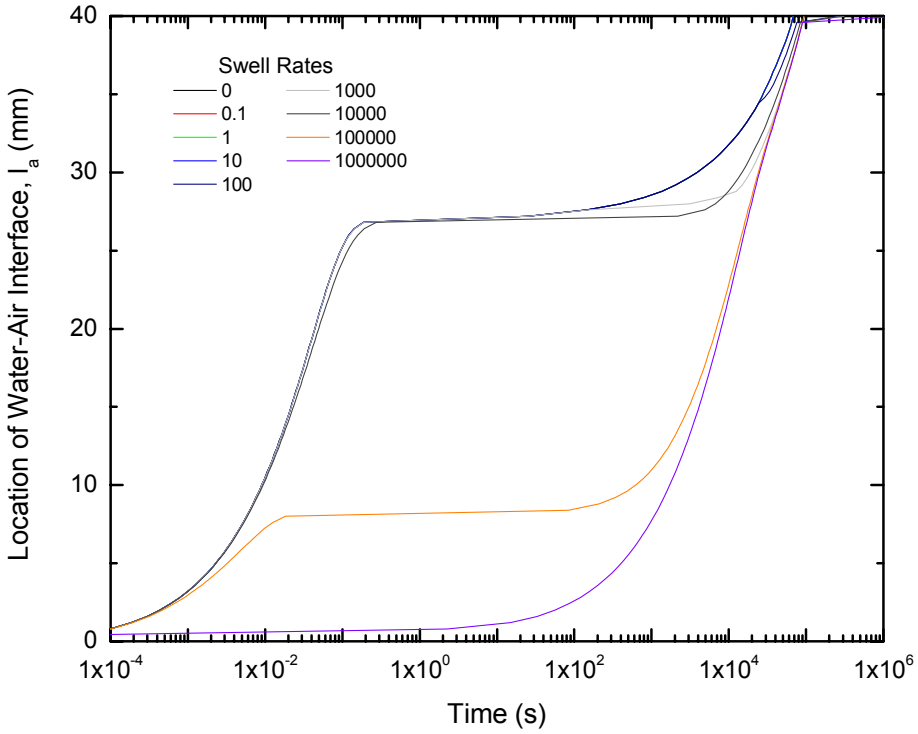

a. Increase initial main diameter (30 μm).

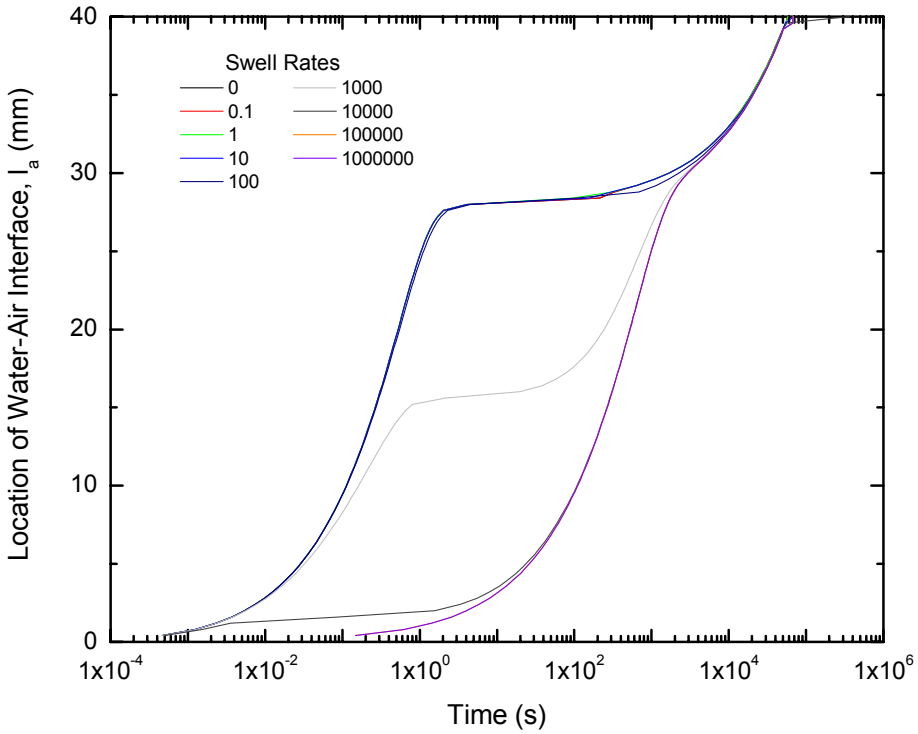

b. Decrease initial main diameter (8 μm).

Figure 8.17. Closed end – diffusion model Case #1 – initial main diameter (d1).

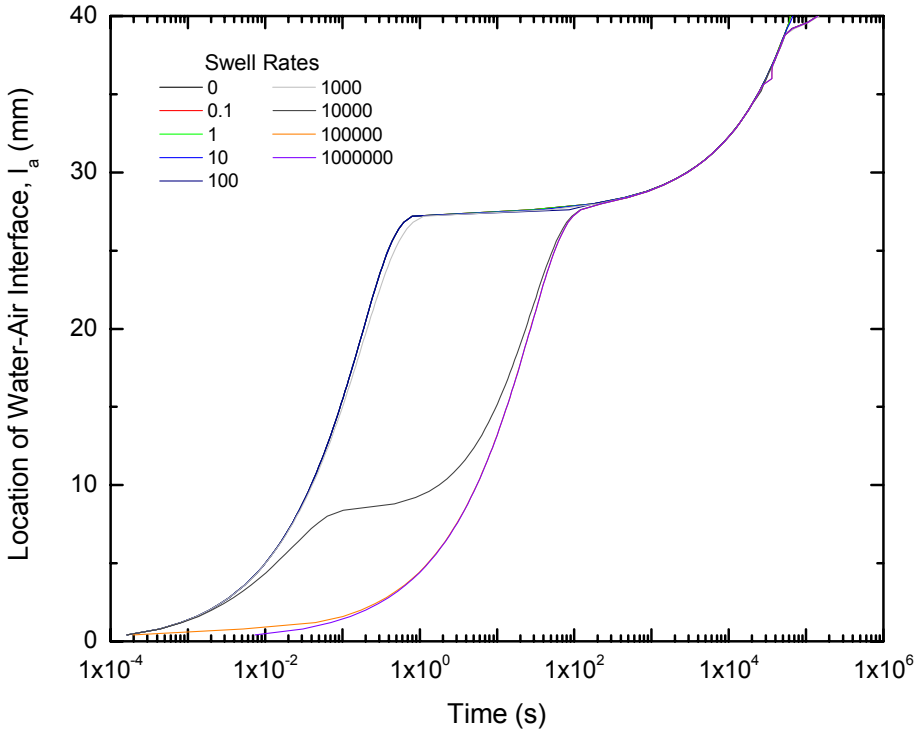

a. Increase minimum main diameter (4 μm).

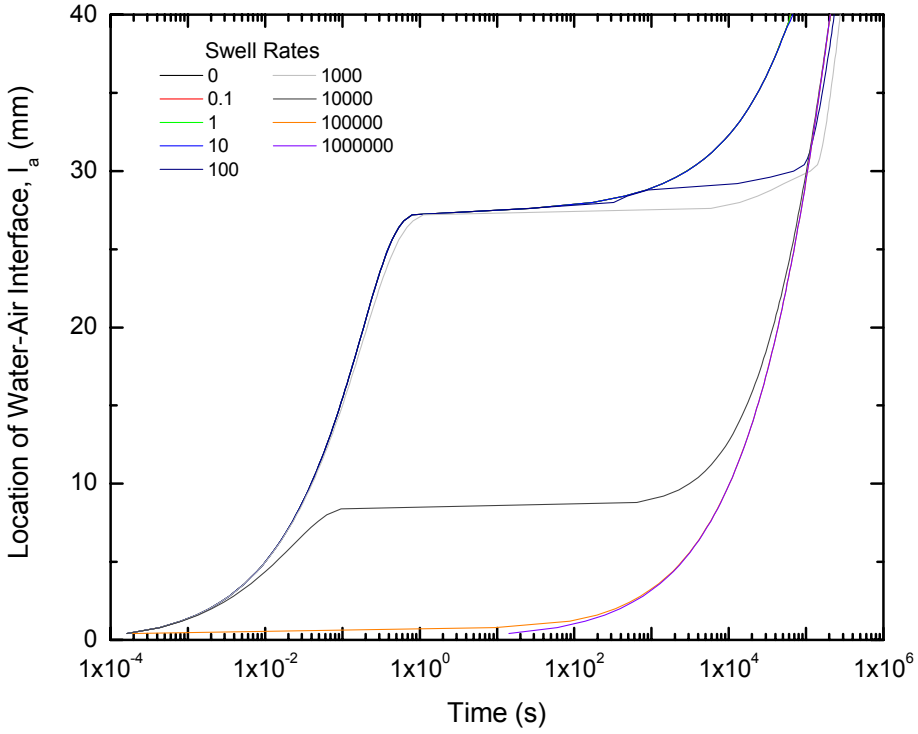

b. Decrease minimum main diameter (0.6 μm).

Figure 8.18. Closed end – diffusion model Case #2 – minimum main diameter (d2).

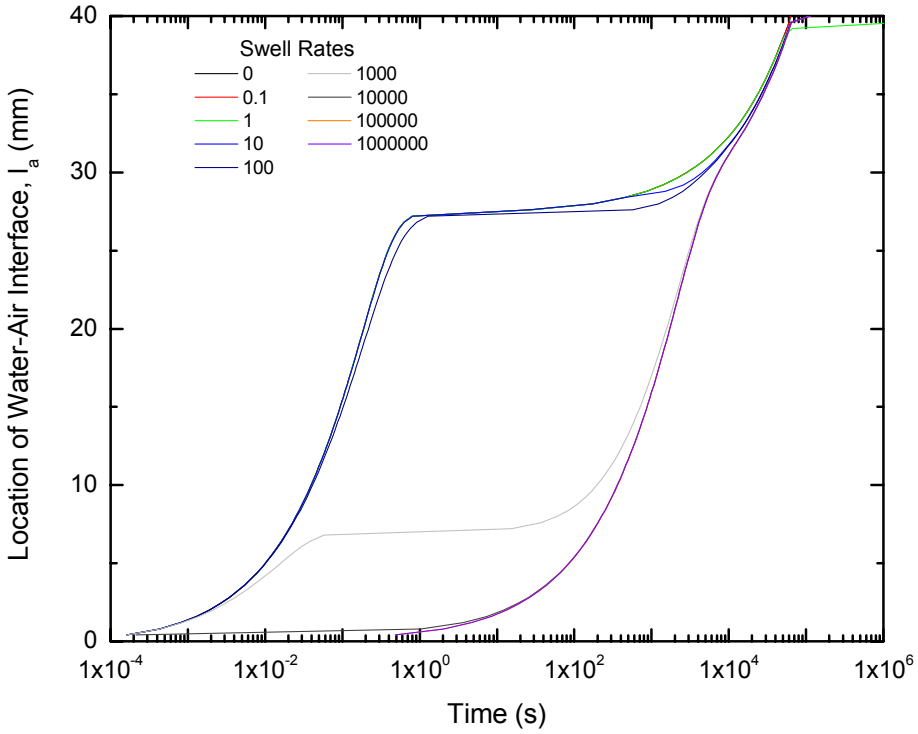

a. Increase peripheral diameter (0.03 μm).

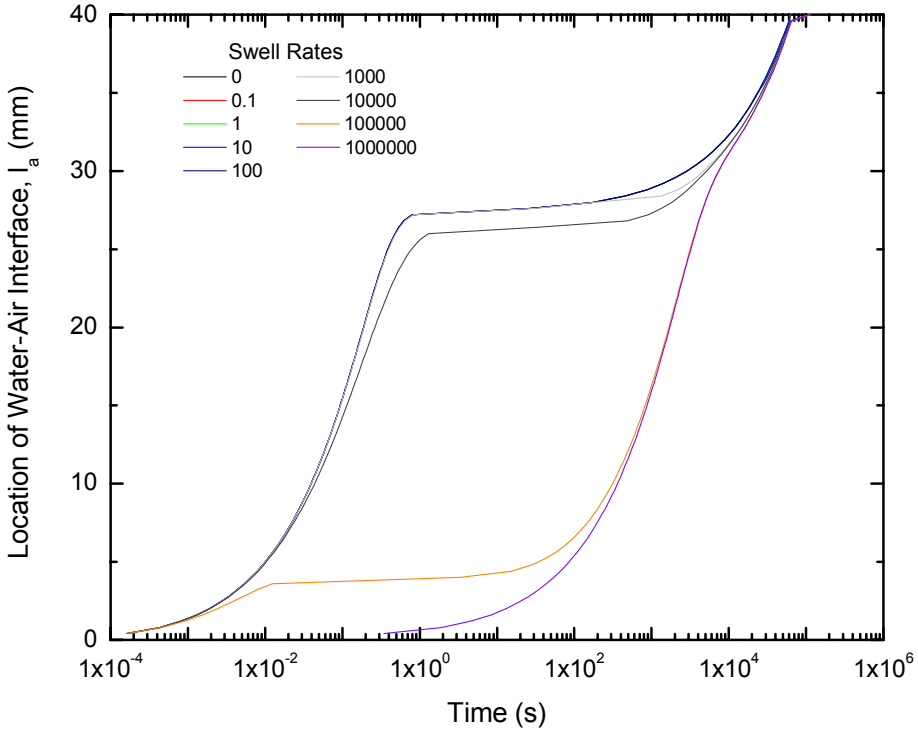

b. Decrease peripheral diameter (0.006 μm).

Figure 8.19. Closed end – diffusion model Case #3 – peripheral diameter (d3).

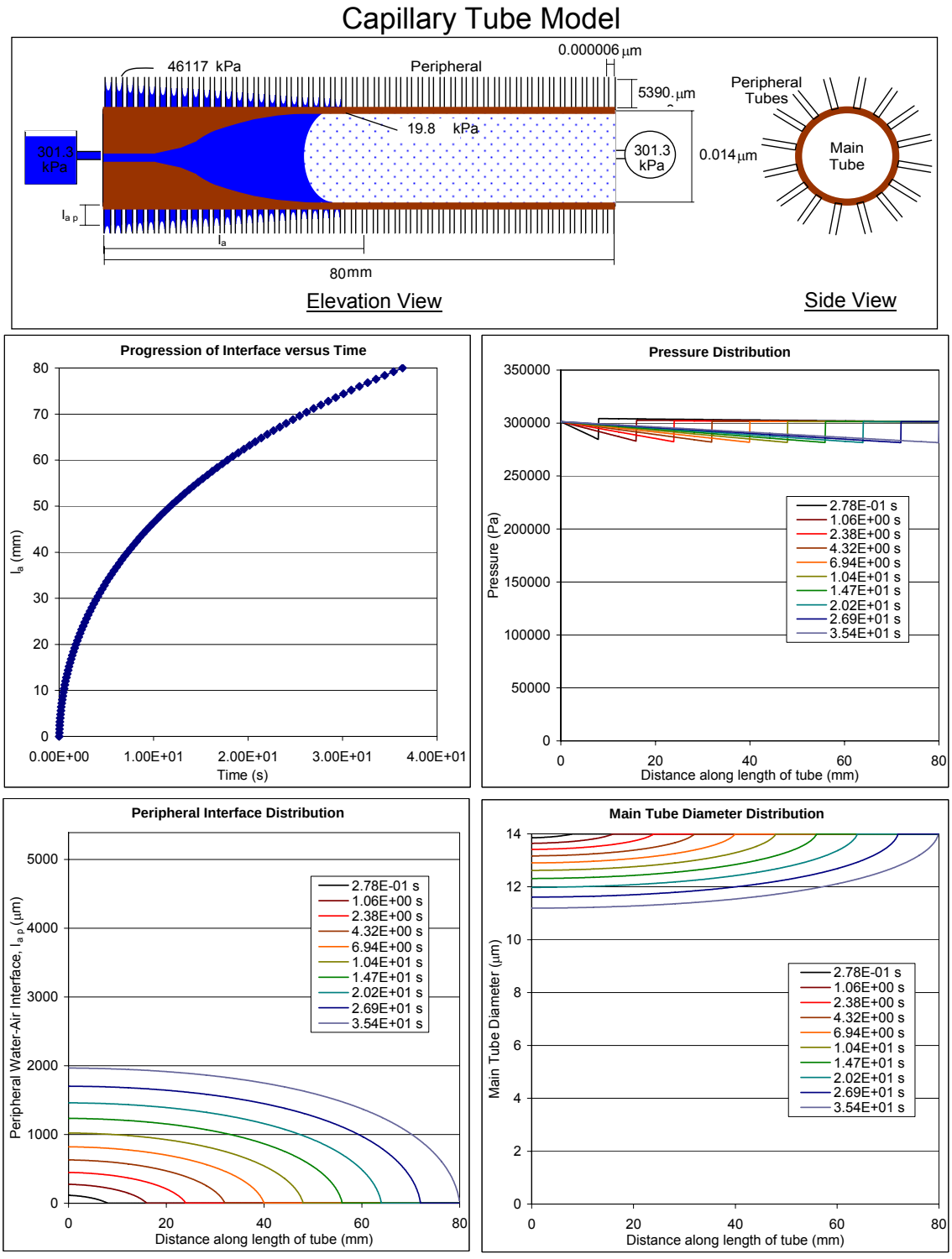

Figure 8.20: Typical output from double length – no gradient models.

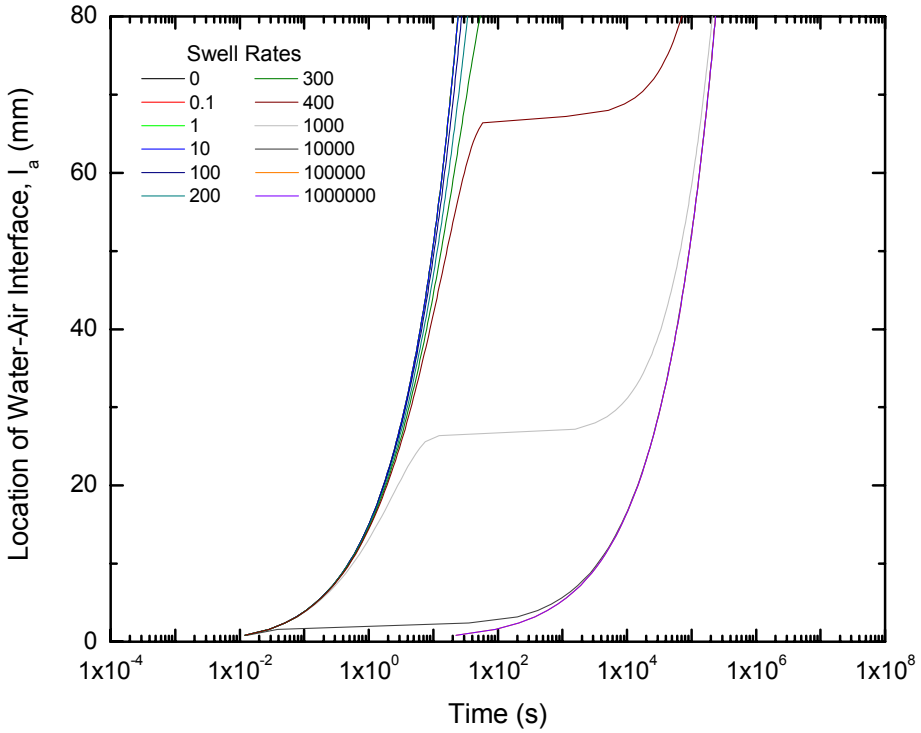

Figure 8.21. Double length – no gradient model base case: initial main diameter (d1) = 14 μm, minimum main diameter (d2) = 1.4 μm and peripheral diameter (d3) = 0.011 μm.

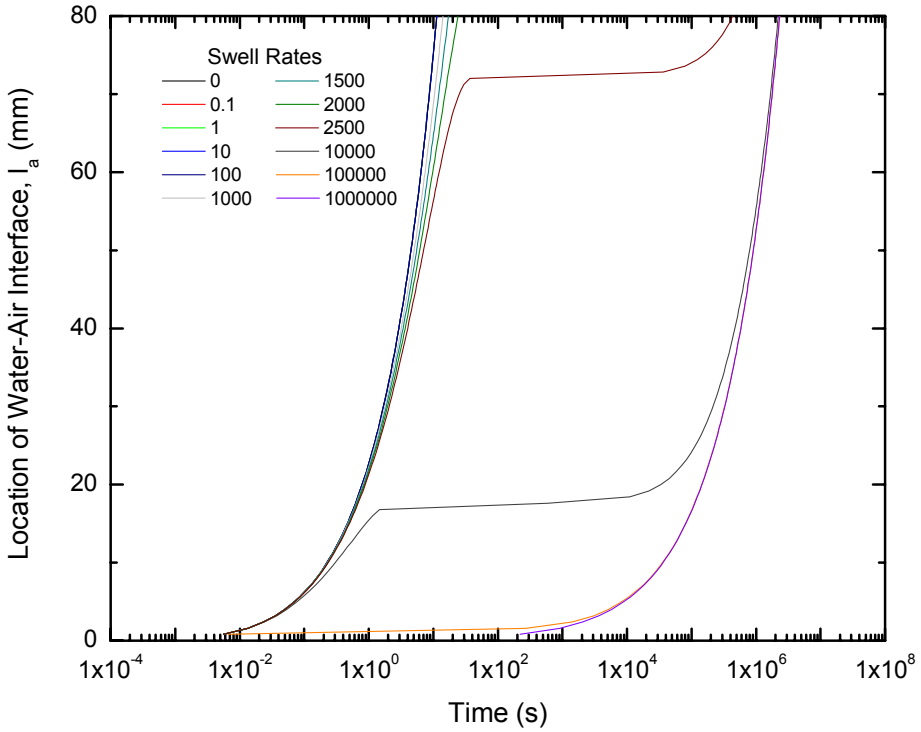

a. Increase initial main diameter (30 μm).

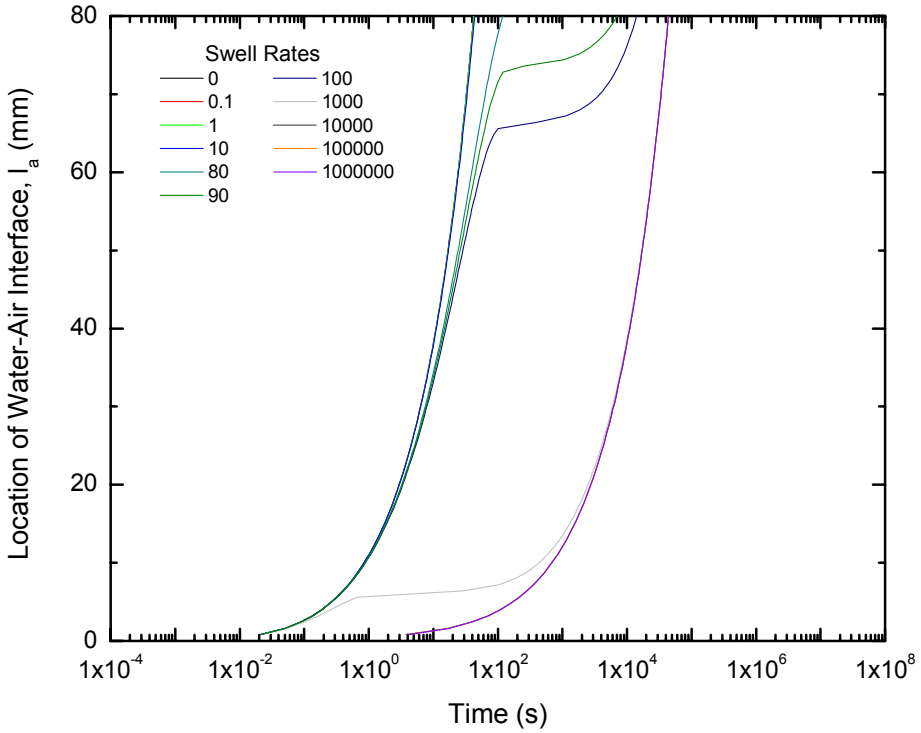

b. Decrease initial main diameter (8 μm).

Figure 8.22. Double length – no gradient model Case #1 – initial main diameter (d1).

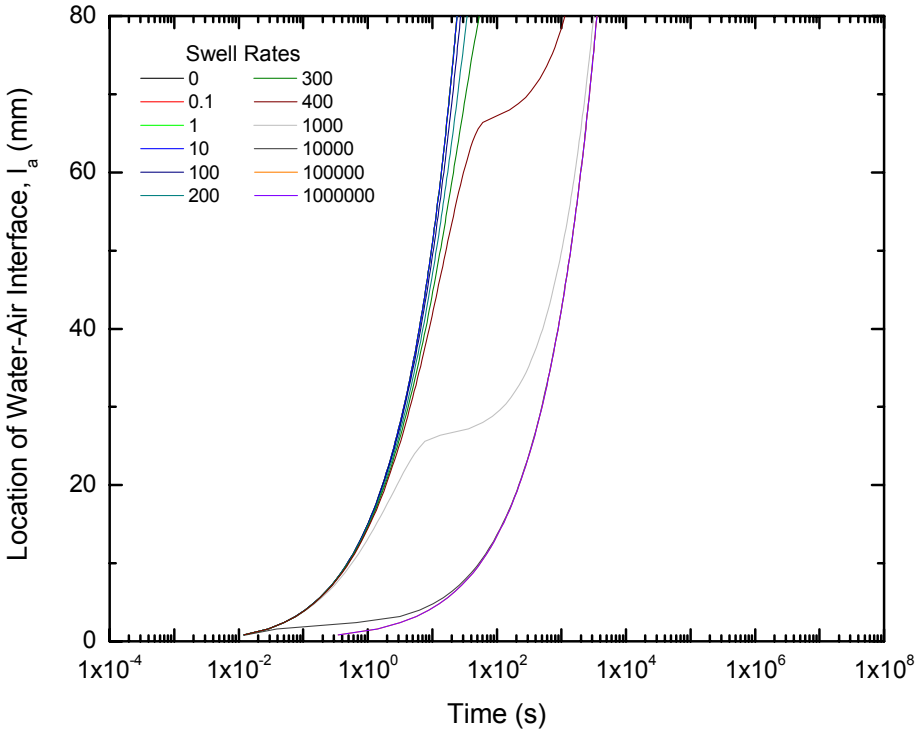

a. Increase minimum main diameter (4 μm).

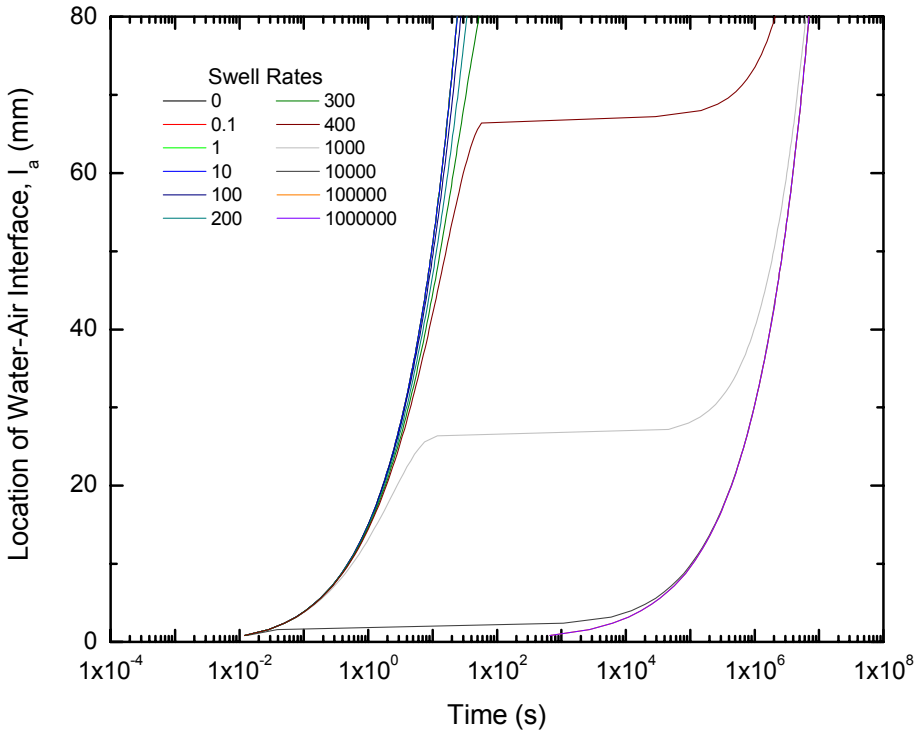

b. Decrease minimum main diameter (0.6 μm).

Figure 8.23. Double length – no gradient model Case #2 – minimum main diameter (d2).

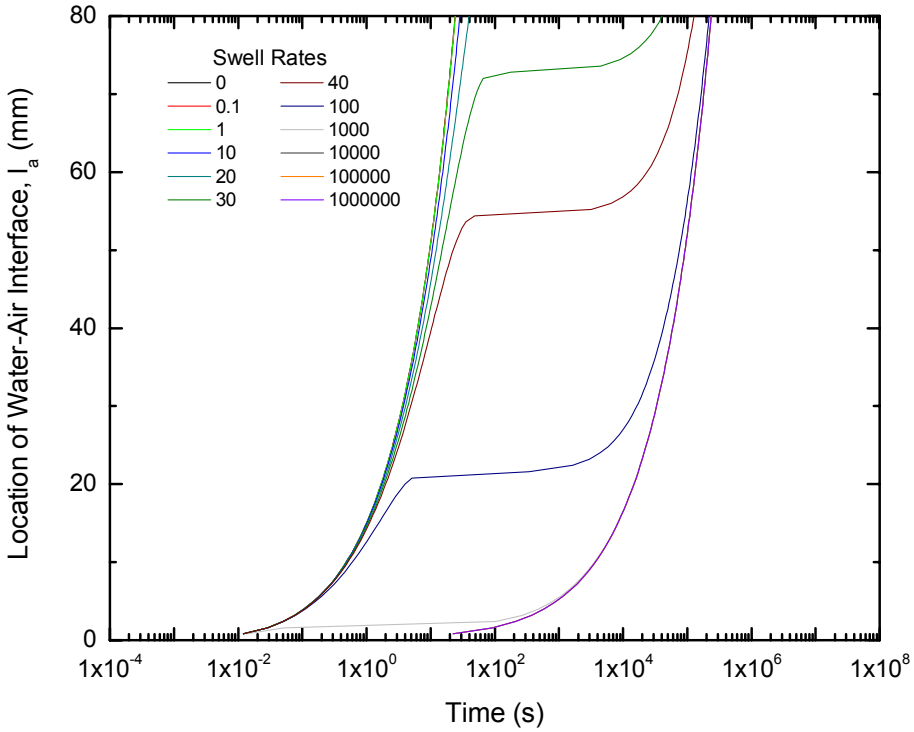

a. Increase peripheral diameter (0.03 μm).

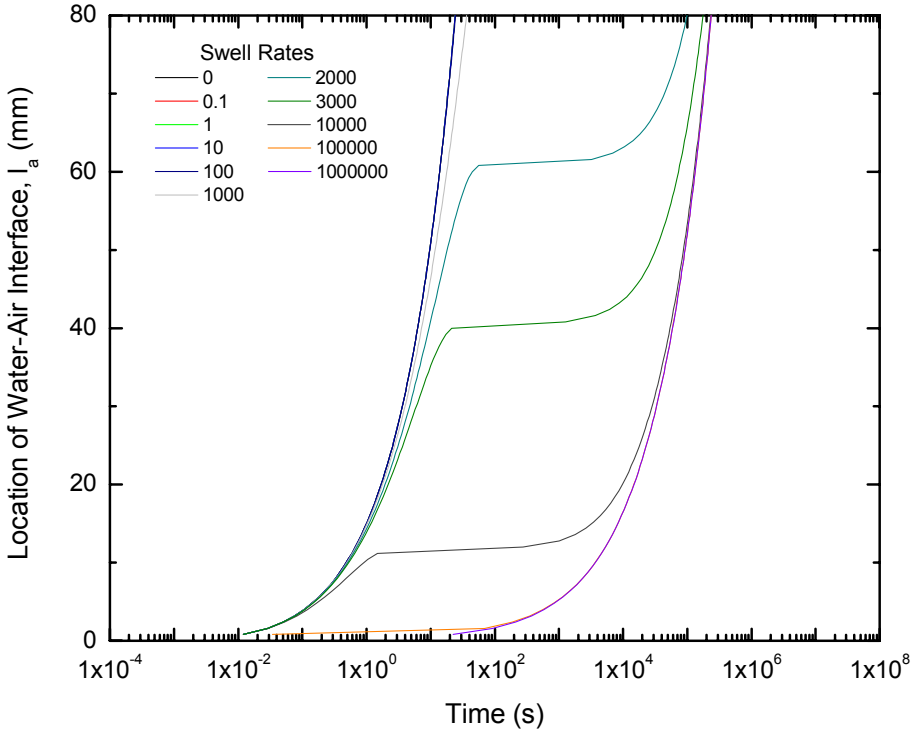

b. Decrease peripheral diameter (0.006 μm).

Figure 8.24. Double length – no gradient model Case #3 – peripheral diameter (d3).

CHAPTER 9: MECHANICAL AND HYDRAULIC MODELING OF INFILTRATION RESULTS[7]

9.1 Introduction

Interpretation of laboratory results by simultaneously considering the hydraulic and mechanical behaviours allows development of a more generalized model to describe the behaviour of unsaturated swelling clay soils. Thus far, results from both a new laboratory infiltration test apparatus with controlled boundary conditions, and a capillary tube model that incorporates a swelling mechanism, have been presented. This chapter provides interpretation of the results in the form of mechanical and hydraulic models.

---

[7] A version of this chapter will be submitted as:
Siemens, G.A. and Blatz, J.A. Modeling hydraulic-mechanical behaviour of unsaturated swelling soil during liquid infiltration under controlled boundary conditions. *In Preparation*.

Modeling of the laboratory test results reveals limits in the mean stress – water content – specific volume states for swelling soil specific to the hydraulic and mechanical conditions applied during testing. The contribution of this research, which to the author's knowledge has not been previously performed, is to show that the infiltration boundary conditions dominate behaviour of swelling clay-sand soil.

Hydraulic modeling is performed to represent the laboratory results with capillary tube data. Since the laboratory specimens have infiltration from their entire perimeter, while the capillary tube model represents flow through a single pore, normalization of the results must be performed to allow for direct comparison. The results show how the boundary conditions and main tube area control flow through the capillary tube, and that they capture behaviour observed in the laboratory specimens. Flow results are also represented using a hyperbolic empirical model as well as D'Arcy's Law.

Finally some additional findings and observations are presented including a new three-dimensional water retention curve (WRC) based on experimental data, comparisons with Atomic Energy of Canada Limited's previously published laboratory and full-scale test results, and evidence for anisotropic behaviour in the compacted specimens.

9.2 Modeling of Unsaturated Swelling Soil Behaviour

A limit in mean stress – water content – specific volume for unsaturated swelling soil shown in this section using the laboratory results presented in Chapter 6. The 250 kPa infiltration tests are interpreted in detail, and then the model is defined to predict swelling behaviour. A surface that limits swelling behaviour is proposed and trends in swelling behaviour are predicted based on altering initial water content and volume.

9.2.1 250 kPa Infiltration Test Interpretation

Interpreted results from the 250 kPa infiltration tests are shown in Figure 9.1, Figure 9.2, Figure 9.3, and Figure 9.4 as total specific volume versus mean stress, gravimetric water content versus mean stress, suction versus mean stress, and total specific volume versus gravimetric water content respectively. Specific volume and gravimetric water content are calculated based on the initial measurements and the break up specimens along with the laboratory test measurements. They are both representative of the entire specimen. During infiltration, the constant mean stress test (CMS) plots as a vertical line along with the 250 kPa constant mean stress - drained (CMSD) test. The x = -25kPa/% and x = -75kPa/% constant stiffness tests (CS25 and CS75 respectively) plot along the applied slopes, and the 250 kPa constant volume test (CV) is shown as a horizontal line. All specimens have nominally similar initial water content and density from the mixing and compaction process. Following isotropic compression, all five (5) specimens are at the same mean stress, volume, water

content, and suction states. Therefore the influence of boundary conditions can be observed directly.

Gravimetric water content and suction responses versus mean stress (Figure 9.2 and Figure 9.3) show they are related to the boundary conditions. Greatest expansion and water content increase occur in the CMSD and CMS tests although end of test suction values are similar. Although assumed suction values were added due to malfunctions in the Xeritron sensor, the added values are plausible as a result of increasing water content and increasing mean stress conditions during individual tests combining to reduce suction from the as-compacted value. End of test suction values are likely within a 200-300 kPa range for all tests with the main component being the osmotic suction.

During infiltration, the magnitude of water content increase is limited by the boundary condition imposed (Figure 9.2) and the physical limits of the soil. Because the specimens are prepared using the identical procedure and brought to the same initial stress and volume states, the clay particles in each specimen have the same swell potential at the beginning of infiltration. As the clay particles are given access to water, they expand. This includes expansion of the clay peds into the macro pore space, as well as bulk expansion of the specimens, depending on the boundary condition. Constant volume boundary conditions do not allow bulk expansion, while constant stiffness allows expansion against a flexible spring type boundary. Constant mean stress allows the clay peds to

expand to their limit given initial conditions. Increasing the mean stress during infiltration, against which the clay particles swell, reduces total water infiltration. Although even the constant volume specimen still takes in water as it is initially unsaturated.

Figure 9.4, which is gravimetric water content versus total specific volume, illustrates the rationale for the limit in water content increase. As liquid infiltration continues, specimens reach an apparent limit to water content increase against which they cannot take in any more water without increasing in volume. The boundary conditions imposed during liquid infiltration limit expansion along a mean stress – specific volume relationship. Both the CV and CS75 specimens increase in water content up to the limit and then no further water content increase nor volume expansion occurs. The CS25, CMS and CMSD specimens expand up to the apparent limit and then follow the limit until no further infiltration is observed.

The post-test distributions, shown in Figure 9.5, Figure 9.6, Figure 9.7, and Figure 9.8, illustrate the boundary condition controlled bulk behaviour observed during the tests, as well as internal behaviour that cannot be measured from the perimeter of the specimen. Gravimetric water content distributions (Figure 9.5) are non-linear for all specimens. Water content is greatest near the perimeter. Even in the drained specimen, that experienced infiltration for 250 days, the average center measurement is lower than the perimeter. At the perimeter, there

is no soil to push against in order to expand, while soil at the center must push against the remaining specimen. This does not allow the same water content to be achieved at the center as the perimeter. The dry density distributions (Figure 9.7) also illustrate the influence of boundary and flow conditions. The CMSD specimen swells the most and results in the lowest dry density. The CV specimen has the greatest dry density since no bulk expansion was allowed during infiltration. Again non-linear relationships are observed for dry density, as anticipated, since it is related to water content at the end of test. As water infiltrates from the perimeter, expansion occurs there first and proceeds as infiltration continues. Clay ped expansion continues until it comes into balance with the imposed boundary conditions. If overall specimen volume is held constant and expansion is occurring at the perimeter, compression at the center of the specimen is also expected under these boundary conditions. For the CV, CS25, and CMS specimens, the highest dry density is observed at the middle measurement between the center and perimeter. This could be due to the small volume of soil used for the center measurement as a result of the presence of the sensor and wire in the top three (3) layers, or some effects of the sensor during the test. Finally, the saturation results, shown in Figure 9.8, give further evidence for the influence of boundary conditions. The CMSD test achieves the greatest degree of saturation followed by the CMS and CS25 tests, and then the CV and CS75 tests. Expansion of the specimen allows further access of water into the specimen and raises saturation closer to the center.

The 250 kPa tests give clear insight into the influence of the boundary conditions on the behaviour of swelling soil during liquid infiltration. The boundary conditions limit overall specimen volume until they reach the water content – specific volume limit, after which infiltration is halted or continues along the limit if expansion is allowed. In numerical modeling of swelling soil systems, the boundary condition must be defined in order to properly predict behaviour. The post-test measurements show gradients in phase relationships within specimens that also would need to be accounted for in modeling.

9.2.2 Swell Limit Definition

A swell limit in mean stress – water content – specific volume is defined in this section. Previously, the 250 kPa liquid infiltration tests were presented and the influence of boundary conditions on the swelling behaviour shown. In this section, discussion is extended to include all infiltration tests completed in this study.

Results from all infiltration tests under controlled boundary conditions are shown in Figure 9.9, Figure 9.10, Figure 9.11, and Figure 9.12, as total specific volume versus mean stress, water content versus mean stress, water content versus total specific volume and suction versus mean stress. A summary table is also provided in Table 9.1. The 250 kPa tests discussed in the previous section are plotted along with the 500, 1000, and 1500 kPa liquid infiltration tests under constant mean stress, constant stiffness, and constant volume boundary conditions. Behaviour, observed at the 250 kPa isotropic compression level, is

similarly observed at the higher mean stress values except at a reduced magnitude. As illustrated in Figure 9.9, less expansion is observed in the CMS, CS25, and CS75 tests, and less mean stress increase is observed in the CV tests at the higher levels. This is reflected in Figure 9.10 as water content increases being not as great for the higher pressure tests.

As mentioned earlier, all specimens are prepared at same nominal water content and density. During isotropic compression, specimens compress and the void space is reduced. Higher isotropic compression levels result in further compression and reduction of the macro pore space available for liquid infiltration. Also, the stress which the clay particles push against when they get access to water is greater, thus restricting expansion. During liquid infiltration, greater initial mean stress allows less expansion and less water infiltration. The controlled boundary conditions set the volume – mean stress relationship that is followed. Figure 9.11 illustrates that the limit which was proposed, based on the 250 kPa tests, is valid over a wider range of specific volumes. During infiltration, water uptake continues until the limit is reached after which further water content increases can only occur with expansion of the specimen. The upper bound of water content versus specific volume appears to be a linear relationship. Finally, suction versus mean stress results (Figure 9.12) show that all specimens end up with similar suction levels despite gravimetric water contents ranging from approximately 20% – 54%. This figure suggests a three-dimensional WRC is

necessary to describe the behaviour of soils that experience volume changes during changes in suction.

From the experimental evidence, a physical limit to swelling is evident as a function of gravimetric water content and specific volume. The limit appears linear over a wide range of water contents and specific volume. To allow analysis, the end of test (equilibrium) states of water content, mean stress, and total specific volume were plotted in Figure 9.13 and Figure 9.14. A second order decaying exponential function is fitted to the water content versus mean stress data and a linear function to the water content versus specific volume. The plots show R^2 values of 0.91 and 0.99 calculated for the two fitted curves respectively. Extrapolating the exponential function to high mean stress values predicts that the initial water content is maintained as the constant in the exponential function is 18.75%. This makes sense intuitively because if initial mean stress was increased to an extremely high level, compression of the macro pore space could eventually result in a saturated material that would not expand due to the high stress boundary it would have to swell against.

The state at which the swell – water content limit is reached is a function of the boundary conditions applied during infiltration and initial conditions. In water content – specific volume space (WC-V, Figure 9.11), CV specimens proceed along a vertical line up to the limit. The other applied boundary conditions allow expansion so angled lines are plotted in WC-V space. Once the limit is reached

under boundary conditions that allow deformation, the limit is followed as long as the clay particles have remaining potential to expand. Once the swell potential is used up, no further expansion occurs and thus, no increase in water content. The boundary conditions applied during liquid infiltration dominate behaviour during water uptake.

Viewing the laboratory data in mean stress – specific volume – gravimetric water content space (p-V-WC) shown in Figure 9.15, allows complete understanding of the behaviour observed. Also shown in the plot is the limit identified in Figure 9.13 and Figure 9.14, plotted as a thick line. During isotropic compression, volume decreases while water content remains constant. During liquid infiltration, the boundary conditions are followed in p-V space throughout. Water content increases during this time and the specimens always go towards the upper bound until it is reached. After this point, only further expansion allows further water content increases although the boundary conditions still dominate the path followed. At the end of tests, all specimens lie on the p-V-WC limit.

9.2.3 Predictions Using New Swell Limit

Altering initial conditions of specimens would change the starting points prior to infiltration but the same limit in water content – specific volume space would eventually be reached during liquid infiltration. This limit appears linear over a wide range of volumes and water contents and likely is specific to the preparation conditions, including mixing water content and initial specific volume. If specimens were dried prior to infiltration, this would only alter the initial state

based on the induced changes to water content and volume. The boundary conditions applied during liquid infiltration would still dominate behaviour and the water content – specific volume limit would eventually be reached.

On the other hand, drying specimens (increasing suction) prior to infiltration would affect the water content – mean stress limit shown in Figure 9.13. As shown on the figure, the constant in the fitted exponential curve is approximately equal to the initial water content. At extremely high initial mean stress levels, this model predicts no (or very little) water uptake by the soil. The 1500 kPa tests only took in between 5.1 - 5.7 mL of water although a 500 kPa mean stress increase occurred during the 1500 kPa CV test. If the initial water content is decreased the shape of the water content – mean stress end of test limit is predicted to be an exponential, but the constant would be the initial water content prior to infiltration. This indicates that an initial mean stress exists above which no (or little) water inflow can occur, specific to this water pressure, regardless of the boundary condition imposed during infiltration. As initial water content decreases, the mean stress required to maintain initial conditions would have to increase due to the increased swell potential. Thus, the other parameters in the fitted curve would also change but the general shape would be predicted to remain an exponential.

9.3 Hydraulic Models for Unsaturated Swelling Soil Behaviour

Modeling the hydraulic behaviour of swelling soil must be completed in order for accurate predictions of the behaviour with time. The previous section described an extended model that predicts expansion and end of test mean stress behaviour but does not provide predictions on the length of time required for those changes to occur. This reinforces the intimate linkage between hydraulic and mechanical behaviour. Several hydraulic models were described in the literature review provided in Chapter 2. In this section, the capillary tube model results are linked to the laboratory data to show insights into swelling soil behaviour. The undrained infiltration results are also represented using an empirical hyperbolic model and the drained results are interpreted using D'Arcy's Law.

9.3.1 Undrained Laboratory Test Modeling With the New Capillary Tube

Capillary tube models allow insight into mechanisms occurring on the micro scale. Discussion presented in Chapter 8 revealed briefly how the capillary tube flow results are similar to the laboratory data.

Flow into the laboratory specimens comprises water entering the specimen from the entire periphery, while the capillary tube represents just one (1) microscopic tube out of the millions which comprise the sample. Therefore, to allow comparison, flow data must be normalized. For initial comparison, the constant

volume and constant mean stress infiltration data are used. Later, the model will be generalized.

Actual data from the closed – low pressure and closed – diffusion models along with CV and CMS infiltration data is shown in Figure 9.16a-d. Capillary tube data are presented in terms of inflow versus time as opposed to location of water-air interface versus time as was shown in Chapter 8. The CS25 and CS75 infiltration data are very similar to the CV in terms of flow modes observed so they are not explicitly included in this discussion. The CMS data did not have such a distinct end of flow, especially in the 250 kPa CMS test, so it is included in the discussion. The laboratory data is zeroed so that all infiltration begins at the left axis. The base capillary model (d1 = 14 μm), along with the initial main tube diameter models for both tube model types, are also plotted. Larger initial main tube diameter represents a lower isotropic compression level as the macro porosity is compressed less.

Similar flow modes are observed for each boundary condition type, with the 250 kPa tests generally taking in the most water as well as having the greatest initial inflow rate. Similarly, the 30 μm tube model also takes in the highest volume of water and has the highest initial flow rate. In the CV specimens, the initial flow rate decreases rapidly at the beginning of tests until it reaches an extremely small inflow. In the CMS tests, the behaviour is not so distinct but occurs over a longer length of time. In both test types at the end of the tests,

although flow has almost ceased, some finite water is still being taken up by the specimens.

The decision to remove a specimen is based on relative changes in water inflow, suction, volume, and mean stress. Tests shown lasted as long as 41 days, which is an extended period of time. Waiting until all flow had entirely ceased was judged to be too long and the information gathered from the remainder of these tests was not required to assess the influence of boundary conditions.

Isotropic compression mainly reduces the size of the macro pores (Wan et al. 1996, Delage et al. 1998, Cui et al. 2001). In the capillary tube model, this is represented by a smaller initial main tube diameter. Also, in this type of material, the swell mechanism is anticipated to impact the flow regime. Thus for comparison, three (3) main tube diameter results from the closed – low pressure and closed – diffusion types are plotted, all of which had high swell rates of $1x10^6$ as shown in Figure 9.16a-b. The largest initial pore size used is 30 μm and the smallest is 8 μm. These diameters bound the range of pore sizes in the initial macro pore mode (Figure 2.2).

In the capillary tube results, increasing initial main tube diameter results in more water inflow as well as an increased flow rate compared with smaller tube sizes. The time until end of flow is also longer in the larger pore size. As described in Chapter 8, in the closed – low pressure models, inflow continues until the

downstream air pressure builds up to equal the upstream plus the capillary pressure at the interface, after which no further inflow occurs. In the diffusion models, downstream air pressure builds, leading to diffusion of air through the water phase. At the end of diffusion models, the capillary tube is filled with water and the initial higher flow rate reduces to a constant value.

The difficulty in normalizing data is choosing what point to normalize to as the choice is somewhat arbitrary, but does impact how the data is presented. Normalization is required to allow for direct comparison since the capillary tube model only comprises one flow tube while flow into the laboratory specimen occurs through millions of flow tubes. Complicating the process is the fact that in the laboratory test results shown, some tests at lower isotropic stress levels last significantly longer than ones at higher levels, and also take in considerably different amounts of water. Also, most inflow takes place during the first third of the test. Normalizing later on during the tests would result in less differences being evident. Several points were normalized to and finally the point chosen for normalization was when 90% of inflow had occurred in the 250 kPa test for each boundary condition type. This is seen as a balance between a high enough flow to normalize to yet early enough that the extended length of 250 kPa tests does not overly impact the normalized data.

All laboratory and model time and inflow data for each boundary condition type were divided by the time and inflow amount for the 250 kPa test when 90% of

inflow had occurred. In most cases, the 250 kPa flow tests provided the greatest inflow of water over the longest time supplying an acceptable point for normalization. As only 10% of inflow remained after this point, most of the changes in flow regime occurred prior to this time. Similarly, the capillary tube data is normalized to the time and inflow in the largest pore size model when 90% of flow had occurred.

Normalized flow data is shown in Figure 9.17 and Figure 9.18 with capillary and laboratory data plotted together. Closed – low pressure model with CV and CMS graphs are plotted in Figure 9.17 and closed – diffusion graphs are plotted in Figure 9.18. The vertical axis is plotted from 0-1.2 since 100% of the inflow on the 250 kPa test corresponds to 1.11 normalized flow. The horizontal axis is plotted from 0-6 representing six (6) times the time required for the normalizing test or model to take in 90% of its total water. Only the 1000 kPa CV test extended past this point of normalized time.

Comparing normalized inflow data shows that the closed end – capillary tube model captures most aspects of the CV laboratory results. This includes initial flow rate as well as sharp attenuation of inflow. The CMS data shows surprisingly close comparison to the capillary tube results at the beginning of infiltration. This is surprising considering the relatively large changes in volume that occurred in the CMS tests compared to the CS25, CS75, and CV tests. In the capillary tube model, no overall expansion of the tube is allowed. During

CMS tests, specimens are expanding in the axial and radial directions leading to increases in tube diameter and length. Later, flow in the closed tube model stops entirely, while flow in the CMS tests continues. General modes of behaviour, including lower stress tests, take in the most water at the highest rate are observed. This is similar to the other tests. Decrease in flow rate does not occur over such a short period in the CMS tests as during tests where increasing mean stress boundary conditions were applied. These complex volume change behaviours cannot be captured by a rigid capillary tube that only decreases in diameter.

Considering the diffusion model results in Figure 9.18 shows similar inflow to the closed end model until air pressure builds. After this point, inflow still occurs if diffusion is considered while without, flow stops. In the laboratory results, a combination of these two (2) mechanisms appears to be occurring. Flow slows down but some water is still entering the specimen at the end of the test. This is likely diffusion taking over to allow further inflow into the specimen. Previously mentioned was modeling of the isothermal experiment by Thomas et al. (2003) where the conductivity versus saturation relationship was modified in order to match measured water contents (Figure 1.1). The capillary tube model shows that decrease in hydraulic conductivity occurs due to reduction of the main tube size; however, the reason for the flow being halted is the downstream air pressure within the soil increasing. This decreases the overall gradient and reduces flow. Once downstream air pressure equals upstream water pressure

plus the capillary pressure from the water-air interface, flow stops unless the air is allowed to diffuse through the water phase.

Similar behaviour is observed in saturated triaxial testing, when during the saturation phase, back pressure is raised in order to increase saturation. Raising back pressure compresses the air and allows more air to be dissolved according to Henry's Law (Sisler et al. 1953). This behaviour would be observed during these infiltration tests had the water pressure been increased. Therefore, both flow and diffusion of air must be accounted for in modeling of these types of systems.

The double length tube model was also proposed as a mechanism for increased saturation but its flow behaviour does not match laboratory data. In models with similar geometric parameters, double length models always had longer saturation times compared to diffusion models (Table 8.4 and Table 8.5). Therefore, given the option, diffusion is the governing mechanism. Also, the flow behaviour shown in double length models has high flow rates decreasing to a constant value. The double length models had the same pressure applied upstream and downstream. In laboratory tests, if the specimen had been given access to water with no additional pressure (0 kPa water pressure) then the double length model might capture behaviour. In that situation, the air density gradient would not build up as fast with slower inflow, and air could be pushed out of pores on the periphery of specimens.

Post-test measurements show saturation values between the extremes observed in capillary tube models. Diffusion models achieve breakthrough (100% saturation) while the closed end – low pressure models achieve approximately 67.5% effective saturation relative to the entire tube. Inflow laboratory results show some inflow occurring even at the end of infiltration tests. The likely mode observed in laboratory tests is a transfer from the closed end reduction in flow, to a situation where inflow can only occur when the air ahead of the interface dissolves into the water phase. This could be the reason why saturation gradients were measured following laboratory tests. Given enough time, the entire specimen would attain the residual air content. This could take an extended length of time, given the slow inflow rate at the end of tests. In this aspect, the diffusion models underestimate the time for complete saturation.

Since the capillary tube model captures behaviour observed during laboratory tests, its parameters can be further modified in order to propose mechanisms that increase times to full saturation. The influence of initial main diameter (d1), final or minimum main diameter (d2), and peripheral diameter (d3) sizes were presented in Chapter 8 along with a range of swell rates for each. The results for closed end – low pressure and diffusion models are shown graphically in Figure 9.19, Figure 9.20, and Figure 9.21 for the influence of d1, d2, and d3 respectively. Plotted on the graphs is time to end of flow or breakthrough versus diameter versus swell rate. As a reminder, closed – low pressure models do not

achieve full saturation of the capillary tube when flow stops, while diffusion models continue until breakthrough.

Downstream air diffusing into the water phase limits flow when altering only the initial main tube diameter, as indicated on Figure 9.19b. For swell rates less than the transitional, times to end of flows are several orders of magnitude less in the low pressure models compared with times to breakthrough in the diffusion models. At high swell rates, times to breakthrough increase with increasing initial diameter for closed end models but are constant for diffusion models. Diffusion limits inflow, resulting in relatively constant times to breakthrough over this range of initial diameter.

Altering the final or minimum main tube diameter (d2), shown in Figure 9.20, reveals a transition between downstream air pressure and pore size dominated behaviour. In closed end models, a clear transition is observed from low to high swell rates for all diameters. In diffusion models, at diameters 1.4 μm and greater, no change in time to breakthrough is observed and no transitional swell rate is observed. At smaller minimum tube diameters (<1.4 μm), a transitional swell rate becomes evident. These models show that based on the swelled diameter, flow changes from being limited by the downstream air pressure to the final (or minimum) pore size dominated at final diameters less than 1.4 μm.

The influence of peripheral diameter (Figure 9.21) shows that the downstream air limits flow for all models. No transitional swell rate is observed in diffusion models and peripheral tube size does not affect times to breakthrough. For closed end models, transitional swell rates are observed but the maximum time to end of flow does not change regardless of peripheral tube diameter.

The capillary tube results show that downstream air dominates over certain tube sizes while minimum pore size (d2) governs in other cases. The relevant pore sizes which represent the laboratory tests were shown in Figure 2.2 and representative diameters were chosen for each parameter. Initial main tube diameter, chosen to represent macro pore sizes at the beginning of infiltration, does not affect time to breakthrough when diffusion is considered. Diffusion models reveal constant times to breakthrough for all models completed. Minimum main tube diameter (d2), plotted in Figure 9.20, shows that at greater minimum diameters, diffusion dominates. As minimum diameter decreases below 1.4 μm, a transitional swell rate is evident and time to breakthrough increases significantly. If the main tube diameter is allowed to decrease as low as 0.1 μm, time to breakthrough jumps to approximately 2000 days.

During laboratory tests, expansion of the clay peds is expected to decrease the macro pore mode and increase the overall micro pore mode resulting in a final unimodal pore size distribution. Thus, the final pore size is likely to be somewhere between the two (2) modes and in the 0.1 – 10 μm range. Capillary

tube model results suggest that the minimum tube diameter or final pore size dominates saturation times if flow diameter reduces below 1.4 μm. Assuming that the final pore size distribution is between the two (2) modes shown in Figure 2.2, the final or minimum pore size dominates.

9.3.2 Undrained Infiltration Modeling Using Empirical Analysis

Modeling inflow rates based on these laboratory results is an extremely complicated procedure that requires in depth numerical analysis using a coupled hydraulic-mechanical model. Another graduate student (Deni Priyanto) is currently working on this particular topic. He is completing a doctoral thesis to create a general hydraulic-mechanical model for swelling soil based on the laboratory results from this work. It is scheduled to be published within the next calendar year.

For the purposes of flow prediction, an empirical curve matching method is used. Considering the flow behaviour observed in Figure 9.16c-d, inflow behaviour appears to follow a hyperbolic curve. The fitting process and generated parameters are shown in Figure 9.22. The original data in water added to specimen versus time (Figure 9.22a) is plotted in Figure 9.22b as water added to specimen divided by time versus time. The data is then fitted with a linear distribution to give the parameters a and b. Parameter a represents the initial slope while parameter b represents the asymptote that the curve approaches. Therefore, in this particular fitting procedure, parameter a represents the initial

flow rate into the specimen and parameter b represents the total water added to specimen.

To determine if the flow data actually followed a hyperbolic curve, the data was plotted as time/inflow versus time as shown in Figure 9.23a-b. If a hyperbolic curve is followed, a linear relationship should be evident in these plots. Linear fitted equations are shown on the graph and for all boundary conditions, R^2 values are 0.99 or greater. The rest of the infiltration tests had R^2 values greater than 0.98 suggesting use of the hyperbolic curve is valid.

Summaries of the inverses of the a and b parameters from all infiltration tests are plotted in Figure 9.24 and Figure 9.25 versus isotropic mean stress. The data show a consistent trend with the inverses increasing in both the a and b parameters for increasing isotropic compression level. For both the inverses of the a and b parameters, the slopes are generally similar for different boundary conditions but with specific intercepts for each. The exception is the anomalous 1000 kPa CS25 a parameter. In the b parameter plot, the CMS shows a consistent slope except for the 1500 kPa point, where similar water uptake was observed in the CV and CMS tests. Removal of the 1500 kPa point from the CMS fitted curve would show a similar slope as the other boundary conditions. This is further evidence that the hydraulic conductivity and the total amount of inflow are functions of the boundary conditions. Also, the fact that the 1500 kPa CMS and CV test specimens performed similarly (Figure 9.25) indicates that the

water content – mean stress limit is close to the starting point in these cases. As such, the fitted lines for the boundary conditions cannot be extrapolated indefinitely due to the coupling between the hydraulic and mechanical behaviour. Finally, inflow data from the infiltration tests can now be modeled empirically to determine the rate and amount of water uptake in these tests.

9.3.3 Modeling Drained Laboratory Tests with the Capillary Tube Model

The drained laboratory tests represent a new hydraulic conductivity test in which volume conditions are measured. Compared to the undrained tests, the drained tests give an explicit location for air and water to exit the specimen. Since volume is measured throughout and the test is axisymmetric, definition of hydraulic conductivity values is possible in tests where equilibrium is established. This occurred in the 250 kPa and 500 kPa radial CMSD tests. Modeling of the drained tests is performed using the capillary tube model and traditional D'Arcy's Law interpretation.

As in the undrained laboratory results, data must be normalized to allow for direct comparison. Open end tube models continue until breakthrough occurs. This represents 100% saturation in the laboratory specimens. After breakthrough occurs, given the same upstream and downstream pressures, flow rates would remain constant in open tube models. In the laboratory results, water is observed flowing out the center of the specimens within approximately 12 days in both radial tests (Figure 6.36 and Figure 6.37). Gravimetric water content still increases for an extended period of time after water outflow is observed as

shown in Figure 9.26. Water content changes continue until upstream and downstream flow rates equilibrate to the same levels. Comparing Figure 9.26 and Figure 6.36 reveals that after water content equilibrium, inflow and outflow rates are relatively constant for the radial tests signifying conductivity equilibrium with the constant mean stress boundary conditions. For normalizing, the point at which 90% of the gravimetric water content increase is completed is the point chosen in the laboratory tests. After breakthrough, flow rates remain constant. This is the point of comparison with the open tube models.

Actual and normalized data from the open capillary tube model and the constant mean stress – drained (CMSD) tests are shown in Figure 9.27 and Figure 9.28 respectively. The actual capillary tube and laboratory data (Figure 9.27) show similar modes with inflow rates decreasing until a constant flow rate is attained. Arrows have been added to the capillary tube data to illustrate that if the model had not been completed, constant flow rates would continue as in the laboratory tests. The normalized data (Figure 9.28) show that modes observed in the laboratory data are captured in the capillary tube model. One interesting aspect to note is the similar final slopes of the capillary tube data. They are almost constant and are always greater than the laboratory data.

Figure 9.29, Figure 9.30, and Figure 9.31 show the influence of the geometric parameters on the time to breakthrough for open tube models. This includes initial main tube diameter, final or minimum main tube diameter, and peripheral

diameter. As shown on Figure 9.30, the time to breakthrough can be increased by reducing the final or minimum main tube diameter for high swell rates. Behaviour observed in the laboratory data shows a relatively steep inflow rate which decreases to a constant rate. The open tube data with high swell rates demonstrates a smooth transfer from initial flow rates to the constant level. The laboratory data show similar trends to flow in tubes with swell rates just below the transitional swell rate. In these models, extremely high inflow rates occurred until the swell mechanism caught up and the minimum main diameter was achieved, after which flow rate reduced quickly to the constant value.

The difference in behaviour is likely due to the volume changes which are occurring during laboratory tests but which are not represented with the rigid capillary tube. Significant expansion occurs during the same time that water content increases are occurring, resulting in axial and radial swell of the specimens. This mode of flow could be represented by reducing the swell rate to approximately the transitional swell rate. This allows initial high flow rates until the swell mechanism attains the minimum diameter, after which relatively constant flow rates are observed. This makes intuitive sense because, at the pore scale level, the clay peds are expanding but also bulk expansion is occurring. The macro pore mode is likely decreasing overall but at a reduced rate since bulk volume is increasing at the same time. In the open tube models, reducing swell rate achieves the same flow response.

9.3.4 Network Model Comparison

In the literature review provided in Chapter 2, a network model for sand bentonite mixtures by Abichou et al. (2004) was summarized. That network model is a three-dimensional static model which does not incorporate dynamic changes to flow area. Both bentonite coated sand mixtures and sand mixed with bentonite pellets were modeled. In individual tubes partially coated with bentonite, flow is calculated using the Hagen-Poiseuille equation through the area not filled with bentonite and a hydraulic conductivity is assigned to the area filled with bentonite. No transient flow data is shown in their publication and only relationships of hydraulic conductivity versus 'degree of bentonation' are reported. Degree of bentonation is defined as the volume of tubes which are filled with bentonite divided by the total tube volume.

Although direct comparisons with flow data reported here are not possible since these results are generated using a single capillary tube model that incorporates dynamic swelling, some insight is gained by comparing the concepts. In Abichou et al. (2004), as degree of bentonation increases, three (3) hydraulic conductivity zones are observed as shown in Figure 9.32. At low bentonation, little change in conductivity occurs until a threshold is reached. After the threshold, a drop in conductivity of several orders of magnitude is observed followed by little further change in conductivity as the bentonite filled tubes dominate flow. Similar observations were made in the open tube models (Figure 9.29) with increasing swell rate.

In Abichou et al. (2004), three-dimensional network results were also used to model hydraulic conductivity tests performed in a rigid cell. Degree of bentonation is related to the minimum main tube diameter (d3) assigned in these models. Reducing d3 is similar to increasing bentonation as area for flow is restricted. In the Abichou et al. (2004) model, flow through individual pipes is calculated by combining different models for flow including Hagen-Poiseuille and D'Arcy's Law as illustrated in Figure 9.33. Use of D'Arcy's Law in this case is questionable because flow is already being calculated at the pore scale and D'Arcy's Law was originally developed for modeling flow at the specimen scale.

Considering the results shown in Chapter 8 with regards to the open tube model, instead of modeling flow through the bentonite using a hydraulic conductivity, they could have used extremely small tubes with equivalent area for flow as shown in Figure 9.33. Instead of switching between a bulk scale and pore scale model within an individual pore, this new concept is consistent with capillary models conceptualizing the entire porous media using tubes and nodes. In this open tube concept, the area for flow remains constant but the resistance to flow increases from the higher number of tubes. This also represents the observed physical changes to the pore size distribution during infiltration which has been proposed by other researchers (Cui et al. 2001, Garcia-Bengochea 1979, Castellanos et al. 2006) where the bimodal distribution coalesces into a unimodal distribution between the two (2) original modes.

To investigate this phenomenon two (2) models which had equivalent total flow area were completed. The first model used one (1) tube with constant diameter of 14 μm and the second model had 100 tubes with 1.4 μm diameter as shown in Figure 9.34. Since individual tubes in the second model have an area one-hundredth ($1/100^{th}$) of the larger tube, total area is constant in both models. As shown in Figure 9.34 the large tube model achieves breakthrough in 0.54 s while the model with small tubes takes 30.0 s and is a time increase of two (2) orders of magnitude for a one (1) order of magnitude decrease in diameter. As a reminder, overall flow area is constant. In the laboratory tests, results indicate a decrease in conductivity with increasing water content even in the constant volume tests. These two (2) models propose a mechanism whereby this is possible. This mechanism is an expansion of the peds into the macro porosity creating a unimodal pore size distribution resulting in smaller pores for water to flow through although total void ratio (porosity) remains constant.

9.3.5 Modeling Drained Laboratory Tests Using D'Arcy's Law

Since the radial flow specimens achieved inflow, outflow, and volume equilibrium, D'Arcy's Law can be applied in a straightforward manner to the end of test flow rates. Due to the axisymmetric nature of the test, conductivity can be calculated from

$$k = \frac{Q\rho g \ln\left(\frac{r_e}{r_w}\right)}{2\pi h(P_e - P_w)} \qquad [9.1]$$

where

k = hydraulic conductivity,

Q = equilibrium flow rate,

ρ = density of fluid (water),

r_e = outside radius of specimen,

r_w = inside radius of specimen,

h = height of specimen,

P_e = pressure applied at perimeter of specimen, and

P_w = pressure applied at inside radius of specimen.

Based on end of test flow rates, volume changes, and applied pressures in the drained tests, conductivity values for the 500 kPa CMSD and 250 kPa CMSD tests have been calculated at 3.9×10^{-13} m/s and 1.0×10^{-12} m/s respectively. Past experience has shown conductivity in compacted swelling materials to be a function of the clay dry density with the remaining dry mass of material serving as filler (Gray et al. 1984). This leads to a definition of effective clay dry density (ECDD). The definition of ECDD is

$$ECDD = \frac{f_c \rho_d}{\left[1 - \frac{(1 - f_c)\rho_d}{G_s \rho_w}\right]} \qquad [9.2]$$

where

f_c = clay fraction,

ρ_d = dry density, and

G_s = specific gravity of non-clay materials.

In the clay-sand specimens tested in this research, the clay fraction is 50% and the specific gravities of all materials is 2.7 (Chandler 2000). From the initial mass, water content, and volume measurements, and volume change measurements during the test, the ECDD can be calculated and compared to previous hydraulic conductivity data. Direct comparison with Dixon et al. (2002a) is provided in Figure 9.35. Drained test results are plotted alongside previous measured points although they should only be compared to the distilled, de-aired water results as no saline solution was used as a permeant. Previous tests were completed in rigid one-dimensional apparatuses but interpreted conductivity values were similar indicating this apparatus provides relevant parameters but with volume measurement instead of forced volume control without explicitly measured states. Increase in conductivity is also observed for the 250 kPa CMSD test which is expected since a lower mean stress boundary condition allows further expansion leading to greater sized pores for water to flow through.

9.4 Additional Findings and Observations

9.4.1 Three-Dimensional Water Retention Curve

As discussed in section 9.2, at the end of infiltration tests under controlled boundary conditions, end of test suction measurements are within a 200-300 kPa range of as shown in Figure 9.12 while specific volume and gravimetric water content measurements range over approximately 1.4 – 2.4 and 20% - 54% respectively (Figure 9.14). Traditionally WRCs are plotted as saturation, volumetric water content, or gravimetric water content versus suction. Implicit in these types of two-dimensional WRCs is that volume remains relatively constant throughout. Another implicit assumption that is often made is that suction alone provides a prediction to the strength and hydraulic behaviour. From the results above it is clear that specimens, although with very similar suction levels, have vastly different hydraulic and volume change characteristics. Although not tested, shear strength characteristics would also vary widely over the range of specimens, although suction measurements are similar. Recognizing that significant volume change does occur during suction changes in some soils, Fredlund and Pham (2006) showed a new combination of curves plotted in mean stress – suction – water content and mean stress – suction – void ratio spaces to represent the water retention behaviour of artificial sand, silt, and clay soils that are dried from an initial slurry state. The shapes of the curves appear reasonable but no experimental evidence was shown to calibrate and validate the proposed relationships.

From the wide range of specific volumes and water contents measured in this research, it is clear that a single two-dimensional WRC does not provide enough information on the state of the soil. Based on laboratory measurements shown in Figure 9.36, that includes data from Blatz et al. (2006), a new three-dimensional WRC is proposed as illustrated in Figure 9.37. The axes are gravimetric water content, specific volume, and suction and were chosen because calculations of values such as saturation and volumetric water content incorporate both water content and volume. Choosing independent axes ensures that changing one (1) variable does not impact another directly. This is distinctly different from the forms proposed by Fredlund and Pham (2006) as mean stress is removed and void ratio and gravimetric water content are plotted together. Also, the soil used in this three-dimensional WRC is a compacted swelling material whereas soil from slurry has a different pore-size distribution based on the hydration and compaction characteristics. In this new WRC, two (2) of the three (3) state variables must be measured in order to determine the third. Trends include, increases in specific volume decreases air entry value and residual water content. Since pore size is greater in this case, this allows for higher desaturation of the pores. At least conceptually, this is reasonable and agrees with measured data shown in Figure 9.36. During infiltration under controlled boundary conditions, water increase and suction decrease occur simultaneously.

9.4.2 Comparison of Previously Measured 'Swell Pressures'

Many previous measurements of 'swell pressure' exist in the literature. As has been proposed in this thesis, a unique value of 'swell pressure' does not exist. Chandler (2005) proposed a means for direct comparison between traditional 'swell pressure' measurements and laboratory results from this research and is summarized here.

An end of test mean stress – volume – water content relationship was shown in Figure 9.15. Dixon et al. (2002a) reported swell pressures for various shrink/swell materials as a function of Effective Montmorillonite Dry Density (EMDD). In general, 'swelling pressure' increases with increasing EMDD. EMDD is similar to ECDD except that all non-swelling materials are removed from the dry density equation which is

$$EMDD = \frac{f_m f_c \rho_d}{\left[1 - \frac{(1-f_c)\rho_d}{G_s \rho_w} - \frac{(1-f_m) f_c \rho_d}{G_n \rho_w}\right]} \qquad [9.3]$$

where

f_m = montmorillonite fraction of clay, and

G_n = specific gravity of non-swelling clay.

In Wyoming bentonite, the montmorillonite fraction is 90% (Dixon 1994) and the specific gravity of all materials is equal to 2.7 (Chandler 2000). The specimen's dry density is a function of volume strain during isotropic compression and

infiltration under controlled boundary conditions. Taking values reported above and in section 9.3.5, the EMDD for this material can be calculated as

$$EMDD = \frac{0.45\rho_d}{1 - 0.2037\rho_d} \qquad [9.4]$$

Converting from dry density to specific volume can be done through the phase relationship

$$\rho_d = \frac{V}{G_s} \qquad [9.5]$$

where

V = specific volume, and

G_s = specific gravity.

Simplification and combination with [9.4] gives

$$EMDD = \frac{0.45}{\frac{V}{2.7} - 0.2037} \qquad [9.6]$$

Most reported measurements of 'swell pressure' are performed in one-dimensional apparatuses. As reported in the literature review, no reports of constant volume tests performed in the triaxial apparatus were found. Therefore

assuming that most, if not all, 'swell pressures' reported by Dixon et al. (2002a) were performed in one-dimensional apparatuses is reasonable. For comparisons with laboratory results from this research, these 'swell pressures' must be converted to end of test mean stress. As an assumption, elasticity is used to calculate stresses.

From elasticity (Davis and Selvadurai 1996), radial strain is defined as

$$\varepsilon_x = \frac{1}{E}\left[\sigma_x - \nu\left(\sigma_y + \sigma_z\right)\right] \qquad [9.7]$$

where

ε_i = strain in the i^{th} plane,

E = Young's Modulus,

ν = Poisson's Ratio, and

σ_i = total stress in the i^{th} plane.

In one-dimensional apparatuses, radial strain (x and z directions) equals zero and the two (2) horizontal stresses are equal to the radial stress. Also, the vertical stress (y direction) is equal the 'swell pressure' so [9.7] can be reduced to

$$\sigma_r = \left(\frac{\nu}{1-\nu}\right)P_{swell} \qquad [9.8]$$

where

σ_r = radial stress, and

P_{swell} = 'swell pressure'.

Mean stress (p) is defined as

$$p = \frac{\sigma_x + \sigma_y + \sigma_z}{3} \qquad [9.9]$$

where

p = mean stress, and

σ_i = total stress in the i^{th} direction.

Therefore, end of test mean stresses from the one-dimensional apparatuses measurements of 'swell pressure' can be calculated as

$$p_{equil} = \frac{P_{swell} + 2\sigma_r}{3} = \frac{P_{swell}}{3}\frac{(1+\nu)}{(1-\nu)} \qquad [9.10]$$

where

p_{equil} = equilibrium mean stress.

In modeling the ITT, Chandler (2000) calculated a Poisson's ratio of 0.18 for BSB. This is seen as a best-estimate, although there were small differences in dry density and water content, and is reasonable considering the anisotropy of

this type of material. Finally, fitting an exponential function through the distilled, de-aired water data shown in Dixon et al. (2002a) produces

$$P_{swell} = 0.00643 x \left(\exp\{4.687 x (EMDD)\}\right) \quad [9.11]$$

Substituting [9.6] and [9.10] into [9.11] and solving for p_{equil} results in

$$p_{equil} = 0.003084 x \left(\exp\left\{ \frac{2.109}{\frac{V}{2.7} - 0.2037} \right\} \right) \quad [9.12]$$

To summarize, previous relationships between EMDD and 'swell pressure' have been proposed based on a number of swell/shrink materials as presented in Dixon et al. (2002a). These relationships are likely based on measuring the vertical pressure required to maintain constant volume during one-dimensional wetting tests. To compare with laboratory tests completed for this research, conversion of the 'swell pressure' to mean stress was required. Also, EMDD was converted to total specific volume and the results are plotted in Figure 9.38. The dashed line is the end of test fit presented earlier while the dotted line is [9.12]. This is based on the relationship proposed by Chandler (2005). As observed in Figure 9.38, the dotted line plots at the end of test point at the end of infiltration for the undrained specimens which shows good promise for the assumptions made in the derivation. This indicates that the 'swell pressure' – EMDD

relationship measured in one-dimensional apparatuses may actually be a general end of test mean stress – volume relationship for swelling materials.

9.4.3 Comparisons with AECL Full-Scale Experiments

In Chapter 1 a model by Thomas et al. (2003) was presented that used a hydraulic conductivity curve and had decreasing conductivity with increasing saturation. Understanding this mechanism was a motivation for this research. The mechanism has been determined to be a function of the pore size distribution changes that occur, and are dominated by, the boundary conditions during infiltration.

The isothermal test (ITT) configuration is similar to the undrained laboratory apparatus except that it allowed water flow through the base. Therefore changes in density and water content are anticipated to be comparable. Approximate limits of dry density measurements from de-commissioning of the ITT are shown in Figure 9.39. Also shown on the figure is the initial density of BSB (buffer) in the ITT. The initial dry density of 500, 1000, and 1500 kPa infiltration specimens as well as end of test average dry density of the 1500 kPa CV test have been added to the figure for comparison. From this figure, the ITT appears to be approximately a large-scale 1500 kPa CV infiltration test. On Figure 9.39, the initial density of BSB (buffer) is shown as a solid horizontal line. This is highly idealized as Kjartanson et al. (1992) reported that the initial dry density, formed using compaction procedures as in the ITT, was in a small range of around this

ideal value. Swelling in the BSB (buffer) is reported at the boundary and compression occurred at the center in the ITT. This is consistent with post-test measurements in the laboratory tests. One of the differences between the large scale and laboratory tests is that in the laboratory, the entire specimen periphery is surrounded by water but in the ITT inflow only occurs through discrete fractures in the rock. Therefore, it is not surprising that water uptake took relatively longer compared with a two week CV test.

The end of test distribution of water content is also included in Dixon et al. (2002b). Approximately one-third from the top of the large scale specimen was taken to be an approximation of the radial flow conditions applied in the laboratory tests allowing direct comparison of end of test spatial water contents. Figure 9.40 includes gravimetric water content versus normalized distance for the 1500 kPa CV and CMS tests and Layer C from the ITT. Water content measurements at the end of the 1500 kPa CV test are inside the bounds of measurement from the ITT. At the 1500 kPa stress level, little water content increase is allowed until the water content – specific volume limit is reached and the large and small scale tests show similar water uptake limits.

Additionally, swelling induced pressures measured during the ITT also coincide with the 1500 kPa constant volume test. A range of swelling induced pressure from between 1250 kPa and 2000 kPa was reported in Dixon et al. (2002b). End of test mean stress observed during the 1500 kPa CV test was 1900 kPa.

Further evidence that similar boundary conditions were observed in the buffer container experiment (Dixon et al. 2002b) as the ITT and laboratory tests is displayed in Figure 9.41a and Figure 9.41b. Dry density versus gravimetric water content measurements are plotted following de-commissioning. Figure 9.41a is taken from Dixon et al. 2002b and Figure 9.41b plots all the average post-test dry density versus gravimetric water content measurements from this research. Measurements from this testing program plot inside the limits of the existing database. Greater water content and lower dry density measurements have been made in this research program and a linear relationship appears to exist outside the current database. This agrees with the linear water content – specific volume limit reported above.

From the discussion in this chapter, fundamental new understanding into the behaviour of unsaturated swelling soils, during liquid infiltration under controlled boundary conditions has been discovered. These plots show that previous large scale experiments that were difficult to model now are being represented in the laboratory. Now the influence of the boundary conditions is better understood and can be incorporated into future research. As reported by Dixon et al. (2002b), swelling occurred at the perimeter and compression at the center of the borehole. Both of these mechanisms reduce the macro pore space (Cui et al. 2001, Blatz and Graham 2003) and lead to a decrease in hydraulic conductivity. From the capillary tube model, inside the borehole, ahead of the

water front, the air pressure increased, which decreased the gradient for flow. These mechanisms led to a decrease in water uptake and the lower measured water contents. Now these mechanisms can be properly input into numerical models being developed by researchers at the Geotechnical Group at The University of Manitoba to validate against the insitu experiments in order to gain confidence in their applicability. After calibration and validation, the models can be used to predict more general behaviour of proposed repositories.

9.4.4 Anisotropic Behaviour of Compacted Clay Sand Specimens

Specimens prepared in this research are compacted in a one-dimensional mold. The compaction process likely results in the clay particles being preferentially oriented in a horizontal manner. As such, anisotropic behaviour is anticipated during isotropic compression and infiltration. From the initial orientation and compaction procedure, axial stiffness is anticipated to be greater than radial. As an example, axial strain and radial strain versus volume strain for the 250 kPa undrained tests are plotted in Figure 9.42 and Figure 9.43 respectively. Axial strain data shows that during expansion, when boundary conditions allow, axial strain increase continues until a limit is reached. After this point, volume strain continues to decrease due to radial expansion but axial strain remains constant. Also shown on Figure 9.42, during constant volume infiltration, some axial expansion is noted although total volume is maintained constant by the data acquisition system. Radial strain data (Figure 9.43) shows a broadly linear relationship between radial strain and volume strain over the 250 kPa tests and is similar in both compression and expansion. Also, in the 250 kPa constant

volume test, radial compression is noted during infiltration while overall volume is maintained constant. Radial compression occurs during constant volume infiltration because the specimen is stiffer in the axial direction due to the compaction process.

Axial and radial strain versus volume strain for all infiltration tests is plotted in Figure 9.44 and Figure 9.45 and similar behaviour is observed as in the 250 kPa undrained tests. Axial data shows expansion up to a limit, while radial strain versus volume strain shows a linear relationship over a wide range of measurements. Although it is hard to observe due to the amount of data shown on this plot, during the 250, 1000, and 1500 kPa CV tests, axial expansion and radial compression is observed during infiltration and are plotted individually in Figure 6.16. This gives further evidence to the anisotropic behaviour in these compacted clay-sand specimens. During the 500 kPa CV test, some loss of volume occurred during initial infiltration and likely led to the difference in observed behaviour.

9.5 Summary

This chapter has provided interpretation on the mechanical and hydraulic behaviour of the swelling clay-sand material while referencing their interaction. The domination of boundary conditions on the behaviour of swelling clay soil during liquid infiltration has been shown using the laboratory and capillary tube results, as well as definition of a swell limit, D'Arcy's Law and empirical hydraulic

modeling. In each section discussion centered on how the mechanical behaviour affected the hydraulic and vice versa. For accurate modeling which properly represents the physics of real-life systems, hydraulic and mechanical performance must be considered together. In materials that experience large volume changes with changes in water content, this need for coupling is magnified. Since one is affected by the other, they must both be considered in modeling these types of systems.

Table 9.1. Summary of laboratory test results.

Test Type	Infiltration Summary				Average Final Measurement Summary			
	Volume Change (%)	Equilibrium Mean Stress (kPa)	Water uptake (g)	Suction Change (MPa)	Gravimetric Water Content (%)	Bulk Density (Mg/m^3)	Dry Density (Mg/m^3)	Saturation (%)
250 kPa Constant Mean Stress - Drained	-43.8	250	112.4	N/A	53.5	1.67	1.09	97
250 kPa Constant Mean Stress	-14.7	250	70.0	-	40.2	1.76	1.26	94
250 kPa Constant Stiffness - X=25kPa/%	-9.0	470	38.4	-	29.2	1.83	1.47	95
250 kPa Constant Stiffness - X=75kPa/%	-4.4	582	24.0	0.5	25.9	1.91	1.52	90
250 kPa Constant Volume	0.0	920	16.0	2.6	23.8	1.93	1.56	88
500 kPa Constant Mean Stress - Drained	-11.3	500	46.0	N/A	30.0	1.88	1.45	94
500 kPa Constant Mean Stress	-4.7	500	25.6	2.2	26.6	1.90	1.50	90
500 kPa Constant Stiffness - X=25kPa/%	-5.7	670	21.0	3.0	25.8	1.92	1.53	91
500 kPa Constant Stiffness - X=75kPa/%	-2.7	700	17.0	3.0	24.4	1.96	1.58	93
500 kPa Constant Volume	0.0	960	16.0	2.5	23.9	1.91	1.54	86
1000 kPa Constant Mean Stress	-2.4	1000	12.8	0.9	23.2	1.96	1.59	90
1000 kPa Constant Stiffness - X=25kPa/%	-2.3	1050	11.5	-	22.3	2.00	1.63	92
1000 kPa Constant Stiffness - X=75kPa/%	-1.5	1120	9.6	-	22.1	2.01	1.64	93
1000 kPa Constant Volume	0.0	1390	9.6	-	21.6	1.97	1.62	87
1500 kPa Constant Mean Stress	-0.9	1500	5.1	0.4	20.9	1.97	1.63	86
1500 kPa Constant Volume	0.0	1900	5.7	-	20.2	2.00	1.66	88

N/A = not measured

- = test not completed or sensor malfunction

Note: All infiltration tests summarized in this table were completed with 200 kPa water pressure.

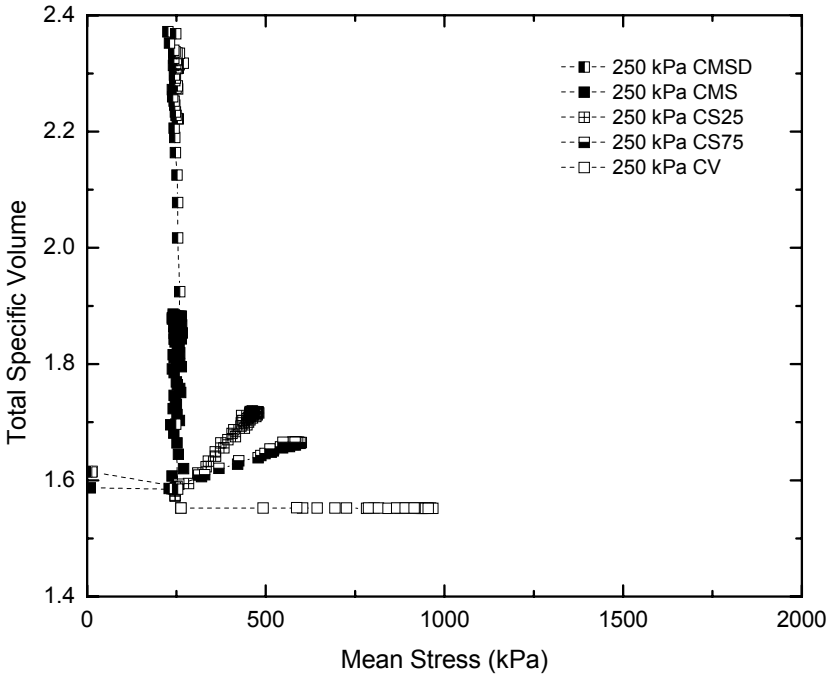

Figure 9.1: Specific volume versus mean stress for 250 kPa infiltration tests (after Blatz and Siemens 2005).

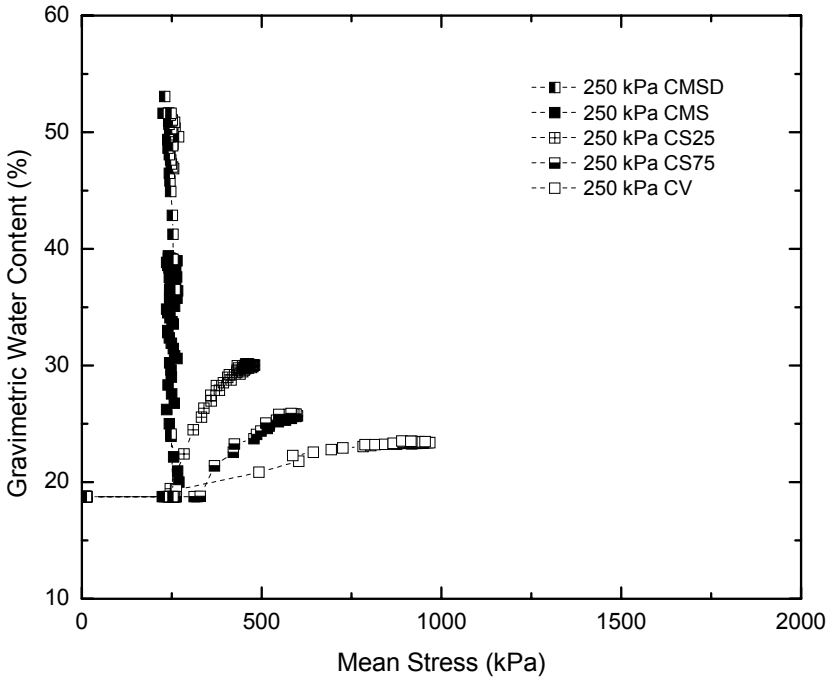

Figure 9.2: Gravimetric water content versus mean stress for 250 kPa infiltration tests.

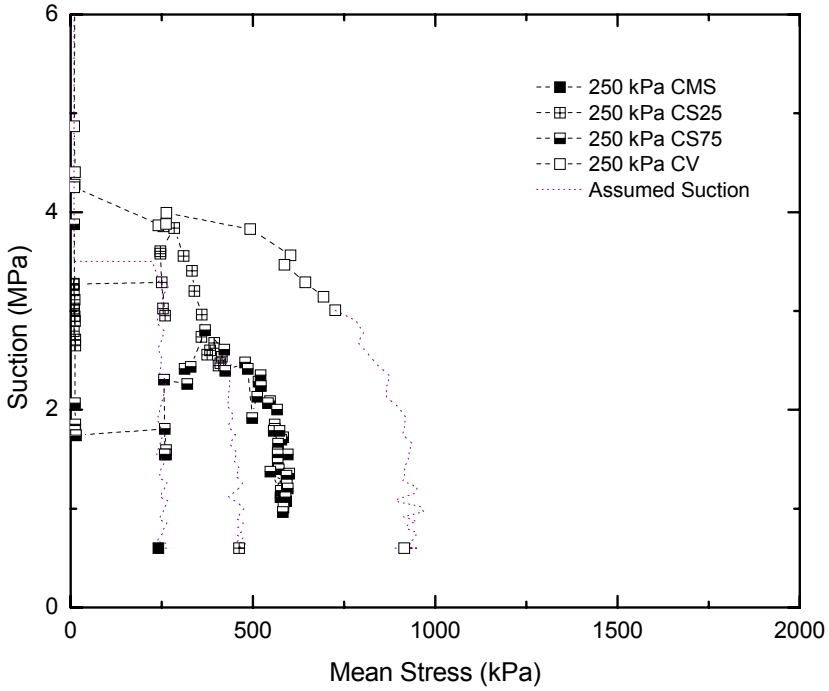

Figure 9.3: Suction versus mean stress for 250 kPa infiltration tests (after Blatz and Siemens 2005).

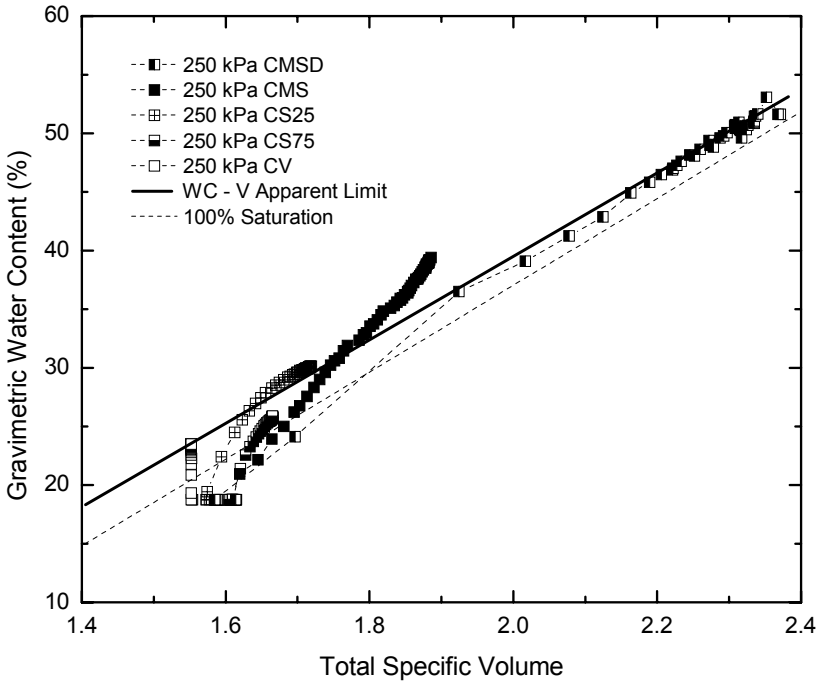

Figure 9.4: Gravimetric water content versus total specific volume for 250 kPa infiltration tests.

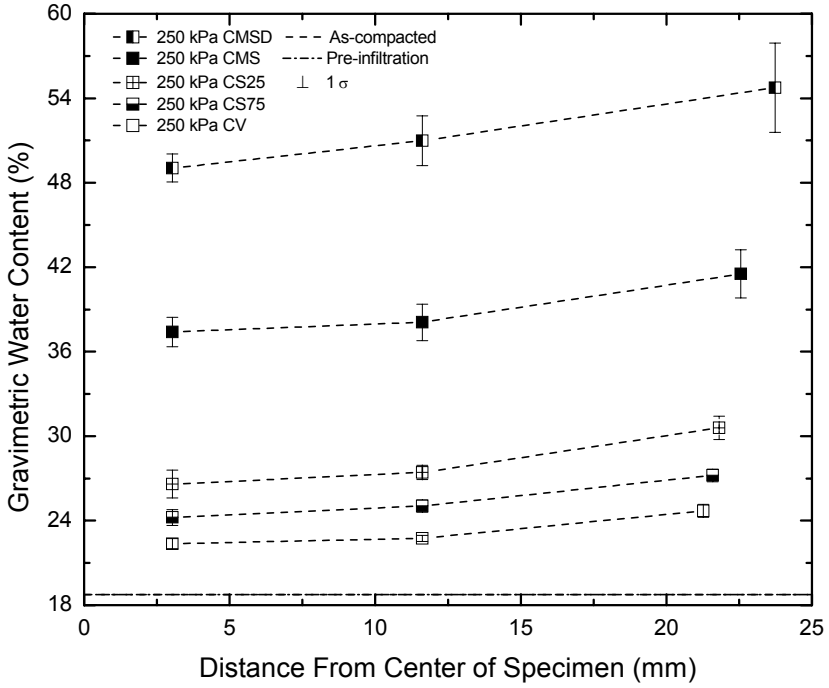

Figure 9.5: End of test gravimetric water content distribution – 250 kPa tests (after Blatz and Siemens 2005).

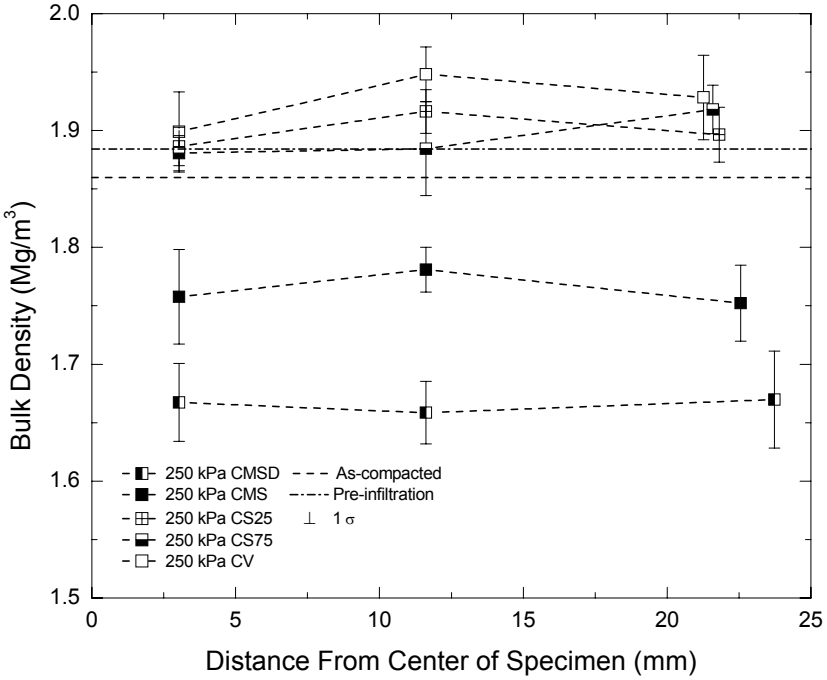

Figure 9.6: End of test bulk density distribution – 250 kPa tests (after Blatz and Siemens 2005).

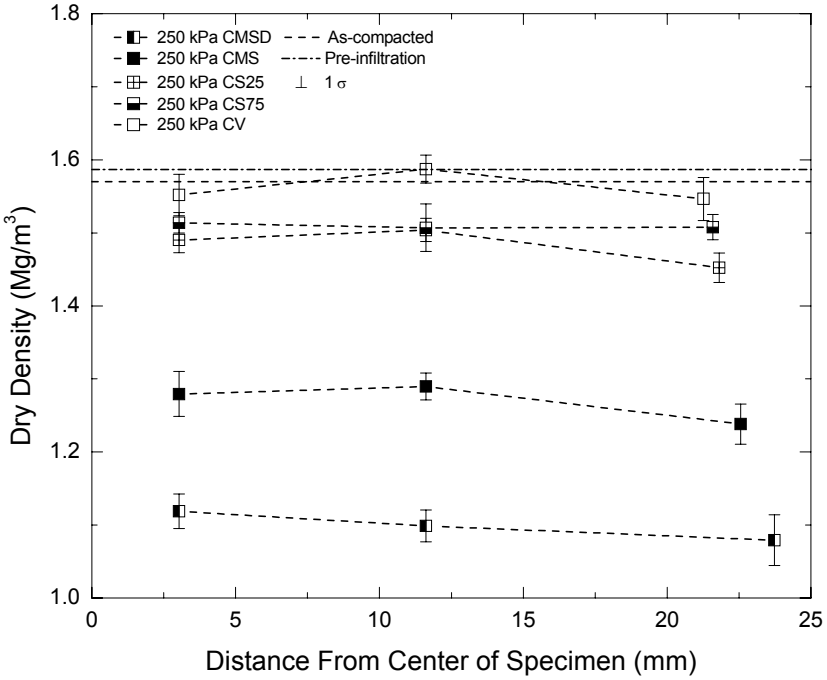

Figure 9.7: End of test dry density distribution – 250 kPa tests (after Blatz and Siemens 2005).

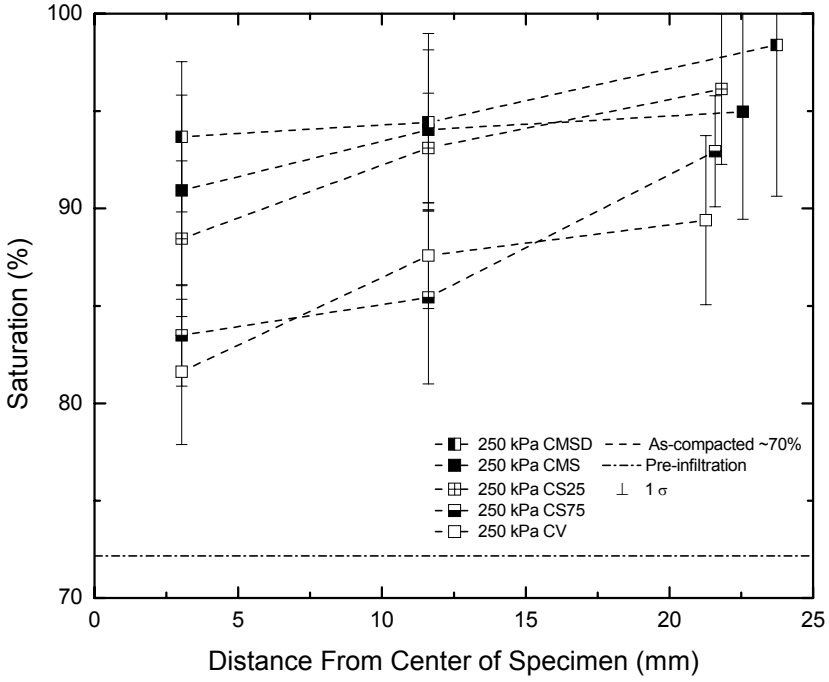

Figure 9.8: End of test saturation distribution – 250 kPa tests (after Blatz and Siemens 2005).

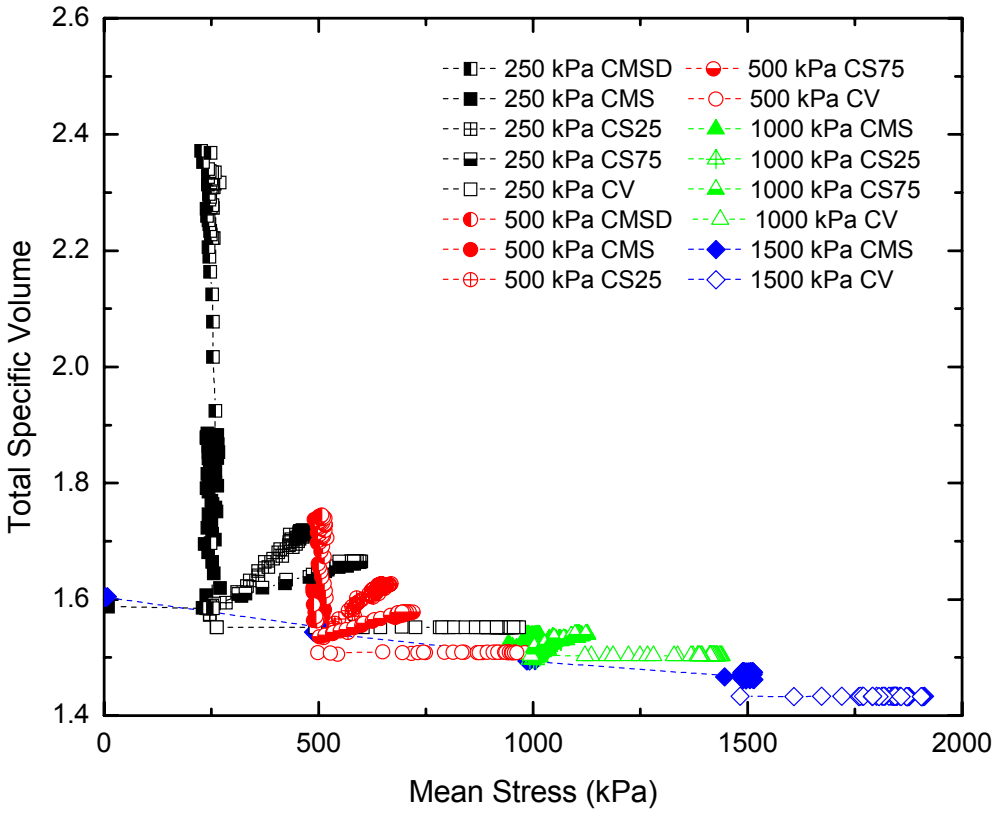

Figure 9.9: Specific volume versus mean stress for all infiltration tests.

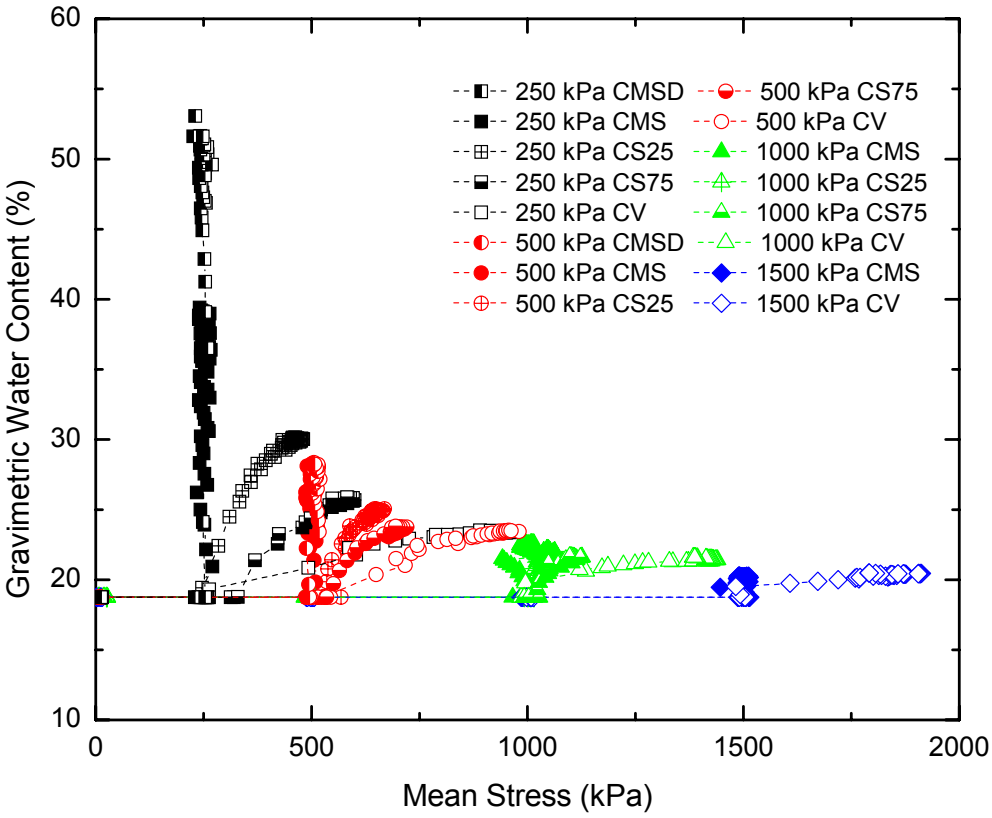

Figure 9.10: Water content versus mean stress for all infiltration tests.

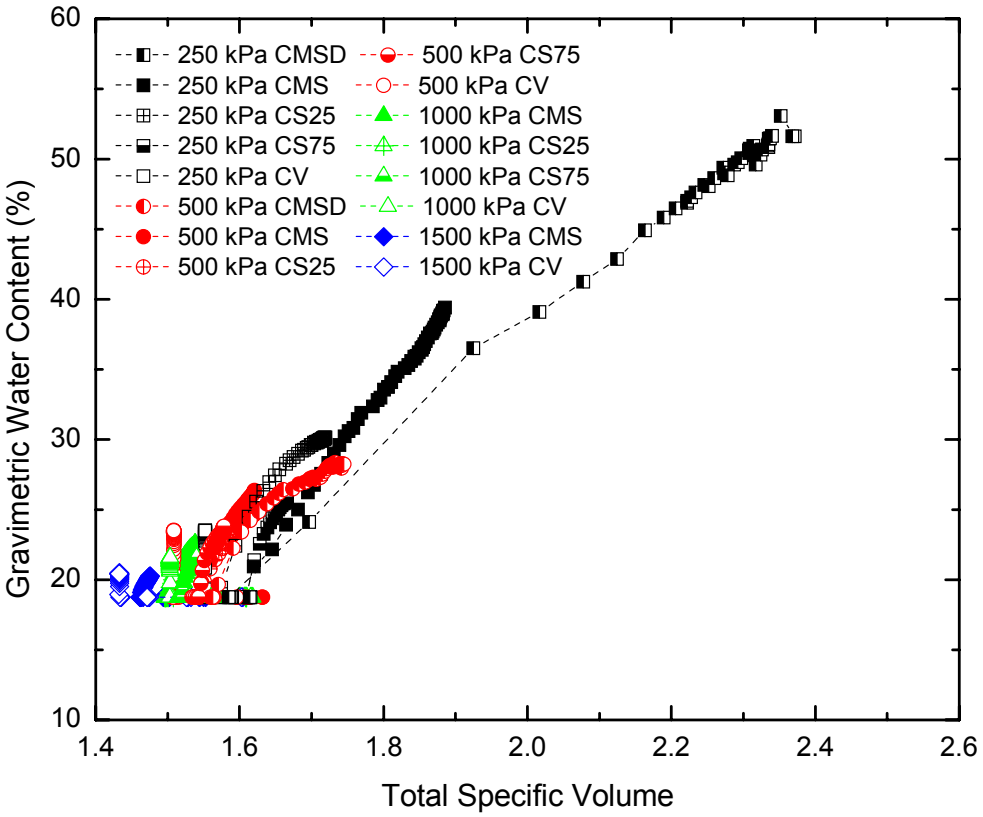

Figure 9.11: Water content versus specific volume for all infiltration tests.

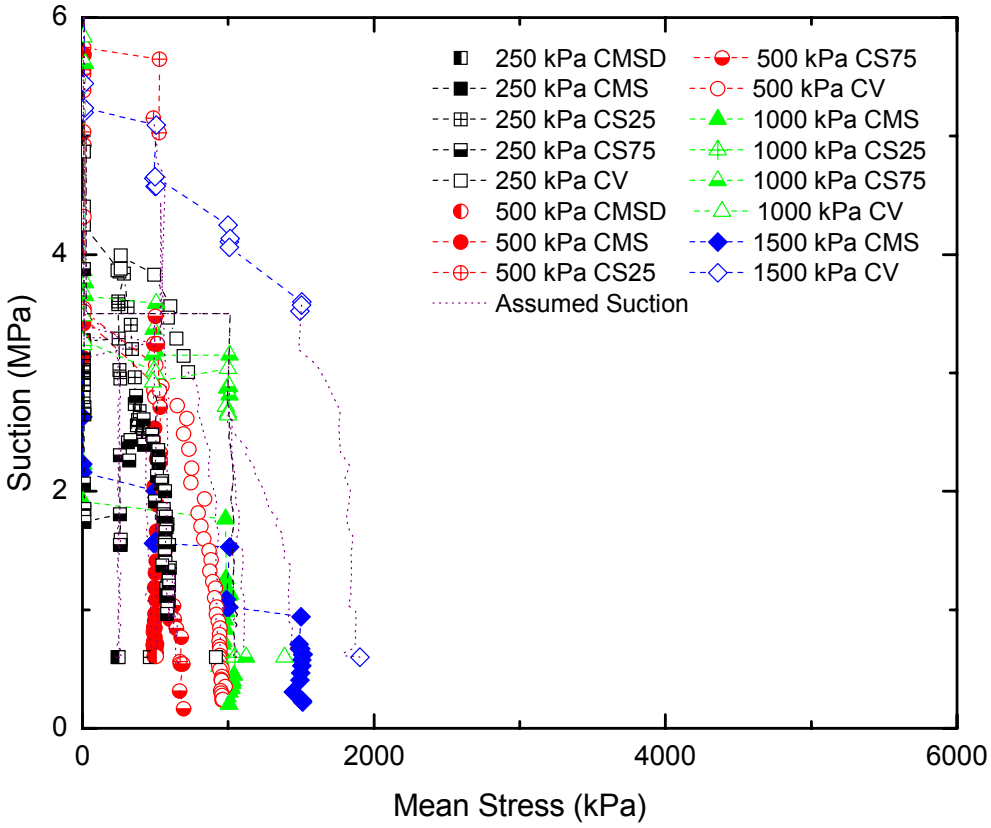

Figure 9.12: Suction versus mean stress for all infiltration tests.

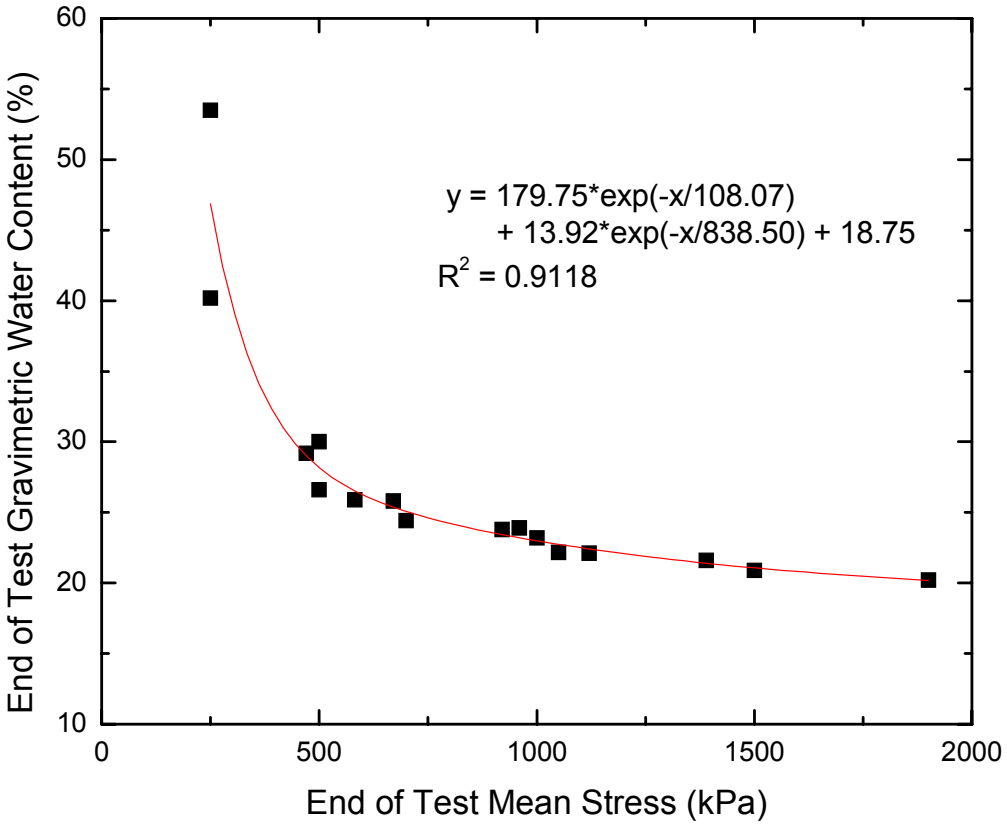

Figure 9.13: End of test gravimetric water content versus end of test mean stress for all infiltration tests.

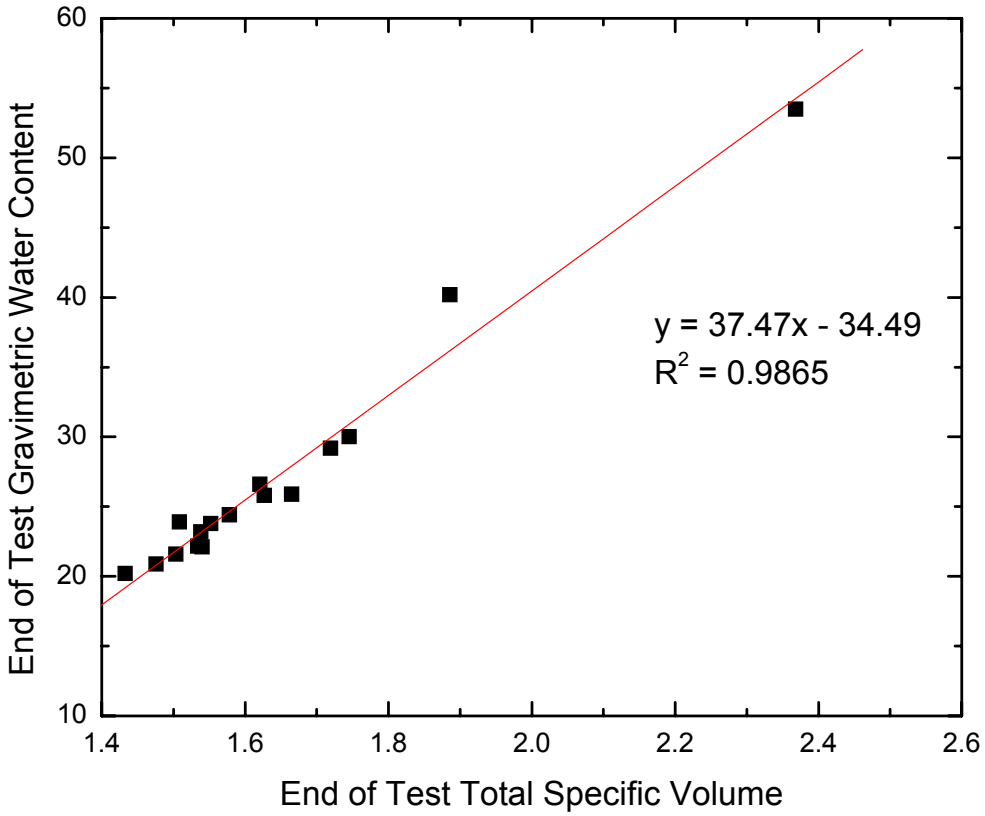

Figure 9.14: End of test gravimetric water content versus end of test specific volume for all infiltration tests.

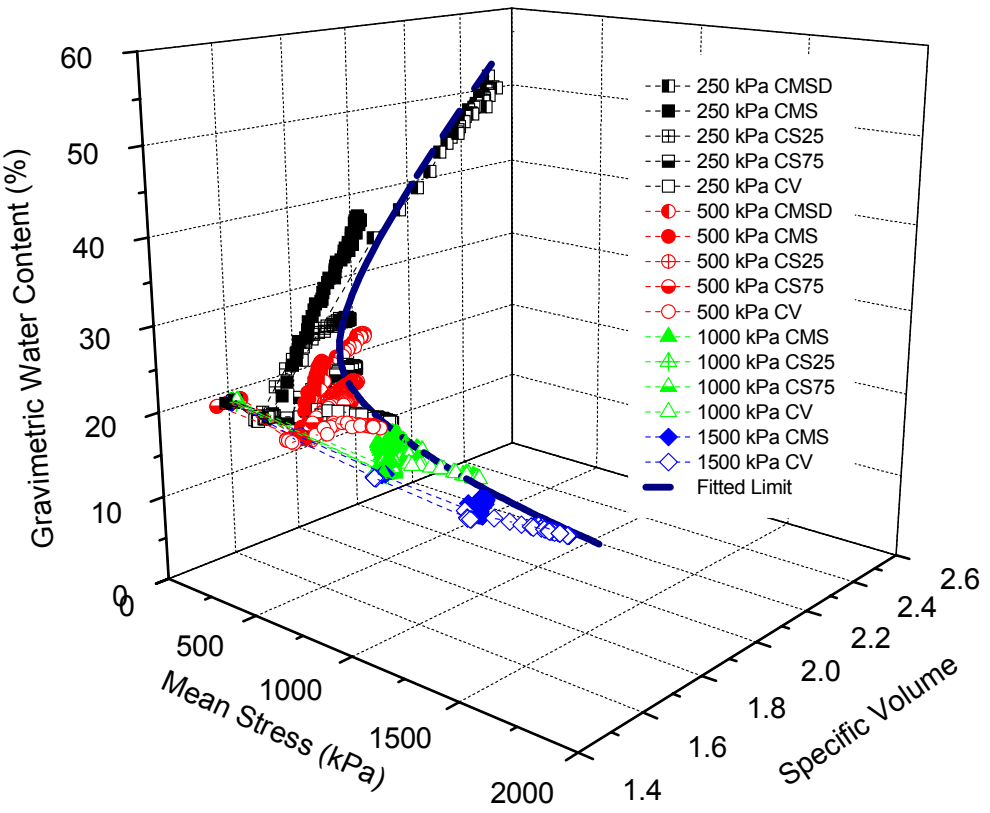

Figure 9.15: Mean stress – specific volume – gravimetric water content results for all infiltration tests.

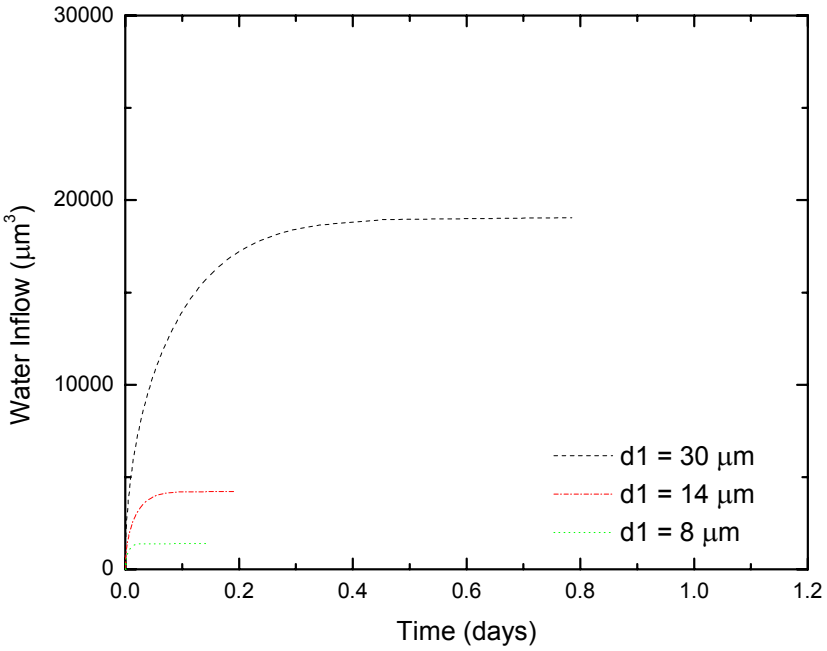

a. Closed end – low pressure data

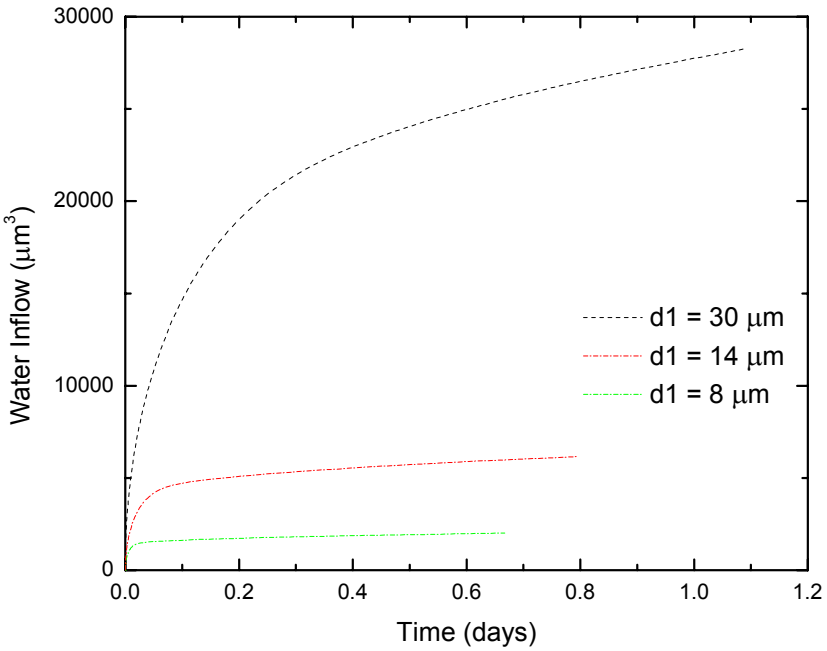

b. Closed end – diffusion data

Figure 9.16: Closed – low pressure, closed – diffusion, constant volume (CV) and constant mean stress (CMS) water inflow data.

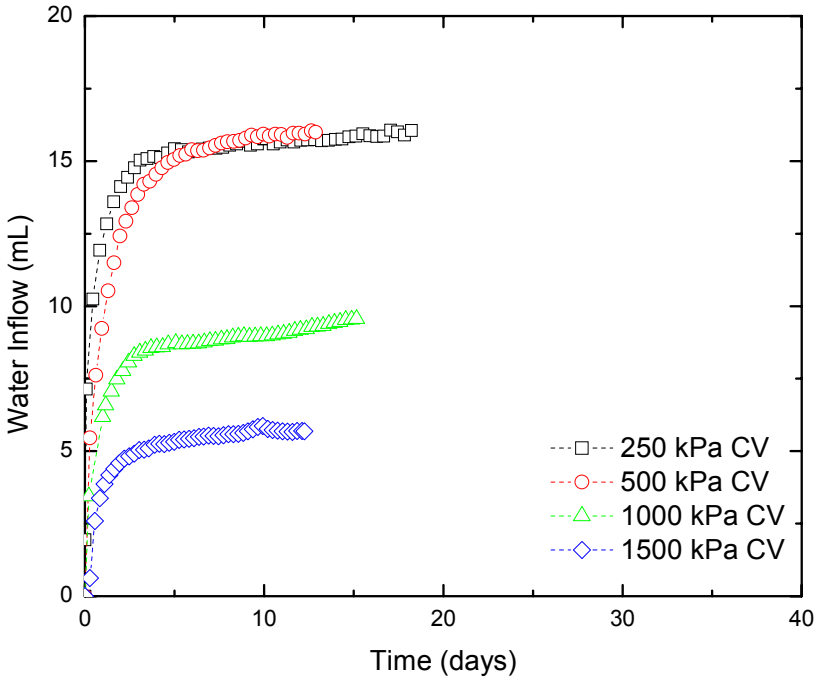

c. Constant volume data

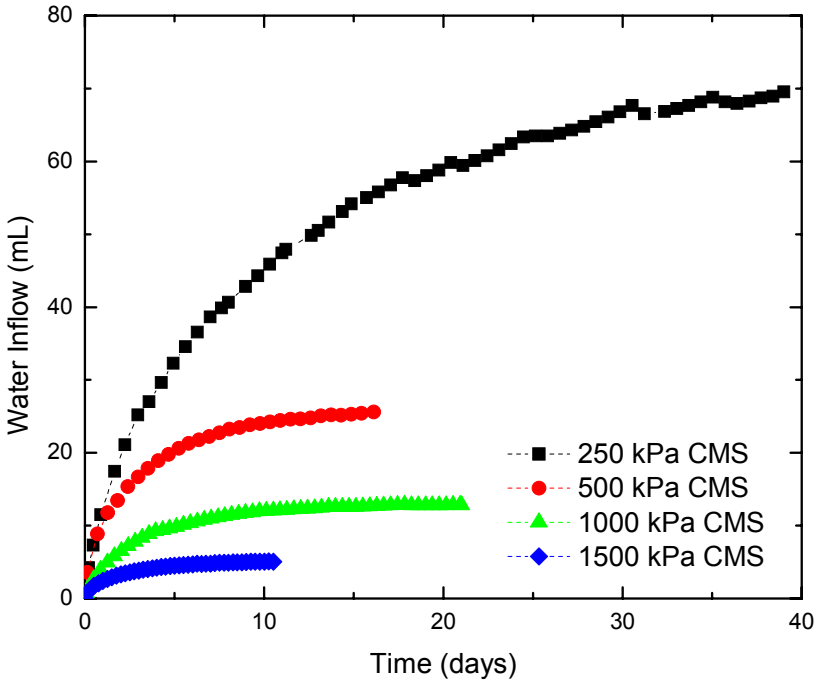

d. Constant mean stress data

Figure 9.16: Closed – low pressure, closed – diffusion, constant volume (CV) and constant mean stress (CMS) water inflow data.

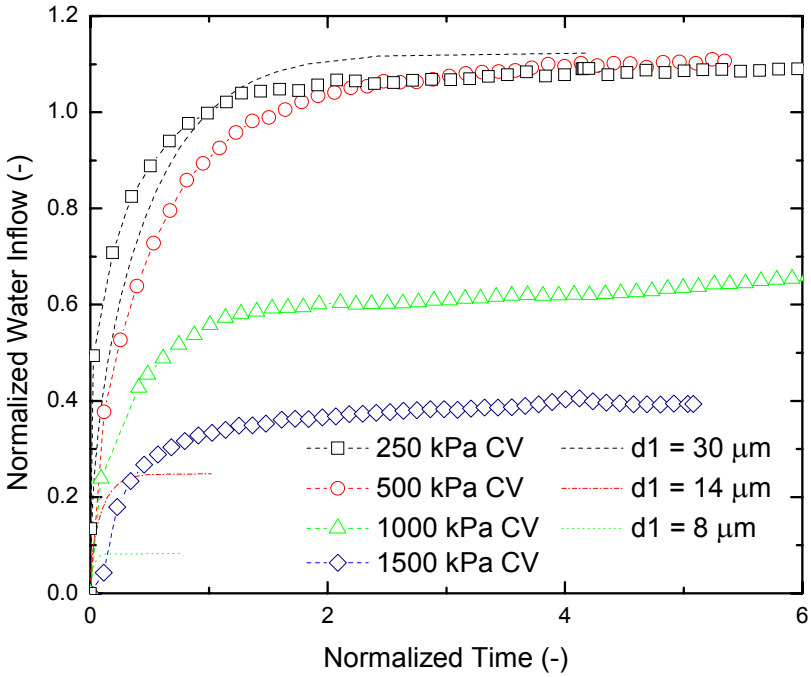

a. Normalized constant volume and closed – low pressure

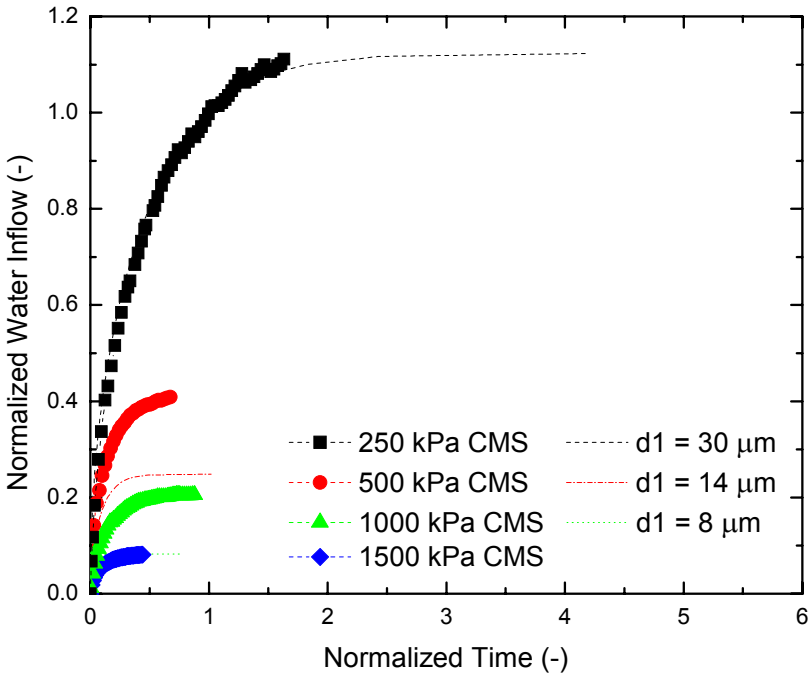

b. Normalized constant mean stress and closed – low pressure

Figure 9.17: Normalized closed – low pressure, constant volume and constant mean stress inflow versus normalized time.

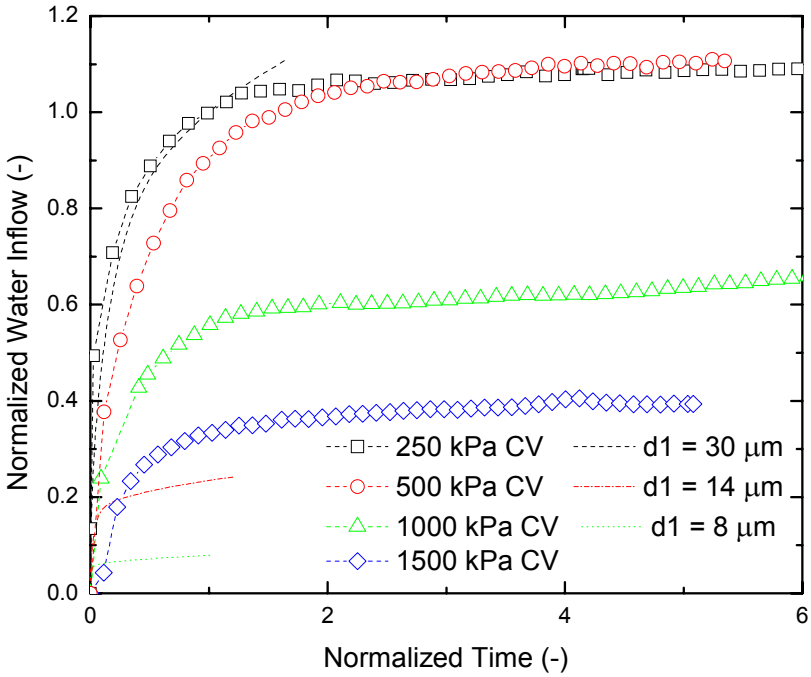

a. Normalized constant volume and closed – diffusion

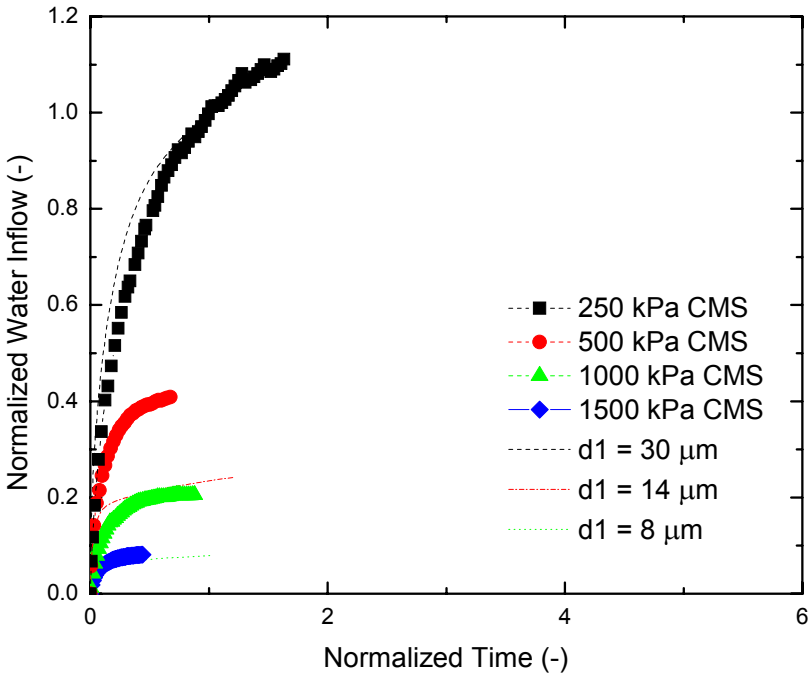

b. Normalized constant mean stress and closed – diffusion

Figure 9.18: Normalized closed - diffusion and constant volume inflow versus normalized time.

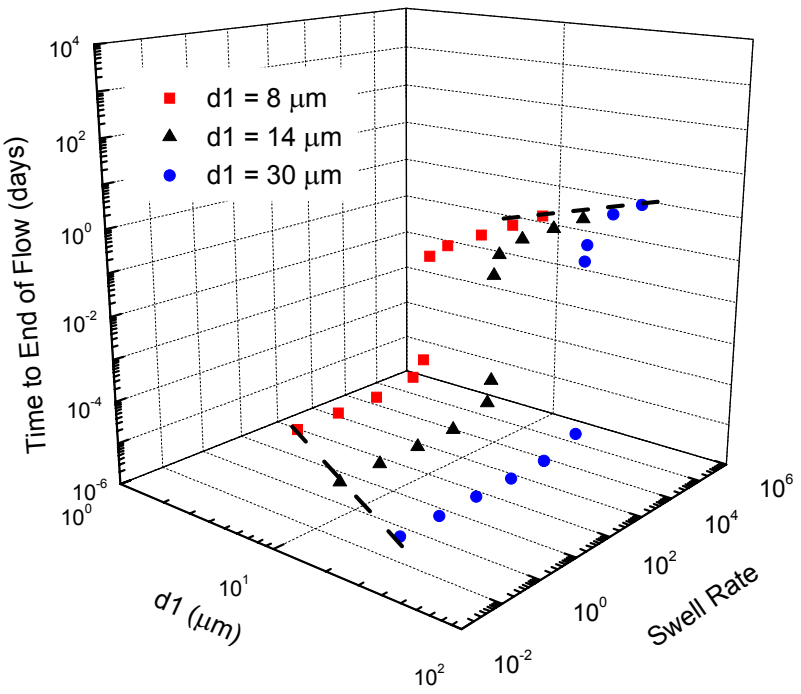

a. Closed – low pressure

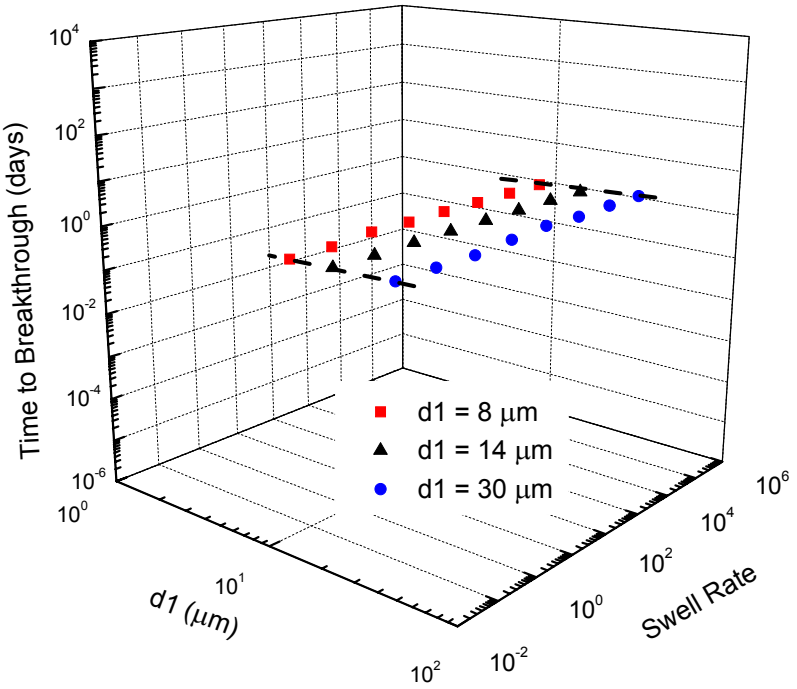

b. Closed - diffusion

Figure 9.19: Closed – low pressure and diffusion model summaries – influence of initial main tube diameter (d1).

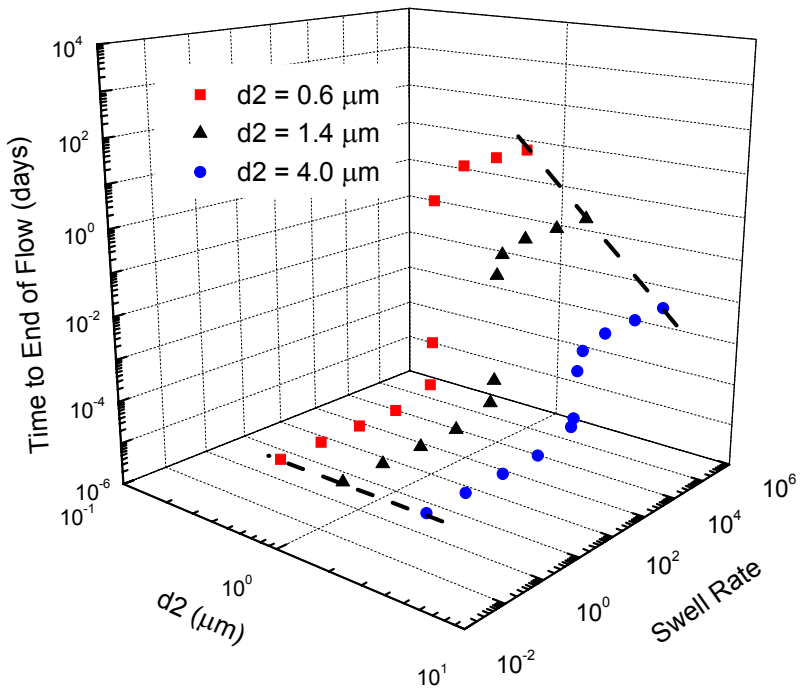

a. Closed – low pressure

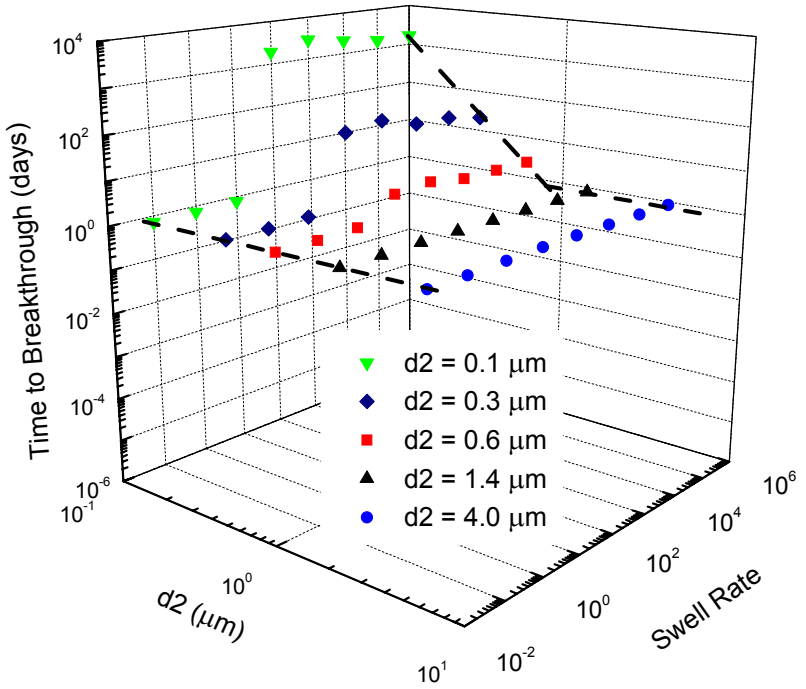

b. Closed - diffusion

Figure 9.20: Closed – low pressure and diffusion model summaries – influence of final or minimum main tube diameter.

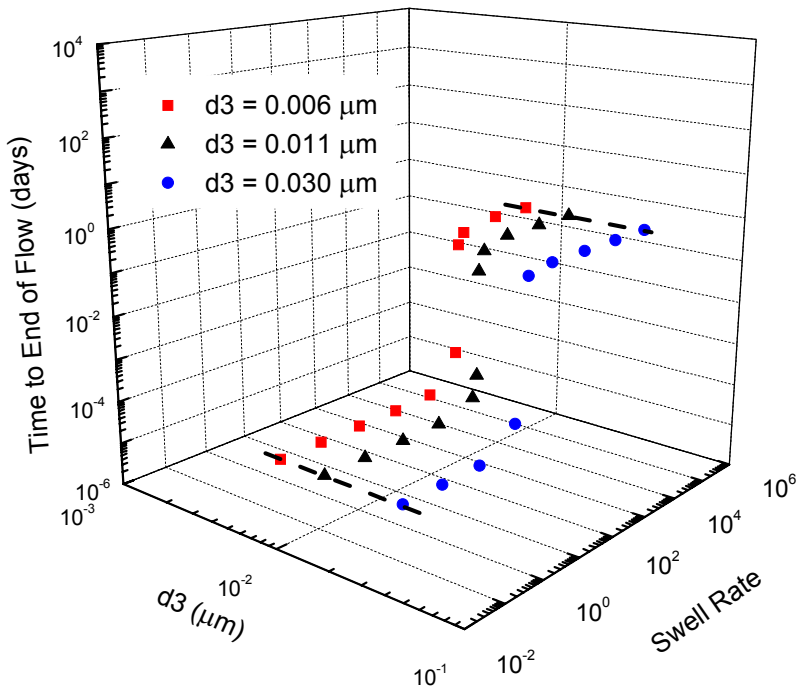

a. Closed – low pressure

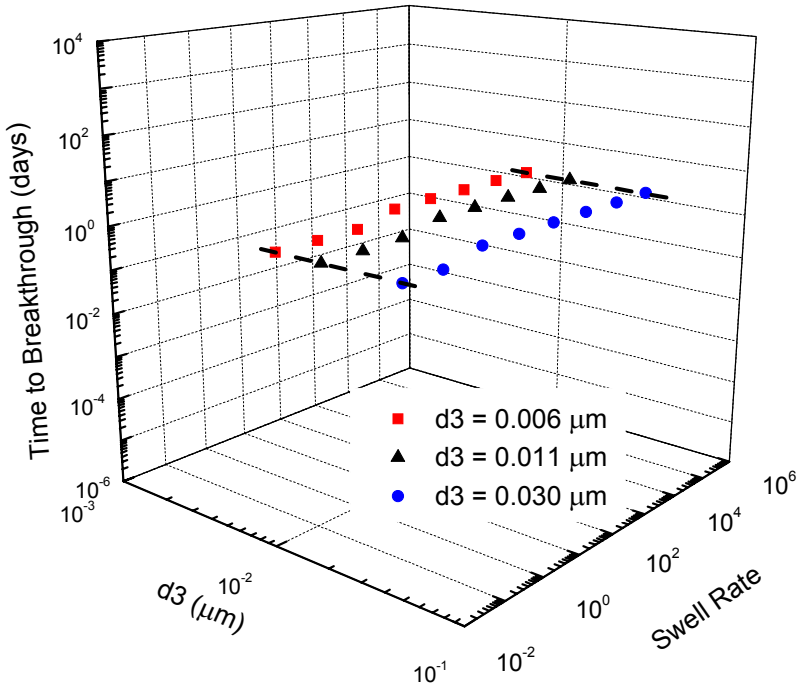

b. Closed - diffusion

Figure 9.21: Closed – low pressure and diffusion model summaries – influence of peripheral tube diameter.

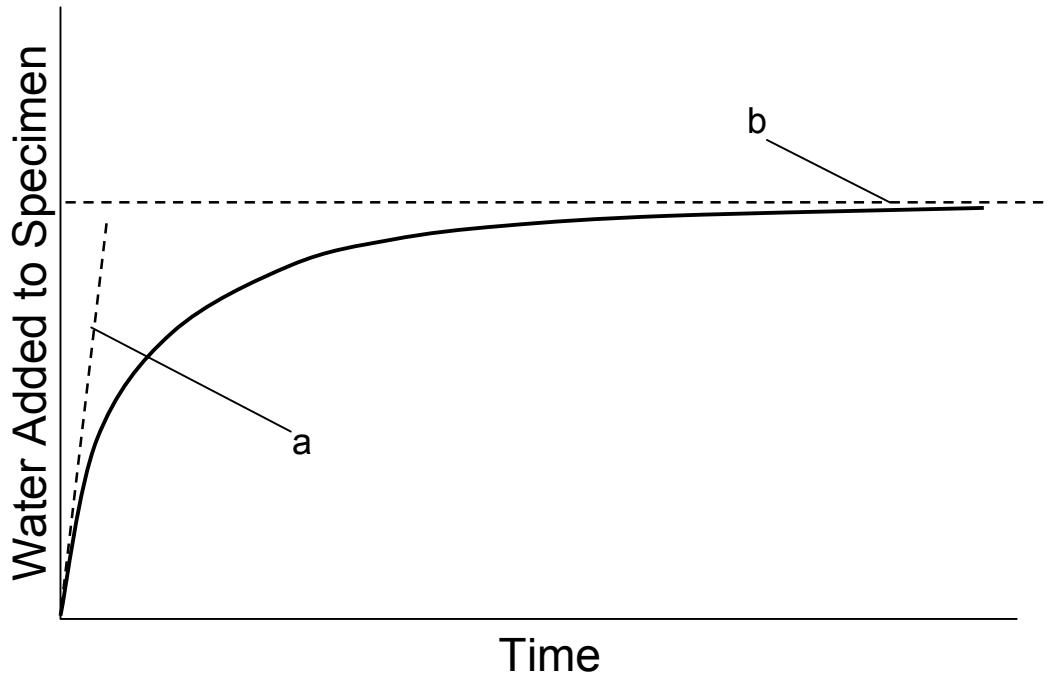

a.

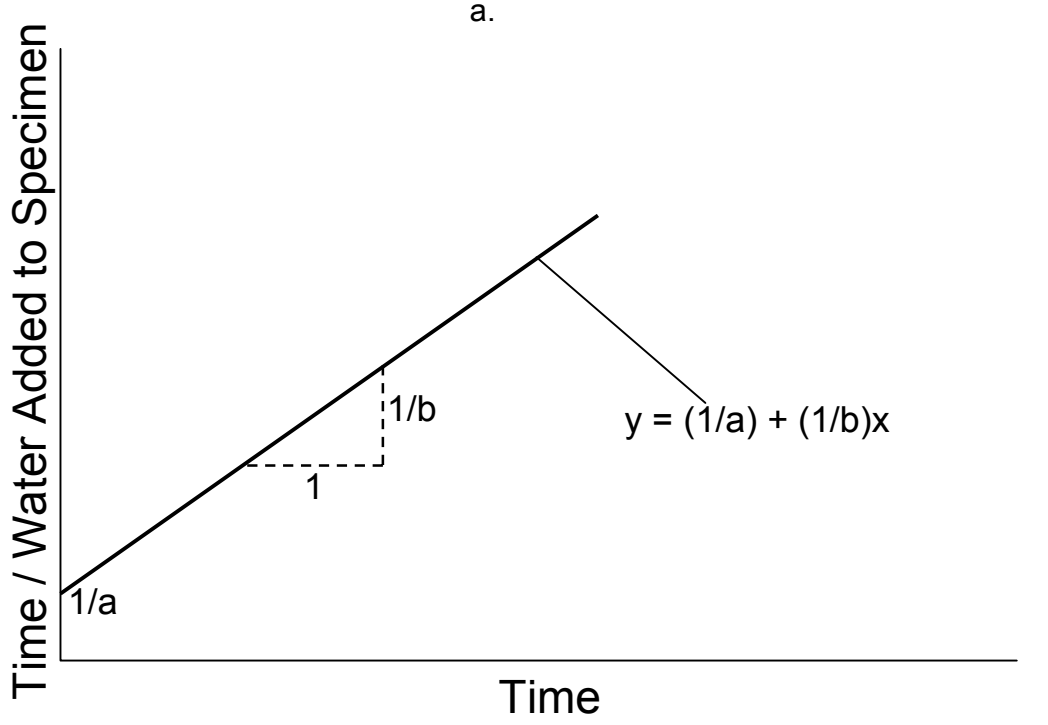

b.

Figure 9.22: Hyperbolic curve fitting.

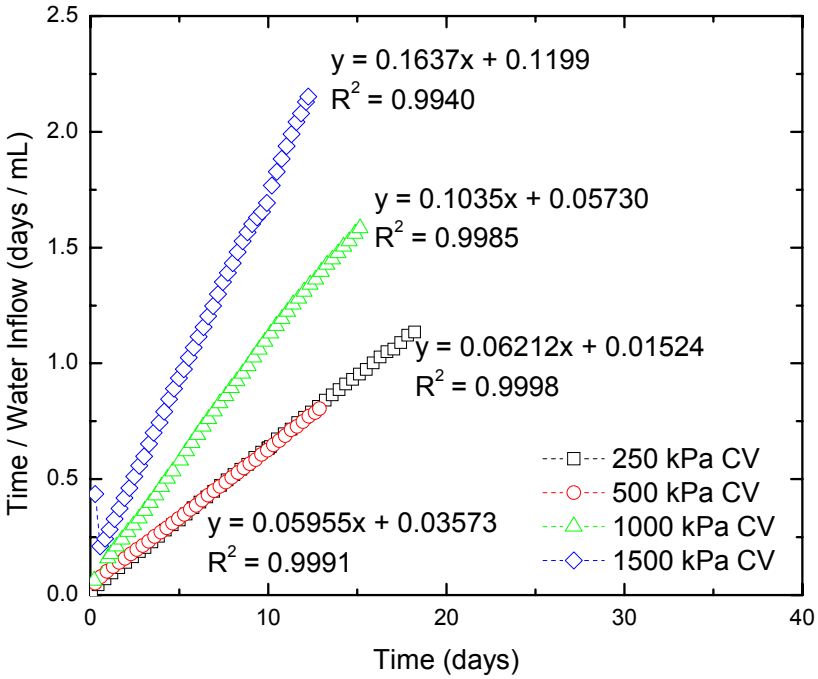

a. Constant volume (CV)

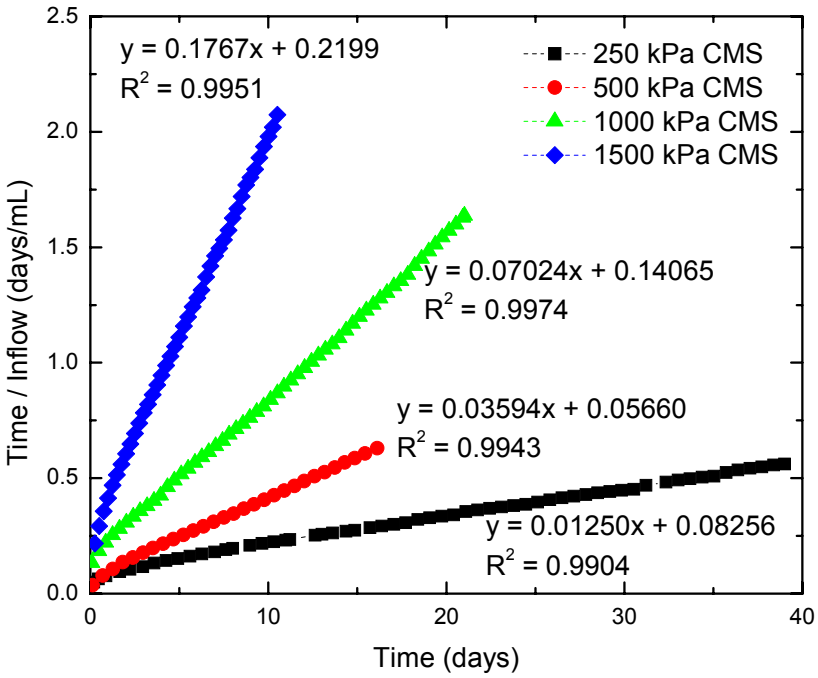

b. Constant mean stress (CMS)

Figure 9.23: Time/inflow versus time for constant volume (CV) and constant mean stress (CMS) tests.

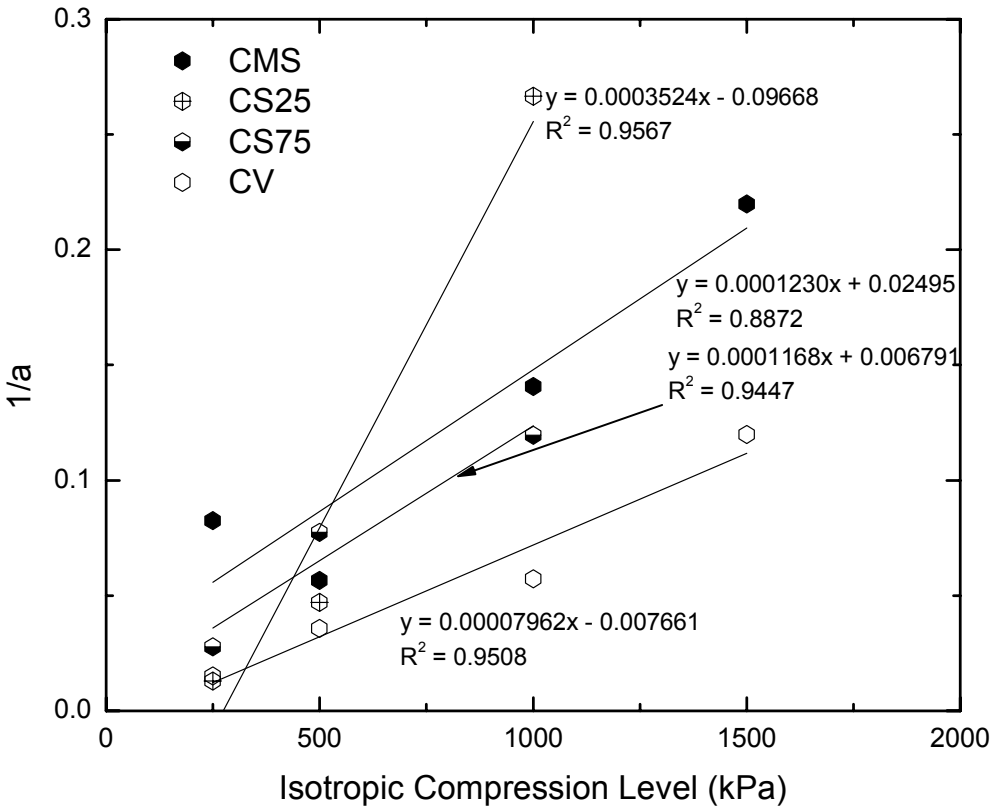

Figure 9.24: Fitted parameter a versus isotropic compression level for infiltration results.

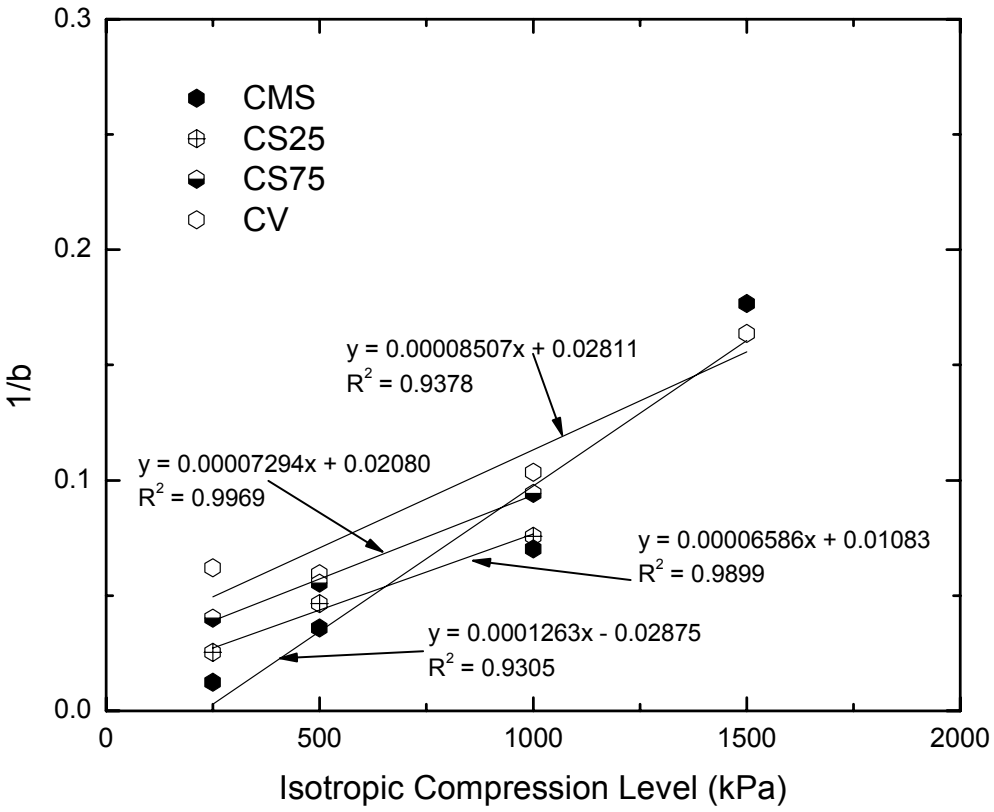

Figure 9.25: Fitted parameter b versus isotropic compression level for infiltration results.

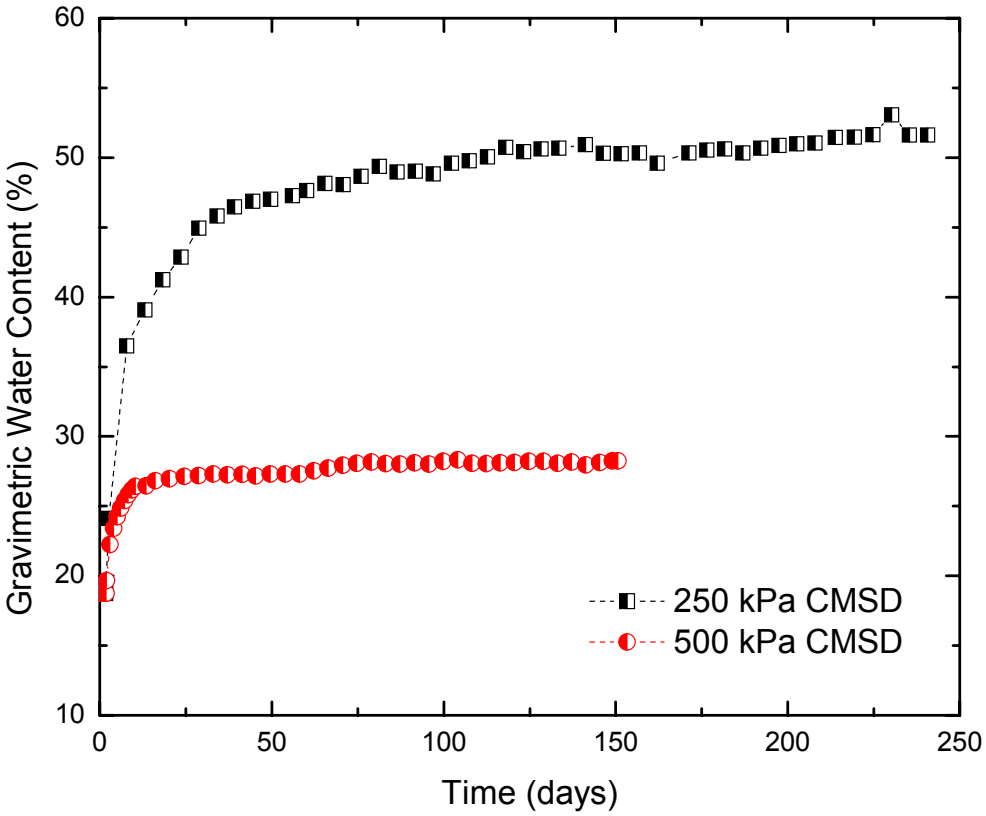

Figure 9.26: Gravimetric water content versus time for constant mean stress – drained tests.

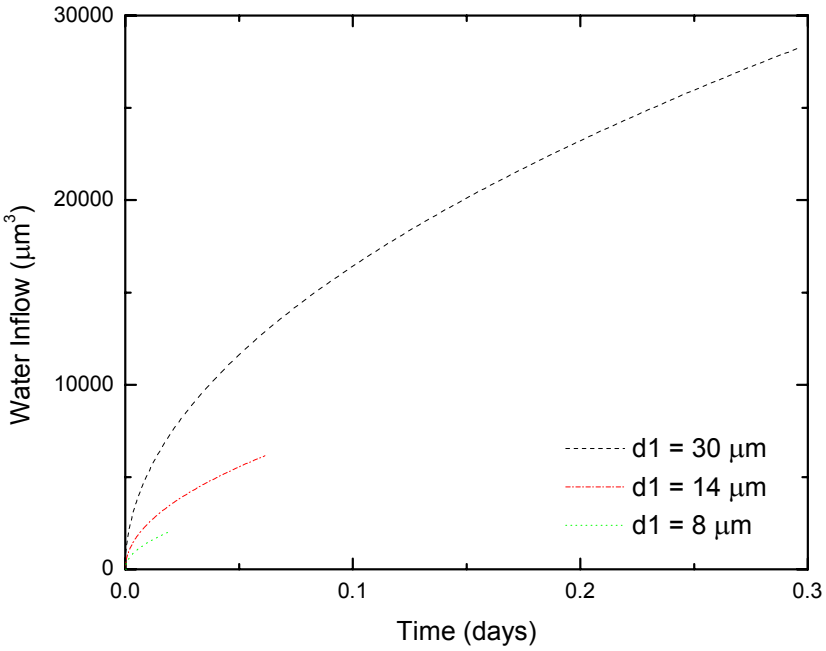

a. Open tube data

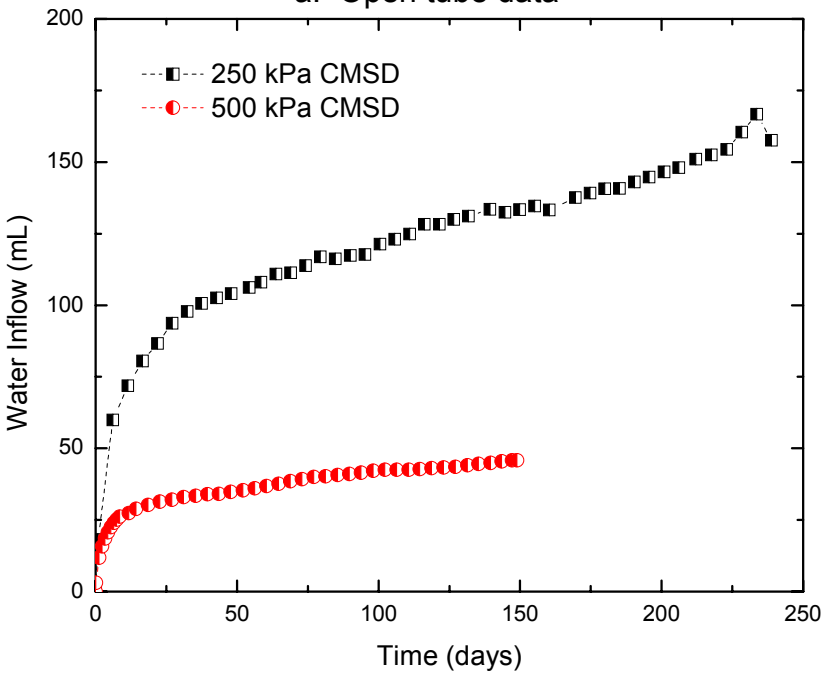

b. Constant mean stress – drained data

Figure 9.27: Open tube and constant mean stress – drained (CMSD) inflow data versus time.

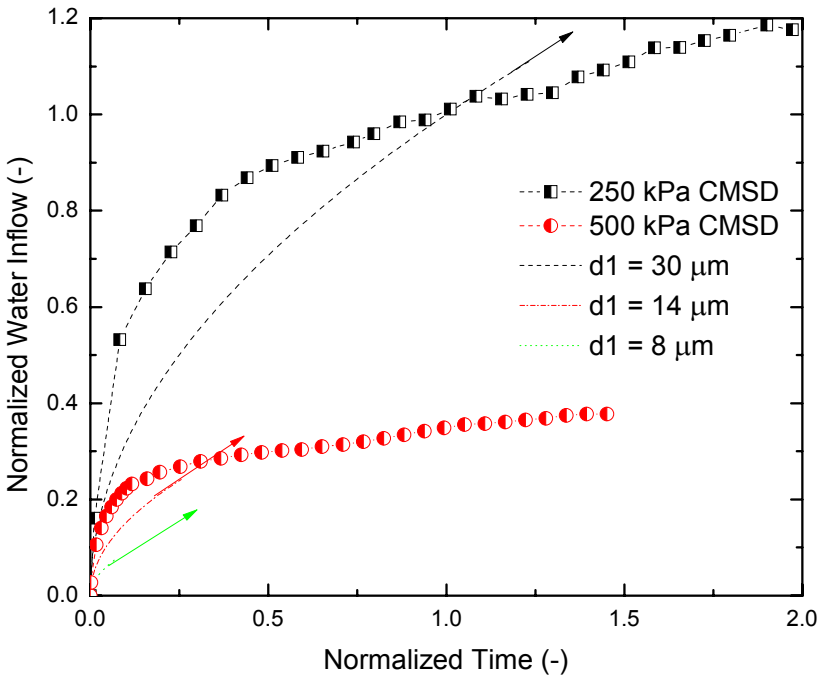

Figure 9.28: Normalized open tube and constant mean stress – drained inflow versus normalized time.

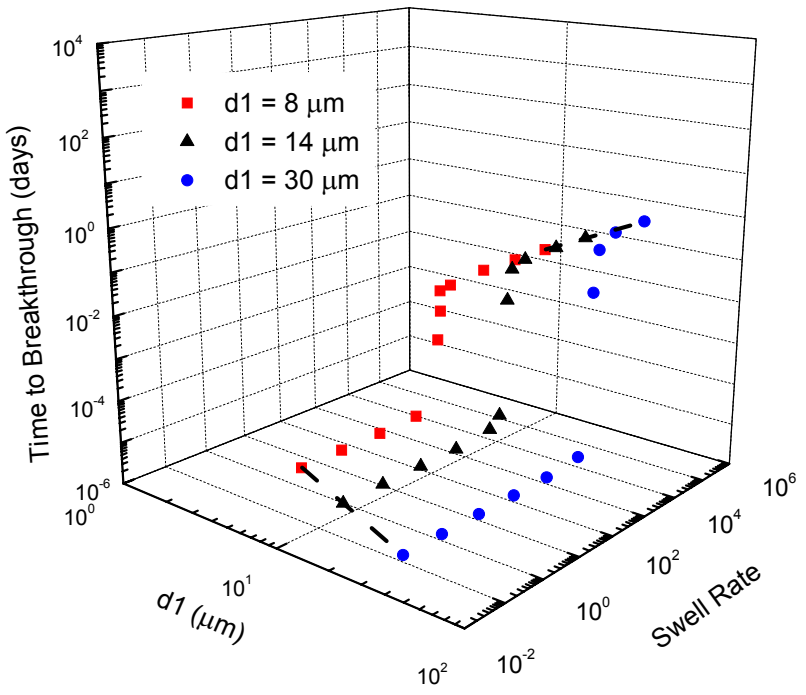

Figure 9.29: Open model summary – influence of initial main tube diameter.

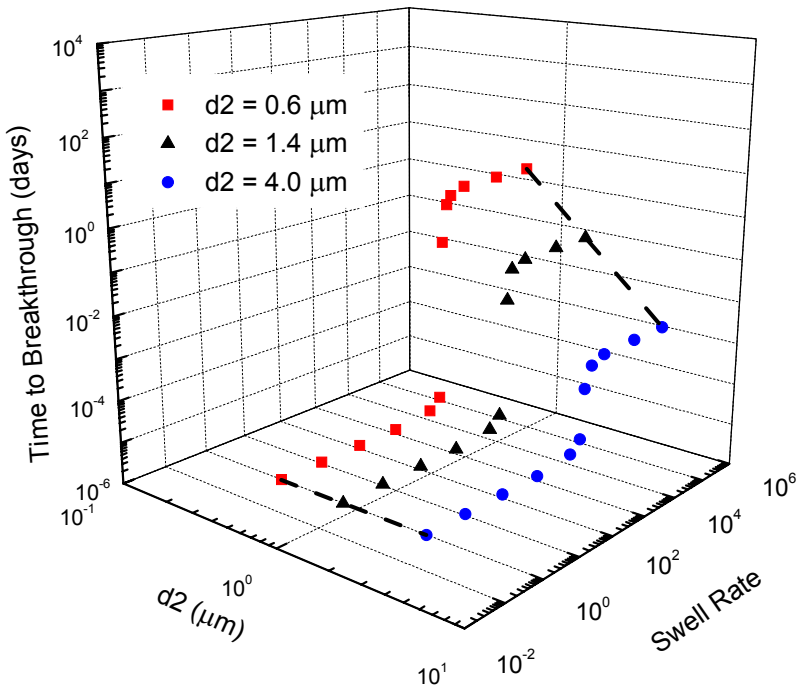

Figure 9.30: Open model summary – influence of final or minimum main tube diameter.

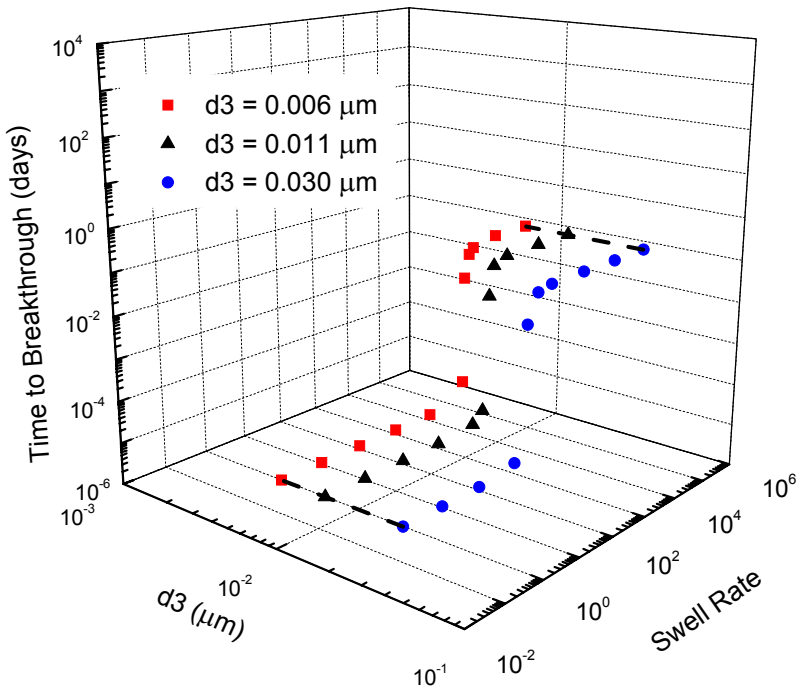

Figure 9.31: Open model summary – influence of peripheral tube diameter.

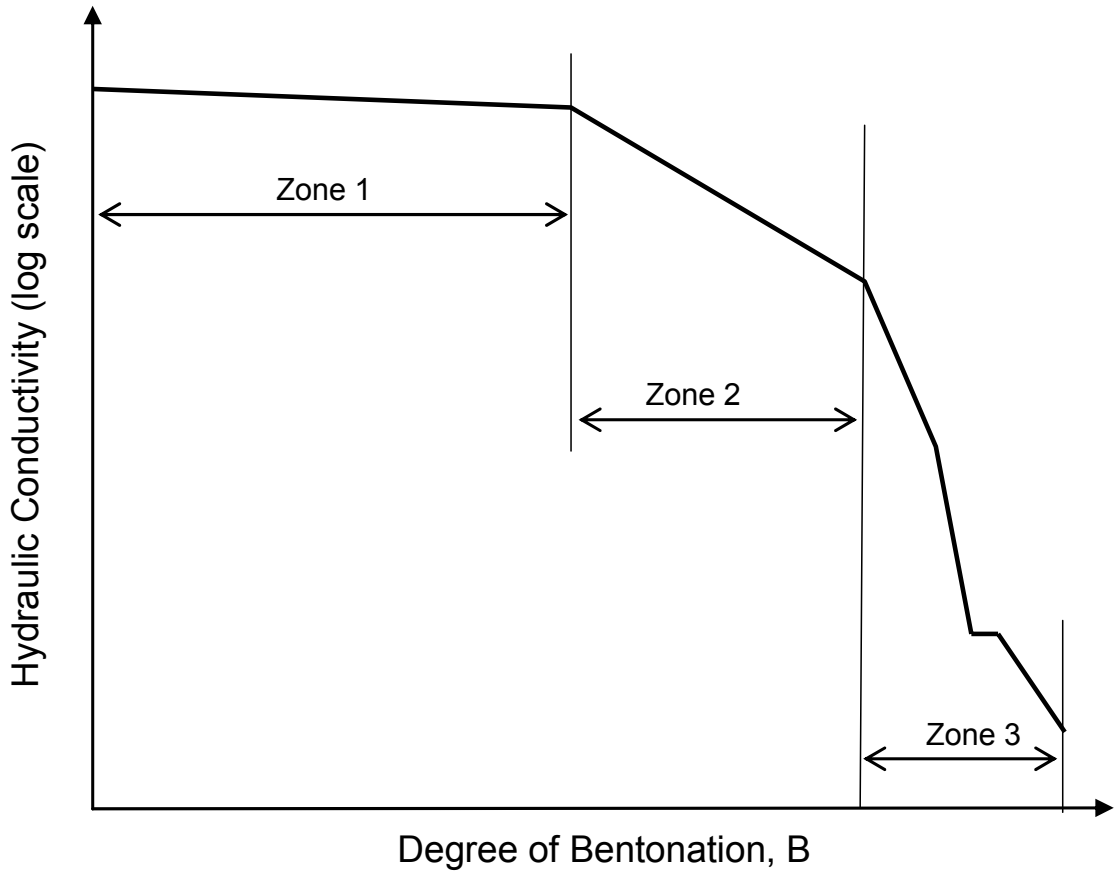

Figure 9.32. Hydraulic conductivity versus degree of bentonation for grain-coated models (after Abichou et al. 2004).

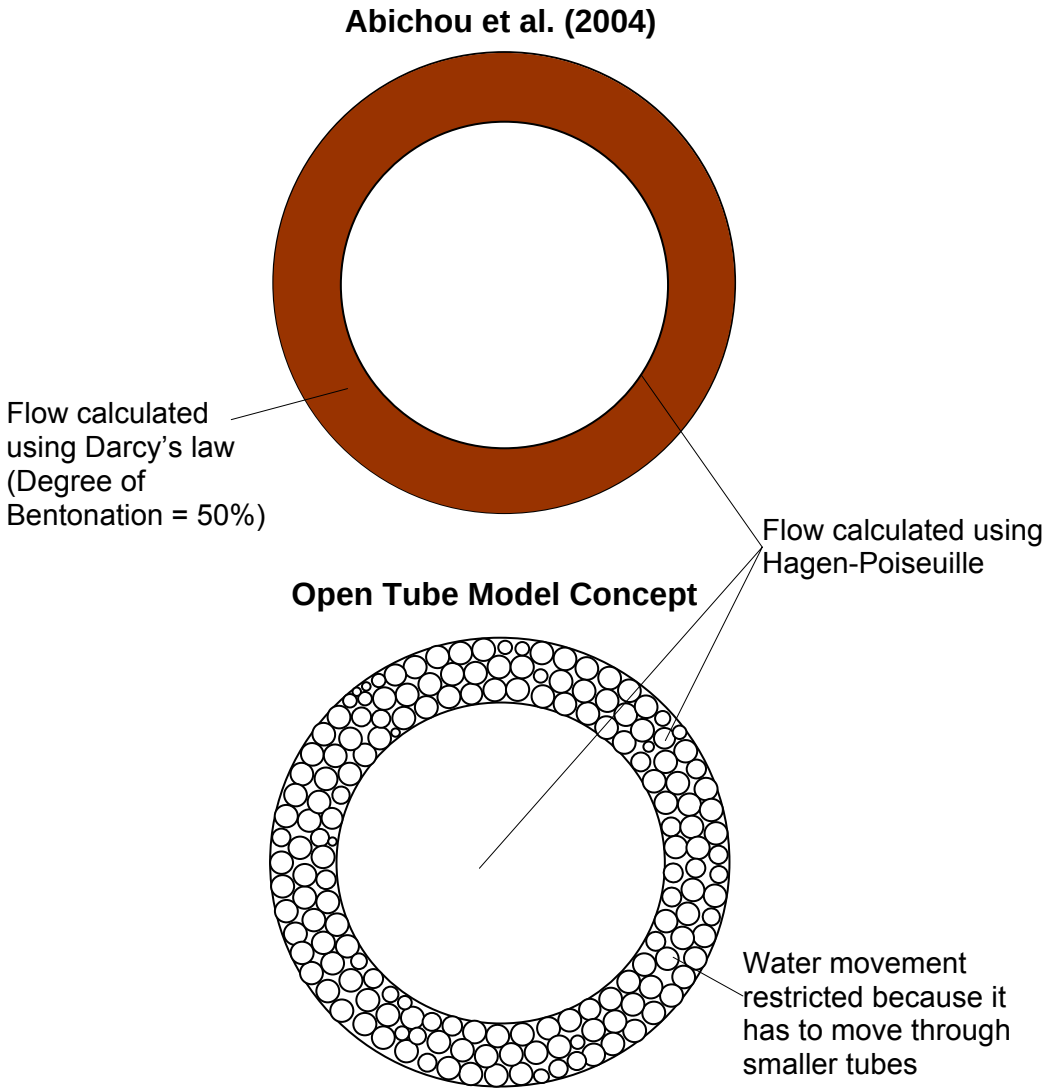

Figure 9.33. Comparison of open tube model and Abichou et al. (2004) and concepts.

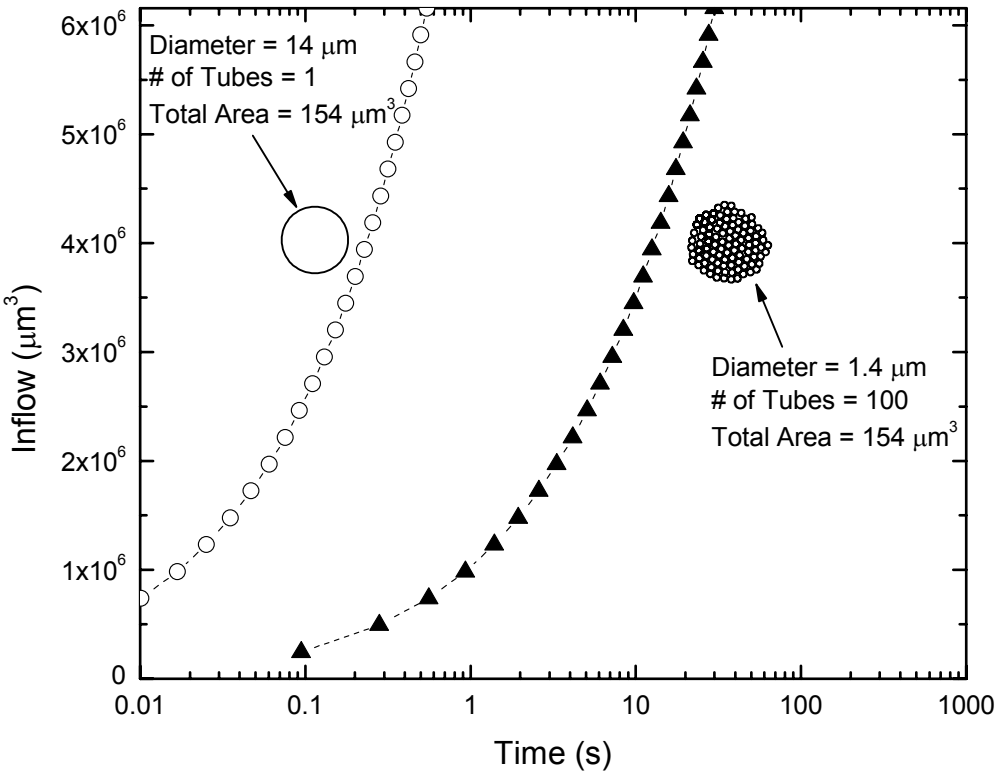

Figure 9.34: Equivalent area flow comparison for one (1) large tube and one hundred small tubes.

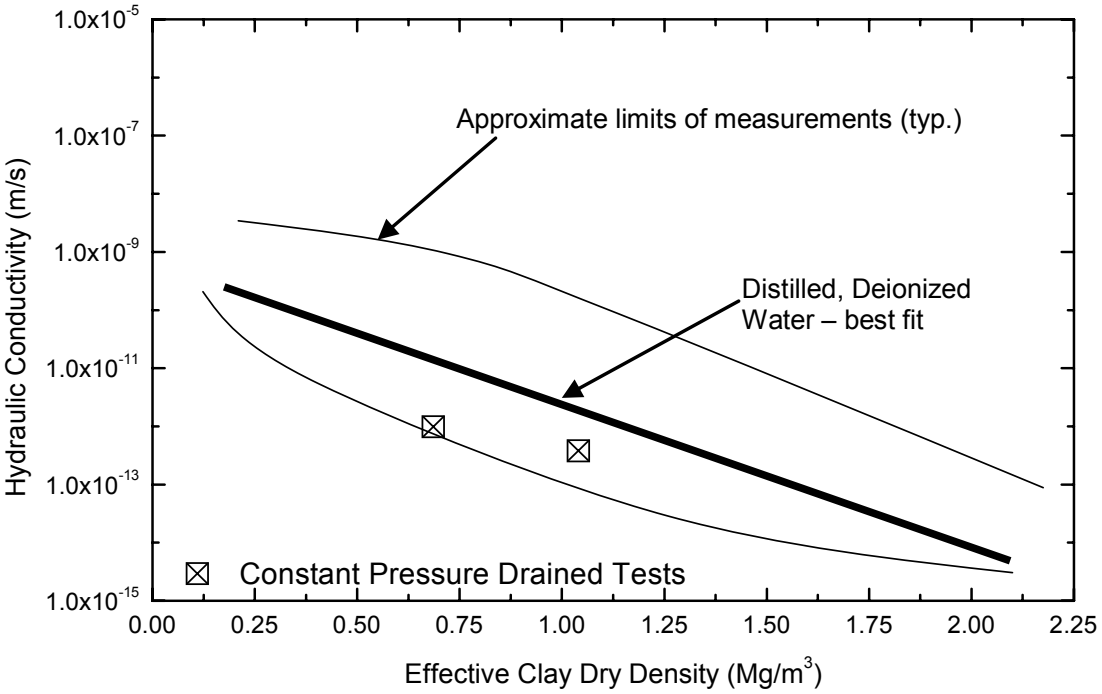

Figure 9.35. Variability of hydraulic conductivity versus permeant salinity (after Dixon et al. 2002a)

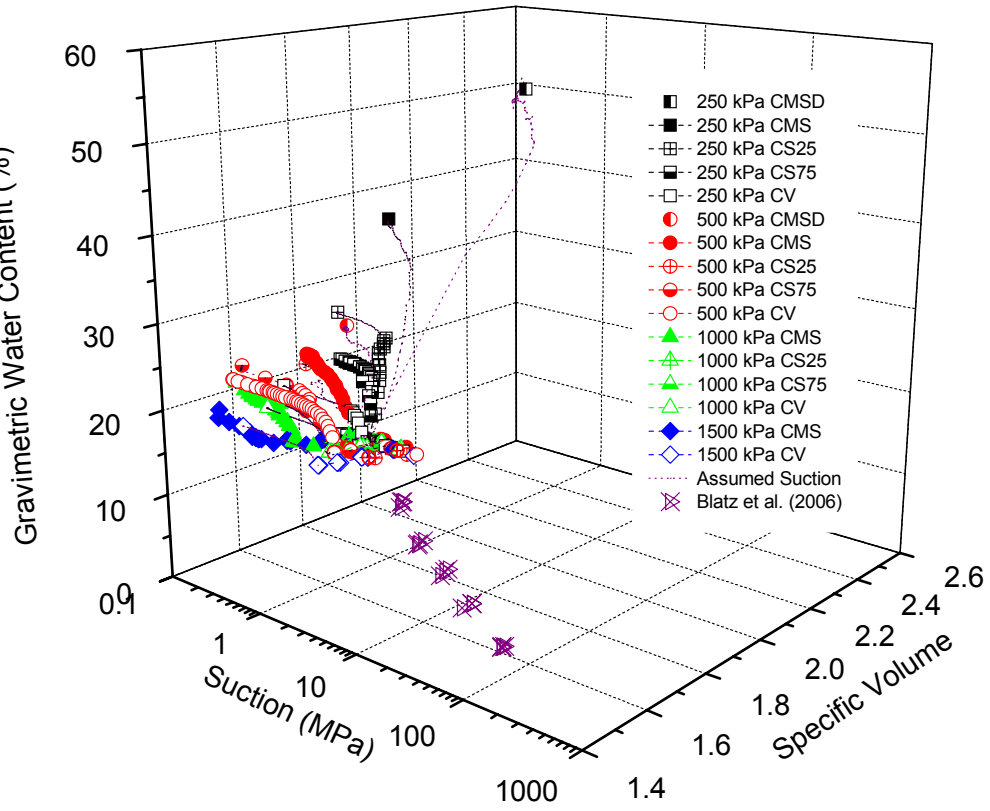

Figure 9.36. Three-dimensional water retention curve – specific volume versus suction versus gravimetric water content with data from Blatz et al. (2006).

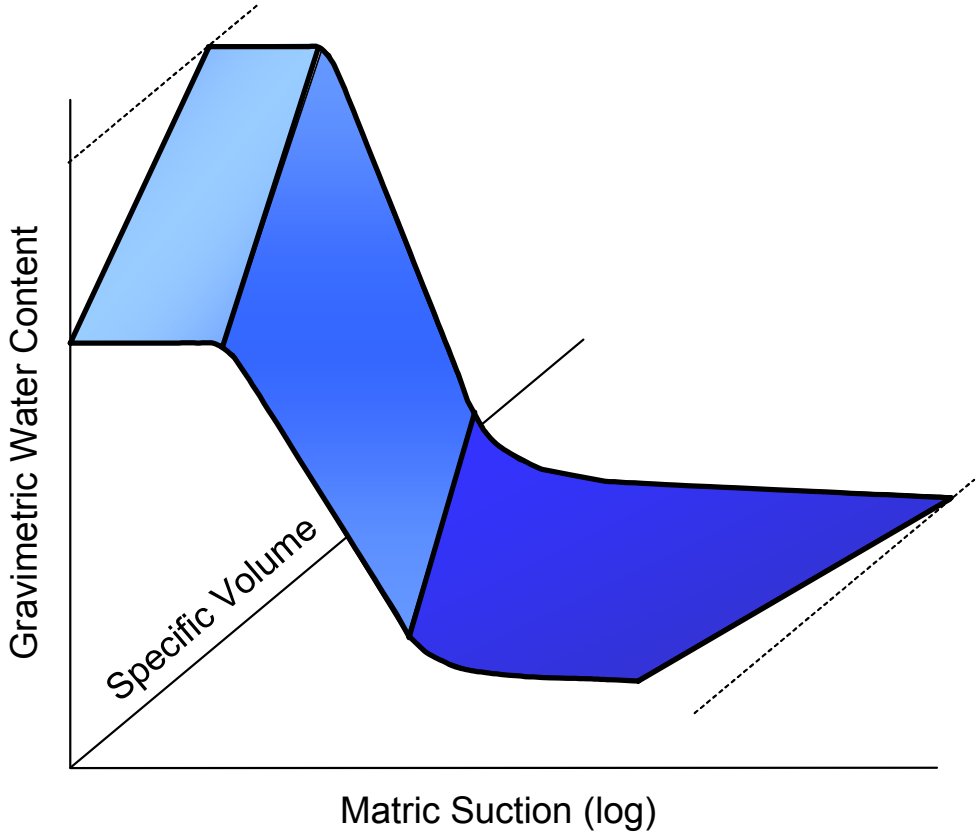

Figure 9.37. Three-dimensional water retention curve – proposed wetting curve.

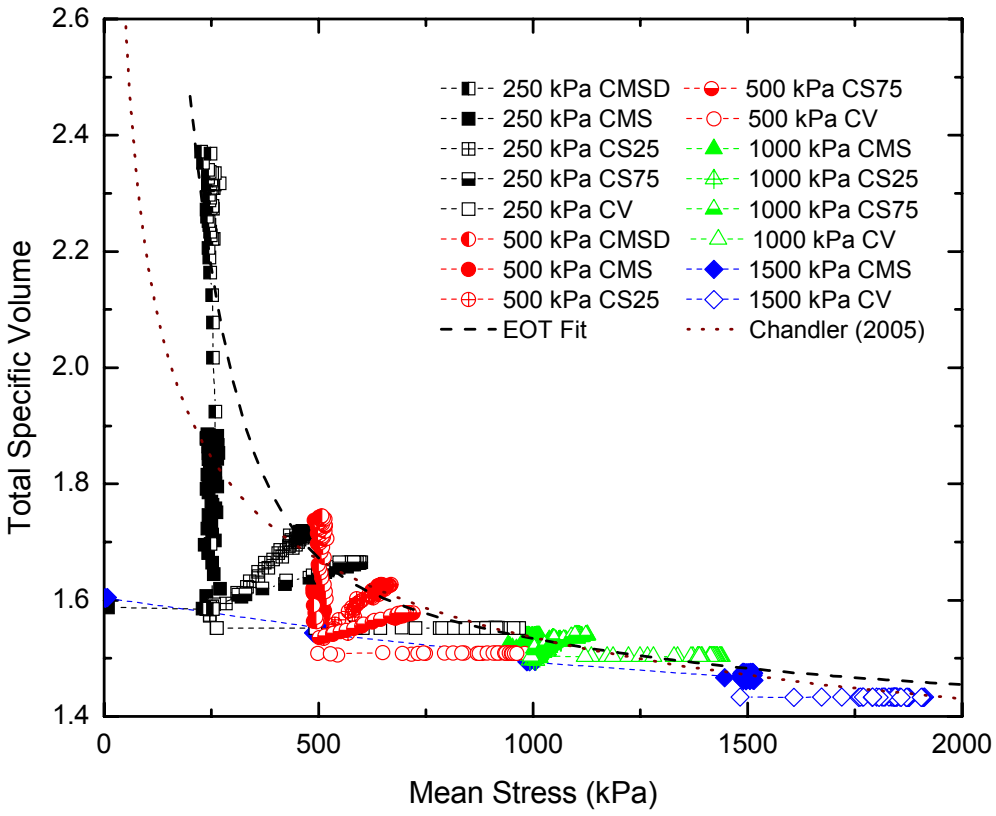

Figure 9.38. Total specific volume versus mean stress for all infiltration tests with end of test relationship based on one-dimensional 'swell pressure' measurements.

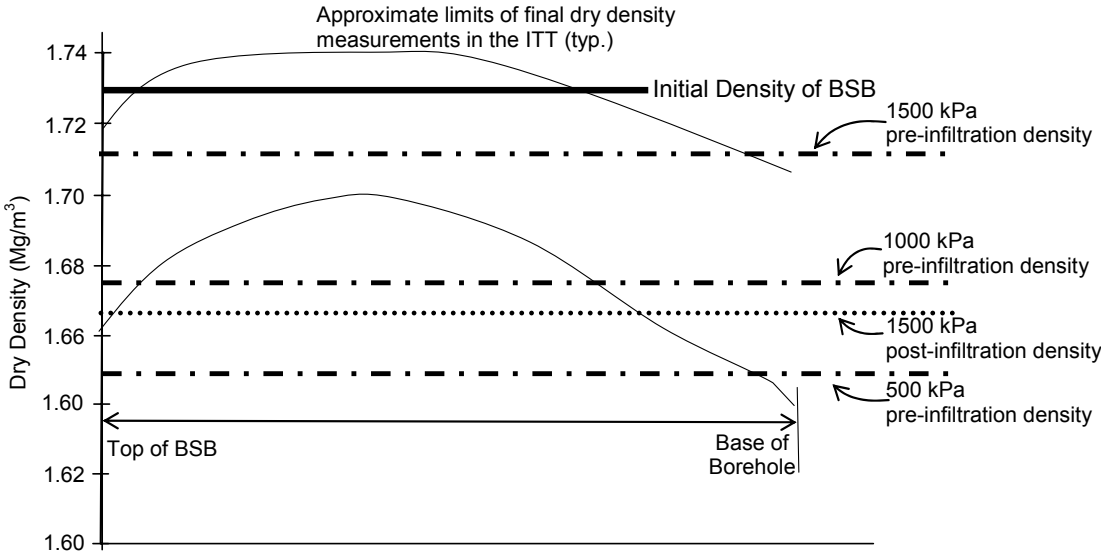

Figure 9.39. Dry density measurements from de-commissioning of isothermal test with pre-infiltration densities added (after Dixon et al. 2002b).

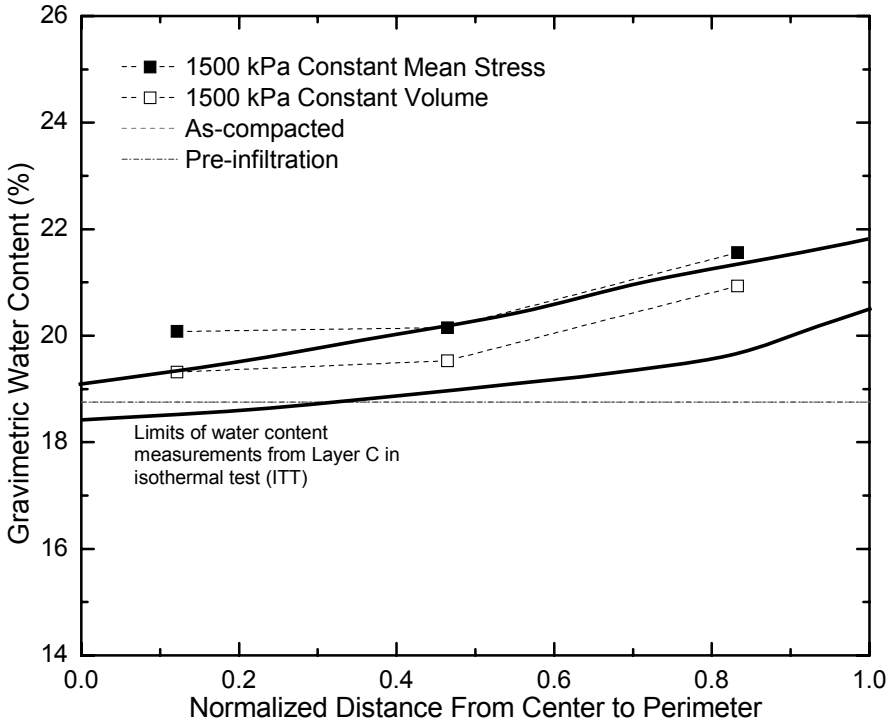

Figure 9.40. Gravimetric water content versus normalized distance from center to perimeter for 1500 kPa infiltration tests and Layer C from isothermal test (after Dixon et al. 2002b).

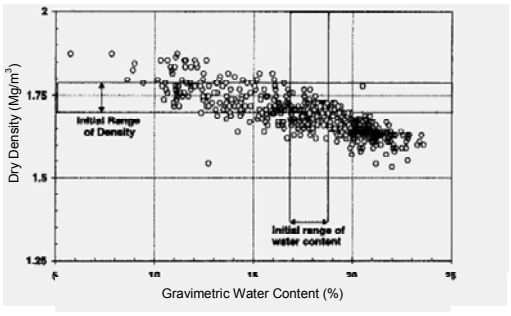

a.

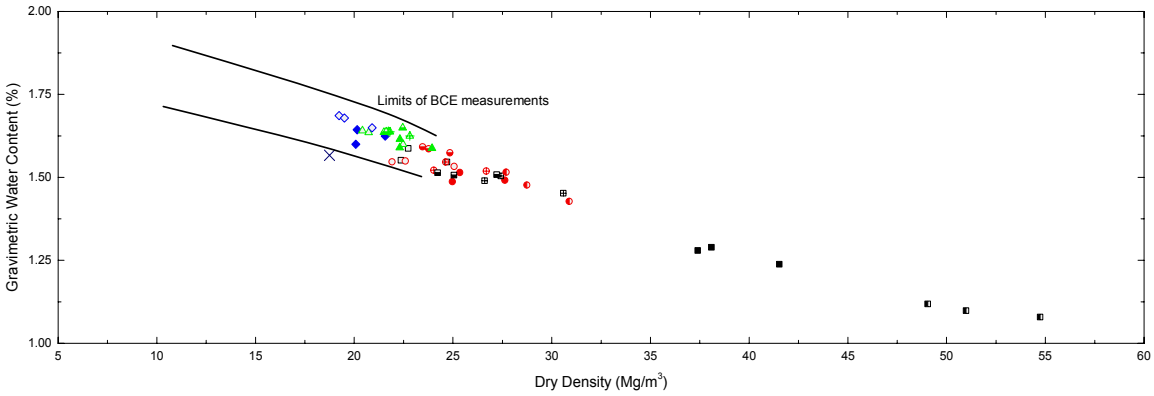

b.

Figure 9.41. Dry density versus gravimetric water content measurement comparison with Buffer Container Experiment (after Dixon et al. 2002b).

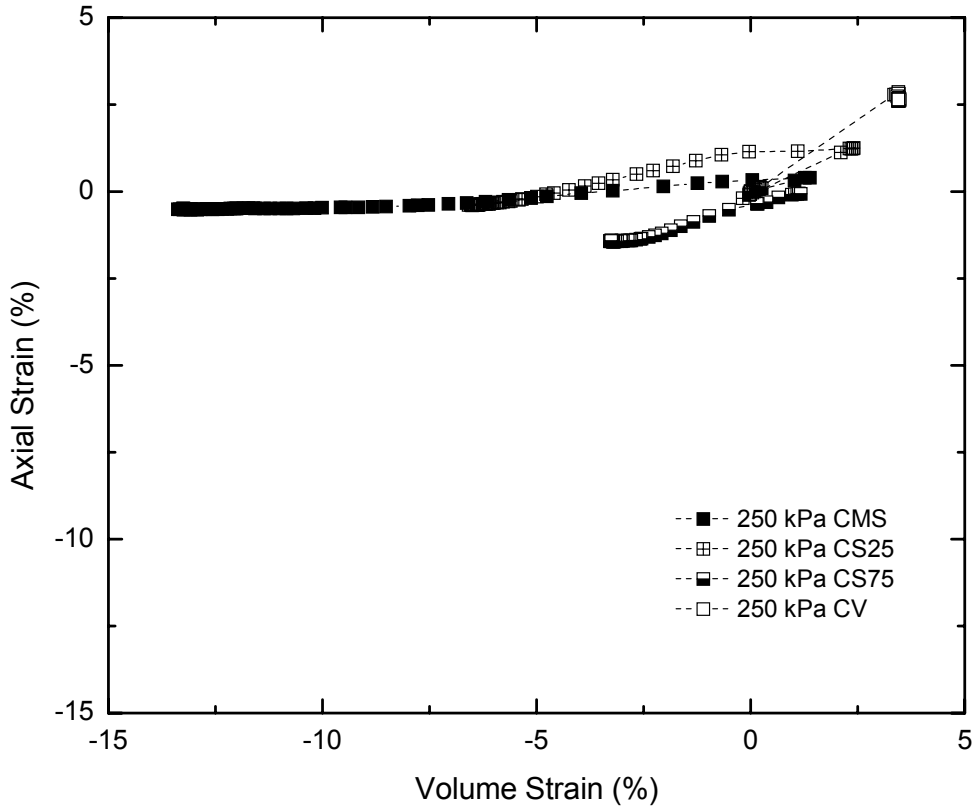

Figure 9.42. Axial strain versus volume strain – 250 kPa undrained tests.

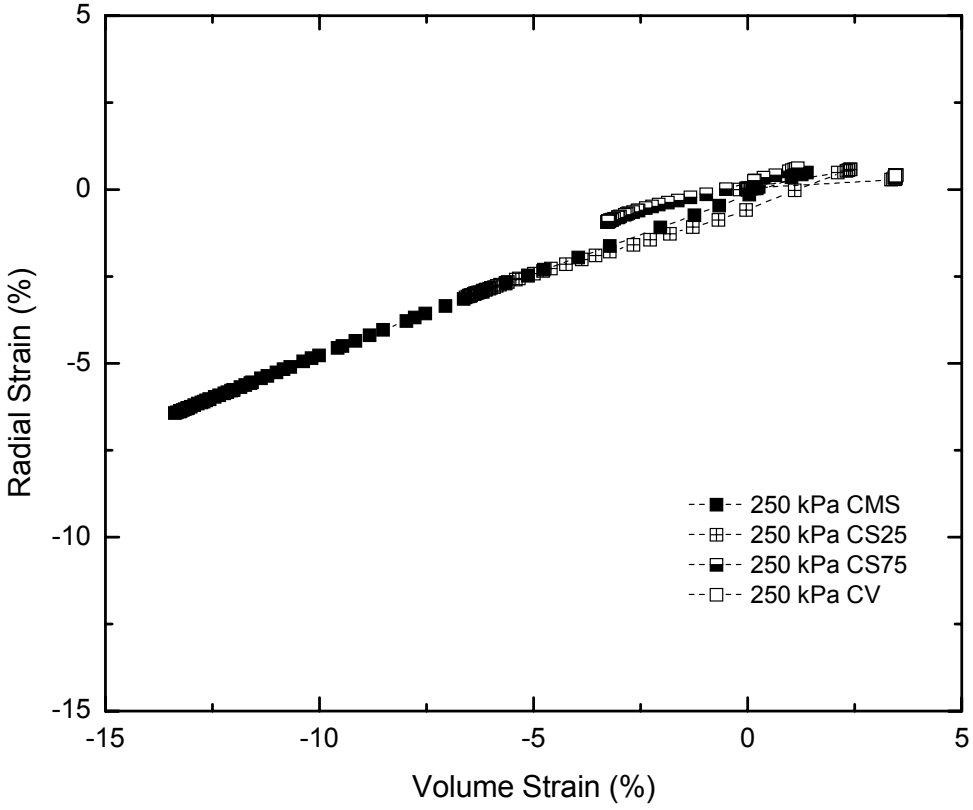

Figure 9.43. Radial strain versus volume strain – 250 kPa undrained tests.

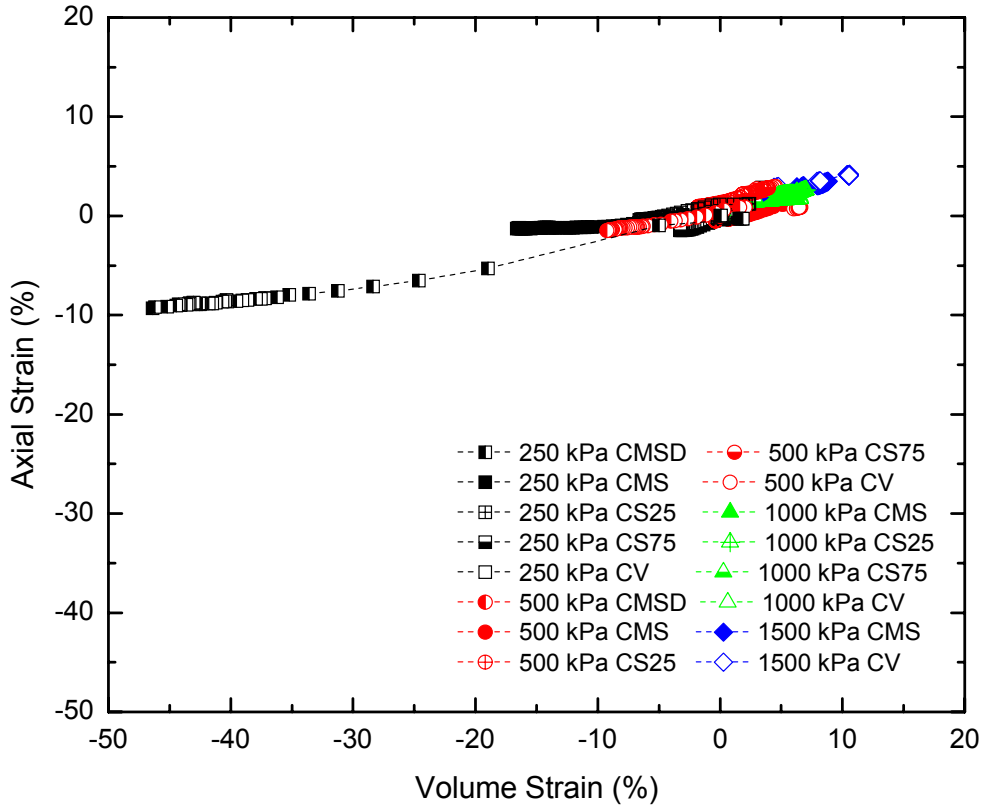

Figure 9.44. Axial strain versus volume strain – all infiltration tests.

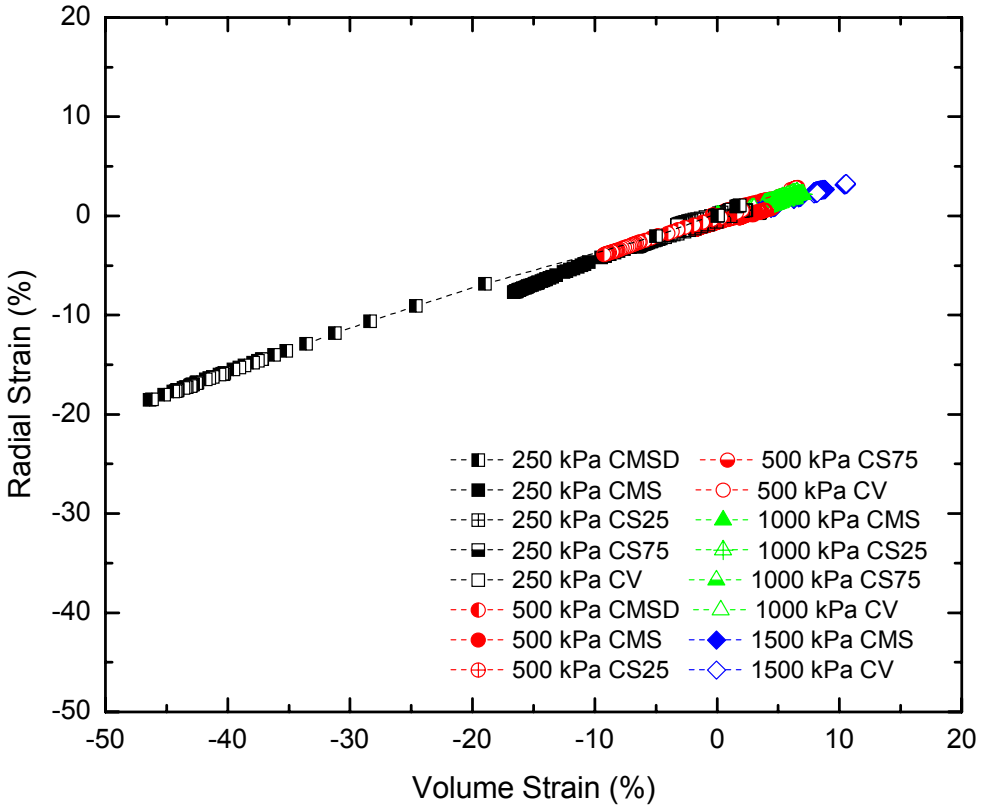

Figure 9.45. Radial strain versus volume strain – all infiltration tests.

CHAPTER 10: CONCLUSIONS AND RECOMMENDATIONS FOR FURTHER WORK

10.1 Review and Summary of the Work

This research is aimed at identifying the influence of boundary conditions during liquid infiltration of a swelling clay-sand soil. Laboratory testing and numerical modeling were performed to examine this hypothesis. The laboratory testing included development of a new liquid infiltration apparatus that combined measurement of stress and volume states including internal measurement of suction. The numerical modeling aspect included creation of a new capillary tube model for expansive soils, interpretation of the laboratory results, as well as using an empirical hydraulic model and D'Arcy's Law. The following sections summarize the work completed.

10.1.1 Development of Liquid Infiltration Apparatus with Controlled Boundary Conditions

An apparatus was modified for applying liquid infiltration in the triaxial cell. The apparatus applies radial flow to cylindrical specimens with internal measurement of suction using the Xeritron sensor. Simulated field boundary conditions are applied during liquid infiltration testing including constant volume, constant mean stress, and constant stiffness. After testing, spatial distributions of gravimetric water content and bulk density are measured, and dry density and saturation are calculated. Results indicate boundary conditions dominate soil behaviour including hydraulic, volume change, water uptake, and mean stress.

10.1.2 Development of a New Capillary Tube Model for Swelling Soils

A new capillary tube model was created which represents a swell mechanism to restrict flow as water moves along its length. The model was used to model flow behaviour during laboratory tests. Boundary conditions including open and closed models were applied to the model. Mechanisms for movement of air out of specimens including diffusion and outflow of air at the perimeter of the specimens were investigated. Model results were shown to represent both undrained and drained infiltration tests under controlled boundary conditions.

10.1.3 Development of a Limit for Unsaturated Swelling Materials

A second aspect of the numerical modeling included interpretation of the laboratory results. Laboratory test results were plotted in stress, volume, and water content states and interpreted. The boundary conditions applied during

infiltration were shown to dominate the water uptake, volume change and mean stress behaviour using in-test results, and post-test measurements. A limit of water content and specific volume for this particular material was shown from the results. The limit appeared to be a linear relationship over a wide range of gravimetric water content and specific volume. Once specimens reached the limit during liquid infiltration, expansion was required to allow further infiltration of water. The boundary and initial conditions determined the point where specimens reached this limit. A second limit in gravimetric water content – mean stress space was also identified for this particular water pressure applied (200 kPa). This was found using the end of test equilibrium points and later confirmed as agreeing with behaviour proposed by Chandler (2005). Previously established relationships of one-dimensional 'swell pressures' were converted to end of test mean stress levels and shown to agree with laboratory data produced in this research.

10.2 Principal Hypotheses and Conclusions

Hypothesis #1

Mechanical boundary conditions dominate the behaviour of a compacted unsaturated swelling clay-sand soil that is subjected to liquid infiltration. Boundary condition effects can cause compacted swelling clay to decrease in permeability while at constant volume (void ratio).

Hypothesis #2

Boundary conditions and swell characteristics control the flow of water through a capillary tube which incorporates transient changes to its diameter.

The new testing apparatus allowed examination of the first hypothesis. Mechanical boundary conditions were applied to swelling clay-sand soil specimens during liquid infiltration. The boundary conditions determined the volume – mean stress path taken during infiltration. This, in turn, permitted water uptake during tests. Interpretation of the results showed clear control of the behaviour of swelling clay-sand during liquid infiltration by the boundary conditions. In particular, the empirical analysis of the flow data showed the influence of the boundary conditions and the isotropic mean stress on the hydraulic behaviour. The MIP and SEM results showed decrease in the macro porosity resulting from isotropic compression and liquid infiltration boundary conditions and the models with constant flow area indicated how this would affect the soil's hydraulic conductivity. That is, at constant volume, hydraulic conductivity would decrease due to smaller sized pores for flow to occur through at constant void ratio (constant area for flow).

The capillary tube model created for this research gave insight to microscopic mechanisms that dominate behaviour on a macro scale. Open and closed boundary conditions drastically changed flow behaviour in the tube including the flow rate and total inflow. Swell characteristics applied to the boundary

conditions also limited progression of the water-air interface as the tube contracted once in contact with water. Mechanisms for air movement out of closed tubes, including diffusion and physical movement of air, showed that the model can be used to analyze new and proposed behaviour. Model output was used to represent flow measured in the laboratory apparatus. Both the boundary conditions and swell characteristics combined to control movement in this type of capillary tube model. Finally, the constant area capillary models which showed the influence of the pore size on inflow through two (2) models with constant cross-sectional area.

The following conclusions can be drawn from this research:

1. Behaviour of swelling clay material during liquid infiltration is dominated by the boundary conditions. Boundary conditions determine the volume change – mean stress changes that occur during infiltration on swelling clay. Expansion determines how much water uptake is possible as well as the mean stress increase required to maintain the desired path. Traditionally swelling soils are defined in terms of their 'swelling pressure' and swell potential. These are simply the bounds of swelling behaviour represented in laboratory tests as constant volume and constant mean stress boundary conditions. Between there is an infinite number of flexible boundary conditions which can be applied.

These findings have important implications for a wide range of engineering applications from a deep geologic repository to foundation engineering. In order

to properly model these systems, the boundary conditions must be known to predict swelling induced mean stresses and/or volume changes accurately. In design of a deep geologic repository, insights can be gained from this research. For instance, constant mean stress boundary conditions should not be allowed to occur in areas where low mean stresses are located. From the laboratory results, this would result in extreme expansion during infiltration which would change the hydraulic-mechanical properties of the material. If this was followed by a drying stage, large secondary porosity would develop and channels for flow of groundwater would open up. In a foundation application, determination of vertical movement or swelling induced pressure on the basement walls could be performed from results of these tests on the specific soil.

2. Flow in a capillary tube model is controlled by its boundary conditions and swell characteristics. The capillary tube model allowed new understanding of flow occurring through swelling soils by incorporation of a swell mechanism. Model results revealed that flow behaviour observed in laboratory tests could be represented. It also allowed investigation of proposed mechanisms of air and water movement in the undrained tests.

3. Volume change and swelling induced mean stress changes can be modeled and new limits to behaviour were found. Interpretation of the laboratory results allowed volume change and mean stress increase predictions to be made over a wide range of initial volume and stress states. The water content – specific

volume limit provides the bounds for expansion and the direction towards which all liquid infiltration tests proceed. Another limit discovered was between mean stress and gravimetric water content. This relationship is valid, for the initial conditions and water pressure applied (200 kPa) over the range of stresses examined in this research. At some higher mean stress, when that water pressure is applied, no increase in water content would occur. This is due to lack of pore space and the mean stress being greater than the pressure from expansion of the clay peds. The mean stress limit would be dependent on initial water content. Decreasing the initial water content would lower the limit in water content – mean stress space but the water content – specific volume limit would likely not be affected.

4. The Xeritron sensor provides accurate measurement of suction over a wider range than has previously been possible for sensors of this size. Internal measurement of suction is important because it is a stress state variable. Previous sensors were limited in suction range measurement while the Xeritron sensor is able to measure RH from 0-100% which spans the entire suction range.

5. A three-dimensional water retention curve or soil water characteristic curve (WRC or SWCC) is required for soils which experience changes in volume during changes in water content. Implicit in two (2) dimensional WRCs is that volume remains relatively constant throughout measurement, but this cannot be assumed in all cases. The laboratory measurements showed a wide range of

water contents and volumes associated with relatively small differences in suction measurements. In order to fully define the WRC, soil volume, gravimetric water content, and suction must be determined.

10.3 Recommendations for Future Work

1. With the current system the following work is recommended:

a. Perform liquid infiltration tests over a wider range of initial water contents and water pressures. Tests performed for this research all involved specimens with the as-compacted water content and density. Drying of specimens in the triaxial cell using the vapour equilibrium apparatus or under zero stress states would allow investigation of the influence of initial water content on behaviour. A water content – specific volume – mean stress relationship at end of test was found from this research and these tests would extend the relationship to different initial states. Testing using higher suctions would also allow the extended measurement range of the Xeritron sensor to be used. A combination of drying – wetting tests would also investigate the hysteretic behaviour of swelling clay-sand material.

b. Perform drained radial infiltration tests under constant mean stress, constant volume and constant stiffness boundary conditions over a range of isotropic compression and water pressure levels. Although suction measurement is not possible in the radial drained apparatus, values can be interpreted from a

three-dimensional water retention curve. Also, perform drained vertical infiltration tests on 25 mm tall specimens to determine the variation of vertical to horizontal hydraulic conductivity. Previous conductivity measurements on this clay-sand material were performed in a constant volume apparatus. This apparatus allows determination of hydraulic conductivity while volume and stress states are measured. In the undrained tests, absolute hydraulic conductivity values cannot be explicitly interpreted without complicated back analysis. Performing drained infiltration tests under a range of pressures and boundary conditions would allow explicit determination of the validity of D'Arcy's Law and interpretation of conductivity values. Infiltration in a deep geologic repository is a three-dimensional application. As such the vertical to horizontal ratio of conductivity is likely to impact water uptake.

c. Perform isotropic compression and triaxial shearing tests on specimens following liquid infiltration. Determination of both isotropic and shear yield curves for specimens that have been subjected to liquid infiltration under controlled boundary conditions could be performed.

d. Determine the bounds of swell potential by testing over higher isotropic compression levels. A limit to water infiltration was proposed based on the decreasing expansion and mean stress increase observed with increasing isotropic compression level. Laboratory measurement of this limit would provide insight to the limits of behaviour.

2. Determine where the air is going during undrained infiltration. During the isothermal test, infiltration rates were significantly lower than anticipated. During these laboratory infiltration tests, air was determined to be diffusing through the water phase based on the capillary tube model. Explicit determination should be performed by creation of a new apparatus in which visual determination of the movement of air can be attained. Although ideal, use of a triaxial apparatus is not necessarily required as a clear Lucite box could be manufactured in which diffusion or physical movement of air could be confirmed under differing hydraulic boundary conditions.

3. Creation of a three-dimensional capillary tube model from the single tube model developed in this research. The three-dimensional model could incorporate bulk volume changes along with micro structural changes to the pore sizes. The capillary tube model should remain consistent to network models and not incorporate D'Arcy's Law at the pore scale. The pore structure should be based on MIP measurements and SEM photography to ensure proper representation of the physical specimens. Results from the capillary tube model could be directly calibrated to the laboratory results instead of having to normalize the data.

4. Numerical modeling of the isothermal experiment using the new swell limit coupled with a hydraulic model for this swelling clay-sand soil. This model is

currently being calibrated by another student based on laboratory tests performed in this research.

5. Perform laboratory infiltration tests at higher temperatures. In a deep geologic repository, temperatures could be elevated during water uptake. Performing similar infiltration tests at higher temperatures would allow investigation of the thermal swell characteristics of swelling materials. This could be followed by numerical modeling of the laboratory tests to calibrate a Thermal-Hydraulic-Mechanical model which could then be used to re-analyze AECL's Buffer-Container Experiment.

REFERENCES

ASTM D 422. Standard test method for measurement of particle size analysis of soils. ASTM, Philadelphia, Pennsylvania, USA.

ASTM D 2216. Standard test method for measurement of laboratory determination of water (moisture) content of soil and rock by mass. ASTM, Philadelphia, Pennsylvania, USA.

ASTM D 4318. Standard test method for measurement of liquid limit, plastic limit and plasticity index of soils. ASTM, Philadelphia, Pennsylvania, USA.

ASTM D 4546. Standard test method for measurement of onedDimensional swell or settlement potential of cohesive soils. ASTM, Philadelphia, Pennsylvania, USA.

Abichou, T., Benson, C.H. and Edil, T.B. 2004. Network model for hydraulic conductivity of sand-bentonite mixtures. Canadian Geotechnical Journal, **41**(4): 698-712.

Agus, S.S. and Schanz, T. 2005. Swelling pressures and soil-water characteristic curves of a highly compacted bentonite-sand mixture. In Proceedings of the International Conference - From Experimental evidence towards Numerical Modeling of Unsaturated Soil, Weimar, Germany, Springer Proceedings in Physics, Tom Schanz (Ed.), **1**: 241-256.

Al-Shamrani, M.A. and Al-Mhaidib, A.I. 2000. Swelling behaviour under oedometric and triaxial loading conditions. GeoDenver 2000: Advances in Unsaturated Geotechnics, ASCE, 344-360.

Alonso, E.E., Gens, A. and Josa, A. 1990. A constitutive model for partially saturated soils. Geotechnique, **40**(3): 405-430.

Alonso, E.E., Vaunat, J. and Gens, A. 1999. Modelling the mechanical behaviour of expansive clays. Engineering Geology, **54**(2): 173-183.

Anderson, D.E.S. 2003. Evaluation and comparison of mechanical and hydraulic behavour of two engineered clay sealing materials. M.Sc. Thesis, Department of Civil Engineering, University of Manitoba, (Winnipeg, Manitoba).

Barbour, S.L. 1998. The soil-water characteristic curve: a historical perspective. Canadian Geotechnical Journal, **35**: 873-894.

Barden, L. and Sides, G. R. 1970. Engineering behavior and structure of compacted clay. Journal of Soil Mechanics and Foundation Engineering, ASCE, **96**(SM4): 1171-1200.

Bartley, J.T. and Ruth, D.W. 1999. Relative permeability analysis of tube bundle models. Transport in Porous Media, **36**: 161-187.

Bishop, A.W. 1959. The principle of effective stress. Teknisk Ukebald, **106**(39): 859-863.

Bishop, A.W. and Wesley, L.D. 1975. A hydraulic triaxial apparatus for controlled stress path testing. Geotechnique, **25**: 657-670.

Blatz, J.A. 2000. Elastic-plastic modeling of unsaturated high plastic clay using results from a new triaxial test with controlled suction. Ph.D. Thesis, Department of Civil Engineering, University of Manitoba, (Winnipeg, Manitoba).

Blatz, J.A., Anderson, D.E.S., Graham J. and Siemens G.A. 2003. Evaluation of yielding in unsaturated clays using an automated triaxial apparatus with controlled suction. Invited Lecture. International Conference From Experimental Methods Towards Numerical Modeling of Unsaturated Soils, Bauhaus-Universität, Weimar, Germany, September 2003, 285-300.

Blatz J.A., Anderson, D.E.S. and Siemens, G.A. 2006. Evaluation of the transitional inelastic behaviour of unsaturated clay-sand mixtures. Submitted to Canadian Geotechnical Journal, In Review.

Blatz, J.A. and Graham, J. 2000. A system for controlled suction in triaxial tests. Géotechnique, **50**(4): 465-469.

Blatz, J.A. and Graham, J. 2003. Elastic-plastic modeling of unsaturated soil using results from a new triaxial test with controlled suction. Géotechnique, **53**(1): 113-122.

Blatz J.A., Graham J. and Chandler N.A. 2002. Influence of suction on the strength and stiffness of compacted sand–bentonite. Canadian Geotechnical Journal, **39**: 1005-1015.

Blatz, J.A. and G.A. Siemens. 2004. Assessing the behaviour of unsaturated buffer subjected to wetting conditions: updated equipment and preliminary results. Ontario Power Generation Report Number: 06819-REP-01300-10083-R00, 38 pages.

Blatz, J.A. and Siemens, G.A. 2005. Assessing the behaviour of unsaturated buffer subjected to wetting conditions. Ontario Power Generation Report Number: 06819-REP-01300-10097-R00, 147 pages.

Blatz, J.A. and Siemens, G.A. 2006. Characterization of material properties of light and dense backfill for numerical modeling. Ontario Power Generation Report Number: 06819(UF)-03782.02-T5, 57 pages.

Blatz, J., Tang, G.X., Graham, J. and Wan, A. 1999. Psychrometer techniques for measuring suction in the triaxial test. Proceedings of the 52nd Canadian Geotechnical Conference, Regina, Saskatchewan, 617-622.

Budhu, M. 2000. Soil mechanics & foundations. John Wiley & Sons, Inc. New York. 586 pages.

Castellanos, E., Gens, A., Lloret, A. and Romero, E. 2006. Influence of water chemistry on the swelling capacity of a high-density bentonite. Geotechnical Special Publication No. 147: Proceedings of the Fourth International Conference on Unsaturated Soils, Carefree, Arizona, 2-6 April 2006, **1**: 962-972.

Chandler, N.A. 2000. Water inflow calculations for the isothermal buffer-rock-concrete plug interaction test. Ontario Power Generation Report Number: 06819-REP-01200-10046-R0, 40 pages.

Chandler, N.A. 2005. Private email communication received 19 May 2005.

Chen, R. and Ng, C.W.W. 2005. Wetting and anisotropic consolidation behaviour of an expansive clay. International Symposium Advanced Experimental Unsaturated Soil Mechanics, Trento, Italy, 27-29 June 2005, 157-162.

Chenu, C., Bissonnais, Y.L. and Arrouays, D. 2000. Organic Matter Influence on Clay Wettability and Soil Aggregate Stability. Soil Science Society of America Journal, **64**: 1479-1486.

Corey, E.C. 1957. Measurement of air and water permeability in unsaturated soil. Proceedings of the Soil Science Society America, **21**: 7-11.

Corey, A.T. 1977. Mechanics of Heterogeneous Fluid in Porous Media. Water Resources Publ., Fort Collins, CO, 259 pp.

Crilly, T. 1996. Unload-reload tests on saturated illite specimens at elevated tempreature. M.Sc. Thesis, Department of Civil Engineering, University of Manitoba, (Winnipeg, Manitoba).

Cui, Y.J. and Delage, P. 1996. Yielding and plastic behaviour of an unsaturated compacted silt. Geotechnique, **46**(2): 291-312.

Cui, Y.J., Loiseau, C. and Delage, P. 2001. Water transfer through a heavily compacted swelling soil. 6th International Workshop on Key Issues in Waste Isolation Research (KIWIR), Paris, 28-30 November 2001, 43-60.

Cui, Y.J., Yahia-Aissa, M. and Delage, P. 2002. A model for the volume change behaviour of heavily compacted swelling clays. Engineering Geology, **64**: 233-250.

D'Arcy, H. 1856. Les Fontaines Publiques de la Ville do Dijon. Dalmont, Paris.

Datcheva, M. and Schanz, T. 2003. Anisotropic bounding surface plasticity with rotational hardening for unsaturated frictional materials. Journal De Physique, IV:JP, **105**: 305-312.

Davis, R.O. and Selvadurai, A.P.S. 1996. Elasticity and geomechanics. Cambridge University Press. 201 pages.

Delage, P., Audiguier, M., Cui, Y.J. and Howat, M.D. 1996. Microstructure of a compacted silt. Canadian Geotechnical Journal, **33**(1): 150-158.

Delage, P and Graham, J. 1995. Understanding the behaviour of unsaturated soils requires reliable conceptual models: state of the art report. Proceedings of the 1st International conference on unsaturated soils (eds. E.E. Alonso and P. Delage), 1223-1256.

Delage, P., Howat, M.D. and Cui, Y.J. 1998. The relationship between suction and swelling properties in a heavily compacted unsaturated clay. Engineering Geology, **50**: 31-48.

Dixon, D.A. 1994. Sodium bentonites of Canada, the United States and Mexico: sources, reserves and properties. Engineering Materials for Waste Isolation, CSCE-Engineering Division-Special Publication, 37-65.

Dixon, D.A. 1995. Towards an understanding of water structure and water movement through dense clays. Ph.D. Thesis, University of Manitoba.

Dixon, D.A., Campbell, S.L. and Hnatiw, D.S.J. 1994. Preplacement quality control and as-placed properties of the buffer materials used in the URL isothermal buffer experiment. AECL Technical Record, TR-612, COG-94-35.

Dixon, D.A., Chandler, N.A., and Baumgartner, P. 2002. The influence of groundwater salinity and influences on the performance of potential backfill materials. Proc. 6th International Workshop on Design and Construction of Final Repositories, "Backfilling in Radioactive Waste Disposal", Brussels, March 2002.

Dixon, D., Chandler, N., Graham, J. and Gray, M.N. 2002. Two large-scale sealing tests conducted at Atomic Energy of Canada's underground research laboratory: the buffer-container experiment and the isothermal test. Canadian Geotechnical Journal, **39**: 503-518.

Dixon, D.A., Graham, J. and Gray, M.N. 1999. Hydraulic conductivity of clays in confined tests under low hydraulic gradients. Canadian Geotechnical Journal, **36**: 815-825.

Dixon, D.A., Gray, M.N. and Graham, J. 1996. Swelling and hydraulic properties of bentonites from Japan, Canada and USA. Proceedings of the second International Congress on Environmental Geotechnics, Osaka, Japan, 5-8 November 1996, 43-48.

Fatt, I.I. 1956. The network model of porous media, I. Capillary pressure characteristics. AIME Petroleum Transactions, **8**(7): 144-177.

Fredlund, D.G. and Morgenstern, N.R. 1977. Stress State Variables for Unsaturated Soils. Journal of the Geotechnical Engineering Division, Proceedings of the ASCE, **103**(GT5): 447-467.

Fredlund, D.G. and Rahardjo, H. 1993. Soil mechanics for unsaturated soils. Wiley-Interscience, New York.

Fredlund, D.G. and Pham, H.Q. 2006. A volume-mass constitutive model for unsaturated soils in terms of two independent stress state variables. Geotechnical Special Publication No. 147: Proceedings of the Fourth International Conference on Unsaturated Soils, Carefree, Arizona, 2-6 April 2006, **1**: 105-134.

Fredlund, D.G. and Xing, A. 1994. Equations for the soil water characteristic curve. Canadian Geotechnical Journal, **31**: 521-532.

Gallipoli, D., Gens, A., Sharma, R. and Vaunat, J. 2003. An elasto-plastic model for unsaturated soil incorporating the effects of suction and degree of saturation on mechanical behaviour. Geotechnique, **53**(1): 123-135.

Garcia-Bengochea, I., Lovell, C.W. and Altschaffl, A.G. 1979. Pore distribution and permeability of silty clays. Journal of the Geotechnical Engineering Division, Proceedings of the ASCE, **105**(GT7): 839-856.

Garitte, B., Vaunat, J. and Gens, A. 2006. A constitutive model that incorporates the effect of suction in cemented geological materials. Geotechnical Special Publication No. 147: Proceedings of the Fourth International Conference on Unsaturated Soils, Carefree, Arizona, 2-6 April 2006, **2**: 1944-1955.

Gelmich-Halayko, K.S. 1998. Gas flow in compacted clays. M.Sc. Thesis, Department of Civil Engineering, University of Manitoba, (Winnipeg, Manitoba).

Gens, A. and Alonso, E.E. 1992. A framework for the behaviour of unsaturated swelling clays. Canadian Geotechnical Journal, **29**:1013-1032.

Gouy, G. 1910. Sur la constitution de la charge electrique a la surface d'un electrolyte. Anniue Physique (Paris). **4**(9): 457-468.

Graham, J., Tang, X., Wiebe, B., Rajapakse, R.K.N.D. and Zhou, Y. 1995. Progress report on second year of contract no. WS102679: Modeling of Sand-bentonite Buffer for use in the Canadian Nuclear Fuel Waste Management Program. AECL-Research., July 1995. 170 pages.

Graham, J., Gelmich Halayko, K., Hume, H., Kirkham, T., Gray, M. and Oscarson, D. 2002. A capillarity-advective model for gas break-through in clays. Engineering Geology, **64**: 273-286.

Gray, M.N., S.C.H. Cheung and D.A. Dixon. 1984. The influence of sand content on swelling pressures developed by statically compacted Na-bentonite. Atomic Energy of Canada Limited Report, AECL 7825.

Hilf, J.W. 1956. An investigation of pore-water pressure in compacted cohesive soils. Ph.D. dissertation, Tech. Memo. No. 654, U.S. Department of the Interior, Bureau of Reclamation, Design and Construction Division., Denver, CO, 654 pages.

Hillel, D. 1980. Fundamentals of soil physics. London: Academic Press.

Hoffman, C., Romero, E. and Alonso, E.E. 2006. Hydro-mechanical small-scale tests on compacted bentonite. Geotechnical Special Publication No. 147: Proceedings of the Fourth International Conference on Unsaturated Soils, Carefree, Arizona, 2-6 April 2006, **1**: 973-984.

Huang, S., Fredlund, D.G. and Barbour, S.L. 1998. Measurement of the coefficient of permeability for a deformable unsaturated soil using a triaxial permeameter. Canadian Geotechnical Journal, **35**: 426-432.

Hume, H.B. 1999. Gas breakthrough in compacted Avonlea bentonite. M.Sc. Thesis, Department of Civil Engineering, University of Manitoba, (Winnipeg, Manitoba).

Jones, D.E., Jr. and Holtz, W.G. 1973. Expansive soils-the hidden disaster: Civil Engineering, **43**(8): 49-51.

Juang, C.H. and Holtz, R.D. 1986. Fabric, pore size distribution and permeability of sandy soils. ASCE Journal of Geotechnical Engineering, **112**(9): 855-868.

Katti, D.R. and Shanmugasundaram, V. 2001. Influence of swelling on the microstructure of expansive clays. Canadian Geotechnical Journal, **38**: 175-182.

Kaye, G.W.C. and Laby, T.H. 1973. Tables of Physical and Chemical Constants. 14th ed. Longman, 386 pages.

Kirkham, T. 1995. Development of test equipment and procedures for determination of the gas-breakthrough pressure of compacted clay materials with preliminary results. M.Sc. Thesis, Department of Civil Engineering, University of Manitoba, (Winnipeg, Manitoba).

Kjartanson, B.H., Chandler, N.A., Wan, A.W.L., Kohle, C.L. and Roach, P.J. 1992. Use of a method specification for in situ compaction of clay-based barrier materials. Proceedings of the International High- Level Radioactive Waste Management Conference, Las Vegas, Nevada, April 1992, 1129-1136.

Komine, H. and Ogata, N. 1994. Experimental study of swelling characteristics of compacted bentonite. Canadian Geotechnical Journal, **31**: 478-490.

Komine, H. and Ogata, N. 2004. Predicting swelling characteristics of bentonites. Journal of Geotechnical and Geoenvironmental engineering. **130**(8): 818-829.

Komornik, A., Livneh, M. and Smucha. 1980. Shear strength and swelling of clays under suction. Proceedings of the 4th International Conference on Expansive Soils – Denver, Colorado, 206-226.

Lambe, T.W. and Whitman, R.V. 1969. Soil Mechanics. Wiley, New York, 553 pages.

Leroueil, S., Bouclin, G., Tavenas, F., Bergeron, L. and Rochelle, P.LA. 1990. Permeability anisotropy of natural clays as a function of strain. Canadian Geotechnical Journal, **27**: 568-579.

Likos, W.J. 2004. Measurement of crystalline swelling in expansive clay. Geotechnical Testing Journal. **27**(6): 1-7.

Lingnau, B.E. 1993. Consolidated undrained triaxial behaviour of a sand-bentonite mixture at elevated temperature. Ph.D. Thesis, Department of Civil Engineering, University of Manitoba, (Winnipeg, Manitoba).

Maak, P. and G.R. Simmons. 2005. Deep geologic repository concepts for isolation of used fuel in Canada. Proc. Canadian Nuclear Society conference Waste Management, Decommissioning and Environmental Restoration For Canada's Nuclear Activities: Current Practices and Future Needs, 8-11 May 2005, Ottawa.

Mitchell, J.K. 1993. Fundamentals of Soil Behavior, Wiley, New York, USA.

Mohamed, A-M.O., Yong, R.N., Caporouscio, F., Cheung, S.C.H., and Kjartanson, B.H. 1993. A coupled heat and water flow apparatus. Geotechnical Testing Journal, **16**(1): 85-99.

Murray, E.J. 2002. An equation of state for unsaturated soils. Canadian Geotechnical Journal, **39**: 125-140.

Nofziger, D. L. and D. Swartzendruber. 1976. Water content and bulk density during wetting of a bentonite-silt column. Soil Science Society of America Journal **40**: 345-348.

Oka, F., Kodaka, T., Kimoto, S., Kim, Y.-S and Yamasaki, N. 2006. An elasto-viscoplastic model and multiphase coupled FE analysis for unsaturated soil. Geotechnical Special Publication No. 147: Proceedings of the Fourth International Conference on Unsaturated Soils, Carefree, Arizona, 2-6 April 2006. **2**: 2039-2050.

Oswell, J.M. 1991. Elastic-plastic behaviour of a sand-bentonite mixture. Ph.D. Thesis, Department of Civil Engineering, University of Manitoba, (Winnipeg, Manitoba).

Parker, J.C., Amos, D.F. and Sture, S. 1980. Measurement of swelling, hydraulic conductivity and shear strength in a multistage triaxial test. Soil Science Society Journal of America, **44**: 1133-1138.

Priyanto, D.G., Blatz J.A. and Siemens, G.A. 2006. Evaluation of Two Constitutive Models to Simulate Behavior during Constant Volume Infiltration on a Swelling Clay Soil. Geotechnical Special Publication No. 147: Proceedings of the Fourth International Conference on Unsaturated Soils, Carefree, Arizona, 2-6 April 2006, **1**: 985-996.

Richie, E. B. and R. R. Schnabel. 1992. Parameter estimation of the coefficients in soil hydraulic equations from steady-state unsaturated flow. Ground Water **30**(4): 515-522.

Ridley, A.M. and Wray W.K. 1996. Suction measurement - Theory and Practice. A state-of-the-art-review. In Unsaturated Soils: Proc. 1st International Conference on Unsaturated Soils, Paris (Eds. Alonso & Delage), **3**: 1293-1322.

Rolland, S., Stemmelen, D. and Moyne, C. Experimental hydraulic measurements in an unsaturated swelling soil using the dual-energy gamma –ray technique. International Symposium Advanced Experimental Unsaturated Soil Mechanics, Trento, Italy. 27-29 June 2005, 305-310.

Roscoe, K.H. and Burland, J.B. 1968. On the generalised stress strain behaviour of 'wet clay'. Engineering plasticity. Edited by J. Heyman and F.A. Leckie. Cambridge University Press, 535–609.

Rose, W. 1957. Studies of Waterflood Performance, III. – Use of Network Models. Illinois State Geological Survey Circular 237, 31 pages.

RSView32. Getting Results Guide. USA. Rockwell Software Inc. 1999.

Russell, S.B. and G.R. Simmons. 2003. Engineered barrier system for a deep geologic repository. Presented at the 2003 International High-Level Radioactive Waste Management Conference, March 30-April 2, 2003, Las Vegas, NV.

Saadat, F. 1989. Constitutive modeling of the behaviour of a sand-bentonite mixture. Ph.D. Thesis, Department of Civil Engineering, University of Manitoba, (Winnipeg, Manitoba).

Schwartz, A.M. 1969. Capillarity, theory and practice. Industrial and Engineering Chemistry, **61**(1): 10-21.

Siemens, G.A. and Blatz, J.A. 2005. Soil suction measurement using the Xeritron Sensor in two different types of infiltration tests on a swelling soil. International Symposium Advanced Experimental Unsaturated Soil Mechanics, Trento, Italy. 27-29 June 2005, 23-26.

Siemens, G.A. and J.A. Blatz. 2006. A triaxial apparatus for applying liquid infiltration under controlled boundary conditions with internal suction measurement. ASCE Geotechnical Journal of Geotechnical and Geoenvironmental Engineering, In Review.

Siemens, G.A., Blatz, J.A. and Priyanto, D.G. 2006. Results of long-term infiltration tests on an unsaturated swelling clay. Geotechnical Special Publication No. 147: Proceedings of the Fourth International Conference on Unsaturated Soils, Carefree, Arizona, 2-6 April 2006, **1**: 939-950.

Sisler, H.H., Vanderwerf, C.A. and Davidson, A.W. 1953. General Chemistry – A systematic approach. New York: Macmillan.

Slaughter, M. and Earley, J.W. 1965. Mineralogical and geological significance of the Mowry Bentonites, Wyoming. Geological Society of America, Special Paper 83.

Spanner, D.C. 1951. The peltier effect and its use in the measurement of suction pressure. Journal of Experimental Botany, **2**: 145-168.

Sridharan, A. and Gurtug, Y. 2004. Swelling behaviour of compacted fine-grained soils. Engineering Geology, **72**: 9-18.

Stern, O. 1924. Zur Theorie der Elektrolytischen Doppelschriht, Zeitschrift Electrochem. **30**: 508-516.

Stokes, R.H. and Robinson, R.A. 1948. Electrolyte solutions. 2nd ed. Butterworths, London, United Kingdom.

Sun, B.C.-C. 1986. Stress-strain properties in sand-clay buffer materials. M.Sc. Thesis, University of Manitoba, (Winnipeg, MB).

Tanaka, N. 1995. Thermal elastic plastic behaviour and modeling of saturated clay. Ph.D. Thesis, Department of Civil Engineering, University of Manitoba, (Winnipeg, Manitoba).

Tang, G.X. 1999. Suction characteristics and elastic-plastic modeling of unsaturated sand-bentonite mixture. Ph.D. Thesis, Department of Civil Engineering, University of Manitoba, (Winnipeg, Manitoba).

Tang, G.X. and Graham, J. 2002. A possible elastic-plastic framework for unsaturated high-plastic clay soils. Canadian Geotechnical Journal, **39**(4): 894-907.

Thakur, V.K.S. and Singh, D.N. 2005. Rapid determination of swelling pressure of clay minerals. Journal of Testing and Evaluation. **33**(4): 239-245.

Thomas, H.R. Cleall, P.J. Chandler, N. Dixon, D. and Mitchell, H.P. 2003. Water infiltration into a large-scale in-situ experiment in an underground research laboratory. Geotechnique, **53**(2): 207-224.

Toll, D.G. 1990. A framework for unsaturated soil behaviour. Geotechnique, **40**(1): 31-44.

Toll, D.G. 1996. A conceptual model for the drying and wetting of soil. 1st International Conference on Unsaturated Soils, UNSAT95, Paris, France, 6-8 September 1995, 805-810.

Topp, G. C. and J. L. Davis. 1982. Measurement of soil water content using time domain reflectometry. Canadian Hydrology Symposium: 82, 14-16 June 1982, Fredericton, New Brunswick. 269-287.

Tripathy, Snehasis, Sridharan, and Schanz, T. 2004. Swelling pressures of compacted bentonites from diffuse double layer theory. Canadian Geotechnical Journal, **41**: 437-450.

Tuller, M. and Or, D. 2003. Hydraulic functions for swelling soils: pore scale considerations. Journal of Hydrology. **272**: 50-71.

Tuma, J.J. 1976. Handbook of Physical Calculations. New York: McGraw-Hill, 370 pages.

Vu, H. and Fredlund, D.G. 2004. The prediction of one, two- and three-dimensional heave in expansive soils. Canadian Geotechnical Journal, **41**: 1-25.

Wan, A.W.-L. 1987. Compaction and strength characteristics of sand-clay buffer material formed at swelling pressure-water content equilibrium. M.Sc. thesis. University of Manitoba.

Wan, A.W.L. 1996. The use of thermocouple psychrometers to measure in-situ suctions and water contents in compacted clays. Ph.D. Thesis, Department of Civil and Geological Engineering, University of Manitoba, (Winnipeg, Manitoba).

Wan, A.W.L., Gray, M.N. and Graham, J. 1996. On the relations of suction, moisture content and soils structure in compacted clays. 1st International Conference on Unsaturated Soils, UNSAT95, Paris, France, 6-8 September 1995, 215-222.

Wan, A.W.L., Graham, J. and Gray, M.N. 1990. Influence of soil structure on the stress-strain behaviour of sand-bentonite mixtures. Geotechnical Testing Journal, **13**(3): 179-187.

Wheeler, S.J. 2006. Constitutive Modelling of Unsaturated Soils. Plenary Session given at the Fourth International Conference on Unsaturated Soils, Carefree, Arizona, 2-6 April 2006.

Wheeler, S.J. and Sivakumar, V. 1995. An elasto-plastic critical state framework for unsaturated soil. Geotechnique. **45**(1): 35-53.

Wheeler, S. J., Sharma, R. J. and Buisson, M. S. R. 2003. Coupling of hydraulic hysteresis and stress–strain behaviour in unsaturated soils. Geotechnique, **53**(1): 41-54.

Wiebe, B.J. 1996. The effect of confining pressure, temperature, and suction on the strength and stiffness of unsaturated buffer. M.Sc. Thesis, Department of Civil and Geological Engineering, University of Manitoba, (Winnipeg, Manitoba).

Xeritron Relative Humidity Sensor Model XN 1018. (Company File), 23 September 2002, 3 pages.

Yarechewski, D.S. 1993. Constant mean effective stress tests on sand - bentonite specimens at elevated temperature. M.Sc. Thesis, University of Manitoba, Department of Civil and Geological Engineering, Winnipeg, MB.

Yin, J.-H. 1990. Constitutive modeling of time-dependent stress-strain behaviour of soils. Ph.D. Thesis, Department of Civil Engineering, University of Manitoba, Winnipeg, MB.

Young, J.F. 1967. Humidity control in the laboratory using salt solutions – a review. Journal of Applied Chemistry. **17**.

Young, R.N. and Warkentin, B.P. 1975. Soil properties and behaviour. Elseview: New York.

APPENDIX

Capillary Tube Computer Code

```
#include <iostream>
#include <fstream.h>
#include <vector.h>
#include <cmath>
#include <cstdlib>



/* This program models two-phase flow through a compacted sand-bentonite triaxial specimen.
The model is a single capillary tube that is lined with bentonite.  The expansive nature of bentonite is
modeled
by changing the area of the main tube with time.  Seepage into bentonite is modeled using
using smaller tubes along the periphery of the main tube.  As water seeps into the peripheral tubes, the
area
of the main tube changes at that location equal to the amount of water that flows into the peripheral
tubes.

Notes:
All dimensions (lengths and diameters) are in micrometer
Pressures are in Pa (Newtons / square meters)
Time is in second
Flow rate is in cubic micrometer/second
Viscosity is in Newton-second / square meter
Surface tension is in Newton / meter
Mass is in microgram
Density is in microgram / cubicmicrometer
Mass speed is in microgram / second
Diffusion coefficient is square meter / second
*/
```

```
// Declare Functions

float Usigma (float UsLa, float UsDiameter, int UsinterfaceBlock, float UsBlockLength, vector <float>
UsCurrentDiameter);
float Sum (int SumStart, int SumEnd, float SumLength, vector <float> SumCurrentDiameter);
float Dsigma (float DsLa, float DsDiameter, int DsinterfaceBlock, int DsNumberBlocks, float DsBlockLength,
vector <float> DsCurrentDiameter);
vector <float> pressureUpdate (int PUnumberBlocks, float PUusPress, float PUdsPress, float PUblockLength,
float PULaPressure, float PUcapPressLa, float PULa, float PULength, int PUinterfaceBlock);
void outputmatrix (int OMnumberBlocks, int OMtimeStepCounter, ofstream& OMfout, vector < vector <float> >
OMmatrix);
void outputvector (int OVtimeStepCounter, ofstream& OVfout, vector <float> OVvector);

int main()
{

int modelPause;

// Declare main and periphery tube variables

float l1, d1, l2, d2, d3, l3;


// Declare bentonite properties
//          - d1Min is the minimum diameter of the large tube allowed
//          - rate3 is the number of periphery tubes per micrometer of main tube

float d1Min, rate3;


// Declare boundary conditions variables and defaults

float usPress, dsPress;
int drained, modelStop=0;
```

```
// Declare fluid and gas properties

float lVisc, sigma, cosTheta, gVisc, gAvPress, gVol, gMolMass, gConst, gMass, gTemp;


// Declare air diffusion properties

float diffusionCoeff;


// Input model parameters from file
// Order Main tube length, Main tube diameter, Periphery tube length, Periphery tube diameter,
// Number of periphery tubes per length of main tube, Swell rate of bentonite, Minimum main tube diameter,
// Upstream liquid pressure, Downstream gas pressure, Drained end (1) or undrained end (0),
// Viscosity of liquid, Viscosity of gas, Surface tension of liquid, cos (theta) of interface
// Total volume of water, Diffusion coefficient of air through water

ifstream fin;
fin.open("tubeparam.txt");
fin >> l1 >> d1 >> l2 >> d2 >> d3;
fin >> rate3;
fin >> usPress >> dsPress >> drained;
fin >> lVisc >> gVisc >> sigma >> cosTheta;
fin >> diffusionCoeff;
fin.close();


// Declare model properties and defaults

int interfaceBlock, numberBlocks, timeStepCounter, periphTubeNumber, pressureBlocks, recordCounter,
laCounter, outputSize, laOutputSize, counter, l1Ratio;
float length, dummy, La, capPressLa, LaPressure, timeStepLength, blockLength, eotCriterion, currentTime,
deltaX, maxPeriphVolume, itDiameter, itPeriphTubeLa, itPeriphTubeVol;
length = l1 + l2;
dummy = 0.0;
La = 0.0;
interfaceBlock = 0;
```

```
capPressLa = 4*1000*1000*sigma*cosTheta/d1;
timeStepCounter = 0;
numberBlocks = 5000;
pressureBlocks = numberBlocks+1;
l1Ratio=floor(numberBlocks*l1/length);
blockLength = length / numberBlocks;
currentTime = 0;
recordCounter = 1;
laCounter=1;
outputSize = 0;
laOutputSize = 0;
deltaX = length / numberBlocks;
d1Min=d2;
periphTubeNumber = floor(rate3*l1/((l1/length)*numberBlocks));
l3 = ((d1*d1/4)-(d1Min*d1Min/4))/(rate3*d3*d3/4);
maxPeriphVolume = (3.14159*blockLength/4)*((d1*d1)-(d1Min*d1Min));
gVol = 3.14159*(d1*d1*l1+d2*d2*l2)/4;
gMolMass = 28.966;
gTemp = 298.16;
gConst = 8.31432;
gAvPress = 101300;
gMass = gAvPress*gVol*gMolMass/(1000000000*gConst*gTemp);



// Output properties to screen

cout << length <<" " << d1 << " " << d2 <<"\n";
cout << l3 <<" "<<d1Min<<" "<<d3<<"\n";
cout << rate3 << " "  << d1Min << "\n";
cout << usPress << " " << dsPress << " "  << drained << "\n";
cout << lVisc << " " << gVisc << " " << sigma << " " << cosTheta << "\n";
cout << La <<" "<<capPressLa<<" "<<timeStepLength<< " " <<numberBlocks<<" "<<"\n";
cout<< l1Ratio;
cin>>modelPause;
```

```
//  Declare periphery tube variables

int periphCounter, periphCounterPlus;
float dLadtI, dLaI, periphCapPress, periphDsPress;
periphCapPress = 1000*1000*4*sigma*cosTheta/d3;
periphDsPress = dsPress;



// Declare diameter, pressure, periphery tube volume, la matrices

typedef vector <float> floatRow;
typedef vector <floatRow> floatArray;


//  vectors for use in current timestep

floatRow currentDiameter (numberBlocks, d2);
floatRow currentPressure (pressureBlocks, dsPress);
floatRow currentPeriphTubeLa (numberBlocks, dummy);
floatRow currentPeriphTubeVol (numberBlocks, dummy);

counter=0;

while(counter*blockLength<l1)
{
currentDiameter[counter]=d1;
counter++;
}
```

```
//  Define output matrices and vectors

floatArray diameterDistribution (1, currentDiameter);
floatRow LaDistribution (1, dummy);
floatArray pressureDistribution (1, currentPressure);
floatRow timeDistribution (1, dummy);
floatArray periphLaDistribution (1, currentPeriphTubeLa);


// Declare Us, Ds variables

float Us, Ds, dLadt, dLa;
dLadt=1;

// Continue time step model until EOT criterion attained


while (La < length && dLadt>0)
{


//  update interface block number, Usigma, Dsigma, capPressLa LaPressure and pressure distribution for next
run

interfaceBlock = floor(numberBlocks*La/length);
Us = Usigma(La, currentDiameter[interfaceBlock], interfaceBlock, blockLength, currentDiameter);
Ds = Dsigma (La, currentDiameter[interfaceBlock], interfaceBlock, numberBlocks, blockLength,
currentDiameter);
capPressLa = 4*1000*1000*sigma*cosTheta/currentDiameter[interfaceBlock];

//  if downstream end is sealed calculate LaPressure and downstreamPressure using gasAveragePressure

if(drained < 1)
{
if(La<l1)
{
gVol = 3.14159*(d2*d2*l2+d1*d1*(l1-La))/4;
```

```
}
else
{
gVol = 3.14159*(d2*d2*(length-La))/4;
}
gAvPress = 1000000000*gMass*gConst*gTemp/(gVol*gMolMass);
LaPressure = ((usPress*Ds*gVisc)+(2*(gAvPress-capPressLa)*Us*lVisc))/((2*lVisc*Us)+(gVisc*Ds));
dsPress = (2*gAvPress)-LaPressure-capPressLa;
}
else
{
LaPressure = ((usPress*Ds*gVisc)-(capPressLa-dsPress)*Us*lVisc)/(lVisc*Us+gVisc*Ds);
}


//  calculate pressure distribution along total length

currentPressure = pressureUpdate (pressureBlocks, usPress, dsPress, blockLength, LaPressure, capPressLa,
La, length, interfaceBlock);


//  Calculate speed of interface

dLadt = (1/(32*currentDiameter[interfaceBlock]*currentDiameter[interfaceBlock]))*((usPress-
dsPress+capPressLa)/(lVisc*Us+gVisc*Ds));

if(dLadt>0)
{
timeStepLength = deltaX/dLadt;
dLa = dLadt*timeStepLength;
La = La + dLa;

cout<<"La is "<<La<<" "<<currentTime+timeStepLength<<"\n";
recordCounter++;
laCounter++;
```

```
// Calculate flow into peripheral tubes if the diameter of the block before interface is still greater than
minimum

if(rate3>0 && currentDiameter[(l1Ratio-1)]>d1Min && timeStepCounter > 0)
{

periphCounter = 0;
periphCounterPlus = periphCounter+1;



while ((periphCounter+1) < interfaceBlock)
{
//  Calculate increase in La for peripheral tube

if(currentDiameter [periphCounter] > d1Min)
{

dLadtI = ((d3*d3)/(32))*(( ((currentPressure [periphCounter]+currentPressure[periphCounterPlus])/2) +
periphCapPress - periphDsPress)/((lVisc*currentPeriphTubeLa [periphCounter]) + (gVisc * (l3-
currentPeriphTubeLa[periphCounter]))));
dLaI = dLadtI*timeStepLength;
itPeriphTubeLa = currentPeriphTubeLa [periphCounter] + dLaI;
itPeriphTubeVol = periphTubeNumber*currentPeriphTubeLa [periphCounter]*3.14159*d3*d3/4;


// Calculate decrease in diameter in main tube corresponding to water flow into peripheral tubes

itDiameter = sqrt(((blockLength*currentDiameter[periphCounter]*currentDiameter[periphCounter])-
(periphTubeNumber*dLaI*d3*d3))/blockLength);
if (itDiameter > d1Min)
{
currentDiameter [periphCounter] = itDiameter;
currentPeriphTubeLa [periphCounter] = itPeriphTubeLa;
}
else
{
```

```
currentDiameter [periphCounter] = d1Min;
currentPeriphTubeLa [periphCounter] = l3;
}


}

periphCounter++;
periphCounterPlus++;

}



}


currentTime = currentTime + timeStepLength;

}

//  if interface not moving forward and no diffusion, output last location of interface
else
{
LaDistribution.push_back (La);
timeDistribution.push_back (currentTime);


laOutputSize++;

}
```

```
//  update output vectors and matrices every 500 steps

if (recordCounter > 500 )
{
diameterDistribution.push_back (currentDiameter);
pressureDistribution.push_back (currentPressure);
periphLaDistribution.push_back (currentPeriphTubeLa);


outputSize++;
recordCounter = 1;
}

if (laCounter > 50)
{
LaDistribution.push_back (La);
timeDistribution.push_back (currentTime);


laOutputSize++;
laCounter = 1;
}


timeStepCounter++;


}
```

```
// if La does not reach end update output vectors and matrices with final values

if(La<length)
{
LaDistribution.push_back (La);
diameterDistribution.push_back (currentDiameter);
pressureDistribution.push_back (currentPressure);
timeDistribution.push_back (currentTime);
periphLaDistribution.push_back (currentPeriphTubeLa);

outputSize++;
}


cout<<outputSize<<" "<<timeStepCounter<<"\n";

// Output diameter distribution to text file

ofstream fout;

fout.open ("diameter.txt");
outputmatrix (numberBlocks, outputSize, fout, diameterDistribution);
fout.close();


// Output pressure distribution to text file

fout.open ("pressure.txt");
outputmatrix (pressureBlocks, outputSize, fout, pressureDistribution);
fout.close();
```

```
// Output la distribution to text file

fout.open ("la.txt");
outputvector (laOutputSize, fout, LaDistribution);
fout.close();


// Output time distribution to text file

fout.open ("time.txt");
outputvector (laOutputSize, fout, timeDistribution);
fout.close();


// Output peripheral la distribution to text file

fout.open ("periphla.txt");
outputmatrix (numberBlocks, outputSize, fout, periphLaDistribution);
fout.close();


}
```

```
// FUNCTIONS


/* This function calculates Usigma with inputs of current La, initial diameter of tube, block number where
interface is,
block length, and the vector of current tube diameter distribution */

float Usigma (float UsLa, float UsDiameter, int UsinterfaceBlock, float UsBlockLength, vector <float>
UsCurrentDiameter)
{

float UsUs, UsSum, UsBlockLa;

//  Determine length of la in interface block

UsBlockLa=UsLa;
while(UsBlockLa-UsBlockLength>0)
{
UsBlockLa = UsBlockLa-UsBlockLength;
}

UsSum = Sum (0, UsinterfaceBlock, UsBlockLength, UsCurrentDiameter);

UsUs = ((UsBlockLa) / (UsDiameter*UsDiameter*UsDiameter*UsDiameter))+ UsSum;


return UsUs;
}


/* This function calculates Dsigma with inputs of total length tube, current La, initial diameter of tube,
block number where interface is,
block length, and the vector of current tube diameter distribution */

float Dsigma (float DsLa, float DsDiameter, int DsinterfaceBlock, int DsNumberBlocks, float DsBlockLength,
vector <float> DsCurrentDiameter)
{
```

```
float DsDs, DsSum, DsBlockLa;

//  Determine length of la in interface block

DsBlockLa=DsLa;
while(DsBlockLa-DsBlockLength>0)
{
DsBlockLa = DsBlockLa-DsBlockLength;
}

DsSum = Sum (DsinterfaceBlock+1, DsNumberBlocks, DsBlockLength, DsCurrentDiameter);
DsDs = ((DsBlockLength - (DsBlockLa))/(DsDiameter*DsDiameter*DsDiameter*DsDiameter))+DsSum;




return DsDs;
}


/* This function performs summations for both Usigma and Dsigma functions using beginning of sum, one more
than end of sum
length of each block and current tube diameter distribution */

float Sum (int SumStart, int SumEnd, float SumLength, vector <float> SumCurrentDiameter)
{

int SumCounter=SumStart;
float SumSum = 0;

while (SumCounter < SumEnd)
{
SumSum = SumSum +
SumLength/(SumCurrentDiameter[SumCounter]*SumCurrentDiameter[SumCounter]*SumCurrentDiameter[SumCounter]*Sum
CurrentDiameter[SumCounter]);
SumCounter++;
}
```

```
return SumSum;
}


//  This function calculates the pressure distribution for the next time step

vector <float> pressureUpdate (int PUnumberBlocks, float PUusPress, float PUdsPress, float PUblockLength,
float PULaPressure, float PUcapPressLa, float PULa, float PULength, int PUinterfaceBlock)
{
typedef vector <float> floatRow;

floatRow PUpressure (PUnumberBlocks, 0.0);
int PUcounter = 0;

// Set upstream and downstream pressures
PUpressure[0]=PUusPress;
PUpressure[PUnumberBlocks]=PUdsPress;
PUcounter++;

while (PUcounter <=PUinterfaceBlock)
{
PUpressure [PUcounter] = PUusPress-((PUusPress - PULaPressure)*PUcounter*PUblockLength/PULa);

PUcounter++;
}

while (PUcounter < PUnumberBlocks)
{
PUpressure [PUcounter] = PULaPressure + PUcapPressLa - ((PULaPressure + PUcapPressLa -
PUdsPress)*((PUcounter*PUblockLength-PULa)/(PULength-PULa)));
PUcounter++;
}

return PUpressure;
}
```

```
//  This function outputs matrices to an open file


void outputmatrix (int OMnumberBlocks, int OMtimeStepCounter, ofstream& OMfout, vector < vector <float> >
OMmatrix)
{
int OMrowCounter = 0;
int OMcolCounter = 0;
int OMoutputCounter = 1;
int OMoutputCounterCol = 1;

while (OMcolCounter < OMnumberBlocks)
{

while (OMrowCounter <= OMtimeStepCounter)
{

if(OMoutputCounter = 10)
{
OMfout<<OMmatrix[OMrowCounter][OMcolCounter];
OMoutputCounter = 1;
}

OMrowCounter++;
OMoutputCounter++;

if (OMrowCounter <= OMtimeStepCounter)
{
OMfout<<" ";
}
}

OMfout<<"\n";
OMrowCounter = 0;
OMoutputCounter = 1;
OMoutputCounterCol=1;
```

```
OMcolCounter=OMcolCounter+10;

}

}


//  This function outputs vectors to an open file

void outputvector (int OVtimeStepCounter, ofstream& OVfout, vector <float> OVvector)
{
int OVcounter = 0;
int OVoutputCounter = 1;

while (OVcounter <= OVtimeStepCounter)
{

if(OVoutputCounter=4)
{
OVfout<<OVvector[OVcounter]<<"\n";
OVoutputCounter=1;
}
OVcounter++;
OVoutputCounter++;
}
}
```